

Crashworthiness and constitutive relationships for engineering materials

15th Technical Meeting, 2004
Metz, France

IDENTIFICATION OF METALLIC MATERIAL BEHAVIORS UNDER HIGH-VELOCITY IMPACT: A NEW TENSILE TEST

H. Abichou, O. Pantalé, I. Nistor, O. Dalverny and S. Caperaa

*L.G.P, C.M.A.O - Grandes Transformations Thermomécaniques Rapides
E.N.I.T, 47 Av d'Azereix BP 1629, 65016 Tarbes Cedex, France.
E-Mail : Hammadi.Abichou@enit.fr*

Summary: The main objective of this paper is to present a new tensile test used to identify metallic material behaviours under dynamic loading at high strain rates. The identification methodology adopted is based on numerical-experimental optimization and uses a combined Monte-Carlo and Levenberg-Marquardt algorithm developed by the CMAO team. The basic idea of this methodology is to compare predicted final results from finite element model (like geometrical dimensions of the deformed shape, etc.) to the same experimental results measured using a macro-photographic device. The experimental set-up is a ballistic gas gun used to launch the projectile, in vacuum conditions; up to 300m/s. Numerical simulations are carried out using Abaqus Explicit finite element code. The device used for conducting tensile testing at high strain rate encloses three principal parts: a target, a target support and a projectile. The target is designed in an attempt to ensure a useful zone of high plastic strain in tension. The paper ends by a presentation of an identification obtained by this test for two metallic materials (42CrMo4 Steel and Aluminum 2017T3) assumed to follow the Johnson-Cook strain-stress law.

INTRODUCTION

It has been widely demonstrated that the resistance of materials to applied loading depends significantly on the rate at which loads are applied. That is why a great interest has been accorded to the study of the impact at high strain rate in many mechanical domains, industrial activities (machining, sheet forming...) and transport infrastructure (aeronautic, cars ...). The objective is to predict the behaviour of material under such sollicitation, which explains the development of computational methods and specially finite element method. As the reliability and accuracy of obtained numerical results are directly conditioned by constitutive laws, an accurate identification of the material used is needed.

Our objective is the development of experimental tests and identification methodology of material constitutive laws specific to test types and adapted to high strain rates. This paper is concerned by a tensile test. Other tests (Taylor tests, shear tests, extrusion tests) have been already carried out [2] [3] [4][5].

Whatever the law identified by impact tests, the presented identification method implies the use of three tools or steps:

- a specific test to the studied law,
- a parameterised finite elements model of the test,
- an algorithm of optimisation allowing minimization of the difference between the experimental data and the responses resulting from the numerical simulation.

In this paper, we present an identification of two metallic materials (42CrMo4 Steel and Aluminium 2017T3) using a tensile test. These two materials are assumed to follow the Johnson-Cook strain-stress law.

IDENTIFICATION METHOD

The identification methodology used in this paper is based on a combination between experimental and numerical techniques. This combination is piloted by a numerical code based on the Monte Carlo method and the Levenberg-Marquardt algorithm. The identification methodology used is equivalent to an optimisation technique. The basic idea of this technique is to compare predicted results (easy to measure and to control like geometrical dimensions) obtained using a finite element model to the same experimental results. The difference between these two sets of parameters is minimised by the driving code.

The identification methodology is structured into two steps. In the first step a coarse research is done by a derived Monte-Carlo random-stochastic method. In the second step, a refinement of the research is achieved using a Levenberg-Marquardt algorithm, where results provided by coarse research are used as initial condition.

The idea to use a Monte-Carlo method for this kind of identification is related to the need of exploring the topological space parameters law with the aim of numerical simulation. The principal steps of the Monte-Carlo algorithm are described below:

1. Introduction of the starting input data;
2. Drawing of lots which generates the sets of parameters;
3. Solving the numerical model for all the sets of parameters;
4. Evaluating the objective function of each set of parameters;

5. If the convergence criteria is not satisfied, repositioning the new start point and return to the second step.

The accuracy of the results obtained and the rate of convergence are meaningfully influenced by the choice of the objective function. The objective function represents the difference (to be optimized) between experimental and numerical results. Now, according to the used methodology, two forms of the objective function are used:

Simple-test methodology:

In this methodology each attempted test is considered separately and an identification is made on each one. Consequently the identification is only based on the deviation between responses of one test and the numerical model corresponding. In this case, the Euclidian norm used for the objective function is:

$$f = \frac{1}{m} \sqrt{\sum_{j=1}^m w_r(j) \left(\frac{R_EF(j) - R_EXP(j)}{R_EXP(j)} \right)^2}$$

where m is total number of responses;
 R_EF is the vector of the finite element responses;
 R_EXP is the vector of experimental responses;
 w_r is the vector of the response weights.
 For more details concerning this subsection, refer [3].

Multi-test methodology:

The simple-test methodology gives as many tests of parameters as there are tests. The difficulty, thereafter, is to make the choice of the optimal set of parameters.

The alternative method recently developed is not to consider each test separately but to consider several tests at the same time and build the objective function with all the deviations between experimental and numerical responses.

In this methodology the objective function is written as follows:

$$f = \frac{1}{m.n} \sqrt{\sum_{i=1}^n \left(\sum_{j=1}^m w_r(j) \left(\frac{R_EF(ij) - R_EXP(ij)}{R_EXP(ij)} \right)^2 \right)}$$

where n is the number of the considered tests and m keeping the value for each test.

This methodology allows to make an average of the different parameters and to minimise the deviation between each experimental parameter of all the tests at the same time and the answers given by the different numerical models.

EXPERIMENTAL SET-UP: TENSILE TEST DEVICE

Domains (ranges) for which we develop the methodology of identification under high speed impact implies a level of high strain rate (10^5 s^{-1}). Because of this characteristic, a gas-gun device has been chosen to carry out impact tests. On the other hand post-mortem analyses of impacted specimens are needed.

The gas-gun has a calibre of 20 mm and a length of barrel of 1400 mm. The projectile can be propelled up to 350 m/s for a 30 gr mass, the propulsion being provided by a mixture compressed gas nitrogen-oxygen. All tests are achieved in vacuum conditions. Projectile velocities are measured just before impact by an opto-electronic system.

This gas-gun has been initially designed for the Taylor test. Making some adaptations and taking into account some specifications it can be exploited to set-up many other tests.

In this work we present a tensile test carried out by the help of this gas-gun. To identify the constitutive law, by such test, for studied materials, the test consists in launching a projectile into the target as showed in figure 1.

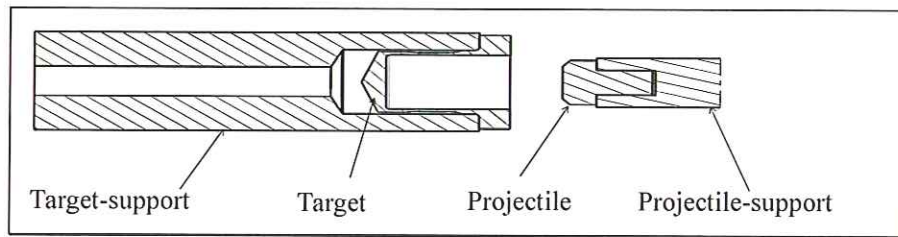


Figure 1: The tensile test device (schematic concept)

The device used for conducting tensile testing at high strain rate encloses three principal parts: a target, a target support and a projectile. The target support is designed to simplify the installation of the target in the gas launcher and to ensure a tensile loading. The projectile-support (in polycarbonate) ensures, by the help of a plastic O-ring, the sealing in the pneumatic part at the time of setting high pressure. Furthermore this latter will facilitate the displacement and guidance of the projectile in the barrel.

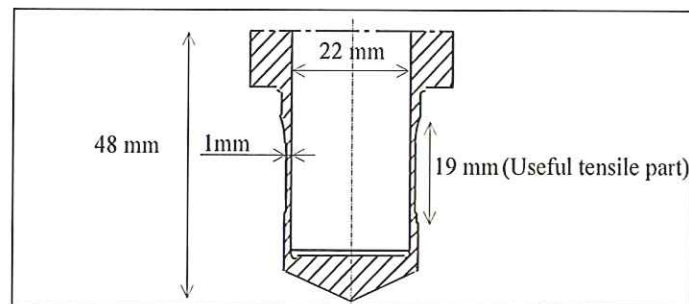


Figure 2: The target used for the tensile test

In the designing step of the target two specifications and requirements have been taken into account:

- according to the type of the studied test, the target is designed in an attempt to ensure a useful zone of high plastic strain in tension.

- ability of the designed device (target, target-support and projectile) to be simply logged in the existing gas launcher.

The experimental tests presented in this paper were done to identify the constitutive law for two metallic materials: a 2017T3 aluminium alloy and a 42CrMo4 steel. In each test the target and the projectile are made with the same material. Materials used for the projectile-support (polycarbonate) and the target-support (35CrMo4 steel) have usually the same properties and are known.

The two studied materials are assumed to follow the Johnson-Cook strain-stress law. In his original form, this law has the following expression:

$$\sigma = (A + B\bar{\epsilon}^n)(1 + C \ln \frac{\dot{\bar{\epsilon}}}{\dot{\bar{\epsilon}}_0})(1 - T^{*m})$$

Where σ , $\bar{\epsilon}$ et $\dot{\bar{\epsilon}}$ represent respectively the Von Mises equivalent stress, the equivalent plastic strain, the equivalent plastic strain rate. $\dot{\bar{\epsilon}}_0$ is the quasi-static strain rate or a reference strain rate. T^* is a term depending only on

temperature : $T^* = \frac{T - T_0}{T_{melt} - T_0}$ where T is the absolute temperature, T_{melt} is the melting temperature of the

material and T_0 is the transition temperature.

Parameters A , B , n , C and m are material constant characteristics and represent the subject of the identification study (except the parameter m which is not considered for the identification in this work).

A represents the yield stress of the material, while B and n influence the curve of work hardening. C characterises the sensitivity to the rate strain and m represents the sensitivity to the rise in temperature. In this work only the parameter m is not considered in the identification study. The used experimental means are not yet equipped with a system allowing the application and the control of thermal loading. In the numerical simulation to overcome the problem of the presence of the thermal term, we choose values of T_{melt} and T_0 ensuring a value of zero to the T^* parameter.

In the experimental part, many tests have been carried out for the two studied materials. For each material we start by trying to approach approximately the critical impact speed *i.e.* speed corresponding to the failure. Then, we vary the impact speed for several values under the critical impact speed, but large enough to ensure high strain and strain rate. In this study, tensile tests were performed at impacting velocities ranging from 30 m.s⁻¹ to 135 m.s⁻¹.

NUMERICAL TEST MODEL

Numerical simulations were carried out using Abaqus/Explicit [1]. The test model is an axially-symmetric as shown in figure 1. The finite element used in all simulations is CAX4R. The mesh is refined enough and uniform in the useful tensile as well as in the contacting surfaces (target/projectile, target/target-support and projectile/projectile-support). A non uniform density of mesh is used in the other regions of parts constituting the assembly of the model. The problem is modelled using about of 2400 elements. In the following figure (figure 3) are presented respectively the post-mortem picture of the target and the final finite element model state.

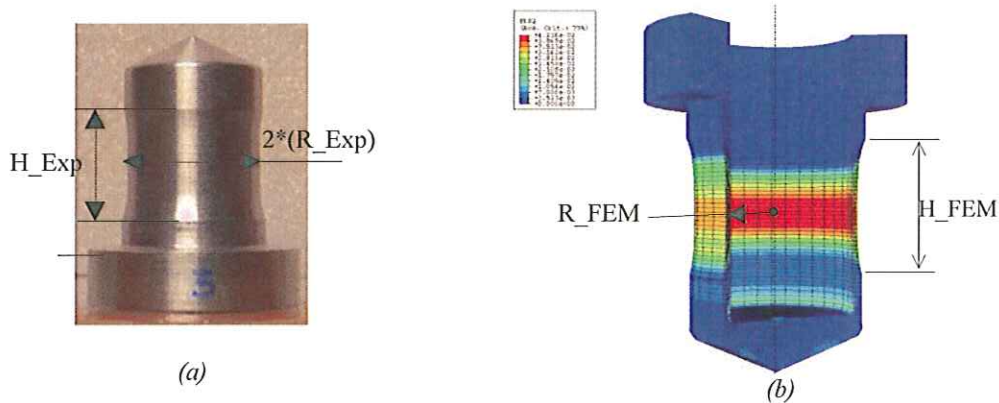


Figure 3: a) Post-mortem picture of the specimen, b).Final state of the FEM;

Responses, generally geometrical dimensions, taken into account in the identification procedure depend on the studied test and the design of the specimen. In this test two responses are taken into account; the height of the tensile zone and the radius in the medium of this later.

RESULTS AND CONCLUSIONS

After experimental tests all impacted targets are measured in order to get the experimental response. For the studied tensile tests we have chosen the useful tensile height and the radius of the target as responses to be taken into account in the optimisation procedure of the identification algorithm. Figure 3 (a) and (b) show the two controlled responses respectively in the experimental or the post-mortem and the finite element model one. In this test (tensile test) the plastic elongation of the specimens has been considered

We have noticed, from the finite elements model that the useful part of the target is submitted exclusively to tensile loads. Maximum values of strains are localised in the medium of the useful zone, where the radius of the target is controlled to get a second controlled response.

In the table 1, we present experimental results (H_{EXP} and R_{EXP}) for the two studied materials and for each impacting velocity. These responses are measured using a macro-photographic device and treated with a local soft : ImageAnalyser.

Material	Velocity (m/s)	H_{EXP} (mm)	R_{EXP} (mm)
Steel	99.0	20.16	11.50
	113.8	20.74	11.30
Aluminium	46.9	19.03	11.92
	60.0	19.18	11.87
	76.9	19.46	11.79

Table 1: Experimental results for the two studied materials

These results are injected in the identification procedure. For the 42CrMo4 steel material, we obtain the following parameters with an objective function value of 0.0018:

Test Type	A (Mpa)	B (Mpa)	n	C
Tensile test	817.865	699.529	0.157	0.0088
Taylor test	806.226	614.580	0.168	0.0089

Table 2: Results of the identification by the tensile test; comparison with results obtained by the Taylor test.

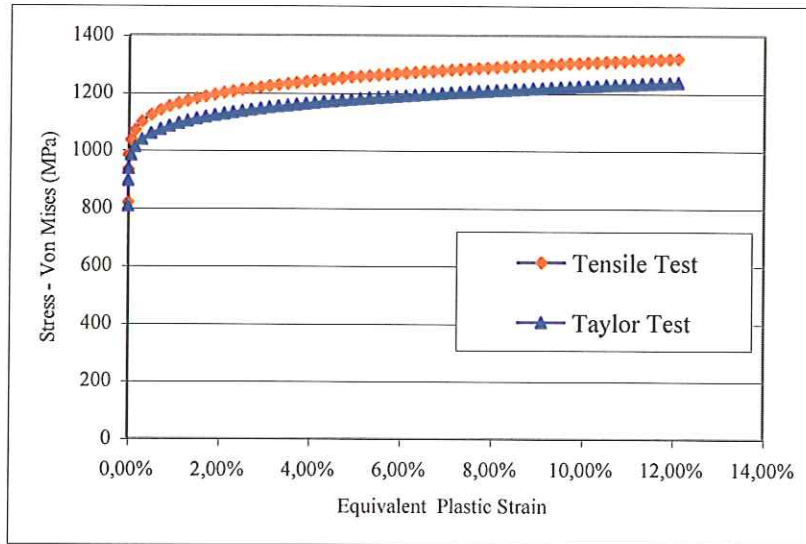


Figure. 4: Identified Constitutive law of the 42CD4 steel: comparison between Taylor test and tensile test

One remarks, a slight difference between results obtained with the tensile test and those obtained by the Taylor tests [5]. This difference can be explained by the presence of the friction phenomenon, between the contacting surfaces, in the Taylor test.

For the aluminium alloy 2017T3, the identification procedure gives the following results with a an objective function value of 0.0021.

Test Type	A (MPa)	B (MPa)	n	C
Tensile test	563.680	381.400	0.279	0.0265
Taylor test	360.080	316.550	0.289	0.0188

Table 2: Results of the identification by the tensile test; comparison with results obtained by Taylor test.

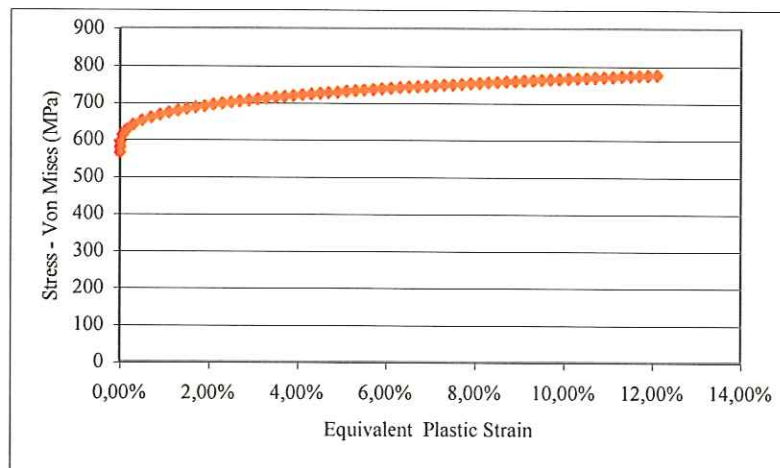


Figure. 5: Identified Constitutive law of the 2017T3 aluminium alloy.

Complementary explanations will be given in a study (currently in progress) for a multi-test approach by the methodology of identification used and presented in this paper.

In this paper we have presented a dynamic tensile test to identify two metallic materials; a 2017T3 aluminium alloy and a 42CrMo4 steel. The presented results show, the reliability and the accuracy of the used methodology to identify materials. As it has been shown, in other tests, obtained results of identification are specific to the type of the considered test. Thus a strategy to choose the appropriate test or to take into account several tests is now developed to get more accurate results of identification.

References:

- [1] Habbitt Karlsson & Sorenson. ABAQUS/Explicit Users' Manual Version 6.2, 200
- [2] I. Nistor, O. Pantalé, S. Caperaa and C. Sattouf. A New dynamic test for the identification of high speed friction law using a gas gun device. Journal of Physics IV, France, 100, 2003.
- [3] I. Nistor, O. Pantalé, S. Caperaa and C. Sattouf. Identification of a dynamic visco-plastic flow using a combined Monte-Carlo and Levenberg-Marquardt algorithm. VII International Conference on Computational Plasticity, Barcelona, 2003.
- [4] O. Dalverny, S. Caperaa, O. Pantalé, C. Sattouf. Identification de lois constitutives et de lois de frottement adaptées aux grandes vitesses de sollicitation. 1ier Colloque : Interactions Modèles - Expériences en Mécanique du Solide, 3 - 5 juillet 2002 : Besançon – France
- [5] C. Sattouf, Caractérisation en dynamique rapide du comportement de matériaux utilisés en aéronautique. Thesis, INP Toulouse, 2003.
- [6] O. Pantalé, I. Nistor, S. Caperaa. Identification et modélisation du comportement des matériaux métalliques sous sollicitations dynamiques, "Modern Technologies in XXI Century", Academia Tehnica Militara, Bucuresti, 2003

DYNAMIC SCRATCH TESTING OF WEAR RESISTANT MATERIALS BY A MODIFIED HOPKINSON SPLIT BAR DEVICE

Veli-Tapani Kuokkala, Mikko Hokka, Jari Rämö and Taina Vuoristo

Institute of Materials Science, Tampere University of Technology, POB 589, 33101 Tampere, Finland

Summary: A compressive Hopkinson split bar apparatus has been modified for single-pass scratch testing of wear resistant materials. In the present method, the incident pressure bar of a HSB device has been replaced with a special specimen holder bar and a vertical load unit attachment, which enable the specimen to be accelerated to velocities of 1-30 m/s under normal loads of 0-500 N. The scratching element is a conical tungsten carbide stylus with a 120 degrees apex angle and a 350 μm tip radius. Compared with the pendulum scratching method the advantage of the present method is that the depth of the scratch is not forced but depends on the normal load, scratching velocity, and the properties and behavior of the test material. Another advantage of the present test method is that it allows much higher tip velocities and, consequently, strain rates than the pendulum method.

INTRODUCTION

In many industrial processes wear causes significant direct and indirect economical losses, which are becoming even more substantial with increasing production rates and therefore shortening maintenance intervals. Higher production rates also often lead to higher loading rates, for example, in crushing of minerals and demolition debris and shredding of recycled automobile bodies. In the same way as the loading rate affects the strength of materials, it also affects the mechanisms of wear by changing their characteristics or the conditions of their occurrence. To optimize the use of materials in applications where wear causes failure or degradation of structures and components, information about the effects of loading rate is therefore also needed.

In abrasive wear, the main mechanisms of material removal are ploughing, cutting, and microcracking. In pure ploughing, a single pass of abrasive particles does not remove any material from the surface but only pushes it aside from the groove track, while in pure cutting the abrasive particle removes material from the surface leaving the sides of the groove intact. Microcracking occurs mostly in brittle materials, where microscopical cracks are formed in the material with the pass of the abrasive particle, leading to the gradual removal of material as flake-like particles. In many practical applications, the different basic mechanisms often occur simultaneously or, in microscale, sequentially. For example, high load direct compression of a mineral particle against the crusher liner may lead to a high velocity scratching of the liner material upon the breakage of the particle.

To study abrasive wear, a wide variety of testing techniques, experimental set-ups and data evaluation methods have been presented. For example, a commonly used technique to study the overall resistance of materials to wear is the rubber wheel test. The intent of this test method is to produce data that will reproducibly rank materials in their resistance to scratching abrasion under a specified set of conditions [1]. For many practical applications, the information obtained from this kind of 'averaging' tests is sufficient, but in scientific research the isolation of mechanisms or single events is often needed. For example, modifications of pendulum impact test devices have been used to produce a single scratch on the surface of the studied material [2]. In such devices, the control of impact velocity is very straightforward and the groove depth is predetermined by the relative position of the specimen and the scratching tip. To obtain precise control of both the impact velocity (energy) and the normal loading force, we have modified a compressive Hopkinson Split Bar device by replacing the incident bar with a special specimen holder bar and a vertical load unit attachment. In this paper, the construction of this device, measurement techniques, testing procedures and data reduction methods with some examples of actual test results will be discussed.

DESCRIPTION OF THE HSB SCRATCH TESTING SYSTEM

To simulate the dynamic scratch formation on the surface of the studied material, the testing system must facilitate the control of two independent variables, *i.e.*, the normal load and the velocity of the relative motion of the material surface and the abrading particle. In a real application, the relative motion may be caused by a constant velocity impact of the particle on the surface at a certain angle, or by a rapid acceleration of the particle virtually from rest to a high speed under a constant normal load. The latter may happen, for example, when a larger particle breaks under a compressive load into smaller fragments.

The current system is based on a conventional compressive Hopkinson Split Bar (HSB) system, where the specimen holder bar, carrying the specimen, is accelerated to a desired speed using the impact energy of the striker bar. The vertical loading unit contains a ball bearing linear unit so that the depth of the scratch is controlled by the indentation resistance of the material rather than by the settings of the testing system, as in the pendulum type of a device. Both the striker bar and the specimen holder bar are instrumented with speed sensors, which measure their velocity during the

test and enable the calculation of the energy used to create the scratch. The scratching element is a conical tungsten carbide stylus with a 120 degrees apex angle and a 350 μm tip radius. The scratching element is mounted on the vertical slide so that constant normal loads of 0-500 N can be applied on the specimen surface during the test. Also other types of scratching elements, *e.g.*, titanium nitride coated hard metal tool tips, were tested but they typically failed after a few tests. With the conical tungsten carbide stylus, several tens of tests can be done without observable wear of the tip, which is examined microscopically at regular intervals. A scanning electron micrograph of the tungsten carbide stylus is shown in Fig. 1.

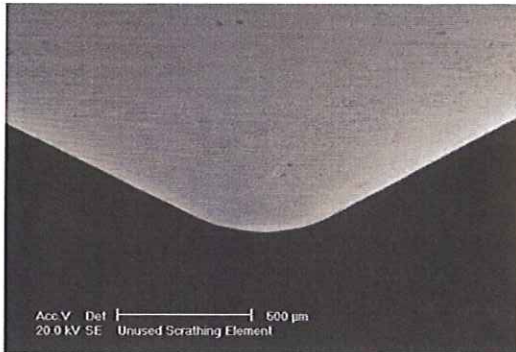


Fig. 1. Tungsten carbide hard metal scratching stylus.



Fig. 2. Dynamic scratch testing system at IMS/TUT.

At the beginning of the test the stylus rests either on the specimen, or slightly above it on a thin slide plate if some initial velocity for the specimen is needed. In the test, the striker bar is shot at a speed of 1-30 m/s at the end of the specimen holder bar, which is first accelerated by the momentum transfer and then decelerated by the energy spent in the forming of the scratch. The speed (and energy) of the specimen holder bar is measured as a function of time (and distance) and correlated with the scratch profile, which is measured after the test with a laser profilometer. Comparison of the removed or displaced volumes with the consumed energy is used to obtain information about the wear mechanisms, specific energy, and relative wear resistance of the studied materials.

Fig. 2 shows an overall view of the testing system where all the functions, including loading of the striker, pressurizing of the gun, firing of the striker, and acquisition of the data are computer controlled. Data from the optical speed sensors is recorded on a 12 bit 10 MHz digital oscilloscope, which is read by the controlling PC through the GPIB -bus. Fig. 3 shows a schematic and a close-up of the scratch attachment, which also shows the barcode-based optical velocity measurement systems for both the striker bar and the specimen holder bar. The sensing element used in the optical speed measuring system is a Honeywell HOA1406 IR sender-detector component. The B/W barcode provides a relative distance resolution of 1 mm.

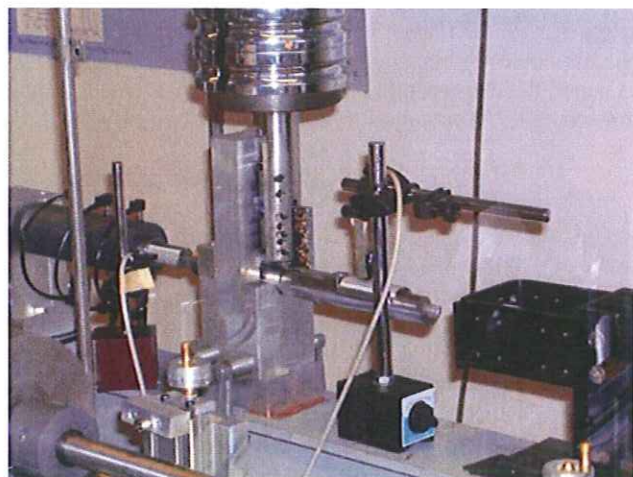
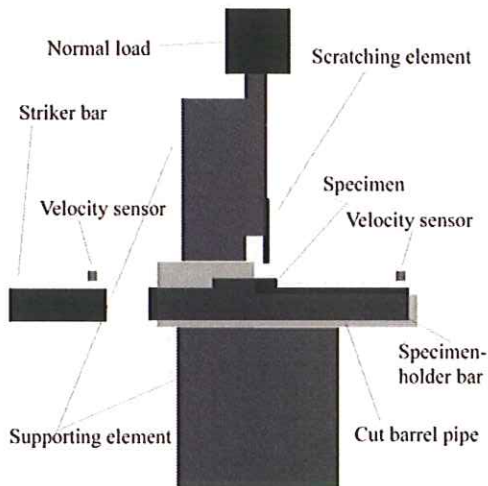


Fig. 3. A schematic and a close-up of the scratching attachment.

EXAMPLES OF TESTS WITH THE HSB SCRATCH TESTING SYSTEM

The aim of the tests is to produce a single scratch on the specimen surface under controlled conditions, *i.e.*, at a known normal load and a known relative velocity of the specimen and the scratching element. The normal load is adjusted simply by placing appropriate weights (0-500 N) on the loading unit. The velocity of the specimen is calculated from the signals of the velocity sensors, an example of which is shown in Fig. 4. From the velocity *vs.* time (or distance) curve, the kinetic energy of the specimen holder (and the specimen) and, more importantly, the energy loss during scratching can be calculated. The total energy loss is determined as the difference between the initial energy and the residual energy, which are obtained by fitting two straight lines to the measured data, as shown in Fig. 4c. The initial energy is obtained by extrapolating the energy curve to the moment of impact and the residual energy from the part of the curve where the stylus has left the specimen. The drop in the velocity and energy curves at the end of the test is due to an energy-absorbing stopper placed behind the specimen holder support tube.

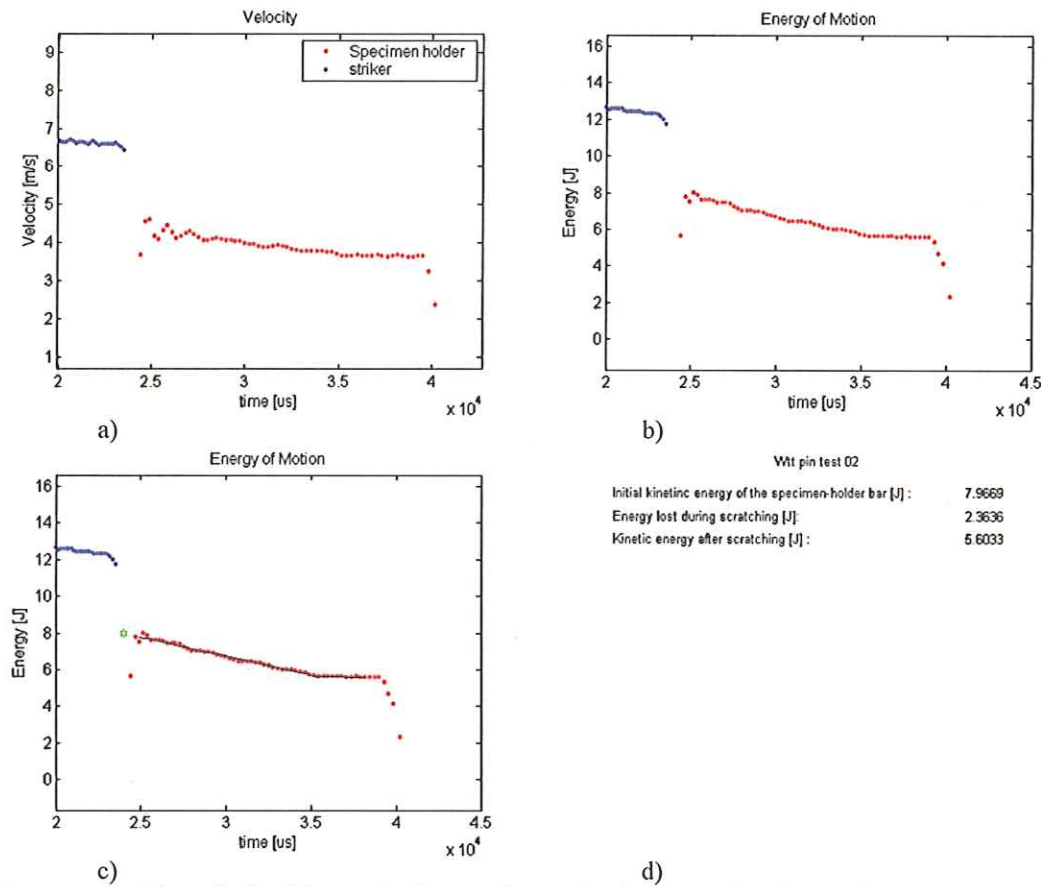


Fig. 4. An example of data obtained from a single-scratch test, a) velocity as a function of time, b) energy as a function of time, c) energy with lines fitted to the measured data, d) results from the measurement. Normal force $F_N = 300$ N.

To correlate the used energy to the removed or displaced volume, the created scratch is scanned perpendicular to the groove track with a laser profilometer at equal distances. From the profiles, the areas of the groove and the side ridges are determined as shown in Fig. 5a. For each cross-section, equation (1) gives the ratio of cutting to ploughing, which can be used as a measure of the wear mechanisms, *i.e.*, $F_{ab} = 1$ for pure cutting and $F_{ab} = 0$ for pure ploughing [3]. Fig. 5b shows an example of an actual scratch cross-section in a Hadfield manganese steel.

$$F_{ab}(x) = \frac{A_3(x) - [A_1(x) + A_2(x)]}{A_3} \quad (1)$$

The removed area and volume can be calculated as

$$A(x) = A_3(x) - [A_1(x) + A_2(x)] \tag{2}$$

and

$$V(x) = \int_0^x A(x) dx \tag{3}$$

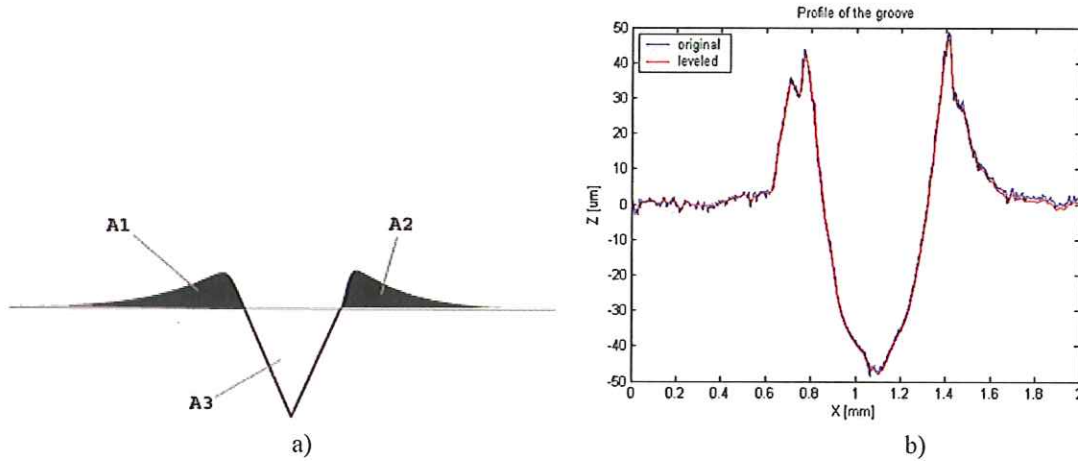


Fig. 5. Scratch cross-sections: a) ridges (A1 and A2) and groove (A3), b) an example of a scratch cross-section in a Hadfield manganese steel.

The behavior of different materials can be compared, for example, by plotting the cumulative removed or groove volume against the cumulative energy (*i.e.*, determined along the groove track). A clear difference in the behavior is observed, for example, between ductile and brittle materials, as shown in Fig. 6 for a Hadfield manganese steel and a Hardox steel. The ratio F_{ab} for a Hadfield manganese steel and a metal-metal composite are shown in Fig. 7, which also indicates that in a brittle material cutting dominates the removal of material at the beginning of the test.

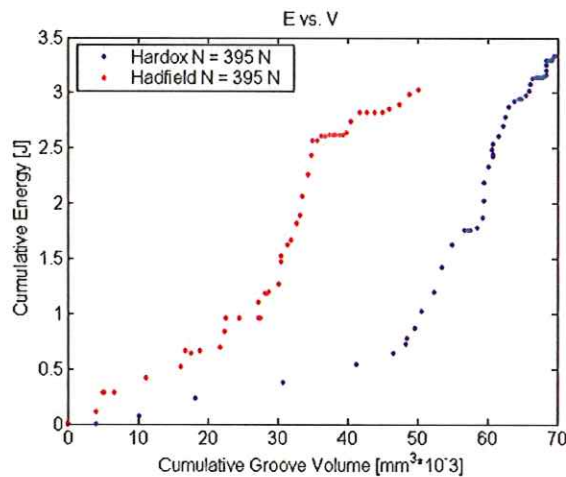


Fig. 6. Comparison of the groove volume vs. used energy for Hadfield and Hardox steels.

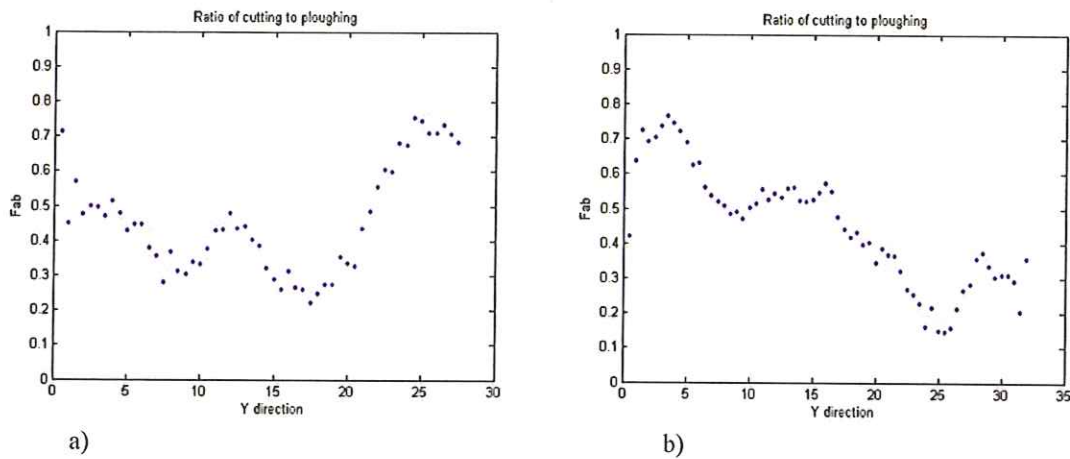
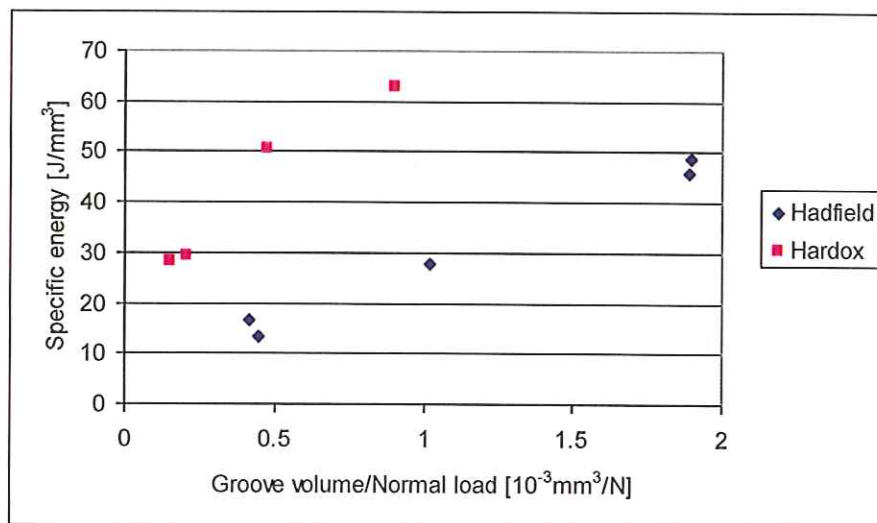


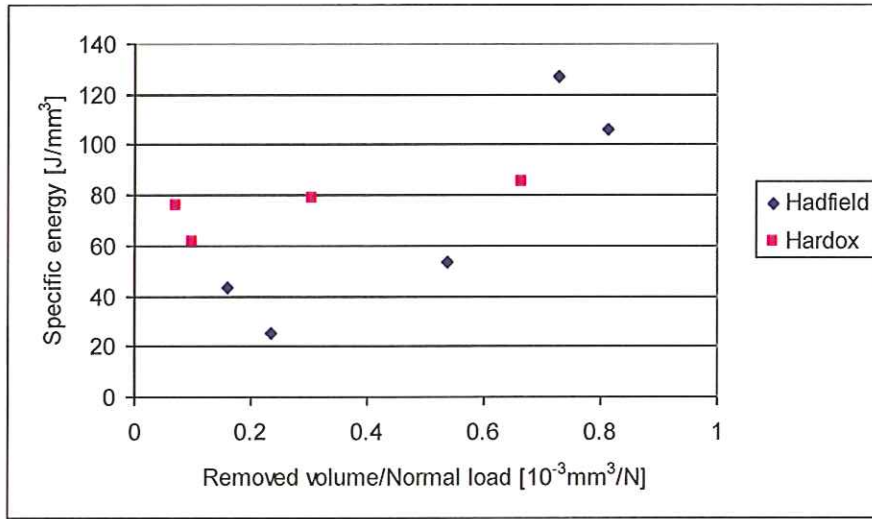
Fig. 7. Cutting to ploughing ratio along the groove track for a ductile (a) and a brittle material (b).

The specific energy (*i.e.*, energy per removed unit volume) can also be used as a measure of the wear properties of materials. Liang *et al.* [4] have shown that there exists a linear relationship between the specific energy and the tangential dynamic hardness of materials in a single-pass pendulum scratching test. The specific energy, however, is not necessarily constant for a material but may depend, for example, on the removed volume. In the pendulum test, the specific energy has been reported to decrease with increasing removed volume, which has been explained by the scratch depth dependence of energy absorption [5]. When the scratch is shallow, most of the energy goes to plastic deformation and work hardening. With deepening groove, the work hardened fraction of the volume decreases inversely proportional to the groove depth. On the other hand, the energy spent on friction between the stylus and the groove surfaces and on the forming new surfaces increases linearly with depth, while the removed volume increases proportional to its square. The net effect of these three energy-absorbing mechanisms is that the specific energy decreases with increasing removed volume.

In the current tests the dependence of the specific energy on the removed volume differs from that observed in the pendulum tests, as the specific energy increases with increasing removed volume. An example of this behavior is shown in Fig. 8 for two different types of steels, a Hadfield manganese steel and a Hardox steel. This result indicates that the two test types are not fully comparable, probably because in the pendulum test the groove depth is determined by the settings of the testing device whereas in the present test method the depth is not forced but depends on the normal load, scratching velocity and, above all, the properties and behavior of the test material. The present test method may therefore also be more sensitive to strain rate effects, which can increase the flow stress of the material considerably.



a)



b)

Fig. 8. Specific energy vs. volume for a Hadfield manganese steel and a Hardox steel, a) the groove volume normalized by the normal load F_N , b) the removed volume normalized by the normal load F_N . Hadfield steel was tested at $F_N = 240$ N and Hardox steel at $F_N = 395$ N.

Precise calculation of strain during a scratching test is very difficult because the material flows both forwards, sideways and upwards in the forming groove. In addition, strain hardening complicates the calculation, especially because the strain is unlikely to be uniform. Rough estimates for the strain, however, can be given on purely geometrical basis. For example, if we assume that the deformation is pure shear perpendicular to the groove track, for a 120 degrees apex

angle scratching tip we would simply obtain a shear strain of $\sqrt{3} = 1.73$. On the other hand, to estimate the strain rate, we also need to know the average deformation time at each cross section, which can be approximated as x/v , where x is the half-width of the groove and v is the velocity of the tip. From these two rough estimates we can get an approximate expression for the strain rate, which is $\dot{\gamma} = \sqrt{3}v/x$. In the literature, a commonly used approximation for the strain rate is v/a , where a is half of the distance between the ridges formed on opposite sides of the groove (residual half-width of the scratch) [6]. If we plot the specific energy against the strain rate, estimated in the way discussed above, we get a straight line with a positive slope, as shown in Fig. 9. The different slopes for the Hadfield and Hardox steels may reflect the differences both in the work hardening behavior and strain rate sensitivity of these two materials. An additional feature in a high rate scratching test which further complicates the analysis of the test results is the (adiabatic) heating of the deforming material, which can locally change the material properties considerably.

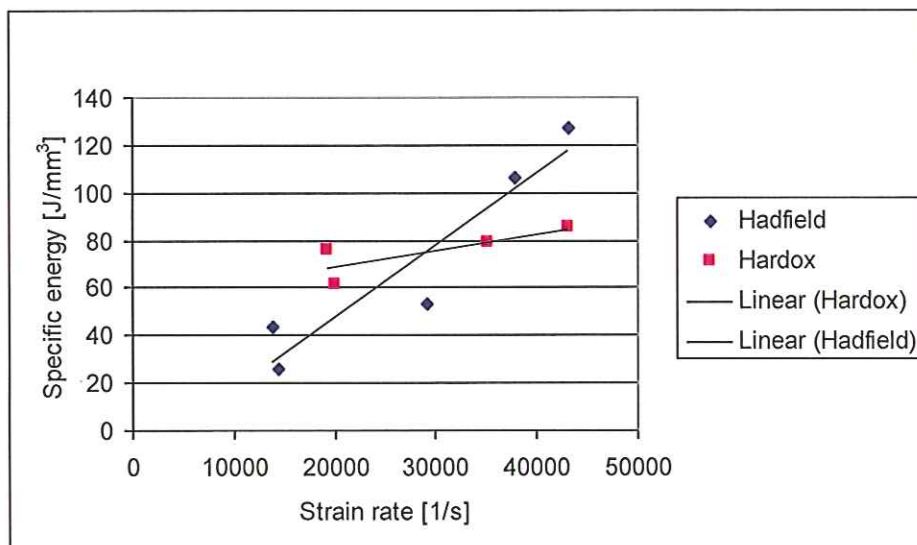


Fig. 9. Specific energy for the Hadfield and Hardox steels as a function of strain rate.

CONCLUSIONS

A single-pass scratch testing technique based on a modification of a compressive Hopkinson split bar apparatus has been used to study the wear resistance of different types of materials. The presented method differs from the commonly used pendulum type scratch testing technique because in the current method the depth of the scratch is not forced but depends on the normal load, scratching velocity, and the properties and behavior of the actual test material. Another advantage of the present test method is that it allows much higher tip velocities and, consequently, strain rates than the pendulum method.

The removed and displaced volumes of the groove are correlated with the consumed energies, which are calculated from the changes in the specimen velocity during scratching. The volumes are determined with a laser profilometer, which scans the groove cross-section at predetermined intervals along the groove track. From the measured data, for example the cutting-to-ploughing ratio and the specific energy (energy/unit volume) can be calculated for the studied materials, which enable the direct comparison of the materials and identification of the dominant wear mechanisms.

References

- [1] ASTM G65-00e1 "Standard Test Method for Measuring Abrasion Using the Dry Sand/Rubber Wheel Apparatus", ASTM International
- [2] Vingsbo O, Hogmark S., Single-pass pendulum grooving—a technique for abrasive testing, *Wear* 1984;100:489–502.
- [3] J. Jiang, M. Yao, F. Sheng, X. Gao, Dynamical analysis of the wear behaviour of steels during the pendulum single particle gouging wear test, *Wear* 181-183 (1995), 371-378.
- [4] Y.N. Liang, S.Z. Li, D.F. Li, S. Li, Some developments for single-pass pendulum scratching, *Wear* 199 (1996), 66-73.
- [5] J.M. Velez, D.K. Tanaka, A. Sinatora, A.P. Tschiptschin, Evaluation of abrasive wear of ductile cast iron in a single pass pendulum device, *Wear* 251 (2001), 1315-1319.
- [6] V. Jardret, P. Morel, Viscoelastic effects on the scratch resistance of polymers: relationships between mechanical properties and scratch properties at various temperatures, *Progress in Organic Coatings* 48 (2003), 322-331.

EFFECT OF STRAIN RATE AND TEMPERATURE ON THE DYNAMIC FRACTURE BEHAVIOUR OF AUTOMOTIVE SHEET STEELS

Patrick Larour, Annette Bäumer, Vitoon Uthaisangasuk, Aida Bajric, Min Wang*, Wolfgang Bleck

RWTH University of Aachen; Dpt. of Ferrous Metallurgy, Intzestrasse 1, D-52072 Aachen Germany

** Bao Tou Iron & Steel (Group) Co. Metallurgical Research Institute of Bao Tou, Steelmaking Dpt. 014010 Inner Mongolia, P.R.China*

Summary: The fracture behaviour of tensile sheet specimens at different strain rates and temperatures has been analysed. The aim of this work is to classify various steel grades with regard to their fracture behaviour during dynamic tensile loading. A ferritic deep drawing steel DC04, a dualphase steel H300X (DP500) and an austenitic steel 1.4301 have been investigated at three different temperatures (-40°C, RT and 100°C) and five strain rates (0.005, 1, 20, 200 and 500s⁻¹) using servohydraulic tensile testing machines. Mainly three characteristic fracture types and various combinations of them have been observed. Round (R), shear (S) and terrace (T) fracture shapes mainly occur for those steels. It is therefore intended to correlate the observed fracture behaviour with the microstructure and the strain rate and temperature dependent mechanical properties of the steels. Since SEM analysis show an essentially ductile rupture mechanism, the experimental results are interpreted according to the modified Gurson-Tvergaard-Needleman model of porous metal plasticity for rate and temperature dependent hardening. First quasistatic simulation results are presented as well.

EXPERIMENTAL PROCEDURES

Test set up

It is essential for steel producers and steel users to have a deep quantitative knowledge on materials behaviour in order to supply reliable input data for computer aided design and manufacturing. In a joint project between the German automotive and the German steel industry the mechanical properties and flow curves for the most relevant car body steels have been measured and collected in a data base. Steels grades for car body application have been tested at the strain rates 0.005, 1, 20, 200 and 500s⁻¹ (500 s⁻¹ only at room temperature) and temperatures between -40°C and +100°C. 3 replicates per set of parameter were performed [1].

High speed tensile tests were performed on a 100kN servohydraulic Schenck tensile testing machine for ram speeds from 0.0001 to 4m.s⁻¹. A climatic chamber enables tensile tests within a temperature range from -180°C to 180°C, Fig. 1-a. A 20kN servohydraulic Roell-Amsler tensile testing machine was used for higher ram speeds up to 10m.s⁻¹ at room temperature. The test set up and testing techniques have already been described in a previous publication [2]. Damping has been used for strain rates over 50s⁻¹, the force has been measured either from the piezoquarz load cell or calibrated strain gages on the grips. The strain was derived from the piston displacement by means of a standard LVDT system (Linear Variable Differential Transformer).

Fig.1.b shows the sample form used for dynamic sheet tensile testing. The gauge length of 20mm allows a maximum strain rate of 200s⁻¹ with the Schenck machine and 500s⁻¹ with the Roell-Amsler machine.

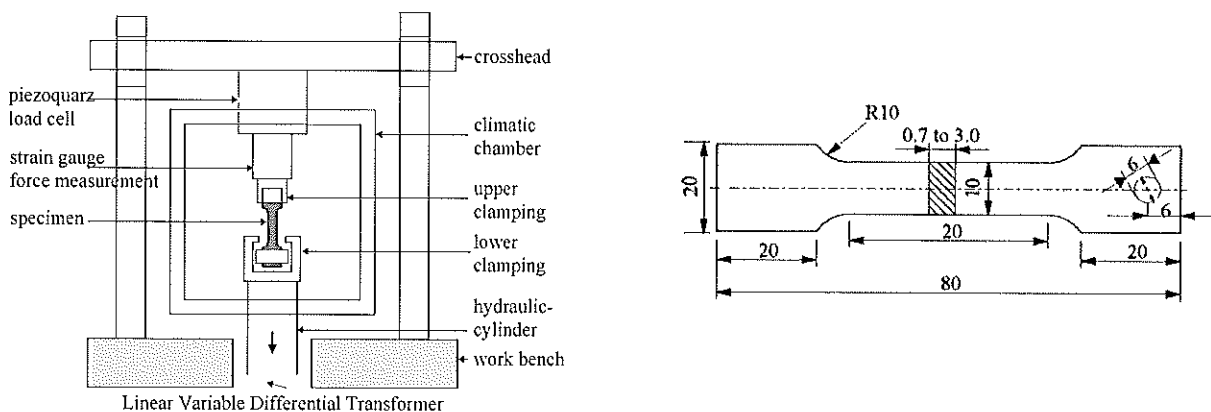


Fig. 1.a- Test set up of the 100kN-Schenck machine, b- Specimen geometry used for dynamic tensile testing (all dimensions in mm)

Materials

Table 1 gives the chemical composition of the investigated steels. The elements not mentioned stay within the usual limits for cold-rolled steels. The ferritic deep drawing steel DC04 has a pure ferritic microstructure. The dualphase steel H300X (DP500) is characterised by martensite and bainite islands (respectively 1.5% and 8% vol. fraction) in a ferrite matrix. The austenitic steel 1.4301 has a pure austenitic microstructure in the as-delivered condition. All investigated steels have been industrially melted, hot and cold-rolled, annealed and temper rolled to a final thickness of 1mm. No surface coating was applied. Fig. 2 shows the microstructure of the steels investigated with the corresponding rolling

direction. Table 2 gives the quasistatic mechanical properties and grain size of the investigated steels at room temperature.

Steel	Type	C	Si	Mn	P	Cu	Al	Nb	Ti	Cr	Ni
DC04	LC	0.025	0.01	0.19	0.008	0.013	0.054	0.001	0.002	0.02	0.03
H300X	DP	0.082	0.07	1.48	0.017	0.04	0.059	0.001	0.026	0.46	0.04
1.4301	Austenitic	0.034	0.55	1.22	0.029	-	-	-	-	18.23	8.10

Table 1. Chemical composition of the investigated steels, contents in mass %

Material	Type	R _{p0.2} MPa	R _m MPa	A _u %	A ₈₀ %	Grain size ASTM	Grain size μm
DC04	LC	173	300	24	41	9 (Ferrite)	16
H300X	DP	349	540	15	25	12 (Ferrite)	6
1.4301	Austenitic	304	700	52	56	8.5 (Austenite)	19

Table 2. Mechanical properties and grain size of the investigated materials

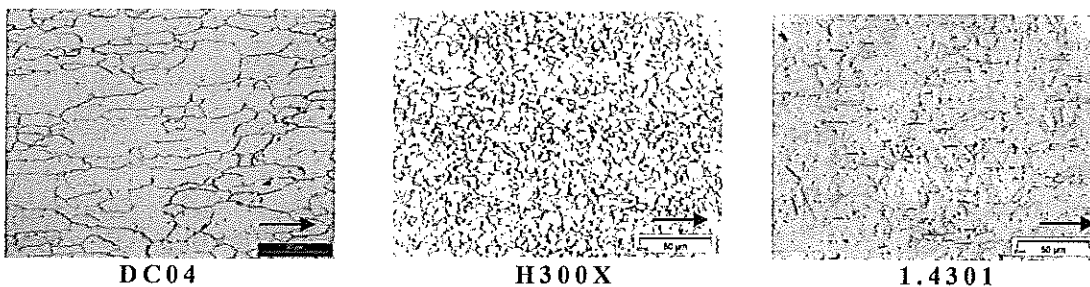


Fig. 2. Microstructure of the investigated steels: DC04, H300X, 1.4301 (magnification: 500x)

EXPERIMENTAL OBSERVATIONS

Fracture shape

Macroscopically, a crack progresses either perpendicular to the maximum tensile stress (normal stress fracture) or in the direction of maximum shear stress (shear stress fracture). Combination of both types of fractures can occur in round bar tensile specimens as so-called cup and cone fracture with a normal stress fracture in the interior and a shear stress fracture at the border [3-5]. Until now little attention has been paid to the fracture behaviour of flat tensile sheet specimens.

Four representative fracture shapes have been observed for the investigated flat tensile sheet specimens: round or flat fracture (R), round and shear fracture (R+S), terrace fracture (T) and pure shear fracture (S), Fig.3.

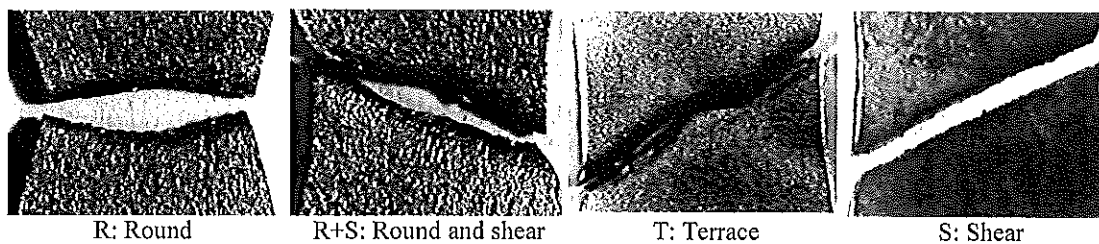


Fig. 3. Typical fracture shapes for the steel grades investigated

DC04 shows a round fracture (R) at strain rates from 0.005 to 1s⁻¹ for all temperatures. At strain rates over 1s⁻¹ a mixed fracture with both characteristic of round and shear fracture (R+S) and a resulting wavy shape is observed for all temperatures, Fig. 4-a. H300x shows shear (S) and terrace (T) fracture shape, without any clear dependency from strain rate or temperature, Fig. 4-b. The so-called "terrace" fracture appears together with pronounced shear bands crossing in the centre of the necking zone. The austenitic steel grade 1.4301 shows like H300X shear (S) and terrace (T) fracture, Fig. 5-a. For this steel grade shear fracture happens however almost exclusively at -40°C for all strain rates. Terrace fracture is more likely to happen at room temperature and 100°C. Since only three replicates have been tested for each strain rate, those results have to be interpreted carefully. However some general trends can still be recognised. Fig 5-b shows the relative elongation from necking to fracture of all three steel grades defined as follows:

$$\epsilon_{necking, relative} = \left(\frac{A_{20} - A_u}{A_{20}} \right) \tag{1}$$

$\epsilon_{necking, relative}$: relative elongation from necking to fracture; A_{20} : fracture elongation with a 20mm gauge length; A_u : uniform elongation

DC04 shows the highest relative necking elongation values with early localisation of strain with increasing strain rate, followed by H300X and 1.4301 with the lowest values, Fig. 5-b.

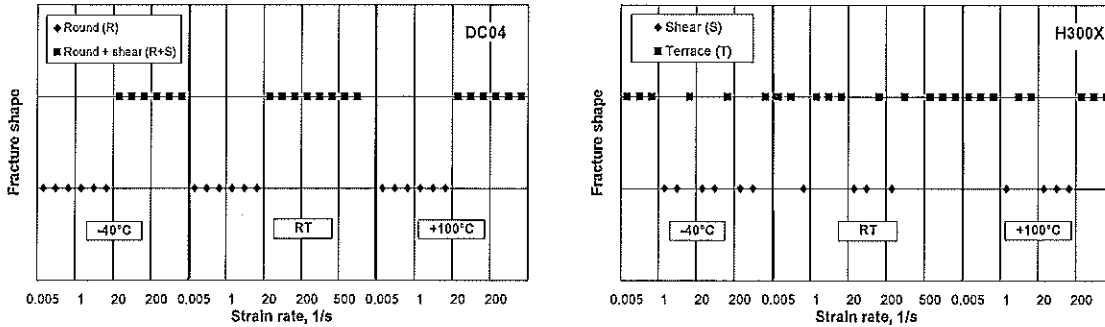


Fig. 4.a- Influence of strain rate and temperature on the fracture shape of steel grades: DC04, b- H300X

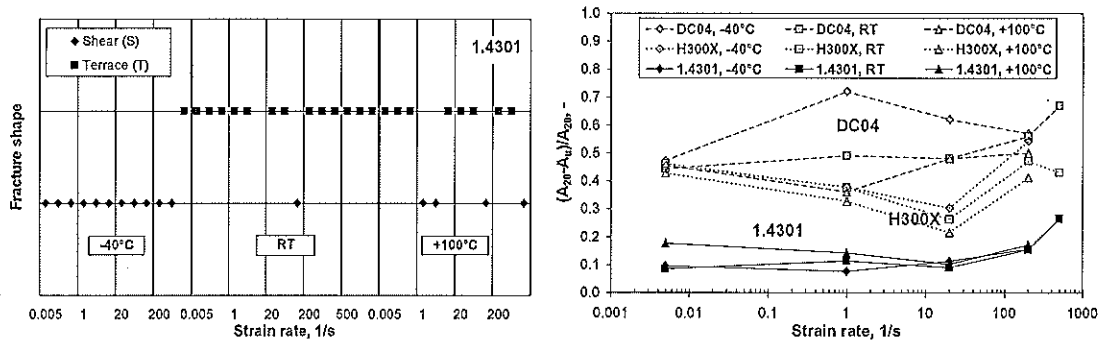


Fig. 5.a- Influence of strain rate and temperature on the fracture shape of 1.4301 steel grade; b- Relative elongation values from necking to fracture

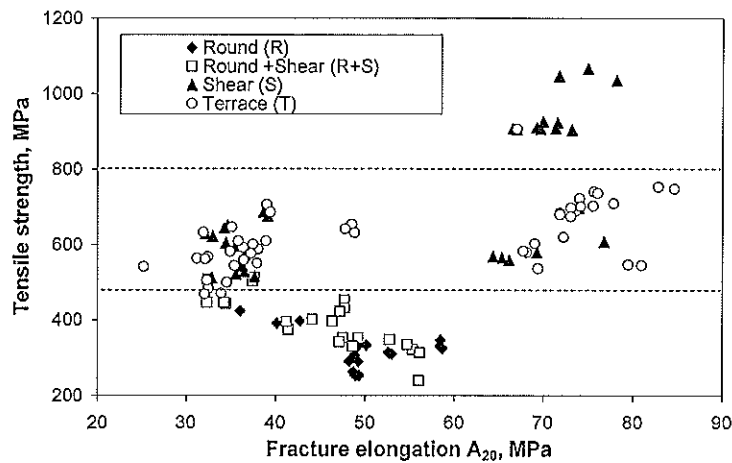


Fig. 6. Fracture shape as a function of tensile strength and fracture elongation

Fig. 6 shows the fracture shape distribution depending on the strength and ductility values. The elongation values for 1.4301 with low yield ratio values are largely overestimated since strain measurement is derived from piston displacement. Round and shear fracture occurs with DC04 when the strength level is increased. At tensile strength levels over 500MPa, no round fracture is observed anymore. For 1.4301 most of the shear fractures occur with the highest strength levels at -40°C . Round and shear, shear as well as terrace fracture shapes are found in the strength range between 500 and 800 MPa. Round and shear as well as terrace fracture are similar fracture modes. DC04 presents some higher relative elongation from necking to fracture so that more plastic deformation is allowed on the crack edges in comparison with sharper terrace fracture for H300X or 1.4301, Fig.3.

Austenite stability:1.4301 steel grade

The austenite to martensite transformation occurring during the cold forming of metastable 1.4301 austenitic stainless steel deeply affects its microstructure [6]. The relative amount of martensite formed during tensile testing was determined by means of a ferritescope Fisher MMS, measuring the relative magnetism of the fractured end of specimens and in the uniform elongation zone of the sample, Fig.7a-b. Around 60% of martensite (vol. content) has been found at -40°C . The amount of transformed martensite decreases sharply with increasing temperature due to the enhanced austenite stability (25% at room temperature, almost no transformation at 100°C). Furthermore increasing strain rate decreases the amount of martensite being formed due to the adiabatic heating in the sample preventing further martensite formation. The amount of martensite found in the fracture zone is always higher than in the uniform elongation zone, due to the additional plastic strain in the necking region. The lower the martensite content, the more terrace fracture is observed. At -40°C almost no terrace fracture is observed, except at the highest strain rate of 200s^{-1} with the lowest martensite content. At room temperature and $+100^{\circ}\text{C}$ mainly terrace fracture is observed, Fig. 5-a.

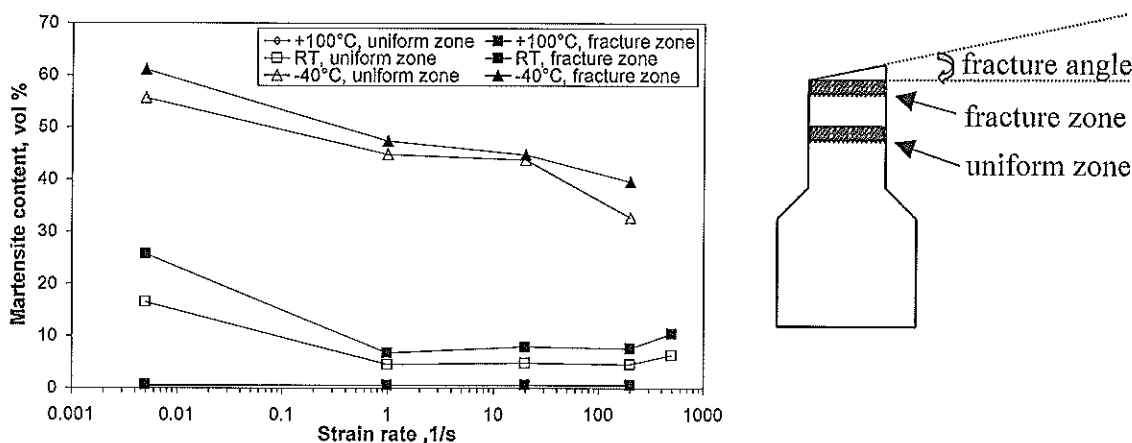


Fig. 7-a. Influence of temperature and strain rate on martensite content for austenitic steel 1.4301; b- Location of the magnetic measurements and definition of fracture angle

Fractography

All steels present a characteristic transgranular dimple fracture at all temperatures and strain rates. The model of microvoids nucleation growth and coalescence can be applied for the simulation. Even 1.4301 with a high content of martensite at -40°C presents a characteristic ductile fracture, Fig. 8.

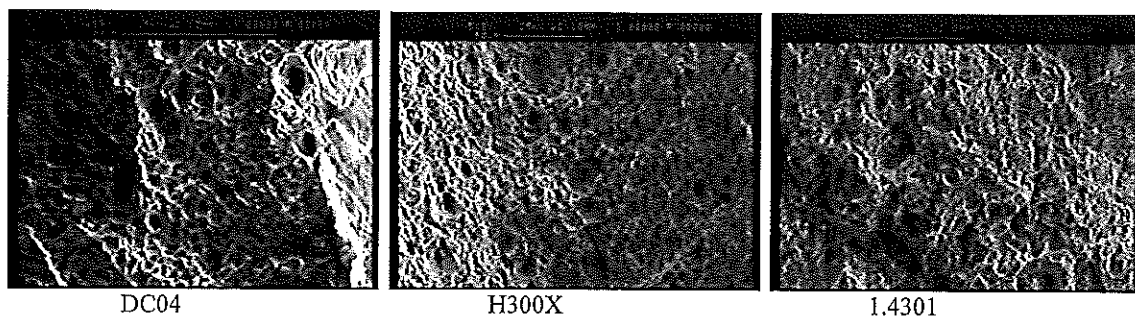


Fig 8. SEM microfractographs of the investigated steel grades (-40°C , 200s^{-1})

High speed video pictures

High speed video film have been recorded in order to follow the fracture path during the dynamic tensile tests. The origin of the crack is always located in the centre of the necking zone with the highest hydrostatic stress. The crack progresses until the sample borders perpendicular to the maximum tensile stress for round or flat fracture, it can also deviate before reaching the borders into a localised shear band for terrace fracture or propagate from the first crack initiation stage into a pure shear mode, Fig. 9.

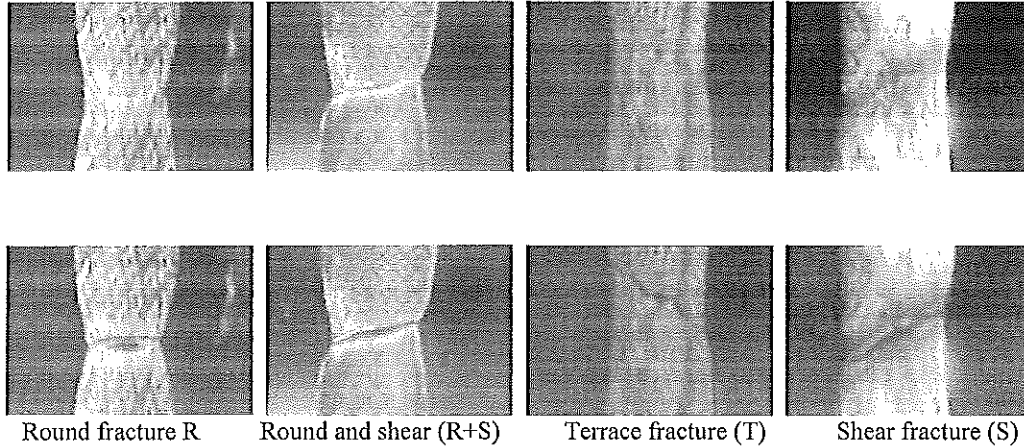


Fig. 9. High speed video camera pictures: crack initiation (upper pictures) and crack propagation (lower pictures)

Inclination of shear fracture

Shear fracture does not propagate 45° to the normal direction. The inclination of fracture to the normal direction is defined as in fig. 7-b. It lies between 15° and 25° for H300X and 20° to 30° for 1.4301. The fracture angle for pure shear fracture is slightly higher than for terrace fracture. No clear dependency can be observed with strain rate or temperature.

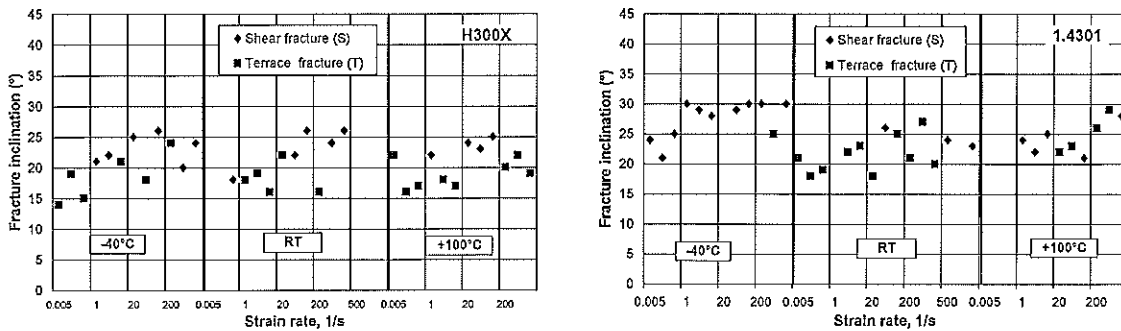


Fig.10. Influence of strain rate and temperature on the fracture angle

NUMERICAL SIMULATION OF FRACTURE PROPAGATION

A user-material subroutine has been provided in order to incorporate the modified porous metal plasticity constitutive equations in the finite element program ABAQUS (modified Gurson-Tvergaard-Needleman model). The constitutive relations take into account the modified damage parameters f_v^* and the nucleation of voids controlled by plastic straining. An elastic – rate and temperature dependent isotropically hardening plasticity model is assumed to predict the deformation behaviour of the matrix material surrounding the voids [7]. Adiabatic heating conditions as well as a rate dependent yield and temperature dependent softening of the matrix material are implemented in this model. Some standard values have been chosen for the material parameters, table 3.

Parameter	Unit	Value	Name	Material	T(K)	D	P	β^*
E	MPa	210000	Young's modulus	DC04	233	452	6.7	0.0025
ν	-	0.3	Poisson ratio		296	6233	4.0	
f_0	-	0.002	Initial porosity		237	55857	5.9	
ϵ_n	-	0.3	Nucleation strain	H300X	233	5526683	6.1	0.0017
f_n	-	0	Nucleatable porosity		296	142264	3.5	
s_n	-	0	Standard deviation for nucleation		237	548406	5.1	
f_o	-	0.05	Onset of accelerated pore growth	1.4301	233	4860458	6.8	0.0025
k	-	4.0	Rate of accelerated pore growth		296	9552	1.7	
RFAC	-	0.95	Factor for onset of stiffness reduction		237	21985832	6.8	
RED	-	0.25	Increment reduction factor					
q_1	-	1.5	Flow surface parameter					
q_2	-	1.00	Flow surface parameter					
q_3	-	2.25	Flow surface parameter					
η	-	0.9	Proportion of heat produced by plastic dissipation					
T_0	°C	20	Temperature reference					
ρ	kg.m ⁻³	7800	Density of the matrix					
c_p	Nmkg ⁻¹ K ⁻¹	4.65E+02	Specific heat of the matrix					

Table 3. Parameters of the modified GTN model

The rate and temperature dependence of the matrix material is introduced with the Cowper and Symonds law. A linear dependence of the dynamic flow stress $R^{(3)}$ with temperature is also assumed for the considered temperature range between -40°C and 100°C.

$$R^{(3)}(\epsilon^{pl}, \dot{\epsilon}^{pl}, T) = R^{(1)}(\epsilon^{pl}) \left[-\beta^* (T - T_0) \right] \left[\left(\frac{\dot{\epsilon}^{pl}}{D} \right)^{\frac{1}{P}} + 1 \right] \quad (2)$$

$R^{(1)}$ designates the uniaxial stress-plastic strain curve under static loading condition at the reference temperature T_0 . The values for the parameter D and P have been determined from uniaxial stress-plastic strain curves at different strain rates using last square methods. The difference in the yield strength at different temperature is taken into account by the material parameter β^* and the reference temperature T_0 set here to 23°C [7].



Fig. 11. Initial 3D mesh used for numerical simulations

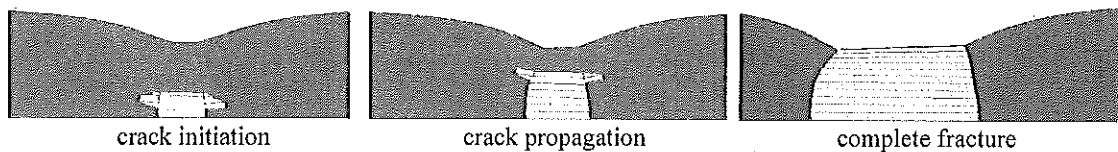


Fig. 12. Simulation of crack propagation, modified damage parameter f_u^* (initially f_0), DC04, 0.005s⁻¹, 23°C

First satisfying results have been obtained with DC04 for which fracture propagation in the normal direction could be simulated quasistatically at room temperature, Fig. 12. Difficulties arise however when intending to simulate shear or terrace fracture. Mesh size is a critical parameter when performing such simulations [3, 5, 7]. Initial 8 nodes cells of 0.45mm width, 0.385mm length and 0.025mm thickness in the centre of the sample may be too coarse to reproduce shear or terrace fracture, Fig.11. Further work is currently being performed to improve simulation results and implement the strain rate and temperature dependency of the material properties.

CONCLUSIONS

Three representative fracture shapes to classify the fracture behaviour of dynamic tensile flat specimens have been found: round or flat fracture (R), pure shear fracture (S) and a terrace like zig-zag fracture (T). With increasing strength level, the fracture mode turns from round into terrace and ultimately a pure shear mode. DC04 shows a clear transition from round to round and shear fracture at 20s^{-1} for all temperatures. H300X shows a mix of shear and terrace fracture, without any clear strain rate or temperature dependency. The metastable austenitic steel 1.4301 shows a transition between shear at -40°C and mainly terrace fracture at higher temperature for any strain rate. This is due to the pronounced austenite to martensite transformation at this temperature. First quasistatic simulation for DC04 using the modified Gurson-Tvergaard-Needleman model show a crack initiation in the centre of the necking zone and subsequently a normal fracture propagation. Further work is currently being undertaken in order to implement the strain rate and temperature effects.

References

- [1] Research Project, Characteristic values for thin sheet, co-operation between German steel producers and German car manufacturers. German Steel Association (VDEh), to be published in Stahl und Eisen (2004)
- [2] Bleck, W., Larour, P., Measurement of the mechanical properties of car body sheet steels at high strain rates and non ambient temperature, DYMAT 2003 conference proceedings, Porto, J. Phys. IV France 110 (2003), pp. 489-493
- [3] Besson, J., Steglich, D., Brocks, W., Modelling of crack growth in round bars and plane strain specimens, Int. J. Solids & Structures, Vol. 38 (2001), pp. 8259-8284
- [4] Zhang, Z.L., Thaulow, C., Ødergård, J., A complete Gurson model approach for ductile fracture. Engng. Fract. Mech., Vol. 678 (2000), pp. 155-168
- [5] Tvergaard, V., Needleman, A., Analysis of the cup cone fracture in a round tensile bar, Acta Metall Vol.32 (1984), pp. 157-169
- [6] Bressanelli, J.P., Moskowitz, A., Effects of strain rate, temperature and composition on tensile properties of metastable austenitic stainless steels, Transactions of the ASM, Vol. 59 (1966), pp 223-239
- [7] Mühlich, U., Siegmund, T., Brocks, W., A user-material subroutine of the modified Gurson-Tvergaard-Needleman model of porous metal plasticity for rate and temperature dependent hardening, Technical Note GKSS/WMG/98/1 internal report (1998/1)

ANALYSIS OF THE DYNAMIC PLANE SHEAR TEST ON SHEET METALS

Renaud Merle, Han Zhao, W.K. Nowacki[†] and Achille Awade^{*}

Laboratoire de Mécanique et Technologie de Cachan, 61 avenue du Président Wilson, 94 235 Cachan, France

[†] IPPT PAN, ul. Świętokrzyska 21, 00-049 Warszawa, Poland

^{*} TCR Renault, LAB 0 35, 1, Avenue du Golf, 78 288 Guyancourt Cedex, France

Summary: This paper describes the analysis of a test which provides mechanical data under large strain and at high strain rates of loading. It is based on shear test. Experimental problems (slipping, homogeneity of fields in the specimen, plane wave assumption in an SHPB, treatment of data) are discussed here.

INTRODUCTION

The crash simulation is now an indispensable tool in the car industry. However, it is not yet sufficiently reliable. Compared with the experiment, a difference in overall stiffness for the energy absorbing components is sometimes observed. As the main crash energy absorbing components in a car are the hollow columns composed of sheet metals, it is natural to doubt whether or not we can extend the experimental behavior data obtained at about 15 % of strain, to the case of large strains (80 % as experimentally observed at the corner of the columns).



Fig.1. Hollow column crushed, the strain measured with grid technique reach 80 % in the corners.

This paper aims at describing the shear experiment under impact which provides data under large strain and high strain rates, because it is the most adapted one to get a large strain of sheet metals without any fracture. A new shear device is presented, especially made for high strength sheets. The load is imposed by a large-diameter SHPB.

The equations of Davies [1] are re-examined to verify if the plane wave assumption is still valid for this kind of bars. The definitions of different strains under large strain consideration are discussed, especially the cumulated Eulerian strain tensor in the corotational frame, which is used in the usual finite elements codes.

The analysis of the strain and stress fields are operated experimentally using a digital image correlation technique and numerically by finite elements simulations. The local displacement measurement shows that the strain is homogeneous even under large strains [2]. First quasi-static tests with Arcelor's TRIP 800 steel are performed with a digital thermovision camera and acquisition system. Experimental results show that the martensitic transformation is homogeneous in the specimen and goes with an increase of temperature. The transformation is also exothermic.

DESCRIPTION OF THE EXPERIMENTAL SET-UP

Dynamic shear tests were initially performed by Campbell [3]. Under this general principle, Gary, Nowacki and Klepaczko have developed different versions of this test [4, 5]. However these researchers were more focused on the shearing loading and criterion aspect so that they rather investigated the small strain range. The device we have designed is made for testing sheet metals used in absorbing components for automotive industry. These sheets can be thicker than 1 mm and can have high strength capability (e.g. TRIP steel). That is why we use a bigger tightening system. This specification requires a bigger device. The shear device is composed of two coaxial parts made of a specially elaborated for high stresses steel. To apply shear strain to the specimen, it is necessary to impose a relative coaxial displacement to the parts (see Figure 2). When the two coaxial parts move, two rectangular zones are sheared during the test. Then the shear device can be placed under a classic hydraulic machine for low strain rates, and between the bars of an SHPB bench, for high strain rates. Experimentally we use a 60 mm-diameter SHPB to perform such tests. We put the fixing device in an SHPB set-up. The measurement of input, reflected and transmitted waves ε_{inc} , ε_{ref} and ε_{tra} allows the calculation of the forces and velocities on both sides of the specimen:

$$\begin{aligned} V_e(t) &= C_0 [\varepsilon_{inc}(t) - \varepsilon_{ref}(t)] & F_e(t) &= S_B E [\varepsilon_{inc}(t) + \varepsilon_{ref}(t)] \\ V_s(t) &= C_0 \varepsilon_{tra}(t) & F_s(t) &= S_B E \varepsilon_{tra}(t) \end{aligned}$$

where S_B , E and C_0 are respectively the bar's cross-sectional area, Young's Modulus and elastic wave velocity.

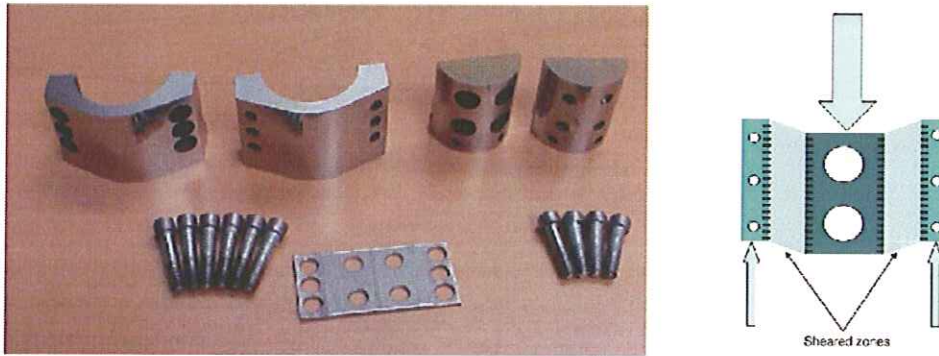


Fig.2. Principle of the shear device.

TREATMENT OF SIGNAL GIVEN BY LARGE DIAMETER SHPB - VERIFICATION OF THE PLANE WAVE ASSUMPTION

According to the size of our device, it is necessary to use large diameter bars. The input bar is 4.5 m-long and the output bar is 2 m-long. In this kind of bars, it is well-known that there is a dispersive effect, originally geometric, but it is assumed that the waves are plane in a cross section of the bar.

The wave dispersion aspect is carefully taken into account according to Davies [1] and [6]. Assuming the waves in a bar are longitudinal and harmonic:

$$\varepsilon_{zz}(x, t) = \int_{\mathbb{R}} \varepsilon_{zz}^*(\omega) e^{i[\xi(\omega)x - \omega t]} d\omega$$

where ε_{zz} and ε_{inc}^* are the strains in the time domain and the frequency domain, and ω the pulsation, and ξ the wave number, the $\xi(\omega)$ dispersion relation is given by the Pochhammer-Chree equation:

$$\frac{2\alpha}{a}(\alpha^2 + \xi^2)J_1(\alpha a)J_1(\beta a) - (\beta^2 - \xi^2)J_0(\alpha a)J_1(\beta a) - 4\xi^2\alpha\beta J_1(\alpha a)J_0(\beta a) = 0$$

with $\alpha^2 = \frac{\omega^2}{C_1^2} - \xi^2$ and $\beta^2 = \frac{\omega^2}{C_2^2} - \xi^2$

where J_0 and J_1 are the Bessel functions, and C_1 and C_2 are the velocities of the longitudinal waves and the transversal waves in the homogeneous isotropic elastic material. The dispersion is taken into account here:

$$\varepsilon_{zz}(x + \Delta x, t + \Delta t) = FFT^{-1} \left[e^{i(\xi(\omega)\Delta x - i\omega\Delta t)} FFT[\varepsilon_{zz}(x, t)] \right]$$

where FFT is the Fast Fourier Transformation, and FFT^{-1} the inverse transformation. The necessity of this correction has already been shown in [6].

The equations of Davies [1] are also re-examined to verify the assumption of plane wave in cross section in such large diameter bars. The main equation gives the strain and the stress as functions of the radial position:

$$\varepsilon_{zz} = -\xi^2 A \frac{J_1(\alpha a)}{\alpha a} \left[\alpha a \frac{J_0(\alpha r)}{J_1(\alpha a)} + \beta a \frac{1 - SZ}{Z - 1} \frac{J_0(\beta r)}{J_1(\beta a)} \right] e^{i(\xi z - \omega t)}$$

$$\sigma_{zz} = -2\mu\xi^2 A \frac{J_1(\alpha a)}{\alpha a} \left[(1 + Z + SZ) \frac{\alpha a J_0(\alpha r)}{J_1(\alpha a)} + \frac{1 - SZ}{Z - 1} \frac{\beta a J_0(\beta r)}{J_1(\beta a)} \right] e^{i(\xi z - \omega t)}$$

where the factor A defines the amplitude of the oscillations of the waves, ν the Poisson ratio of the material and $Z = (1 + \nu)C(\omega)^2/C_0^2$ and $S = (1 - 2\nu)/(1 - \nu)$. A schematic variation over a cross section of the strain and the stress is given in Figure 3.

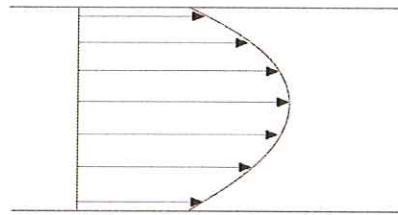


Fig.3. Schematic variation of the strain and the stress over a cross section of the bar.

The average of an arbitrary function f in a cross section can be obtained as: $\bar{f} = \frac{2}{a^2} \int_0^a f(r) r dr$
 Then we define the correction coefficients on the strain and on the stress as:

$$F_1(\omega) = \frac{\bar{\varepsilon}_{zz}}{\varepsilon_{zz}(a)} \quad \text{and} \quad F_2(\omega) = \frac{\bar{\sigma}_{zz}}{E\varepsilon_{zz}(a)}$$

F_1 is the ratio of average strain over the measured strain, F_2 the ratio of average stress over the appearing stress. The coefficients F_1 and F_2 are plotted in Figure 4 for an application of a 60 mm-diameter Aluminium bar.

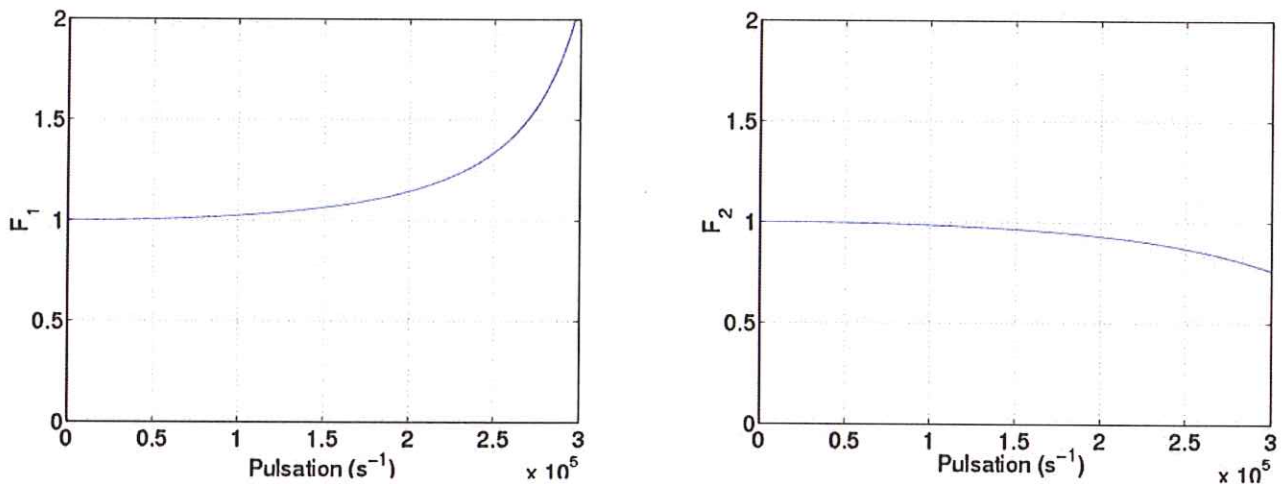


Fig.4. Variation of the F_1 and F_2 factors.

We notice that the factor F_1 increases very highly. This is due to the fact that $\varepsilon_{zz}(a)$ decreases to 0 for the pulsation roughly equal to $350\,000\text{ s}^{-1}$. The influence of the non-homogeneity of the strain and the stress is very small until the pulsation equals $100\,000\text{ s}^{-1}$. To quantify this influence, we have corrected a real signal with a frequency domain analysis:

$$\varepsilon_{corrected}(t) = FFT^{-1} [F_1(\omega)FFT(\varepsilon_{measured})] \quad \text{and} \quad \frac{\sigma_{corrected}(t)}{E} = FFT^{-1} [F_2(\omega)FFT(\varepsilon_{measured})] \quad (1)$$

The result of this correction is shown in Figure 5. We notice that in the case of our bar (Aluminium, diameter: 60 mm), the influence of non-homogeneity over a cross section is negligible, we can extend this result to the case of all bars in aluminium with a diameter inferior to 60 mm.

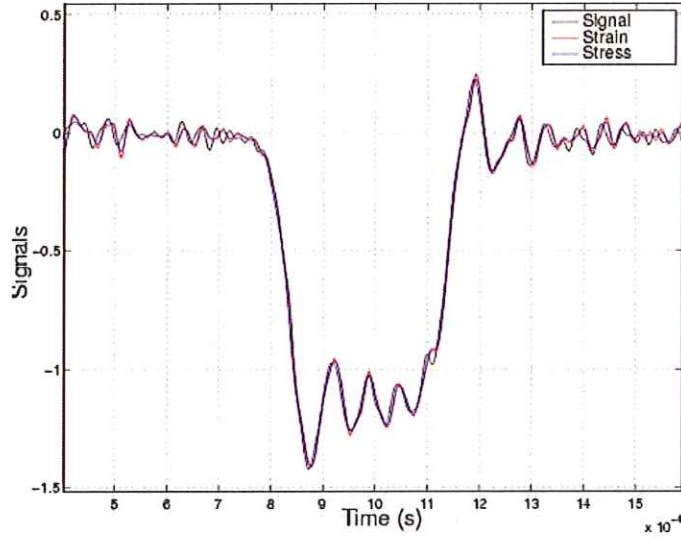


Fig.5. Correction with the F_1 and F_2 factors. The line named "Signal" is the measured signal, the line named "Strain" is the corrected strain according to equation (1), the line named "Stress" the appearing stress according to equation (1).

TREATMENT OF EXPERIMENTAL DATA - EULERIAN CUMULATED STRAIN TENSOR

To treat experimental data, it is necessary to choose a strain tensor which takes finite strain assumption into account. A possible answer is the Eulerian cumulated tensorial strain, calculated in the corotational frame [7]. We briefly describe the principle of the calculation of this strain tensor here. In an Eulerian approach, the velocity is decomposed into its symmetrical part - velocity gradient D - and its antisymmetrical part - vorticity Ω . To easily integrate tensor D , D can be calculated in the corotational frame, where the rotation vanishes: $\Omega=0$. In this case tensor D is equal to the Jaumann derivative of the strain tensor. This tensor is the default tensor calculated in ABAQUS and in LS-DYNA, which validates the choice of this tensor. Moreover this tensor is fully objective. Concerning the pure shear test, many authors use separately true (tension) strain, and shear strain. The use of the cumulated tensorial strain is an answer to this question.

In our case of pure shear, the non-zero terms of the Eulerian cumulated strain tensor are :

$$\mathbb{E}_{11}^S = -\mathbb{E}_{22}^S = -\frac{1}{2}(1 - \cos \gamma) \quad \text{and} \quad \mathbb{E}_{12}^S = \mathbb{E}_{21}^S = \frac{1}{2} \sin \gamma$$

where γ is the shear strain. In this case, the Von Mises equivalent strain is:

$$\varepsilon_{eq} = \sqrt{\frac{2}{3}(1 - \cos \gamma)}$$

The equivalent strain and equivalent stress are then defined as:

$$\varepsilon_{eq} = \sqrt{\frac{2}{3}(1 - \cos \frac{d}{l})} \quad \text{and} \quad \sigma_{eq} = \frac{F}{S} \sqrt{3} \quad (2)$$

where d is the relative displacement, F the corresponding force, and l the width of the sheared zone.

ANALYSIS OF THE FIELDS IN THE SHEARED ZONE

The available data in this type of shear test are global data, relative displacement and corresponding force. We thus have to take into account the possible non-homogeneity of the fields in the specimen (3 mm x 20 mm rectangle). The strain and stress fields in the sheared zone are relatively homogeneous (see [2]). Simulations with LS-DYNA show that the strains in the homogeneous zone (about 15 mm-long) of the specimen are very close to the analytical ones, corresponding to equation (2). The identified stress is also very close to the input behavior (see Figure 6), that means we can neglect the non-uniformity of strain and stress effects.

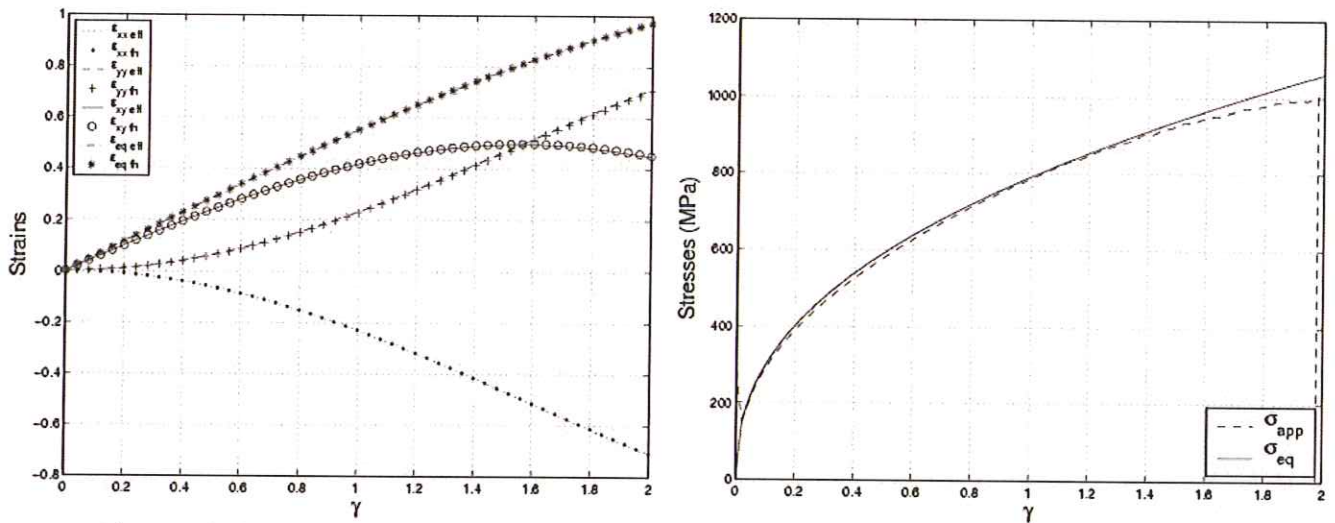


Fig.6. Analytical strain (ϵ_{th}) and effective strain (ϵ_{eff}), analytical stress (σ_{eq}) and appearing stress (σ_{app}).

TEMPERATURE MEASUREMENT ON TRIP STEEL

The first experiments were made on Arcelor's TRIP Steel. Tests were conducted on 1 mm-thick sheets under quasi-static loading. A hydraulic machine imposed the loading, both displacement and force were registered vs. time. In addition, TRIP steels' behavior is highly dependent on temperature because of the martensitic transformation. That is why the temperature was measured here using an infrared radiation technique [8]. In shape memory alloys, it has been observed that the transformation is localised in bands [8] in the case of a test at a temperature between A_f (temperature at the end of the austenitic transformation) and M_s (temperature at the start of the martensitic transformation). The first observation in the case of TRIP 800 steel is that the temperature distribution has the same aspect as in the case of ES mild steel (see Figure 7 and [9]) where no transformation occurs, but the amplitude is clearly higher.

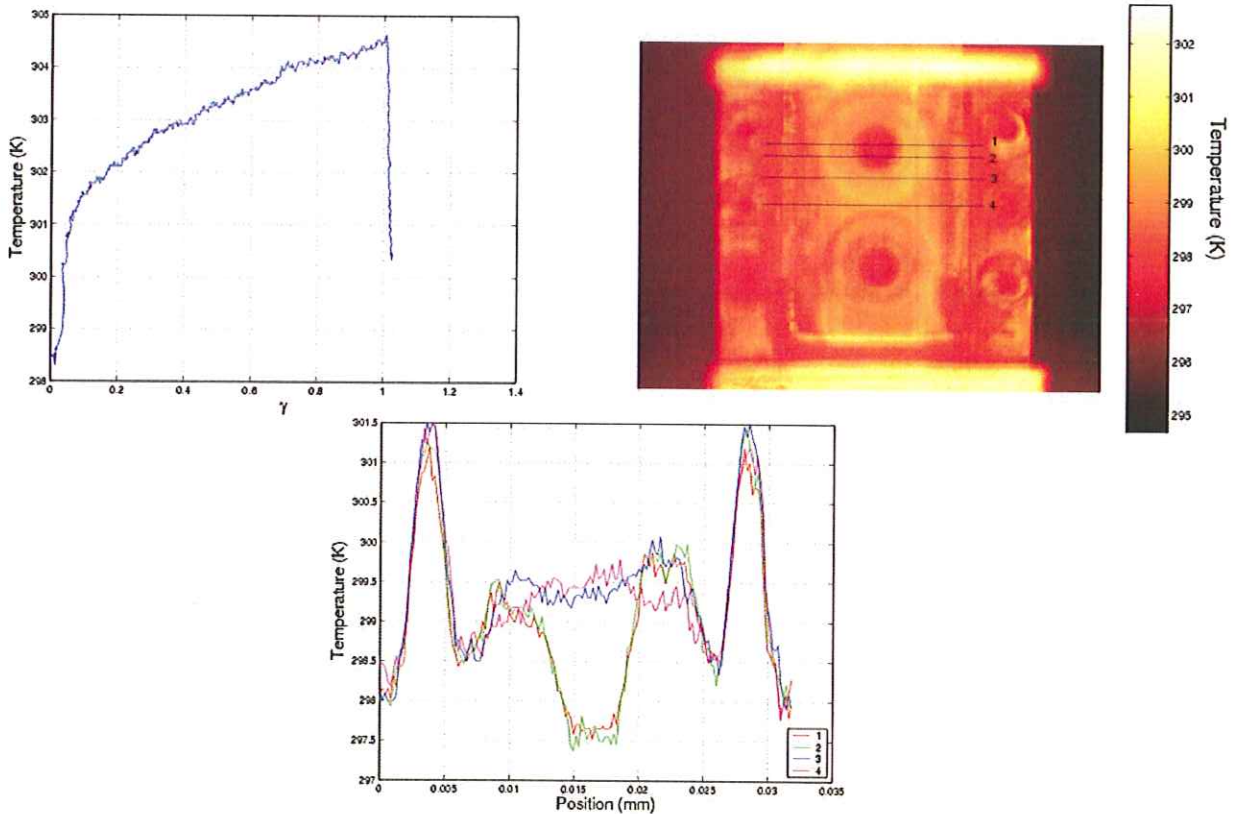


Fig.7. Temperature evolution during shear test at $\dot{\gamma} = 0.1 \text{ s}^{-1}$. The lines on the second picture correspond to the plots on the third picture.

In order to show that the transformation exists, an energetic balance can be made. The heat equation writes as follows:

$$\rho \frac{de}{dt} = \sigma : \mathbb{D} - \text{div } \vec{q}$$

where e is the internal energy, ρ is the density, σ the stress tensor and \mathbb{D} the strain rate tensor. We have assumed that the internal energy can be expressed as:

$$\rho \frac{de}{dt} = \rho C_p \frac{dT}{dt} - C$$

where C_p is the heat capacity and T the temperature, and C is a complementary power. We have assumed Fourier's Law in the specimen:

$$\vec{q} = -\lambda \overrightarrow{\text{grad}} T$$

where λ is the thermic conductivity. With the measurement of the temperature in the specimen, we can numerically calculate the gradient of the temperature, then the divergence of the heat flux $\text{div} \vec{q}$. The time derivative of the temperature is taken as the difference in temperature between two images over the time increment $\frac{dT}{dt} = \frac{\Delta T}{\Delta t}$, and with the evolution of the shear stress and shear strain, we can calculate the term $\sigma : \mathbb{D}$. We can then calculate a map of term C . In Figure 8, we have plotted the average of term C in the specimen vs. γ . The average of C is clearly positive. It means that the process is exothermic. The martensitic transformation is then an exothermic transformation.

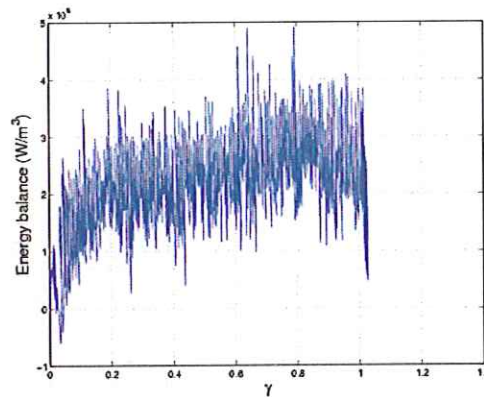


Fig.8. Energy balance in 1 mm-thick sheets. Evolution of the average of the complementary term C . $\dot{\gamma}=0.1 \text{ s}^{-1}$.

CONCLUSION

In this paper, we described a technique to exhibit mechanical data of sheet metals under large strains. This technique is based on double shear technique. The usually used assumption of plane wave in a cross section is verified for SHPB of large diameter. In addition we proposed a method based on the cumulated tensorial strain to treat the data in large strains. Then experiments on TRIP steel were presented. They showed the transformation is homogeneous in the specimen, and the martensitic transformation is accompanied by an increase in temperature.

References

- [1] Davies R.M., A Critical Study of the Hopkinson Pressure Bar, Philos. Trans. Roy. Soc. London, vol. A 240 pp 375-457, (1948).
- [2] Merle R., Zhao H., Analysis of the Dynamic Plane Shear Test on Sheet Metals, Journal de Physique 110, pp 453-459 (2003).
- [3] Campbell, J.D., Ferguson W.G., The Temperature and Strain Rate Dependence of the Shear Strength of Mild Steel, Phil. Mag., vol. 21, pp 63—82 (1969).
- [4] Gary G., Nowacki W.K., Essai de cisaillement appliqué à des tôles minces, Journal de Physique IV, vol. C8, pp C8-65--C8-70 (1994).
- [5] Klepaczko J.R., N'Guyen H.V., Nowacki W.K., Quasi static and dynamic shearing of sheet metals, Eur. J. Mech A/Solids, vol. 18, pp 271—289 (2000).
- [6] Zhao H., Gary G., On the Use of SHPB to Determine Dynamic Behavior of Materials in the Range of Small Strains, Int. J. Solids&Structures, vol. 33, pp 3363—3375 (1996).
- [7] Gilormini P., Rougée P., Roudier P., Les déformations cumulées tensorielles, C.R. Acad. Sci., vol. 316 II, pp 1409—1504 (1993).
- [8] Gadaj S.P., Nowacki W.K., Pieczyska E.A., Temperature Evolution in Deformed Shape Memory Alloy, Infrared Physics and Technology, vol. 43, pp 151—155 (2002).
- [9] Rusinek A., Klepaczko J.R., Gadaj S.P., Nowacki W.K., Simulation of Heat Exchange in Simple Shear test, Journal of Theoretical and Applied Mechanics, vol. 40, pp 317—337 (2002).

HIGH-STRAIN-RATE BEHAVIOR OF α -IRON UNDER SHEAR DOMINANT LOADING CONDITIONS

Daniel Rittel* and Guruswami Ravichandran

Graduate Aeronautical Laboratories, California Institute of Technology, Pasadena, California 91125, USA

*Faculty of Mechanical Engineering, Technion-Israel Institute of Technology, 32000 Haifa, Israel

“This paper is dedicated to Dr. Janusz R. Klepaczko for his pioneering contributions in the areas of Dynamic Behavior of Materials and Experimental Mechanics.”

Summary: A recently developed specimen geometry, the shear compression specimen (SCS) [1,2] has been used in the seamless characterization of the large strain behavior of α -iron over a range of strain rates, 10^{-3} to $2 \times 10^4 \text{ s}^{-1}$. In addition to the mechanical response (stress-strain) obtained using the split Hopkinson (Kolsky) pressure bar, the in-situ temperature rise during dynamic deformation is measured using a high-speed infrared detector. The stress-strain response of the material at low and intermediate strain rates compares well with prior experiments on as received α -iron [3,4]. However, the response of the material deformed at very high strain rates coincides with that of the pre-shocked material [5]. The fraction of the conversion of plastic work into heat is calculated using experimental measurements of temperature during dynamic deformation. The material in the gage section is found to exhibit limited twinning at high-strain-rates and the hardness is comparable to that of pre-shocked α -iron [6].

INTRODUCTION

The high-strain-rate behavior of metals has been recognized to play an important role in many technologies including manufacturing processes such as rolling, forming and high-speed machining, and as well as in ballistic failure, dynamic crack growth and shear banding. Accurate computational modeling of these processes requires the knowledge of material behavior at large strains over a wide range of strain rates. Relevant constitutive data are also essential for validating multiscale material models such as the one proposed recently for bcc metals [7]. The validation of such models require robust experimental measurements that can be used to aid in the refinement of such models aimed at bridging length scales in high strain rate deformation of metals. The dynamic nature of many of the above mentioned processes has motivated the study of high-strain rate deformations. In this paper, results for high-strain-rate, large-strain deformation of as received α -iron (bcc) obtained using the recently developed shear compression specimen [1,2] are presented and discussed.

EXPERIMENTAL

The shear compression specimen (SCS) consists of a rectangular plate or a cylinder into which two slots are machined at 45° to the longitudinal axis [1,2]. A schematic of the planar SCS geometry is shown in Fig. 1a and a photograph of undeformed and deformed cylindrical SCS is shown in Fig. 1b. Upon compression of the plate or cylinder at the ends, the gage section (slotted section) experiences a dominant state of shear deformation. The gage section is defined by its height (w) and thickness (t). The width (B) and the height (L) of the plate are chosen such that the sections adjoining the gage remain nominally elastic during deformation. The gage length is obtained from geometry, $h = \sqrt{2}w$. By adjusting the slot width (w), a wide range of strain rates can be achieved. The typical dimensions of the rectangular SCS are $L=24 \text{ mm}$, $D=9.7 \text{ mm}$, $t=2.54 \text{ mm}$ and the slot width (w) varies in the range of 0.5 to 2.6 mm.

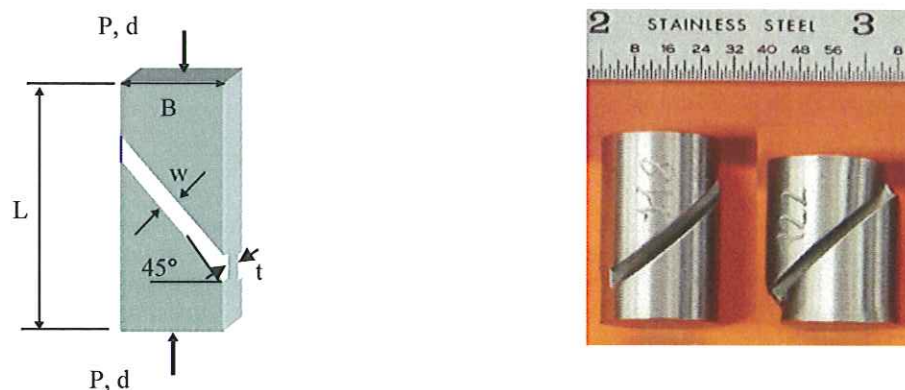


Fig. 1. a-Schematic of the planar shear compression specimen (SCS), b-Undeformed and deformed cylindrical SCS

Quasi-static experiments are seldom carried out at rates in excess of 1 s^{-1} . Consequently, there is a gap in the 1-100 s^{-1} range of strain rates and cannot be bridged easily using conventional testing equipment or specimens. Similarly, there is a gap in the range of strain rates achievable with cylindrical specimens in the split Hopkinson bar (10^3 to 10^4 s^{-1}) [8]

and those achievable in the pressure-shear plate impact experiments (10^5 to 10^6 s^{-1}) [9]. The SCS specimen provides a simple means for bridging these gaps in the aforementioned range of strain rates by varying the gage width (w).

The stress and strain state in the gage section is three-dimensional, though the deformation is shear dominant. Yet, considerable simplification is gained through the introduction of simple approximations for the von Mises equivalent stress and plastic strain which has been aided by analysis and numerical simulations [1,2]. Despite the three-dimensional nature of the deformation in the gage section, it has been shown through detailed 3-D numerical simulations [1,2] that the equivalent stress and strain within the gage section are fairly uniform and a homogeneous state of deformation prevails. The equivalent stress (σ_{eq}), strain (ϵ_{eq}) and strain rate ($\dot{\epsilon}_{eq}$) in the gage section for the rectangular SCS geometry can be expressed in terms of the measured load (P), displacement (d) and the geometrical parameters [1,2],

$$\begin{aligned} \sigma_{eq} &= k_1 \left(k_2 \epsilon_{eq} \frac{P}{Bt} \right) \\ \epsilon_{eq} &= k_3 \frac{d}{h}; \quad \dot{\epsilon}_{eq} = k_3 \frac{\dot{d}}{h} \end{aligned} \quad (1)$$

where k_1 , k_2 and k_3 are material and geometry (w/t) dependent constants. They are determined from numerical simulations and verified by experiments. For α -iron, $k_1=1$, $k_2=0$ to 0.05 and $k_3=0.43$ to 1.

Quasistatic testing was carried out on a servo-hydraulic MTS machine (displacement control) and high strain rate compressive testing was carried out using a split Hopkinson (Kolsky) pressure bar [8]. The load (P) and displacement (d) for each test was calculated using established procedures of converting experimental data [1]. Continuous measurement of the temperature rise (θ) of the specimen during dynamic deformation allows for determination of the thermo-mechanical conversion of plastic work to heat. The temperature was measured using a single HgCdTe high speed infrared detector which measures the radiation from a spot ($100 \mu\text{m} \times 100 \mu\text{m}$) at the center of the gage section imaged through a Newtonian telescopic system [10]. Assuming adiabatic conditions to prevail during dynamic deformation, the conversion of plastic work to heat can be conveniently expressed in terms of the following two factors,

$$\beta_{dif} = \frac{\rho c \dot{\theta}}{\sigma_{eq} \dot{\epsilon}_{eq}}, \quad \beta_{int} = \frac{\rho c \theta}{\int_0^{\epsilon_{eq}} \sigma_{eq} \dot{\epsilon}^P d\epsilon} \quad (2)$$

where ρ is the mass density and c is the thermal heat capacity of the material. The Taylor-Quinney parameters β_{dif} (differential) and β_{int} (integral) represent the rate plastic work converted to heating (as it appears in the heat conduction equation and relevant to coupled thermo-mechanical problems) and the amount of total accumulated plastic work that has been converted to heat. Both these quantities are generally considered to be constant and are generally assumed to be around 0.9. However, a recent investigation [10] has shown that the parameter β_{dif} for metals is not a constant but a function of strain and strain rate. Note that in the absence of internal heat source, β_{int} is necessarily less than 1. However there is no such restriction on β_{dif} .

The experiments were conducted on specimens prepared from an as received cylindrical bar (diameter, 25.4 mm) of 99 weight % pure polycrystalline α -iron.

RESULTS AND DISCUSSION

Typical stress-strain curves obtained over a wide range of strain rates using the SCS and associated hardening for α -iron are shown in Fig. 2. The material exhibits considerable hardening at quasistatic strain rates ($\sim 10^{-3} \text{ s}^{-1}$) and the material can be deformed to large equivalent strains (in excess of 1). Limited number of experiments was also performed using cylindrical specimens. The response of the SCS specimen including strain hardening is nearly identical to that of the cylindrical specimens at quasistatic strain rates. For the SCS specimens, with increasing strain rate, the material exhibited considerable rate sensitivity which is in accord with earlier observations [4]. Also, the strain hardening of the material appears to be highly rate dependent and the strain hardening decreases with increasing strain rate. The stress-strain curve exhibits softening even at small strains immediately following yield at the higher strain rates (in excess of $5,000 \text{ s}^{-1}$). The flow stress at $\epsilon_{eq}=0.1$ is plotted as a function of strain rate in Fig. 3. As stated earlier, the material exhibits considerable rate sensitivity, particularly at strain rates beyond 10^3 s^{-1} .

The highest strain rate achieved for α -iron with the SCS specimen was around $2 \times 10^4 \text{ s}^{-1}$, a strain rate that is generally not achievable in a split Hopkinson (Kolsky) pressure bar using cylindrical specimens. In Fig. 3, the data from torsion experiments of Klepaczko [3] converted to equivalent stress-strain curves is shown for the quasistatic strain rates. The data from the current study compares well with the published data [3] providing validity for the SCS approach, particularly the concept of employing Mises equivalents for stress and strain for characterizing the prevailing three-dimensional state of deformation in the gage section.

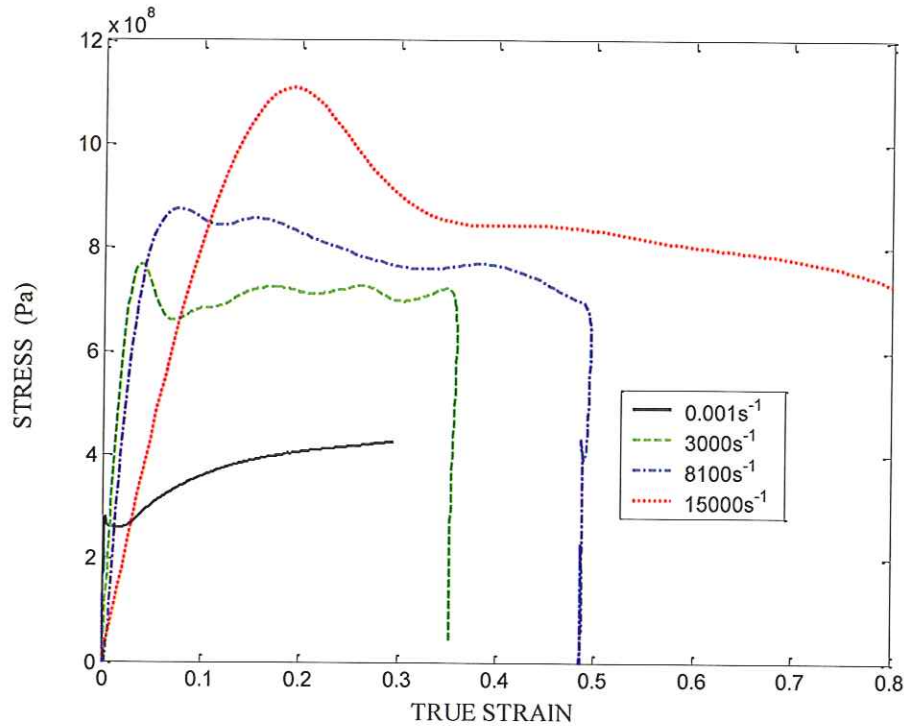


Fig. 2. Typical stress-strain curves for α -iron obtained using the shear compression specimen (SCS)

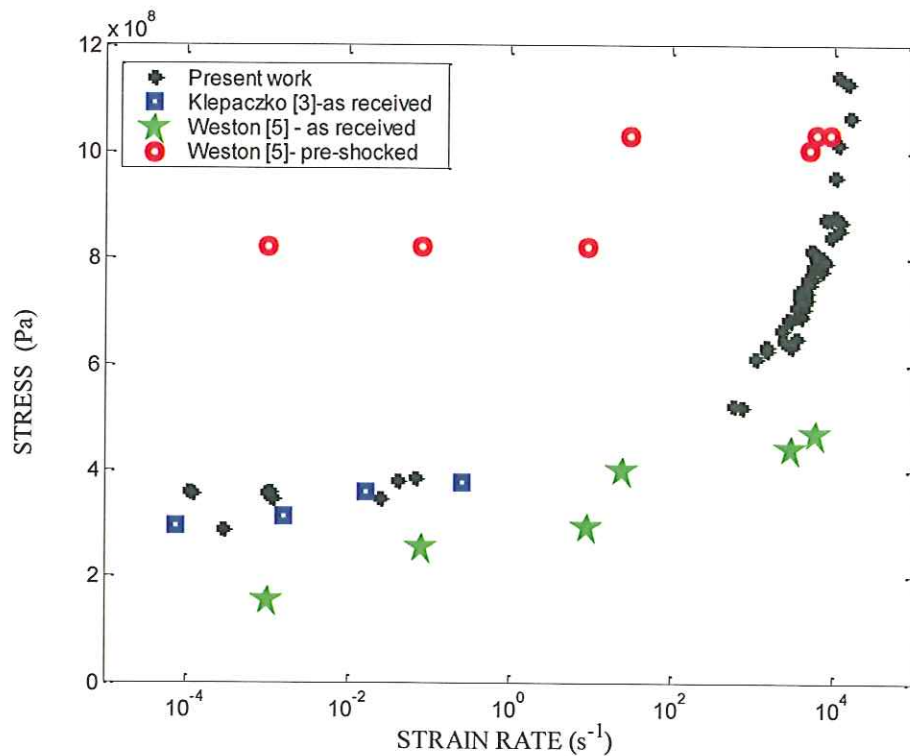


Fig. 3. Rate sensitivity of α -iron

Weston performed quasistatic and high strain rate compression experiments using cylindrical specimens on as-received and pre-shocked α -iron and observed that the stress-strain curves for pre-shocked iron showed considerable softening at high strain rates as observed in the present study. Figure 4 shows the stress-strain curves at a nominal strain rate of $9,000 \text{ s}^{-1}$ from the SCS (as received material) and the cylindrical specimen (pre-shocked material) [5]. It can be seen that the response of the as received material obtained using SCS is in excellent agreement with that of the cylindrical specimen made from the pre-shocked material. This can be contrasted with the data from Ostwaldt *et al.* [4] for a cylindrical specimen of the as received material at the same nominal strain rate. It is seen that the cylindrical specimen of the as received material exhibits substantial hardening. The flow stress of the pre-shocked material at quasistatic strain rates is much higher (by a factor of 2) in comparison to the as received material (SCS) from the present study as seen in Fig. 3. However, at high strain rates ($>5,000 \text{ s}^{-1}$), the flow stresses of the two materials are comparable and this is the regime where one observes the as received material to exhibit strain softening. It should also be noted that the pre-shocked material is only weakly rate sensitive even at the highest strain rates and can be attributed to shock hardening.

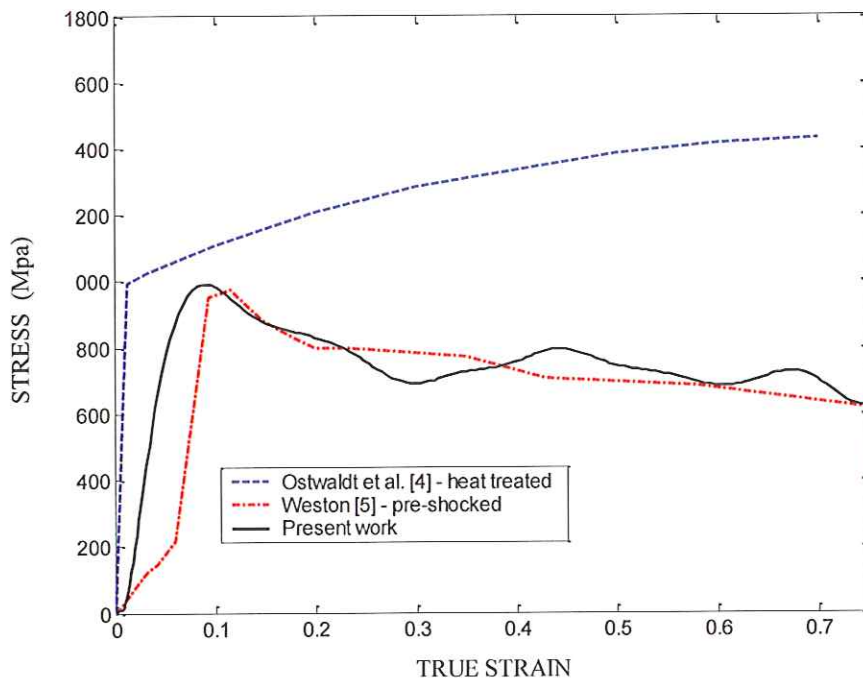


Fig. 4. Comparison of the stress-strain response at $9,000 \text{ s}^{-1}$ for α -iron with Ostwaldt *et al.* [4] and Weston [5]

In-situ temperature measurements during high strain rate deformation are used to gain insights regarding the conversion of plastic work into heat. A typical example of stress and temperature for the SCS deformed at a nominal strain rate of $3,800 \text{ s}^{-1}$ are plotted as a function of strain in Fig. 5. The parameters β_{dif} and β_{int} describing the conversion of plastic

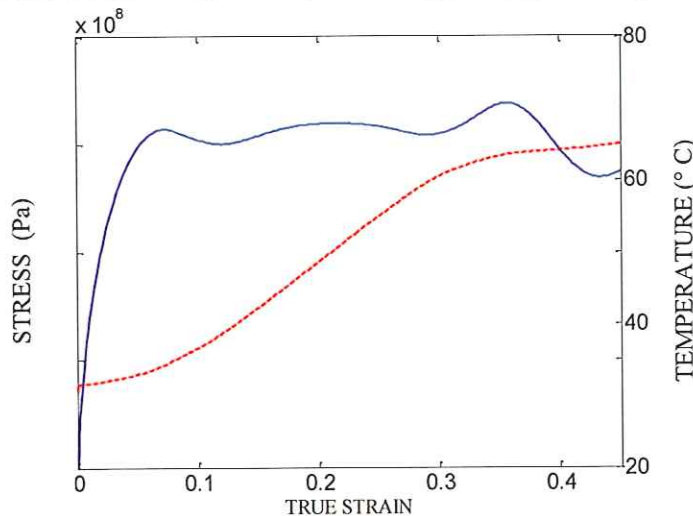


Fig. 5. Stress and temperature rise as a function of strain for dynamically deformed SCS

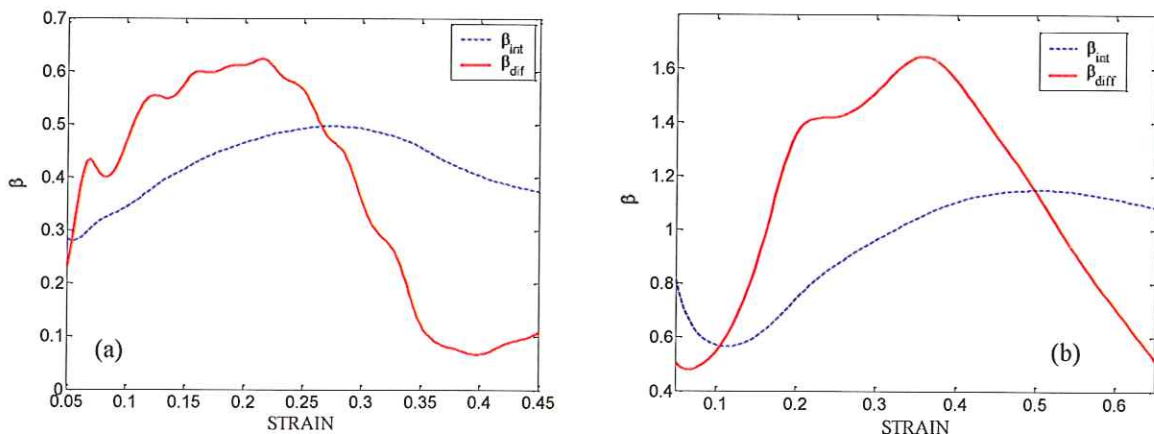


Fig. 6. Parameters for the conversion of plastic work converted to heat plotted as a function of strain at strain rates: a-3,800 s⁻¹ and b-8,400 s⁻¹

work to heat are computed using Eq. (2) from data such as those shown in Fig. 5. Typical examples of the two β parameters are shown in Fig. 6a,b for nominal strain rates of 3,800 and 8,400 s⁻¹, respectively. For deformation at a strain rate of 3,800 s⁻¹ (Fig. 6a), both β values are less than 1, as expected for deformation of metals. However, for deformation at a strain rate of 8,400 s⁻¹ (Fig. 6b), it is seen that β_{int} is greater than 1 beyond a strain of 0.5. This anomalous behavior indicates that there is internal heat release during deformation, giving rise to heating in addition to the thermomechanical conversion of plastic work to heat. It should be noted that at the higher strain rates, the as received material behaves like the pre-shocked material in addition to the strain softening behavior (Fig. 4). The pre-shocked material has undergone a reversible phase transformation from α (bcc) to ϵ (hcp) phase of iron. However, this phase transformation is also accompanied by residual plastic deformation characterized by debris which is the remnant of the phase transformation [6].

The microhardness profile across the gage section of the deformed SCS sample (strain rate, 11,500 s⁻¹) is shown in Fig. 7. It is seen that the hardness in the material surrounding the gage section is around 140 HVN and the hardness is elevated considerably within the gage section to 250 HVN. Also, the hardness in the gage section is comparable to the hardness values quoted for shocked α -iron [6]. The as received and deformed microstructures were examined after etching using optical and scanning electron microscopy. The microstructure of the as received material is shown in Fig. 8a and the micrograph of the dynamically deformed gage section is shown in Fig. 8b. The as received material has an equiaxed microstructure with a nominal grain size of 40 μ m. The deformed material (Fig. 8b) shows extensive recrystallization and as well as a small amount of twinning. Follansbee [11] observed twins in cylindrical samples of pure iron deformed at 4,000 s⁻¹. Nicolazo and Leroy [12] show that at a strain rate 2,500 s⁻¹, annealed iron exhibit twinning while cold-drawn iron does not show twinning. It appears that this recrystallization may be responsible for the heat released that is observed during the deformation at high strain rates as indicated by the anomalous β values (Fig. 6b).

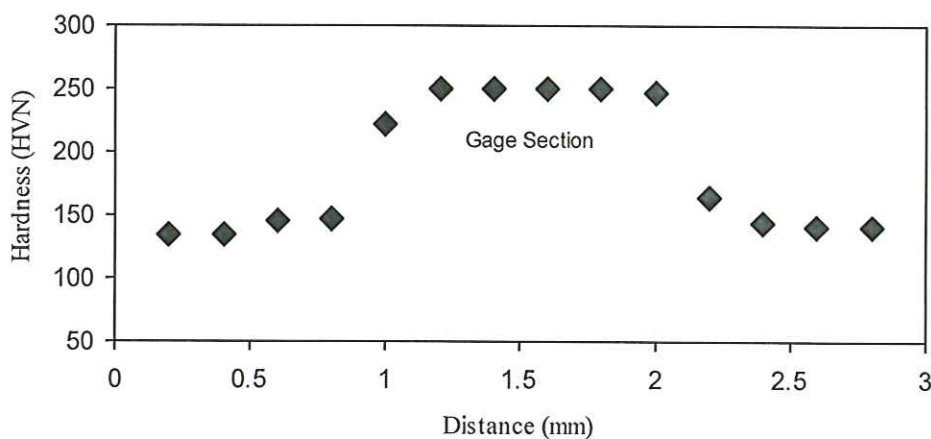


Fig. 7. Microhardness of α -iron deformed at a nominal strain rate of 11,500 s⁻¹

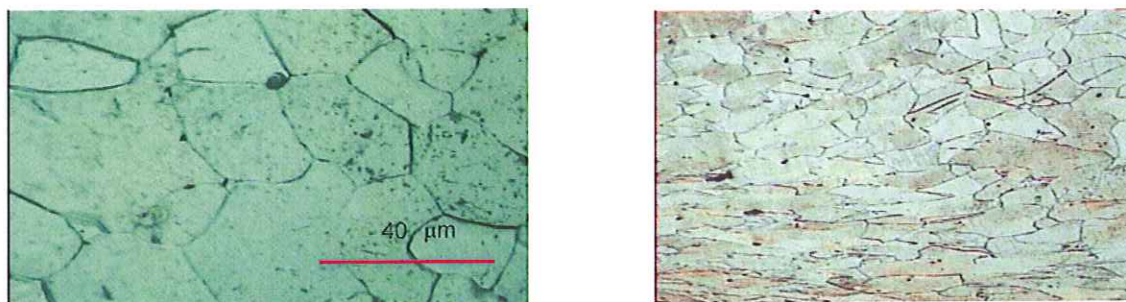


Fig. 8. a-Micrograph of as received α -iron, b-Micrograph of heavily deformed gage section

CONCLUSIONS

A recently developed specimen known as the shear compression specimen (SCS) [1,2] has been used to study the shear dominant dynamic behavior of as received α -iron up to strain rates of $2 \times 10^4 \text{ s}^{-1}$. The material exhibits considerable rate sensitivity at strain rates beyond 10^3 s^{-1} . The material exhibits strain hardening and the response shows good agreement with published literature data [3,4] until up to strain rate of $5,000 \text{ s}^{-1}$. At strain rates beyond $5,000 \text{ s}^{-1}$, the material exhibits strain softening and the material response is in good agreement with high strain rate available for preshocked material [5]. The fraction of plastic converted to heat computed using in-situ dynamic measurements of temperature show anomalous behavior ($\beta_{\text{int}} > 1$) at the higher strain rates where the material exhibits strain softening. The exothermic heat release observed during dynamic deformation is likely the result of recrystallization that accompanies large strain deformation at high strain rates. Microhardness measurements in the gage section show values that are representative of the shocked α -iron [6].

Acknowledgements

The research reported here is supported by the US Department of Energy through the ASCI Center for Dynamic Response of Materials at the California Institute of Technology and is gratefully acknowledged. GR would like to acknowledge the support of the Office of Naval Research (Dr. J. Christodoulou, Program Manager) for his research on dynamic behavior of metals.

References

- [1] Rittel, D., Lee, S., Ravichandran, G., A shear-compression specimen for large strain testing, *Exp. Mech.*, 42 (2002), pp. 58-64
- [2] Vural, M., Rittel, D., Ravichandran, G., Large strain mechanical behavior of 1018 steel over a wide range of strain rates, *Met. Mat. Trans.* 34A (2003), pp. 2873-2885
- [3] Klepaczko, J.R., The strain rate behavior of iron in pure shear. *Int. J. Sol. Structures*, 5 (1969), pp. 533-548
- [4] Ostwaldt, D., Klepaczko, J.R., Klimanek, P., Compression tests of polycrystalline alpha-iron up to high strains over a large range of strain rates, *J. de Physique IV*, 7 (C3) (1997), pp. 385-390
- [5] Weston, G.M., 1992, Flow stress of shock-hardened Remco iron over strain rates from 0.001 to $9,000 \text{ s}^{-1}$, *J. Mat. Sci. Lett.*, 11 (1992), pp. 1361-1363
- [6] Meyers, M.A., *Dynamic Behavior of Materials*, New York, John Wiley & Sons (1994)
- [7] Cuitino, A.M., Stainier, L., Wang, G.F., Strachan A., Cagin T., Goddard, W.A., Ortiz, M., A multiscale approach for modeling crystalline, *J. Comp. Aid. Matls. Des.*, 8 (2002), pp. 127-149
- [8] Gray, III, G. T., Classic Split-Hopkinson pressure bar testing, in: *ASM Handbook*, Vol. 8, Mechanical Testing and Evaluation, ASM International, Metals Park, Ohio (2000), pp. 462-476.
- [9] Clifton, R.J., Klopp, R.W., Pressure shear plate impact testing, in: *Metals Handbook*, Vol. 8, 9th edition, Mechanical Testing, ASM, Metals Park, Ohio (1985), pp. 230-239
- [10] Hodowany, J., Ravichandran, G., Rosakis, A. J., Rosakis, P., Partition of plastic work into heat and stored energy in metals, *Exp. Mech.*, 40 (2000), pp. 113-123
- [11] Follansbee, P.S., Analysis of the strain-rate sensitivity at high strain rates in fcc and bcc metals, *Proc. Inst. Phys. Conf.*, Ser. 102 (1989), p. 213
- [12] Nicolazo, C., Leroy, M., Dynamic behaviour of α -iron under decremental step pulses, *Mech. Matls*, 34 (2002), pp. 231-241

AN EXPERIMENTAL INVESTIGATION OF DRY FRICTION FOR A LARGE RANGE OF SLIDING VELOCITIES

G. Sutter^(a), S. Philippon^(b), A. Molinari^(a)

Laboratory of Physics and Mechanics of Materials, UMR CNRS 75-54,

(a) Université de Metz, (b) Ecole Nationale d'Ingénieurs de Metz

Ile du Sauley, 57045 Metz cedex 01, France

Summary: To extend the field of investigation concerning the friction coefficient measurement, an original experimental device is designed. Using respectively an air gun set-up and a hydraulic test machine, this device allows to explore a large range of sliding velocities. Quasi-static and dynamic conditions are investigated for steel on steel dry friction. Different normal pressures can be applied on the specimens and similar conditions to the friction process at the tool-chip interface are reproduced. The experimental results show the effect of the sliding velocities on the friction coefficient for different normal forces. The usual decreasing friction coefficient with increasing sliding velocity is confirmed. However, for higher velocities an opposite evolution is observed.

INTRODUCTION

For the most engineering applications, the friction is present and plays an important role in the useful life and in performances. This explains the precedence of the works found in the literature. Leonardo da Vinci, the precursor, proposed as early as 1400 a set-up to measure friction. The numerous studies and experimental set-up proposed since then confirm that the friction process is complex and depends on several parameters. To study the influence of the parameters such as the applied normal pressure, sliding velocity, material properties, dimensions and roughness of the contact surfaces and the thermal effects, many experimental devices with different design are necessary. Friction at high sliding velocities is usually tested with different set-up than those used to analyze high pressures.

The most frequently used experiment is the pin-on-disk apparatus [1-6] where the end surface of a cylindrical specimen (material M_A) is pressed against the surface of a large rotating disk (material M_B). In these tests, the effects of friction and wear are generally merged because the specimens rub several times on the same surface. Furthermore, the sliding speed varied along the surface in contact. Generally extreme contact conditions such as high normal pressure are difficult to practice with such devices. However a sophisticated pin-on-disk was designed to explore extreme conditions [6]. The diameter of the pin is very small in comparison with the disk so as to limit the variations of the sliding velocity on the contact surface. The large diameter of the disk allows obtaining high velocities (about 550 m/s). A fresh surface in front of the pin is ensured by the radial moving of the pin during the disk revolution. These experiments were designed in the US for military applications (friction in the bore of a cannon).

Based on the torsional Kolsky bars, other works [7-8-9] are developed in the attempt to get high normal pressures. The friction was produced at the thin tube interface. The interesting aspect was a quasi-instantaneous sliding velocities but the duration time of this process was relatively short-lived (a few milliseconds). For very higher normal pressures (from 100 MPa to 3 GPa) a direct plate impact set-up was designed [10-12]. The impacting surfaces are required to be perfectly flat and parallel to generated one-dimensional waves. Using a spinning steel ball magnetically rotated between three plates, the greatest sliding speed [13-14] (about 800 m/s) was obtained with very light load (0.015 Mpa). The main experimental devices are compared in Fig. 1, with the range of sliding velocities and of normal applied pressures. Excepted in the experiment developed by Montgomery [6], a high normal pressure involves a low sliding velocity.

In this work, an original experimental set-up is designed to reproduce dry friction at large sliding velocities (from 0 to 60 m/s) and high normal pressure (from 8 to 220 MPa). The capacities of our device, reported in Fig. 1, allow to explore an interesting range of sliding velocities V and of normal pressures p . Two sliding pairs of materials were tested to validate this device: steel on steel and steel on tungsten carbide. The later pair reproduced the tool-chip interaction during high speed machining.

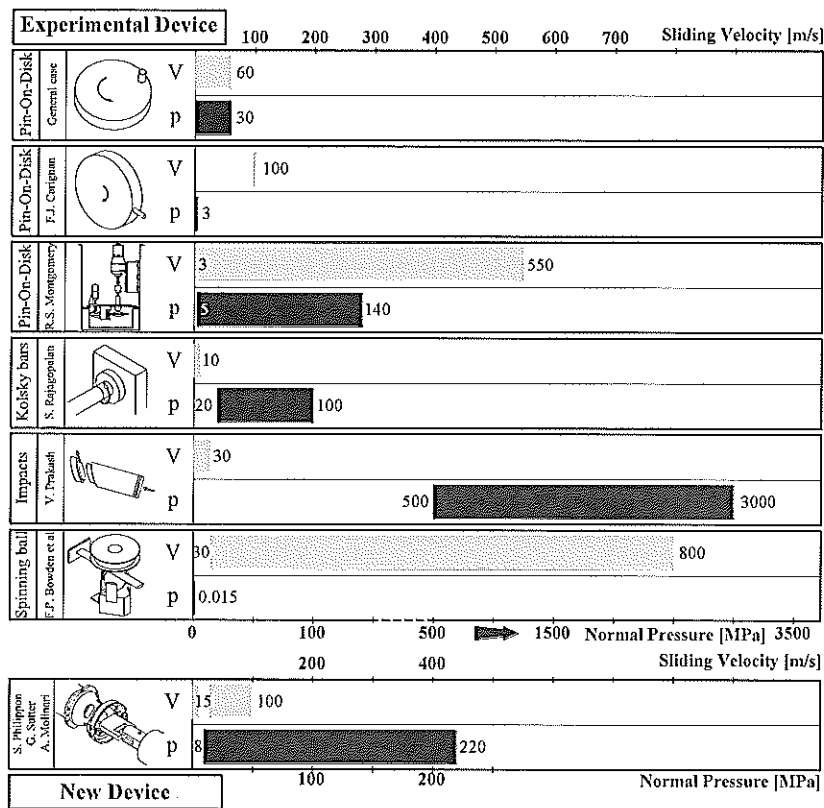


Fig.1. Performances of various experimental friction devices compared to the present system

EXPERIMENTAL DEVICE

The general schematic diagram of the friction system is shown Fig. 2. It consists of a thin tube on which a set of strain gauges are placed and of a dynamometer ring. The dynamometer ring applies a normal pressure between the two specimens A and B and the intensity of this pressure is calibrated by adjusting the dimensions of the specimens.

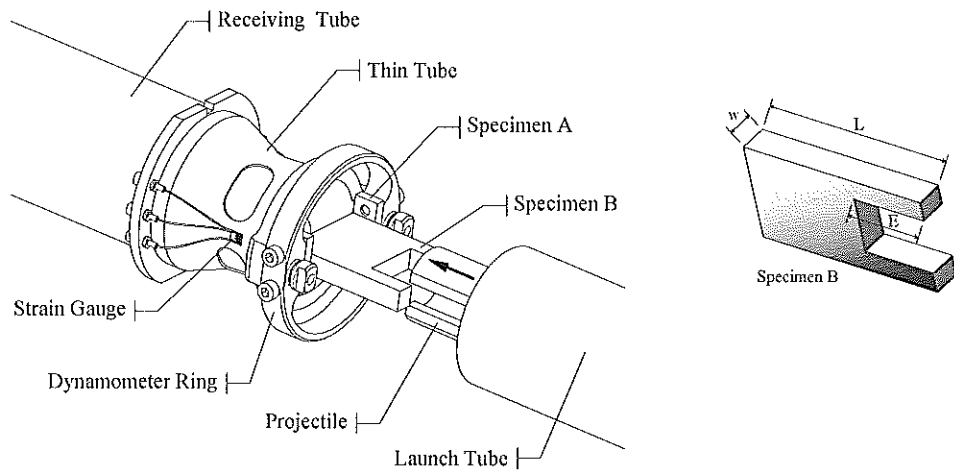


Fig. 2. Schematic illustration of the experimental device adapted on an air gun to measure the dynamic friction coefficient for a sliding speed up to 100 m/s.

The thin tube supports the axial forces generated by friction. An optimal design for the thin tube was obtained by considering successive geometries which were tested with Finite Elements calculations. The axial component of the friction force can be measured from the signal of the strain gauges, while the normal component is initially calibrated with the dynamometer ring.

A gas gun is used to send a projectile on the specimen B, Fig. 2, so as to generate a high sliding speed between the materials M_A and M_B . The lower velocities are investigated with the same friction device which can be adapted on a hydraulic test machine. The movement of the specimen B is controlled by the moving crosshead of the hydraulic machine. This test technique is an adaptation of an experimental set-up developed by Sutter et al [15], for orthogonal cutting tests at very high speed.

Another device based on the pin-on-disk principle has been developed to analyze an intermediate range of sliding velocities, connecting those studied with the ballistic set up to those obtained with the hydraulic machine. This pin-on-disk type set-up is adapted on a NC lathe and allows to explore the sliding velocities from 0.5 m/s to 15 m/s.

The material M_A consists of a disk and the material M_B is fixed on a dynamometer KISTLER allowing to monitor the friction forces. To study the friction at the tool-chip interface, the pin specimen M_B is an uncoated carbide tool. The original design of this pin-on-disk set up is designed for testing standard carbide tools.

EXPERIMENTAL RESULTS

A typical signal record obtained during tests on the hydraulic machine is presented Fig. 3. The similarity of signals obtained with the hydraulic machine cell, at the bottom of the graph, and with the gauges, illustrates the high sensitivity of the proposed set-up. Throughout a sliding duration of about 500 ms, a plateau is observed corresponding to a quasi-stationary process. Then, the reduction of the rigidity due to the geometry of the specimen B (see Fig. 2) explains the decreasing force signal. A constant normal pressure is applied when sliding occurs along the length $L-E$ of the specimen B. The total time duration of contact is 1180 ms and explains the abrupt end of the recorder. The high frequency oscillations superposed on signals are generated by the functioning of the hydraulic machine.

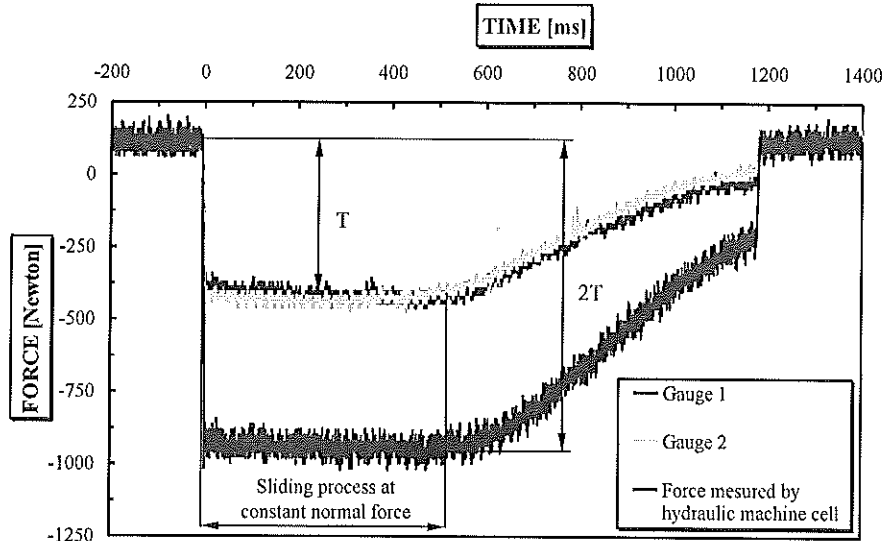


Fig. 3. Typical signal obtained from the strain gauges located on the thin tube and from the load cell of the hydraulic machine. Sliding velocity $V = 0.05$ m/s, normal pressure $p = 27$ Mpa, steel on steel dry friction (XC18)

With the high-speed ballistic set-up, the signals from the left and right gauges are shown in Fig. 4.

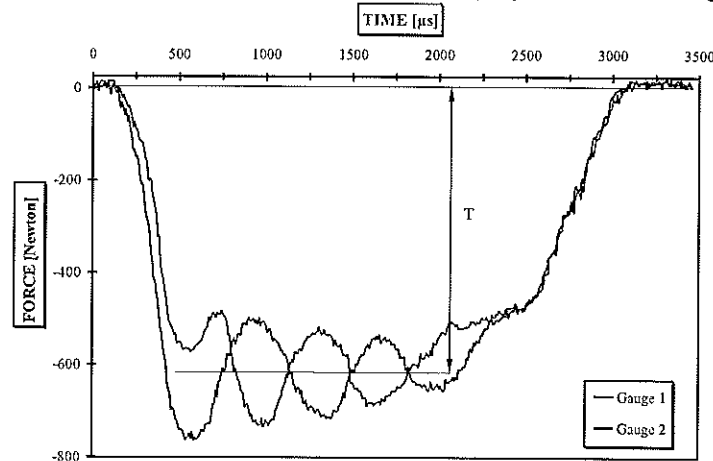


Fig. 4. Typical signal obtained from strain gauges located on the thin tube with the air gun set-up. Sliding velocity $V = 27$ m/s; normal pressure $p = 33$ Mpa, steel on steel dry friction (XC18)

These signals are identical in form but are in phase opposition. This phenomenon can be explained by the positioning of the specimen B related to the projectile. If the back of the specimen is not rigorously parallel to the front of the projectile, the impact is not perfectly plane. A slight flexion movement is induced. The frequency of oscillation of each signal has been characterized by FE calculations [16] and compares well with experimental measurements. The decrease of the rigidity of the specimen can be also observed by decreasing signal after 1800 μ s. For this recorder, the contact between specimens is finished nearly at the time duration of 2220 μ s.

The results obtained for steel on steel dry friction are presented on Fig. 5 with a cross in bold type among a variety of other experimental data reported by Lim and Ashby [17] for steel on steel dry friction. The present results are in agreement with the general trends.

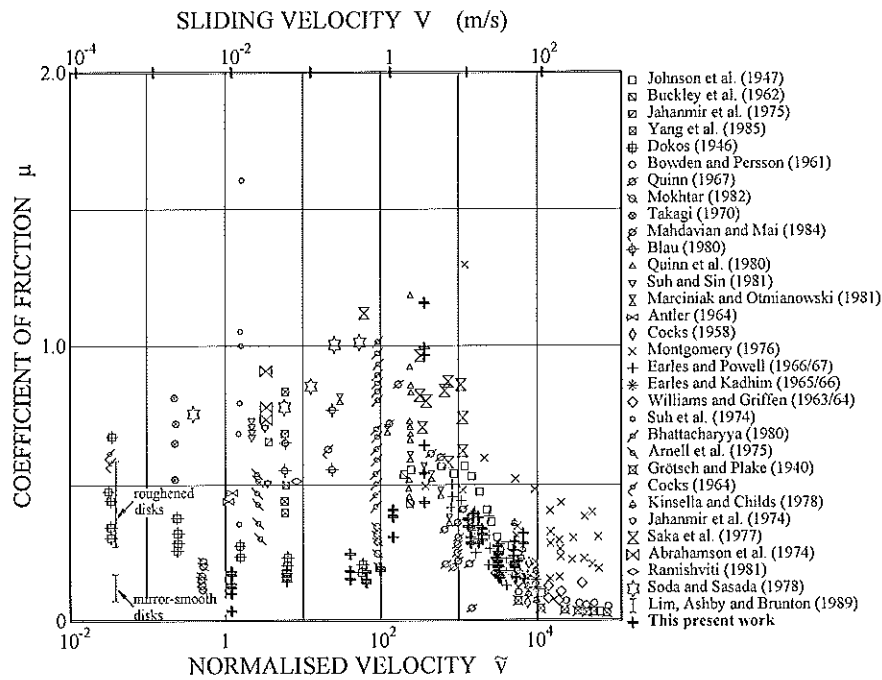


Fig. 5. Summary of experimental data for the friction coefficient μ in terms of the sliding velocity (scaling on the upper part of the figure) for steel on steel dry friction, Lim et al [17]. The results obtained in the present work (+) are superimposed.

For sliding speeds higher than 3 m/s the results obtained are in good agreement with those obtained in the literature. The friction coefficient decreases with increasing sliding speed. The friction heating at the contact surfaces (melting can even occurs) generally explains this evolution. It must be noted that the large dispersion in the results can be partly attributed to differences in the normal applied pressures.

In the slow-sliding regime ($V < 3$ m/s) the roughness of contact surfaces is an important parameter. The asperities create adhering connection like spot-weld which must be sheared during the friction process. Our results are in the lower limit with respect to other experimental data for $V < 3$ m/s, but are compatible with these data. A similar evolution is obtained, namely an increasing of the friction coefficient with the sliding velocity. A possible reason to this trend could be the effect of roughness. The asperities like teeth of gear resist the movement. The resistance of the relative movement is intensified with the increase of the speed.

The other pair of materials tested on this set-up, is a low carbon steel (French reference XC 18) together with an uncoated carbide tool. Using successively the three devices previously described, the friction coefficient against the sliding velocity is shown in Fig. 6. This plot confirms an increase of μ for the lower speed and a decrease for higher speed.

The intense heating at the tool-chip interface, with temperatures of the order of 900°C and more in real cutting conditions, see Sutter et al. [18], causes the decreasing of the friction coefficient sliding velocities up to 30 m/s. However for sliding speeds higher than about 30 m/s, the friction coefficient μ increases slightly. In machining process the minimum value of the friction coefficient can be correlated with the minimum cutting forces already observed [15] for the same workpiece material. A large dispersion in the results is observed for the lowest normal pressure. It is observed that the friction coefficient decreases with increasing normal pressure.

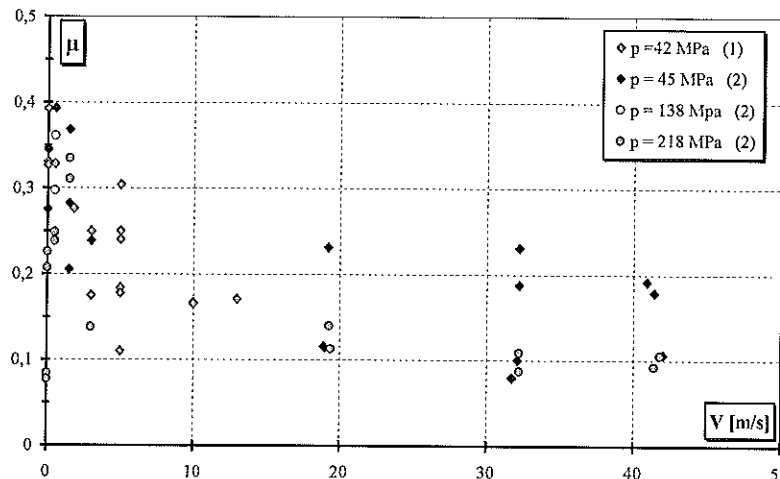


Fig. 6. Dry friction coefficient μ for the sliding of steel on a standard uncoated carbide tool as a function of the sliding velocities V for various values of normal pressure p
 - (1) Pin-On-Disk adapted on a NC lathe - (2) new friction device.

CONCLUSIONS

The experimental set-up presented in this study allows investigating the dry friction process from low to high sliding velocities with the same friction device. The originality of this device is the ability to explore high sliding speeds (> 60 m/s) and high normal pressure (200 MPa). The results obtained for steel on steel dry friction are in good agreement with previous experimental data [17]. Friction between a low carbon steel and an uncoated carbide tool is investigated for application to machining. Two characteristic sliding velocities are found to characterize friction between this pair of materials. The highest value of the friction coefficient is observed at the sliding speed $V \approx 1$ m/s. At larger speeds, the friction coefficient decreases and reaches a minimum at $V = 30$ m/s. The decrease of the friction coefficient against the speed is an important phenomenon in cutting process. In fact during high speed machining, the friction is one of the most important parameters acting on the level of cutting forces. During these tests an increasing normal pressure was conducive to a reduction of the friction force.

References

- [1] Y.M. Chen, J.C. Pavy, B. Rigaut, Test de frottement à grande vitesse sous faibles charges des céramiques, publications CETIM, Senlis, (1990) 79-104.
- [2] D. Paulmier, H. Zaidi, R. Bedri, E.K. Kadiri, L. Pan, Q. Jiang, Steel surface modifications in magnetised sliding contact, *Surfaces & coatings technology* 76-77 (1995) 583-588.
- [3] S. Philippon, G. Sutter, J. Dedourge, A. Molinari, Etude expérimentale du frottement, *International Journal of Mechanical Production Systems Engineering, High Speed Machining* (2003) 57-60.
- [4] D. Ryckelynck, M. Meiller, Friction modelisation of tool workpiece contact for the finite element simulation of cutting process, *Mécaniques & Industries* 3 (2002) 323-332.
- [5] W. Grzesik, Z. Zalisk, P. Nieslony, Friction and wear testing of multilayer coatings on carbide substrates for dry machining applications, *Surfaces and Coatings Technology* 155 (2002) 37-45.
- [6] R.S. Montgomery, Friction and wear at high sliding velocity, *Wear* 36 (1976) 275-298.
- [7] K.A. Hartley, J. Duffy, R.H. Hawley, The torsional Kolsky (Split-Hopkinson) bar, *Mechanical Testing, Metals Handbook* 8, 9 (Ed.), ASM, Metals Park, OH., pp, 218-230, 1985.
- [8] S. Rajagopalan, V. Prakash, A modified torsional Kolsky bar for investigating dynamic friction, *Experimental Mechanics* 39, n°4, (1999) 295-303.
- [9] K. Ogawa, Impact friction test method by applying stress wave, *Experimental Mechanics* 37, n° 4, (1997) 398-402.
- [10] V. Prakash, A pressure-shear plate impact experiment for investigating transient friction, *Experimental Mechanics* 35, n°4 (1995) 329-336.
- [11] V. Prakash, R.J. Clifton, Time resolved dynamic friction measurements in pressure-shear, *Experimental techniques in the dynamics of deformable solids presented at the 1st joint mechanics meeting of ASME 165*, Charlottesville, pp, 33-48, 1993.
- [12] M.A. Irfan, V. Prakash, Time resolved friction during dry sliding of metal on metal, *International Journal of Solids and Structures* 37 (2000) 2859-2882.
- [13] F.P. Bowden, F.R.S. and E.H. Freitag, The friction of solids at very high speeds I. Metal on metal; II. Metal on diamond, *Proceedings of the Royal Society of London, series A : Mathematical and physical sciences* 248 (1958) 350-367.
- [14] F.P. Bowden, F.R.S. and P.A. Persson, Deformation heating and melting of solids in high speed friction, *Proceedings of the Royal Society of London, series A : Mathematical and Physical Sciences* 260 (1960) 433-458.
- [15] G. Sutter, A. Molinari, L. Faure, J.R. Klepaczko, D. Dudzinski, An Experimental Study of High Speed Orthogonal Cutting, *Journal of Manufacturing Science and Engineering* 120 (1998) 169-172.
- [16] Philippon S., Sutter G., Molinari A. : An Experimental Study of Friction at High Sliding Velocities. Submitted to *Wear* 2004.
- [17] S.C. Lim, M.F. Ashby, J.H. Brunton, The effects of sliding conditions on the dry friction of metals, *Acta metallurgica* 37, n°3 (1989) 767-772.
- [18] G. Sutter, L. Faure, A. Molinari, N. Ranc, V. Pina, An experimental technique for the measurement of temperature fields for the orthogonal cutting in high speed machining, *International Journal of Machine Tools & Manufacture* 43 (2003) 671-678.

DYNAMIC BEHAVIOUR OF STEELS: AN ELASTIC-VISCOPLASTIC MICRO-MACRO POLYCRYSTALLINE APPROACH

Véronique Favier, Stéphane Berbenni*, Xavier Lemoine, Marcel Berveiller

Laboratory of Physics and Mechanics of Materials, UMR CNRS 7554, ENSAM
4 rue Augustin Fresnel, 57078 Metz Cedex 03, France

* Permanent address: Department of Mechanical Engineering, Northwestern University, 2145 Sheridan Road, Evanston, IL. 60208-3111, USA

Summary: An elastic-viscoplastic micro-macro approach is proposed to model the tensile dynamic behaviour of polycrystalline steels for strain rates ranging from 10^{-3} s^{-1} to 1000 s^{-1} . Single-crystal constitutive equations based on the thermal activated dislocation motion and the phonon drag mechanism are introduced. The heating up produced at high strain rates by thermo mechanical coupling is also taken into account. The strain-hardening law is based on the storage and the annihilation of dislocations and the evolution of the Peierls stress with temperature. Model predictions are compared with experimental results concerning steels having different microstructures. Owing to the introduction of physical parameters in the modeling, a good description of the differences observed between the constitutive behaviours of IF and Dual-Phase (DP450 and DP600) steels is obtained. These differences concern strength, strain hardening as well as strain rate sensitivity.

INTRODUCTION

The need to lower automobile vehicle weights and thereby improve fuel economy has resulted in the development of steels with increased strength/weight ratios. For example, conventional low-carbon steels are replaced by high-strength low alloy steels or better Dual-Phase steels. The development of these new steels requires correlating microstructure and deformation mechanisms to macroscopic mechanical properties under quasi-static and dynamic loading conditions. The objective of the paper is to present a micromechanical model considering some microstructural and metallurgical features of steels to describe their mechanical behaviour in a large range of strain rates. Based on micro-mechanics analysis and homogenization techniques, it consists in relating accurately the microstructure, the behaviour of each phase and the mechanical interactions between the different relevant components, to the global behaviour. This model is based on a new and non-conventional self-consistent scheme [1-3] developed for the case of elasto-viscoplasticity. It is applied to simulate the behaviour of polycrystalline steels having different microstructures and subjected to various strain rate histories. To properly describe the strain rate sensitivity of steels, the intracrystalline deformation processes here considered is the thermally activated glide of dislocations to overcome the Peierls barrier [4] and the phonon drag mechanism. Tensile behaviours obtained for steels having different microstructures such as a single ferritic phase (Interstitial Free Steel) and two ferritic-martensitic phases (Dual-Phase steels) are simulated for strain rates ranging from 10^{-3} to 1000 s^{-1} and compared with experimental results.

MICROMECHANICAL MODELING

The mechanisms responsible for viscoplastic flow rule of ferritic steels are essentially the crystallographic slip of two main slip systems (110)<111> and (112)<111> related to the body centred cubic crystal structure (bcc). The crystallographic slip of a slip system is the result of a combined dislocation glide on this system. The slip rate is thus classically linked to the mean velocity of dislocations according to the Orowan relation:

$$\dot{\gamma} = \rho_m b v \quad (1)$$

where ρ_m is the density of moving dislocation and b is the magnitude of the Burgers vector. In bcc single crystal, the slip rate is controlled (i) at low strain rates by the glide of screw dislocations assisted by thermal activation to overcome the Peierls barrier and (ii) at high strain rates, it is thought that thermal activation is no longer necessary to assist a dislocation past a barrier, the dislocation velocity is solely limited by drag mechanisms, leading to a high increase of the strain-rate sensitivity. In case (i), the mean velocity v_{la} of dislocations is written [4-5]:

$$v_{la} = v_0 \exp \left[-\frac{\Delta G_0}{kT} \left(1 - \left(\frac{|\tau|}{\tau_r} \right)^p \right)^q \right] \text{sign } \boldsymbol{\epsilon} \quad (2)$$

v_0 is a reference velocity, ΔG_0 is the activation energy when $\tau = 0 \text{ MPa}$, p and q are two adjustable parameters, τ is the resolved shear stress, τ_r is a reference shear stress that describes the strain hardening state, k is the Boltzmann constant and T the absolute temperature. In case (ii), the mean velocity v_d of dislocations is written:

$$v_d = \frac{b\tau}{B} \quad (3)$$

where B is the drag coefficient. For the transition regime from thermally activated to dislocations drag controlled deformation, following many authors, the dislocation velocity is [6-7]:

$$v = \frac{1}{\frac{1}{v_{la}} + \frac{1}{v_d}} \quad (4)$$

Combining Equations (1), (2), (3) and (4) with a multiple system approach provides the slip rate $\dot{\gamma}^g$ on the slip system (g). The strain-hardening model takes into account the creation and the annihilation of dislocations. The evolution of the total dislocation density ρ^g for a slip system (g) can be written as:

$$\dot{\rho}^g = \frac{1}{b} \left(\frac{\sqrt{\sum_{i \neq g} \rho^i}}{K} - 2y_c \rho^g \right) \dot{\gamma}^g \quad (5)$$

where y_c is the characteristic annihilation length. K is a material parameter linked to the mean free path L^g of dislocations by the following equation:

$$L^g = \frac{\sqrt{\sum_{i \neq g} \rho^i}}{K} \quad (6)$$

The evolution of the strain-hardening is captured through the evolution law of the reference shear stress τ_r^g according to the following equation:

$$\dot{\tau}_r^g = \sum_h H^{gh} \dot{\gamma}^h - a \left(T - T_0 \right)^{2/3} \dot{T} \quad (7)$$

where $T_0 = 293K$ and H^{gh} is the hardening matrix [4]. Equation (7) is composed of a classical term of hardening laws plus a thermal softening term that becomes significant for loadings at high strain rates where high heating appears. The thermal softening is not only taken into account through the parameter a but also through the annihilation term because the annihilation length y_c is temperature dependent [8-9]:

$$y_c = \frac{\beta}{\tau_{r0}} \quad (8)$$

where $\beta = \frac{\mu b}{2\pi}$ and τ_{r0} is the Peierls stress at the temperature T .

The uniform temperature T is updated at each step and is calculated from the heat equation.

$$\dot{\theta} + \frac{\theta}{t} = \frac{1}{\xi C_p} \frac{1}{V} \int \sigma_{ij} \dot{\epsilon}_{ij}^{vp} dV \quad \text{with } \theta = T - T_{initial} \quad (9)$$

where ξ is the material density, C_p is its specific heat and V is the volume of the polycrystal. In our formulation, a progressive transition is used so that the system becomes isothermal at low strain rates and adiabatic at high strain rates. Indeed, a constant time t , characteristic of the losses through the sample faces has been introduced. It was chosen to represent an isothermal deformation process for quasi-static loadings and an adiabatic deformation process for strain rates of about 100 s^{-1} [10]. $\dot{\epsilon}_{ij}^{vp}$ and σ_{ij} are the tensors of the viscoplastic strain rate and the stress at the grain level, respectively. From the theory of crystalline plasticity, they are linked to the slip rate and to the shear rate, respectively by the following equations:

$$\dot{\epsilon}_{ij}^{vp} = \sum_g R_{ij}^{(g)} \dot{\gamma}^{(g)} \quad (10)$$

$$\tau^{(g)} = R_{kl}^{(g)} \sigma_{kl} \quad (11)$$

where $R_{kl}^{(g)}$ is the Schmid tensor for the slip system (g). $\dot{\epsilon}_{ij}^{vp}$ and σ_{ij} are related through the tensor of viscoplastic compliances m_{ijkl}^{vp} by:

$$\dot{\epsilon}_{ij}^{vp} = m_{ijkl}^{vp} \sigma_{kl} \quad (12)$$

Finally, the single-crystal behaviour is represented by a Maxwell element as:

$$\dot{\epsilon}_{ij} = \dot{\epsilon}_{ij}^e + \dot{\epsilon}_{ij}^{vp} = s_{ijkl} \dot{\sigma}_{kl} + m_{ijkl}^{vp} \sigma_{kl} \quad (13)$$

where s_{ijkl} is the tensor of elastic moduli.

The behaviour of the polycrystal is determined using a modified self-consistent approximation proposed recently [1-3] for elastic-viscoplastic heterogeneous materials and applied to polycrystalline metals [4]. Its main characteristics are the following.

- Grains exhibiting the same crystallographic orientation belong to the same "phase". These grains are randomly distributed and consequently display an isotropic distribution. In a statistical representation of the microstructure, this complex system can be assumed to be equivalent to one spherical inclusion gathering all the grains of the same phase.
- Stress, strain, stress rate and strain rate fields are uniform in the spherical inclusion.
- The local elastic-viscoplastic behaviour is represented by a Maxwell element (see Equation (13))
- For the concentration step that consists to relate the local to the global fields, a modified self-consistent model is used. It involves simultaneously self-consistency for viscous part and self-equilibrium for elastic part. The viscous strain rate is translated with regarding the self-consistent solution for the heterogeneous material having only viscous properties. The elastic moduli are written as fluctuations regarding elastic reference moduli. Thus, a simple and compact strain rate relation is obtained. In the case of an elastic homogeneous behaviour, it is written :

$$\dot{\sigma} = \dot{\Sigma} + C^e : \left(S^E - I \right) : \left(\dot{\epsilon}^{vp} - A^{B^e} : \dot{E}^{vpe} \right) \quad (14)$$

where $\dot{\Sigma}$ is the macroscopic stress tensor, $\dot{\epsilon}^{vp}$ and \dot{E}^{vpe} are respectively the local and macroscopic viscoplastic strain rate tensors, C^e is the effective tensor of elastic moduli, A^{B^e} represents the strain rate concentration tensor for heterogeneous materials having a pure viscoplastic behaviour, $S^E = \Gamma_I^{C^e} : C^e$ is the well-known Eshelby tensor [11] and I is the fourth-order identity tensor. This interaction formula significantly differs from Kröner-Weng's equation [12-13] by the term A^{B^e} . In particular, Kröner-Weng's model strongly overestimates stresses in the material whereas the present model describes less stiff interactions because representing elastic-viscoplastic intergranular accommodation.

- Finally, the global behaviour of the polycrystal is directly determined by averaging the local fields:

$$\dot{E} = \frac{1}{V} \int \dot{\epsilon} dV \quad \text{and} \quad \dot{\Sigma} = \frac{1}{V} \int \dot{\sigma} dV \quad (15)$$

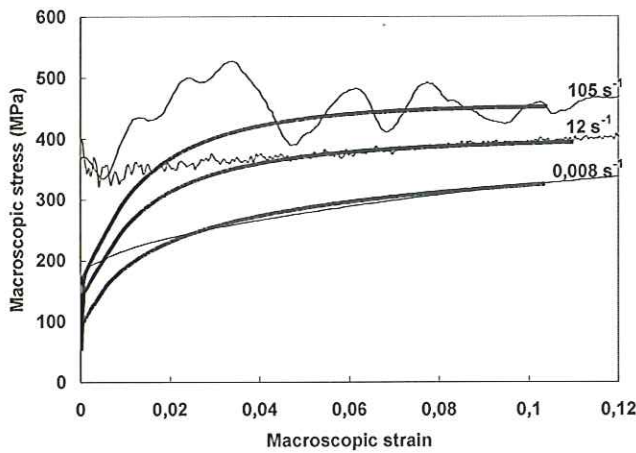
RESULTS AND DISCUSSION

Dynamic tensile tests were conducted in ARCELOR R&D using a dynamic SCHENK machine and Hopkinson bars allowing to reach strain rates ranging from 10^{-3} s^{-1} to 1000 s^{-1} .

First only the thermally activated regime ($10^{-3} \text{ s}^{-1} - 100 \text{ s}^{-1}$) is analyzed. The present model is applied to the behaviour of an IF (Interstitial-Free) steel and to two Dual-Phase steels at various strain rates. The IF steel is a ferritic single-phase material. Its mean grain size is around $20 \mu\text{m}$ with a low texture that is neglected in the modeling. The parameters of the model for the IF steel are indicated on Tables 1 and 2; some of them are chosen from literature data (Tab. 1) [4] and others have been identified after successive comparisons between calculated and experimental σ - ε curves at three strain rates: $8 \times 10^{-3} \text{ s}^{-1}$, 12 s^{-1} et 105 s^{-1} . The identified parameters are bounded to agree with the values reported in the literature (Tab. 2). In particular and as mentioned by Hoc [14], the initial mean free path can be calculated using the

initial dislocation density ρ_0 and Equation (6). It is found equal to $L_{init} = \frac{10}{\sqrt{23 \times 10^{10}}} = 20 \mu\text{m}$ that is the average

grain size of the ferrite. As illustrated on Figure 1, the model correctly describes the increase of stress level as well as the evolution of the hardening curve with the strain rate, particularly thanks to the description of the thermal softening exhibiting a saturation of the σ - ε curve at high strain rates. On the contrary, discrepancies between experimental and simulated curves appear at low strains. They are mainly due to the viscoplastic formulation used in the flow rule. Indeed, no plastic yield criterion is used and all the slip systems are active right from the beginning of the loading. Consequently, the transition from the elastic to the (visco) plastic regime occurs earlier than it does in the experiments.



μ (MPa)	ν	b (m)	$\beta(y_c)$ (m.MPa)	$\frac{1}{\zeta C \alpha}$ (m.MPa)
80000	0,3	$2,5 \cdot 10^{-10}$	$3,2 \cdot 10^{-6}$	0,33

Table 1. Material parameters for ferrite from literature

Fig. 1. Uniaxial flow curves for three indicated macroscopic strain rates for the IF steel: experiments (thin solid lines) et simulations (bold solid lines)

$\dot{\gamma}_0$ (s^{-1})	ΔG_0 (eV)	p	q	τ_{r0} (MPa)	ρ^0 (m^{-2})	K	t (s)	a
$10^6 \text{ s}^{-1} \leq \dot{\gamma}_0$		$0 < p \leq 1$	$1 \leq q \leq 2$		$10^9 \text{ m}^{-2} \leq \rho_0$			
$\leq 10^{11} \text{ s}^{-1}$					$\leq 10^{12} \text{ m}^{-2}$			
$9,6 \cdot 10^7$	0,862	1	2	90	10^{10}	10	$2 \cdot 10^{-2}$	12

Table 2. Material parameters for ferrite identified from experiments on the IF steel bounded to agree with the values reported in the literature

Then, the influence of the microstructure on the dynamic behaviour is studied through Dual-Phase steels having around 8 and 15% of martensite. In the modeling, they are considered as two-phase polycrystals (Tab. 3). The ferrite behaviour is kepted identical as the one identified in the case of the IF steel except some parameters that were modified for metallurgical and microstructural reasons (Tab. 3). Thus, as far as the hardening parameters are concerned: (i) the initial reference shear stress is increased when the ferrite grain size decreases and when the solute carbon rate increases, (ii) the K parameter linked to the grain size is increased with the grain size. For the thermoviscoplastic flow rule parameters, the activation energy is increased to describe the lower strain rate sensitivity of ferrite in two-phase steels due to the extra-hardening of ferrite caused by accommodation dislocation surrounding the "as quenched" as well as the strain induced martensite and the presence of residual stresses created during the material processing [15].

The martensite is, as a first approximation, assumed to be a ductile phase and to follow a thermoviscoplastic flow rule as the ferrite does. However to describe its higher resistance, the values of τ_{r0} and ΔG_0 are strongly increased. The identified value of ΔG_0 has thus no more a physical sense. The K parameter depending of the martensite grain size is taken very low. Table 4 displays the set of the identified parameters of the martensite for the two studied Dual-Phase steels. Figure 2 displays the state of the von Mises equivalent stress calculated in the ferrite and martensite grains for the DP600 polycrystal deformed at 12 s^{-1} strain rate. At step 1 of Figure 2, the ferrite displays plastic deformation even when the martensite is quasi-elastic up to a stress level of about 1500 MPa. The stress level reached in the martensite is in good agreement with those found in literature [15-16], and taking the ratio $\frac{\tau_{r0}^M}{\tau_{r0}^F}$ equal to 5 appears good [16].

Family of steels	Volume fraction of martensite (%)	Mean ferritic grain size (μm)	τ_{r0} (MPa)	K	ΔG_0 (eV)
IF	0	~20	90	10	0,862
DP450	8	~20	100	10	1,293
DP600	15	~15	100	8	1,293

Table 3. Microstructural characteristics of IF and Dual-Phase steels and material parameters for ferrite taking into account the microstructural modifications as obtained from experiments on IF and Dual-Phase steels

$\dot{\gamma}_0$ (s^{-1})	ΔG (eV)	p	q	τ_{r0} (MPa)	ρ^0 (m^{-2})	K	τ (s)	a
$9,6.10^7$	8,62	1	2	540	10^9	2	2.10^{-2}	12

Table 4. Material parameters for martensite identified from experiments on DP450 and DP600 steels.

Figure 2 demonstrates also that the behaviour of the Dual-Phase steel is very close to the ferrite one. The stress level for the IF, DP450 and DP600 at macroscopic strain equal to 5% and 10% is plotted as a function of the macroscopic strain rate in Figure 3. The strain rate sensitivity is well described for strain rates ranging from 10^{-3} s^{-1} to 100 s^{-1} and for the different studied steels. The presence of the martensite involves a stress increase. In addition, the present model captures the hardening difference between the IF and Dual-Phase steels as observed by comparison between the stress levels at macroscopic strains of 5 and 10 %. The hardening is higher in the case of Dual-Phase steels. Indeed, the deformation is limited in the martensite leading to a delay of the occurrence of a softening mechanism in this steel.

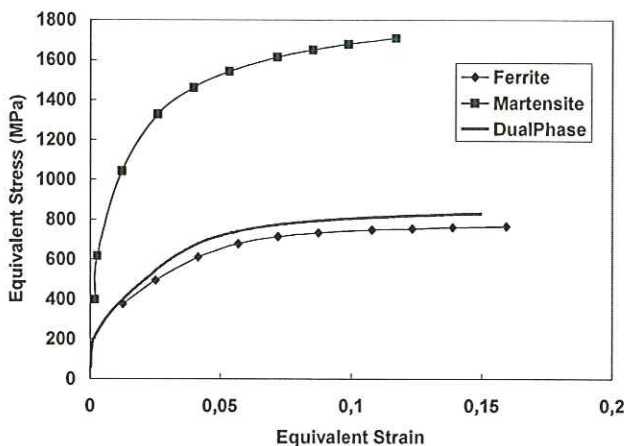


Fig. 2. Von Mises equivalent stress as a function of the Von Mises mean equivalent strain for DP600 and for ferrite and martensite. Loading corresponds to a tensile test at a strain rate of 12 s^{-1} .

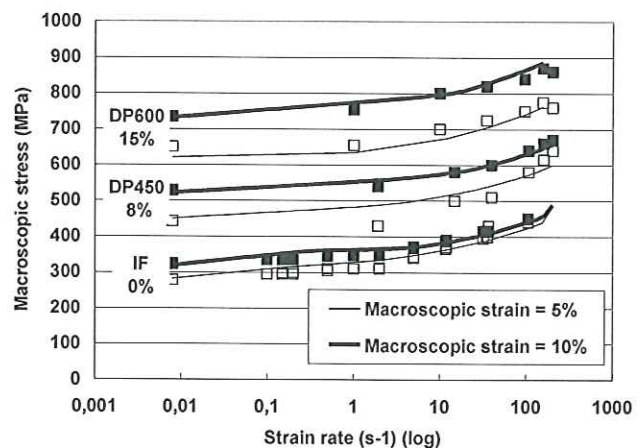


Fig. 3. Macroscopic flow stress as a function of strain rate for indicated macroscopic strains and steels: 0% of martensite (IF), 8% of martensite (DP450) and 15% of martensite (DP600) – Comparison between experimental (dots) and model (solid lines) data.

In this second part, the strain rate sensitivity up to 1000 s^{-1} is studied for the IF steel. Figure 4 shows first results comparing simulated and experimental results. In the modeling, the phonon drag is considered despite it is not clear if this mechanism occurs in this range of strain rates. Accounting for the phonon drag mechanism implies to modify slightly the material parameters for ferrite that still agreed with the values reported in the literature (Tab. 5). A good agreement between experiments and simulations is obtained at high strain rates but more discrepancies appear at low strain rates. The analysis of the transition from the thermally activated regime to the phonon drag one requires further investigations.

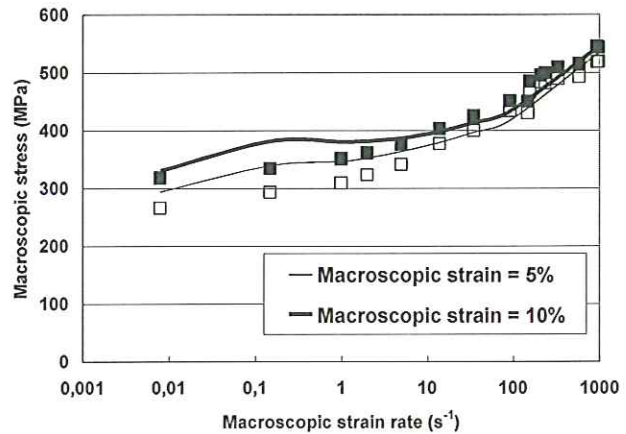


Fig. 4: Macroscopic flow stress as a function of strain rate for indicated macroscopic strains for an IF steel - Comparison between experimental (dots) and model (solid lines) data.

$\dot{\gamma}_0 \text{ (s}^{-1}\text{)}$	$\Delta G_0 \text{ (eV)}$	p	q	$\tau_{r0} \text{ (MPa)}$	$\rho^0 \text{ (m}^{-2}\text{)}$	K	$t \text{ (s)}$	a
$5,1 \cdot 10^8$	1,5	0,66	1	106	10^{11}	5	$2 \cdot 10^{-2}$	12

Table 5. Ferrite parameters identified from experiments on an IF steel bounded to agree with the values reported in the literature

CONCLUSIONS

A new micro-macro model involving simultaneously self-consistency for the viscous part and self-equilibrium for the elastic fields has been developed to describe the elastic-viscoplastic behaviour of heterogeneous materials. It has been in particular applied to the case of polycrystalline steels. The influence of some microstructural characteristics such as the grain size and the martensite content, on the strength, the strain hardening and the strain rate sensitivity of steels is well described. This is mainly due to an efficient formulation of both (i) the elastic-viscoplastic interactions between grains and (ii) the single crystal behaviour based on physical processes namely the thermally activated dislocation glide. The phonon drag mechanism was also introduced to analyze the dynamic behaviour for strain rates around 1000 s^{-1} .

References

- [1] Berbenni, S., Elastoviscoplasticité des aciers polycristallins : Modélisation micromécanique et physique – Applications au comportement dynamique et à l'effet Bake-Hardening, Thèse de Doctorat de l'École Nationale Supérieure d'Arts et Métiers- Centre de Metz (2002)
- [2] Sabar, H., Berveiller, M., Favier, V., Berbenni, S., A new class of micro-macro models for elastic-viscoplastic heterogeneous materials, *Int. J. Solids Struct.*, 39 (2002), pp. 3257-3276
- [3] Favier, V., Sabar, H., Berveiller, M., Berbenni, S., New self-consistent approach for inelastic materials based on translated fields, *J. Phys. IV France*, 105 (2003), pp. 231-238
- [4] Berbenni, S., Favier, V., Lemoine, X., Berveiller, M., Micromechanical modeling of the elastic-viscoplastic behavior of polycrystalline steels having different microstructures, *Mat. Sci. Engng. A* (2004), sous presse
- [5] Kocks, U.F., Argon, A.S. and Ashby, M.F., *Thermodynamics and Kinetics of Slip*, Oxford, Pergamon Press (1975)
- [6] Kumar, A., Hauser, F.E., Dorn, J.E., Viscous drag on dislocations in aluminium at high strain rates, *Acta Metall.*, 16 (1968), pp. 1189-1197
- [7] Follansbee, P.S., Regazzoni, G., Kocks, U.F., The transition to drag-controlled deformation in copper at high strain rates, *Inst. Phys. Conf., Ser.*, 70 (1984), pp. 7180
- [8] Essmann, U., Mughrabi H., Annihilation of dislocations during tensile and cyclic deformation and limits of dislocation densities, *Phil. Mag.*, 40 (1979), pp. 731-756
- [9] Luft, A., Microstructural processes of plastic instabilities in strengthened metals, *Progr. Mat. Sci.*, 35 (1991), pp. 97-204
- [10] Rusinek, A., Klepaczko, J.R., Shear testing of a sheet steel at wide range of strain rates and a constitutive relation with strain-rate and temperature dependence of the flow stress. *Int. J. of Plasticity*, 17 (2000), pp. 87-115
- [11] Eshelby, J.D., The determination of the elastic field of an ellipsoidal inclusion and related problems. *Proc. R. Soc. London A241* (1957), 376-396.
- [12] Kröner, E., Bounds for effective elastic moduli of disordered materials. *J. Mech. Phys. Solids* 25 (1977), pp. 137-155.
- [13] Weng, G.J., A self-consistent Scheme for the Relaxation Behavior of Metals. *J. App. Mech.* 48 (1981), pp. 779-784.
- [14] Hoc, T., Etude expérimentale et numérique de la localisation lors de changements de trajets dans un acier doux, Thèse de Doctorat de l'École Centrale, de Paris (1999).
- [15] Goel, N.C., Sangal, S., Tangri, K., A theoretical model for the flow behavior of commercial Dual-Phase steels containing metastable retained austenite: Part I. Derivation of flow curve equations. *Metall. Trans.* 16A (1985), pp. 2013-2021.
- [16] Sakari, T., Ohnuma, K., Sugimoto, K., Ohtakara, Y., Plastic anisotropy of Dual-Phase steels, *Int. J. Plasticity* 6 (1990), pp. 591-613.

3D FINITE STRAIN MODELLING AND NUMERICAL SIMULATION OF PROPAGATING ADIABATIC SHEAR BANDS

Patrice Longère⁽¹⁾, André Dragon⁽¹⁾, Hervé Trumel⁽²⁾,
Thibaut de Ressaiguier⁽³⁾ and Xavier Deprince⁽⁴⁾

⁽¹⁾ Laboratoire de Mécanique et de Physique des Matériaux, UMR CNRS n°6617 – ENSMA
1 avenue C. Ader, BP 40109, 86962 FUTUROSCOPE-CHASSENEUIL Cedex, France

⁽²⁾ CEA/DAM, Le Ripault, BP16, 37260 MONTS, France

⁽³⁾ Laboratoire de Combustion et de Détonique, UPR CNRS n°9028 - ENSMA
1 avenue. C. Ader, BP 40109, 86962 FUTUROSCOPE-CHASSENEUIL Cedex, France

⁽⁴⁾ GIAT Industries, 7 route de Guerry, 18023 BOURGES Cedex, France

Summary: In the present work, we are interested in the description of the material behaviour in the presence of adiabatic shear bands (ASB). Adiabatic shear banding, considered as an anisotropic damage process, is dealt with within the framework of irreversible thermodynamics including thermodynamic potentials, namely free energy and dissipative potentials. The forms of state and evolution laws reflect the strong couplings between the two viscous dissipative mechanisms of plasticity and damage considered here. In parallel, particular kinematics based on the multiplicative decomposition of the deformation gradient has been developed in the context of large anisotropic damage-plastic deformations. Conditions for shear band initiation have been obtained from a simplified analysis based on the linear theory of perturbations. The 3D constitutive equations have been implemented as user material in the finite element code LS-DYNA. Confrontation of numerical results with experimental ones considering the hat shape structure (HSS) dynamic shearing test have shown the good predictive capacities of the model.

INTRODUCTION

Adiabatic shear banding (ASB) is a phenomenon of notable importance in dynamic deformation. It represents a form of local instability producing thin bands of intense deformation in impacted bodies. The work done in plastic deformation of a metal (intrinsic dissipation) is converted largely to heat which – if not conducted away, as for high strain rate plastic flow – leads to a noticeable rise in temperature. In metals and alloys where the rate of thermal softening (and a corresponding drop in stress) surpasses the rate of work-hardening (a rise in stress), deformation is seen to concentrate in narrow softened bands of adiabatic shear.

Stemming from the pioneering work of ZENER AND HOLLOMON [1], RECHT [2], and more recent experimental studies like the one by MARCHAND AND DUFFY [3], extensive investigation (metallurgical and mechanical, experimental and theoretical) and literature have been devoted to the matter, see f. ex. KLEPACZKO [4], MOLINARI [5] and other references given in LONGERE ET AL. [6]. High strength alloys and steels are primarily concerned by adiabatic shear as preponderant deformation and degradation mode at high strain rates.

The aim of the present work is to incorporate the shear band formation and growth into three-dimensional modelling regarding viscoplastic flow coupled with micro-damage process by adiabatic shear banding embodied by specific internal variables. The model is then applied to predict the ASB induced degradation and post-localization response of a complex structure under dynamic loading.

CONSTITUTIVE RELATIONS

In the present model [6,7], the band is inserted inside the representative volume element (RVE) as a sort of a ‘super-dislocation’ [6]. The anisotropic degradation induced by the bands is described by a 2nd order tensorial variable $\tilde{\mathbf{D}}$ and its evolution, with :

$$\tilde{\mathbf{D}}_{ij} = \sum_{\alpha} d^{\alpha} \tilde{\mathbf{N}}_{ij}^{\alpha} ; \tilde{\mathbf{N}}_{ij}^{\alpha} = \tilde{n}_i^{\alpha} \tilde{n}_j^{\alpha} \quad (1)$$

where d^{α} and $\tilde{\mathbf{n}}^{\alpha} = \mathbf{Q}^{\alpha} \mathbf{n}^{\alpha}$ represent respectively the scalar intensity and the orientation (normal) of the band pattern α , and \mathbf{Q}^{α} the rotation of anisotropy axes during the damage process.

The kinematic consequences of the presence of the bands are described by means of the corresponding part \mathbf{L}^d (in addition to the plastic part \mathbf{L}^p) of the velocity gradient \mathbf{L} :

$$\mathbf{L}^d \propto \sum_{\alpha} \dot{\gamma}^{\alpha} \tilde{\mathbf{g}}^{\alpha} \tilde{\mathbf{n}}_j^{\alpha} ; d_{ij}^d = \left(\mathbf{C}_{ij}^d \right) \propto \sum_{\alpha} \dot{\gamma}^{\alpha} \tilde{\mathbf{M}}_{ij}^{\alpha} ; \omega_{ij}^d = \left(\mathbf{C}_{ij}^{\omega} \right) \propto \sum_{\alpha} \dot{\gamma}^{\alpha} \tilde{\mathbf{T}}_{ij}^{\alpha} \quad (2)$$

where $\dot{\gamma}^{\alpha}$ represents the intensity of the glide velocity, $\tilde{\mathbf{n}}^{\alpha}$ and $\tilde{\mathbf{g}}^{\alpha}$ respectively the normal and the orientation of the band pattern α , while $\tilde{\mathbf{M}}^{\alpha}$ and $\tilde{\mathbf{T}}^{\alpha}$ are respectively symmetric and antisymmetric parts of the tensorial product $\tilde{\mathbf{g}}^{\alpha} \otimes \tilde{\mathbf{n}}^{\alpha}$.

In the following a single band system is considered.

The decomposition of the deformation gradient \mathbf{F} as the product $\mathbf{F} = \mathbf{V}^e \mathbf{Q} \mathbf{F}^{dp}$, where \mathbf{V}^e denotes the pure ‘elastic’ stretching ($\mathbf{F}^e = \mathbf{V}^e \mathbf{R}^e$), and \mathbf{F}^{dp} the ‘damage-plastic’ transformation, yields :

$$\mathbf{d}_{ij} = \mathbf{d}_{ij}^e + \mathbf{d}_{ij}^{dp} ; \quad \omega_{ij} = W_{ij} + \omega_{ij}^e + \omega_{ij}^{dp} \quad (3)$$

where \mathbf{d}^e and ω^e represent respectively the elastic strain rate and spin, \mathbf{d}^{dp} and ω^{dp} respectively the inelastic strain rate and spin, and $\mathbf{W} = \dot{\mathbf{Q}}\mathbf{Q}^T$ the rotation rate.

The objective derivative $\overset{\vee}{\mathbf{A}}$ of a 2nd order tensor \mathbf{A} is thus given by :

$$\overset{\vee}{A}_{ij} = \dot{A}_{ij} - W_{ik}A_{kj} + A_{ip}W_{pj} \quad (4)$$

Assuming small elastic deformation and a weak contribution of the plastic spin ω^p with regards to the damage induced spin ω^d yields :

$$W_{ij} = \omega_{ij} - \omega_{ij}^d \quad (5)$$

The thermo-elastic response of the anisotropic medium is supposed to be described by the specific free energy $\psi(\boldsymbol{\epsilon}^e, T; p, \tilde{\mathbf{D}}) = \psi^e(\boldsymbol{\epsilon}^e, T; \tilde{\mathbf{D}}) + \psi^p(p; \tilde{\mathbf{D}})$, where $\boldsymbol{\epsilon}^e$ represents the elastic deformation, T the absolute 'regular' (outside the band) temperature, and p the scalar isotropic strain hardening ('regular') variable. The elastic potential and the stored energy are assumed as :

$$\left\{ \begin{array}{l} \rho_0 \psi^e = \frac{\lambda}{2} \boldsymbol{\epsilon}_{ii}^e \boldsymbol{\epsilon}_{jj}^e + \mu \boldsymbol{\epsilon}_{ij}^e \boldsymbol{\epsilon}_{ji}^e - \alpha K \boldsymbol{\epsilon}_{ii}^e \Delta T - \frac{\rho_0 C}{2T_0} \Delta T^2 - a \boldsymbol{\epsilon}_{kk}^e \boldsymbol{\epsilon}_{ij}^e \tilde{D}_{ji} - 2b \boldsymbol{\epsilon}_{ij}^e \boldsymbol{\epsilon}_{jk}^e \tilde{D}_{ki} \end{array} \right. \quad (6)$$

$$\left\{ \begin{array}{l} \rho_0 \psi^p = R_\infty \left[p + \frac{1}{k} \exp(\boldsymbol{\epsilon}_{kk}^p) \right] \exp(\boldsymbol{\epsilon}_{kk}^p) \exp(\gamma T) \exp\left(-d_1 \tilde{D}_{ii} - \frac{d_2}{2} \tilde{D}_{ij} \tilde{D}_{ji}\right) \end{array} \right. \quad (7)$$

where $\Delta T = T - T_0$, λ and μ represent LAMÉ's coefficients, K the bulk modulus ($K = \lambda + \boldsymbol{\epsilon}/3$), α the thermal expansion coefficient, ρ_0 the initial density, C the heat capacity, a and b constants related to elastic energy ASB-induced degradation, R_∞ is related to the saturation of hardening, k the plastic hardening parameter, γ the thermal softening parameter, d_1 and d_2 the damage (ASB) related softening constants.

The thermo-elastic KIRCHHOFF stress tensor $\boldsymbol{\tau}$, the strain hardening force r and the damage conjugate force $\tilde{\mathbf{k}}$ are derived from the thermodynamic potential $\psi(\boldsymbol{\epsilon}^e, T; p, \tilde{\mathbf{D}})$ with respect to $\boldsymbol{\epsilon}^e$, p and $\tilde{\mathbf{D}}$:

$$\left\{ \begin{array}{l} \tau_{ij} = \lambda \boldsymbol{\epsilon}_{kk}^e \delta_{ij} + 2\mu \boldsymbol{\epsilon}_{ij}^e - \alpha K \Delta T \delta_{ij} - a \left(\tilde{D}_{nm} \delta_{ij} + \boldsymbol{\epsilon}_{kk}^e \tilde{D}_{ij} \right) - 2b \left(\boldsymbol{\epsilon}_{ik}^e \tilde{D}_{kj} + \tilde{D}_{ik} \boldsymbol{\epsilon}_{kj}^e \right) \end{array} \right. \quad (8)$$

$$\left\{ \begin{array}{l} r = R_\infty \left[-\exp(\boldsymbol{\epsilon}_{kk}^p) \right] \exp(\boldsymbol{\epsilon}_{kk}^p) \exp(\gamma T) \exp\left(-d_1 \tilde{D}_{kk} - \frac{d_2}{2} \tilde{D}_{kl} \tilde{D}_{lk}\right) \end{array} \right. \quad (9)$$

$$\tilde{\mathbf{k}}_{ij} = a \boldsymbol{\epsilon}_{kk}^e \boldsymbol{\epsilon}_{ij}^e + 2b \boldsymbol{\epsilon}_{ik}^e \boldsymbol{\epsilon}_{kj}^e + R_\infty \left[p + \frac{1}{k} \exp(\boldsymbol{\epsilon}_{kk}^p) \right] \exp(\boldsymbol{\epsilon}_{kk}^p) \exp(\gamma T) \exp\left(-d_1 \tilde{D}_{kk} - \frac{d_2}{2} \tilde{D}_{kl} \tilde{D}_{lk}\right) \left[\delta_{ij} + d_2 \tilde{D}_{ij} \right] \quad (10)$$

A single yield function that includes both plasticity and damage effects appears suitable to describe via the generalized normality hypothesis the evolution of corresponding variables :

$$\left\{ \begin{array}{l} F(\boldsymbol{\epsilon}_{ij}, r, \tilde{\mathbf{k}}_{ij}) = \hat{J}_2^p(\boldsymbol{\epsilon}_{ij}, \tilde{\mathbf{k}}_{ij}) - \boldsymbol{\epsilon}_0 + r \end{array} \right. \quad (11)$$

$$\left\{ \begin{array}{l} \hat{J}_2^p(\boldsymbol{\epsilon}_{ij}, \tilde{\mathbf{k}}_{ij}) = \sqrt{\frac{3}{2} s_{ij} P_{ijkl} \boldsymbol{\epsilon}_{mn} s_{kl}} \end{array} \right. \quad (12)$$

where s represents the deviatoric part of the KIRCHHOFF stress tensor, and \mathbf{P} the 4th order tensor inducing damage-prompted anisotropy of the plastic flow, assumed in the following form :

$$P_{ijkl} = \frac{1}{2} \left(\boldsymbol{\epsilon}_{ik} \delta_{jl} + \delta_{il} \boldsymbol{\epsilon}_{jk} \right) + 2 \sum_{q=2}^N \eta_q \left(\boldsymbol{\epsilon}_{mn}^+ \tilde{N}_{nm}^q \right) \tilde{M}_{ij} \tilde{M}_{kl} \quad (13)$$

$$\tilde{k}_{ij}^+ \tilde{N}_{ji} = \langle \tilde{k}_{ij} \tilde{N}_{ji} - k_{inc} \rangle \quad (14)$$

The function R_0 is expressed by :

$$R_0 = R_i \exp \left\langle \gamma T \right\rangle \exp \left(-d_1 \tilde{D}_{kk} - \frac{d_2}{2} \tilde{D}_{mm} \tilde{D}_{mm} \right) \quad (15)$$

where R_i represents an internal stress.

The existence of viscous plastic and damage potentials of PERZYNA's type is assumed :

$$\phi_p^c = \frac{Y}{n+1} \left\langle \frac{F}{Y} \right\rangle^{n+1} ; \quad \phi_d^c = \frac{Z}{m+1} \left\langle \frac{F}{Z} \right\rangle^{m+1} \quad (16)$$

where Y and n represent viscous parameters relative to plasticity, Z and m viscous parameters relative to (time-dependent) damage.

Evolution laws are consequently derived from the normality rule :

$$\begin{cases} d_{ij}^p = \frac{3}{2} \Lambda^p \frac{S_{ij}}{J_2} \\ d_{ij}^d = 3\Lambda^d \frac{\sum_{q=2}^N \eta_q \langle \tilde{N}_{mm} \rangle^q \tilde{S}_{kl} \tilde{M}_{kl}}{\hat{J}_2} \tilde{M}_{ij} \end{cases} \quad \begin{cases} \dot{p} = \Lambda^p \\ \tilde{D}_{ij}^d = \frac{3}{2} \Lambda^d \frac{\sum_{q=2}^N q \eta_q \langle \tilde{N}_{mm} \rangle^{q-1} \langle \tilde{M}_{kl} \rangle}{\hat{J}_2} \tilde{N}_{ij} \end{cases} \quad (17)$$

the viscoplasticity and viscous damage respective multipliers being expressed by :

$$\Lambda^p = \left\langle \frac{\partial \phi_p^c}{\partial F} \right\rangle = \left\langle \frac{F}{Y} \right\rangle^n ; \Lambda^d = \left\langle \frac{\partial \phi_d^c}{\partial F} \right\rangle = \left\langle \frac{F}{Z} \right\rangle^m \quad (18)$$

The damage induced spin ω^d is deduced from (2)₃ and (17)₂ as follows :

$$\omega_{ij}^d = 3\Lambda^d \frac{\sum_{q=2}^N \eta_q \langle \tilde{N}_{mm} \rangle^q \tilde{S}_{kl} \tilde{M}_{kl}}{\hat{J}_2} \tilde{T}_{ij} \quad (19)$$

'Regular' heating caused by plasticity outside the bands is further expressed by the usual relation established with the adiabaticity assumption :

$$\rho_0 C \dot{T} = \tau_{ij} d_{ji}^p - r \dot{p} \quad (20)$$

The constitutive model is completed by a damage incipience criterion based on a simplified analysis of material instability using the linear perturbation method [6,7,8] :

$$G \left(\tau_{ij}, r, \dot{p}; \frac{\partial \tau}{\partial p}, \frac{\partial \tau}{\partial T} \right) = \sqrt{3} |\tau_{res}| - \left(r - \frac{1}{n} Y \dot{p}^{\frac{1}{n}} + \rho_0 C \left(\frac{\partial \tau}{\partial p} / \left(-\frac{\partial \tau}{\partial T} \right) \right) \right) > 0 \quad (21)$$

where $\tau_{res} = \text{Tr} \langle \tilde{M} \rangle$ represents the resolved shear stress, r the isotropic hardening conjugate force, $Y \dot{p}^{1/n}$ the strain rate-induced overstress, $\partial \tau / \partial p$ the plastic hardening and $\partial \tau / \partial T$ the thermal softening. In the present simplified analysis (see [6,7] for further details), the damage process is actually assumed to run as soon as $G = 0$. This latter condition must be interpreted as the auxiliary indicator for the damage process incipience leading to the determination of the damage conjugate force threshold $k_{inc} = \text{Tr} \langle \tilde{N} \rangle_{crit}$ in (14).

ANALYSIS OF THE HSS DYNAMIC SHEARING TEST

The three-dimensional constitutive model has been implemented as ‘user material’ in the finite element code LS-DYNA. The integration algorithm of the evolution equations is purely explicit combined with an adaptive time step procedure following KULKARNI ET AL.’s recommendations [9]. Thanks to the regularizing effects of viscosity (in the model viscosity is double, concerning not only plasticity but also damage), a weak mesh dependency of the numerical results has been observed [7]. Because of the modelling scale we use herein, mesh refining in the areas crossed by the bands – which supposes the a priori knowledge of the band trajectory – is not necessary.

Predictive capacities of the numerical version of the model employing the set of material constants assembled in Tab.1 have been evaluated next considering the boundary value problem of the hat shape structure (HSS) dynamic shearing test (see Fig.1). In this experiment, the HSS geometry (Fig.2) has been designed (see [10, 11]) to favour localization in a well-defined area under constant pressure.

The test aims to study the (relative) susceptibility of various metallic materials to adiabatic shearing. Depending on the load intensity (as function of the striker bar initial velocity $V_{striker}$) and on the loading nominal duration T (as function of the striker bar length $L_{striker}$), shear bands initiate or not, propagate or arrest inside the HSS. In some cases, the loading can lead to the ultimate failure of the structure.

ρ_0 (kg/m ³)	C (J/kg.K)	E (MPa)	ν	α (K ⁻¹)	a (MPa)	b (MPa)
7800	500	200e+3	0.33	1e-6	0	15e+3
R_i (MPa)	R_{oo} (MPa)	k	γ (°C ⁻¹)	d_1	d_2	η_2 (MPa ⁻²) (N=2)
510	400	20	1.5e-3	0.05	0.05	0.12
Y (MPa.s ^{1/n})	n	Z (MPa.s ^{1/m})	m			
100	10	19	2			

Table 1 : HSS material (30 NiCrMo6-6 like steel) constants of the constitutive model

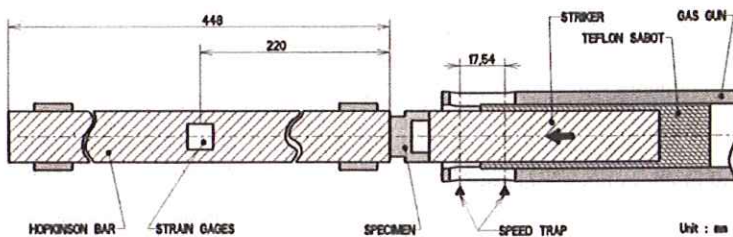


Fig.1 : HSS dynamic shearing test device (GIAT Industries [10])

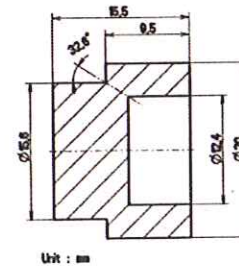


Fig.2 : HSS geometry (GIAT Industries [10])

Post-mortem macrograph in Fig.3a reveals the presence of a crossing adiabatic shear band with a partial crack on the HSS lower side and the presence of a crossing crack on the HSS upper side. Numerical damage map in Fig.3b for $t=2T$ reveals the presence of a crossing damage band. Considering Figs.4 and 5, the junction of both damage branches (each one initiated from each HSS corner, see Fig.4) occurs during the second nominal loading. Superposition of experimental and numerical load transmitted to the output bar is fairly satisfying. These experimental and numerical results are a part of a series of various configurations showing the predictive capacities of the model developed in the previous section. This proves once more the necessity to account for the ASB-induced degradation for the numerical prediction of the life time of a structure under dynamic loading. Thermal softening alone on the one side or brutal failure (while adiabatic shearing preserves matter cohesion keeping on transmitting a part of the loading) on the other one are actually not physically satisfying as description of the ASB-induced deterioration, and these coarse simplifications can yield to erroneous estimations of the life time of the structure. In more complex boundary value problem, considering isotropic damage can also be a source of oversimplification, notably as concerns band trajectory.

CONCLUDING REMARKS AND PERSPECTIVES

A three-dimensional constitutive model, including anisotropic damage embodying the ASB-induced deterioration in the context of finite anisotropic elasto-plastic strains, rate sensitivity, strain hardening, thermal softening, has been developed in the framework of irreversible thermodynamics and implemented as user- material in the finite element code LS-DYNA. A mesh dependence study (not detailed here) shows a significant attenuation effect of double viscosity-induced pseudoregularization, i.e. globally weak mesh-sensitivity in the presence of damage bands. Numerical simulations considering the dynamic shearing for the hat shape structure (HSS) have been performed ; they show good

accordance with the corresponding experimental data. This comparison allows to draw an inference regarding satisfactory predictive capacities of the constitutive model proposed accounting for the 3D character and anisotropy induced by the ASB mechanism.

Transition to failure constitutes the next step in the modelling of ASB-induced effects.

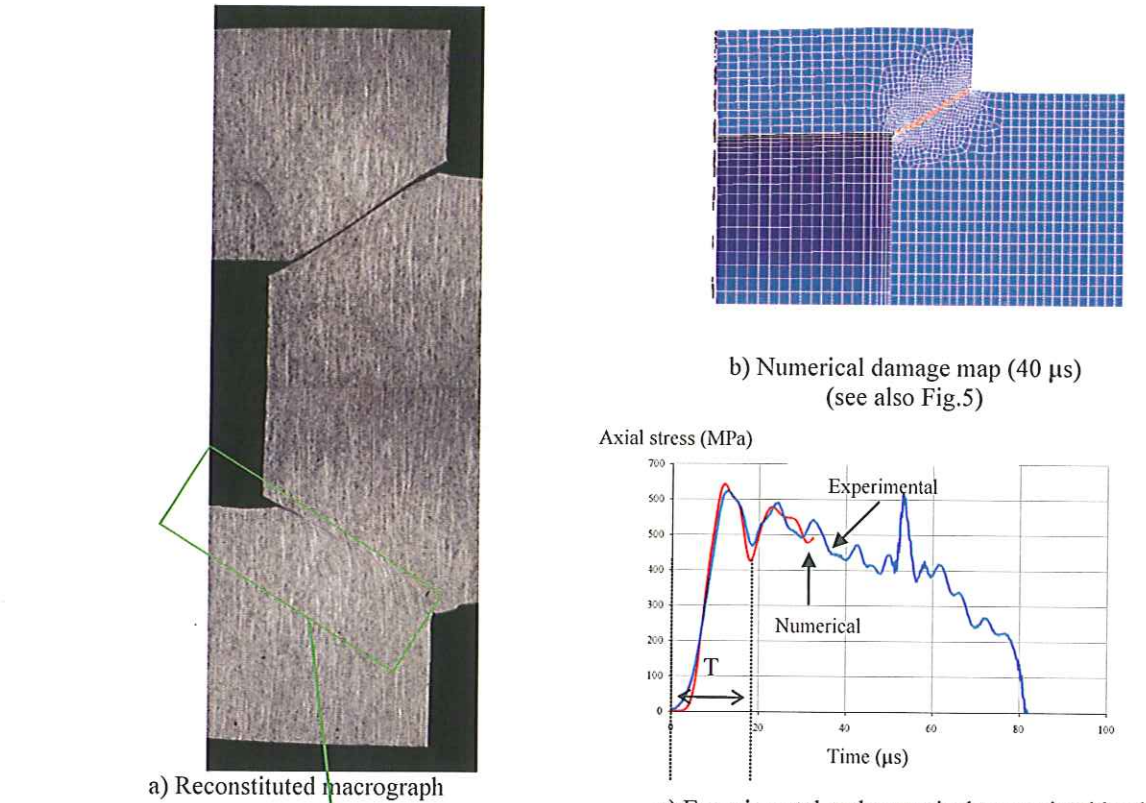


Fig. 3 : Configuration with $L_{striker}=40\text{mm}$; $V_{striker}=35,6\text{m/s}$ ($T=18,7 \mu\text{s}$)

Remark

Loading nominal duration T is given by :

$$T = \frac{2L_{striker}}{c_{striker}} ; c_{striker} = \sqrt{\frac{E}{\rho_{striker}}}$$

In this configuration (Fig.3) the HHS is submitted to several loadings with a decreasing magnitude.

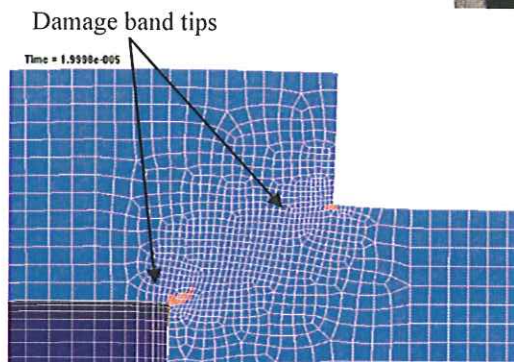
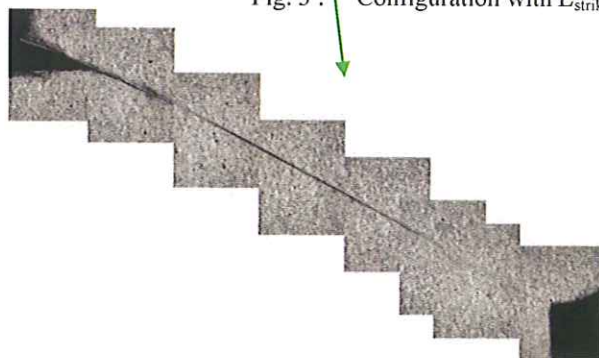


Fig. 4 : Numerical damage map at $t \approx T$
Partial propagation of two damage bands

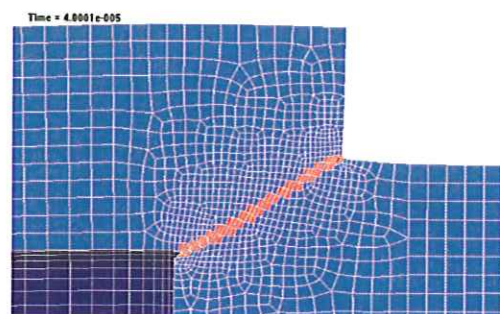


Fig. 5 : Numerical damage map at $t \approx 2T$
Macro-localisation after junction of two damage bands

Acknowledgement – The authors are greatly indebted to Drs. Hervé COUQUE and Bruno SALESSE (GIAT Industries, Bourges, France) who kindly performed the dynamic shearing tests on the HSS and the post-mortem microstructural analyses shown respectively in Figs.3c and 3a.

References

- [1] ZENER C AND HOLLOMON J.H., *Effect of strain rate upon plastic flow of steel*, J. Appl. Phys., 15, pp.22-32 (1944).
- [2] RECHT R.F., *Catastrophic thermoplastic shear*, J. Appl. Mech., 31E, pp.189-193 (1964).
- [3] MARCHAND A. AND DUFFY J., *An experimental study of the formation process of adiabatic shear bands in a structural steel*, J. Mech. Phys. Solids, 36, 3, pp.251-283 (1988).
- [4] KLEPACZKO J.R., *Some results and new experimental technique in studies of adiabatic shear bands*, Arch. Mech., 46, pp.201 (1994).
- [5] MOLINARI A., *Collective behavior and spacing of adiabatic shear bands*, J. Mech. Phys. Solids, 45, 3, pp.1551-1575 (1997).
- [6] LONGERE P., DRAGON A., TRUMEL H., DE RESSEQUIER T., DEPRINCE X. AND PETITPAS E., *Modelling adiabatic shear banding via damage mechanics approach*, Arch. Mech., 55, pp.3-38 (2003).
- [7] LONGERE P., *Modélisation et simulation numérique de la réponse d'un matériau métallique endommagé par des bandes de cisaillement adiabatique*, Thèse de Doctorat de l'Université de Poitiers-ENSMA (2003).
- [8] MOLINARI A., *Instabilité thermoviscoplastique en cisaillement simple*, J. Méca. Théorique et appliquée, 4, pp.659-684 (1985).
- [9] KULKARNI M., BELYTSCHKO T. AND BAYLISS A., *Stability and error analysis for time integrators applied to strain-softening materials*, Comput. Methods Appl. Mech. Engng, 124, pp.335-363 (1995).
- [10] COUQUE H., *A hydrodynamic hat specimen to investigate pressure and strain rate dependence on adiabatic shear band formation*, J. Phys. IV, 110, pp.423-428 (2003).
- [11] COUQUE H., *Essais chapeau hydrodynamique de MARS 190 40 mm*, GIAT-Ind. internal report DSAM/DT/MCP/3050.713.03 Ind. A (2003).

A GENERAL THERMO-VISCO-PLASTIC APPROACH FOR FINITE ELEMENT APPLICATIONS IN DYNAMIC PROCESS

Ramon Zaera^{*}, Alexis Rusinek, Janusz R. Klepaczko and Carlos Navarro^{*}

*Laboratory of Physics and Mechanics of Materials, UMR CNRS 75-54, Université de Metz,
Ile du Saulcy, 57045 Metz cedex, France*

^{} Department of Continuum Mechanics and Structural Analysis, University Carlos III of Madrid, Avda. de la Universidad 30,
28911 Leganés, Madrid, Spain*

Summary: In this contribution thermo-visco-plastic constitutive relations are proposed and analysed [1]. This phenomenological approach is partly based on theory of dislocations and processes of thermal activation. The main advantage of such constitutive relation is reduction in number of material constants in comparison with the complete approach based on materials science. The constitutive relation discussed here has been used so far many times in finite element codes, for example ABAQUS, to simulate dynamic processes of impact loading. This time an original algorithm proposed in [2] which applies J_2 theory of plasticity is presented in this paper. The algorithm is applied to analyse dynamic behavior of steel sheets used in automotive industries like mild steels ES or DP. Numerical analysis of the Taylor test demonstrates applicability of this new algorithm.

CHARACTERIZATION AND EXPERIMENTAL OBSERVATIONS

More recently several new steels were developed to be used in dynamic applications at high strain rates, up to 10^3 s^{-1} . Thus, to reach such strain rates the specimen length must be substantially reduced since the initial length l_0 is directly related to strain rate by the initial impact velocity V_0 ; $\dot{\epsilon} = V_0/l_0$. However, it is not clear if the experimental results obtained with short specimens are representative of the intrinsic mechanical behavior of materials tested. Generally, a reduction of the specimen length induces an increase of the mean stress level and reduce ductility, Fig. 1. In conclusion, an optimal specimen geometry should be used in high strain rate testing. This will allow to obtain the quasi-static and dynamic mechanical properties with the same specimen geometry. For relatively long specimen ($l_0 = 40 \text{ mm}$) a stress peak phenomenon appears at the beginning of loading, as shown in Fig.1. In general, it is believed that the stress peak is due to metallurgical effects (interstitials, inclusions etc...), and due to trapping of mobile dislocations during a short time. In addition, the peak may be amplified by the inertia effects of the system machine-specimen. In present case, during numerical simulations, only inertia effects appear as a stress increase for small deformation $\epsilon < 0.05$, although the constitutive law used during numerical simulation does not take into account the intrinsic peak stress.

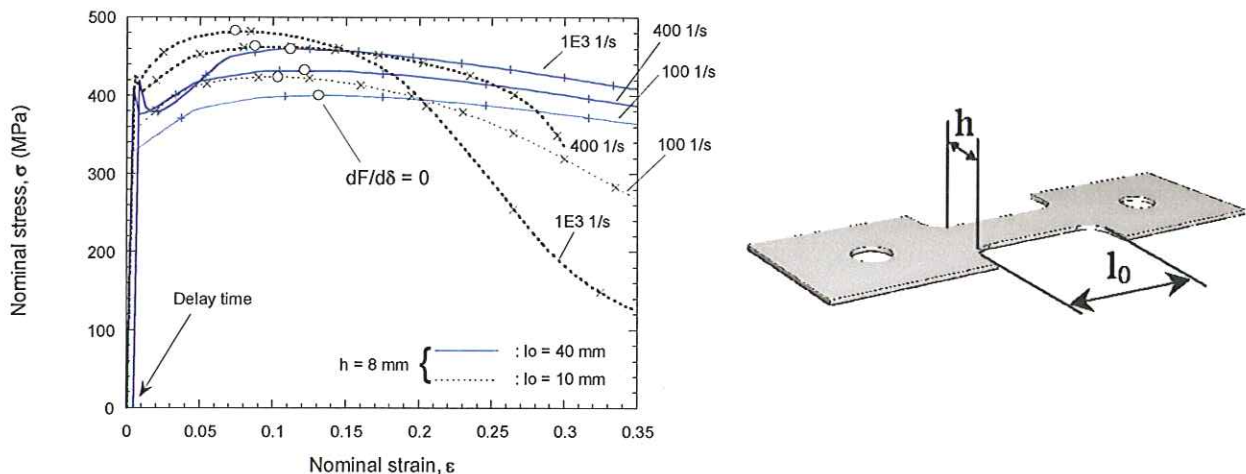


Fig. 1. a- Effect of the initial specimen length on plastic behavior in dynamic tensile test, numerical simulations performed for ES steel sheet [3], b – Optimal specimen geometry (design of LPMM) used in dynamic tensile tests ($h = 8 \text{ mm}$, $l_0 = 20 \text{ mm}$)

The optimal geometry as shown in Fig1- b was used extensively in testing in quasi-static and dynamic conditions. This geometry has been obtained by a recent FE study. The optimal geometry recommended for steel sheets is with length $l_0 = 20 \text{ mm}$ and width $h = 8 \text{ mm}$. Actually, the problem in experimental characterization of sheets at high strain rates is the absence of a normalized tension test in comparison with the quasi-static one. The precise knowledge of the test applied for experimental characterization of a metal and alloy allows to obtain precisely elastic and plastic properties as

a function of strain rate and temperature, Fig. 1-2. On the other hand the properties can be related to the microstructure evolution. Such combination can to predict correctly the resistance of complicated structures during crash for example. However, in dynamic loading, we observe a strong dependency of stress-strain characteristics on strain rate and temperature leading to the transition from isothermal to adiabatic conditions of deformation at specific characteristic strain rate $\dot{\epsilon}_p^{transition}$, [4]. This strain rate limit can be found numerically at the initial temperature T_0 by combining equation of the thermal conductivity and a precise constitutive relation, for example the generalized Arrhenius relation (for the i -th thermally activated process) applied to plasticity, [5]

$$\dot{\epsilon}_p = v_i(T, s_j) \exp\left[-\frac{\Delta G_i(\sigma^*, T, s_j)}{kT}\right] \quad (1)$$

where v_i is the pre-exponential term, ΔG_i is the free energy of activation, k is the Boltzmann constant and σ^* is the effective stress, $\sigma^* = \sigma - \sigma_\mu$, where σ and σ_μ are respectively the total stress and the internal stress, s_j are the set of internal stress variables characterizing evolution of microstructure during plastic deformation. The pre-exponential term is a function of microstructure since it depends of the density of mobile dislocation ρ_m , [5], which is one of the internal state variables. After inversion of equation (1), and applying definition of the effective stress, is possible to find the expression for the total stress σ in the formalism proposed in [5]

$$\sigma = \sigma_\mu + \left[h(\dot{\epsilon}_p, T) G_i^{-1}(s_j, T, \sigma_0^*, G_0) M k T \log\left(\frac{v_i(T, s_j)}{\dot{\epsilon}_p}\right) \right] \quad (2)$$

where $h(\dot{\epsilon}_p, T)$ is the history of strain rate and temperature and $G_i^{-1}(\cdot)$ is the inverted $\Delta G_i(\cdot)$, σ_0^* and G_0 are respectively the obstacle stress at $T=0K$ and the total energy of obstacle at $T=0K$, M is the conversion factor to decimal logarithm. It is clear that the advanced formalism in constitutive modelling which is briefly outlined here is too complicated at this stage of development in automotive engineering. Therefore, it is necessary to obtain relatively precise and simplified constitutive description to obtain a limited number of material constants describing as exact as possible the thermo-visco-plastic relation. This task is the subject of the following part of the paper. It must be mentioned that the constitutive relation directly influences via numerical calculations the structural crashworthiness of a structure, for example as a car, and its ability to absorb the energy of plastic deformation estimated during numerical simulations. Taking also into account the thermal effects allows to study precisely the problem of plastic instabilities present in dynamic conditions, for example dynamic buckling which appears during crash box test, adiabatic shearing, dynamic necking etc. In addition such approach with thermal coupling can predict also the effects of the initial temperature on plastic behavior observed experimentally at low and high strain rates.

CONSTITUTIVE RELATIONS

The original constitutive relation proposed in this paper is based on the formalism proposed in [4], and outlined above, which applies theory of dislocation dynamics. In the original approach, the evolution of microstructure is taken into account by j internal state variables s_j , and in general Eq. (2) can be written in the simplified form

$$\sigma = g\left[s_j, \dot{\epsilon}, T, s_j, h(\dot{\epsilon}, T)\right] \quad (3)$$

However, such complete constitutive formalism is complicated to be implemented directly into FE codes, mainly due to the complexity of each equation coupled with the great number of physical constants. In comparison a phenomenological approach is much simpler to be applied in numerical methods. To reduce the number of constants and to facilitate the utilization in a FE codes, a semi phenomenological approach has been proposed in [6]. The number of constants in proposed constitutive relations is low and limited to eight. This set of constitutive relations allow to take into account the strain hardening and strain rate and temperature sensitivity. In this approach the stress of plastic flow is composed of two terms : σ_μ and σ^* and is given by

$$\sigma(\dot{\epsilon}, T) = \frac{E(T)}{E_0} \left[\sigma_\mu(\dot{\epsilon}, T) + \sigma^*(\dot{\epsilon}, T) \right] \quad \text{with} \quad E(\dot{\epsilon}, T) = E_0 \left\{ 1 - \frac{T}{T_m} \exp\left[\theta^* \left(1 - \frac{T}{T_m}\right)\right] \right\} \quad (4)$$

where $E(T)$ is the temperature-dependent Young's modulus with the characteristic homologous temperature θ^* , E_0 is the Young's modulus at $T=0K$, T_m is the melting temperature. The explicit form proposed to define the two stress

components are inspired by the physical approach [6-7] and the theory of thermal activation [8]. The explicit forms for the internal and effective stresses are given by

$$\sigma_\mu = B(\dot{\epsilon}, T) \left(\epsilon_0 + \epsilon \right)^{n_0}, \quad \sigma^* = \sigma_0^* \left[1 - D_1 \left(\frac{T}{T_m} \right) \log \left(\frac{\dot{\epsilon}_{max}}{\dot{\epsilon}} \right) \right]^m \quad \text{if } \dot{\epsilon} \leq \dot{\epsilon}_c \text{ then } \sigma^* = 0 \quad (5)$$

where $\dot{\epsilon}_c$ is the critical strain rate, typically very low. The best way to define correctly the effect of temperature is to assume that the temperature is taken into account by two expressions.

$$n(\epsilon, T) = n_0 \left[1 - D_2 \left(\frac{T}{T_m} \right) \log \left(\frac{\dot{\epsilon}}{\dot{\epsilon}_{min}} \right) \right] \quad \text{with } n \geq 0 \quad B(\epsilon, T) = B_0 \left[\frac{T}{T_m} \log \left(\frac{\dot{\epsilon}_{max}}{\dot{\epsilon}} \right) \right]^{-v} \quad (6)$$

where n_0 is the strain hardening exponent at $T=0K$, D_2 is a constant, $\dot{\epsilon}_{min}$ is the minimal strain rate assumed in the model, B_0 is a constant, $\dot{\epsilon}_{max}$ is the maximal strain rate assumed in the model and v is the temperature sensitivity. Reduced number of constants is eight and it allows to approximate the same tendencies as predicted by the physical approach. A complete optimization algorithm has been written to determine the unique optimal set of constants for each material [1-7]. In order to apply the set of constitutive relations a scheme integration must be used. Such original integration scheme has been proposed in [7]. Moreover, it is relatively simple to obtain the analytical derivatives in terms of ϵ , $\dot{\epsilon}$ and T for direct application in a FE code. All analytical expressions for derivatives are given in the appendix.

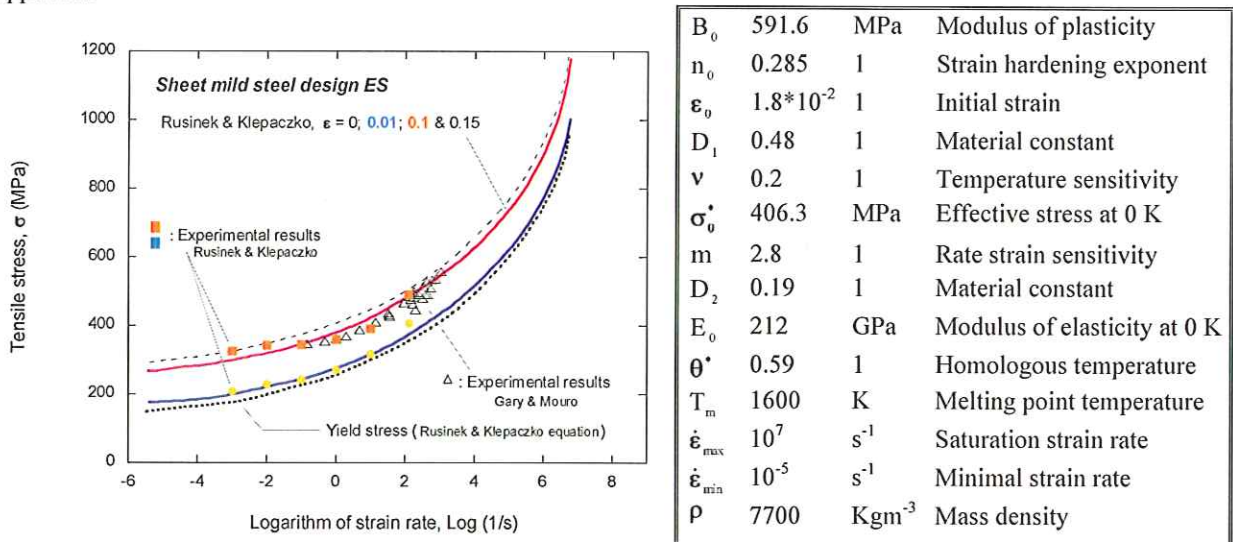


Fig. 2. Evolution of the flow stress for mild steel sheet ES, comparison between experimental results [1-9] and analytical results (isothermal conditions), Eq. 5-6

A good agreement between experimental and analytical predictions are observed on $\sigma - \log(\dot{\epsilon})_{\epsilon, T}$, at both the low and high strain levels. A very high strain rate sensitivity appears for this mild sheet steel for strain rates higher than $\dot{\epsilon} > 10^4 s^{-1}$ which is in agreement with the current experimental observations for mild steels [10]. The beginning of transition from low to high rate sensitivity, as well as the transition isothermal-adiabatic for the ES steel has been observed experimentally for a strain rate $\dot{\epsilon}_p^{transition} = 10 s^{-1}$. This transition is characterized by a thermal softening inducing a decrease of the strain hardening coefficient $n = \partial \log \sigma / \partial \log \dot{\epsilon}$.

IMPLICIT INTEGRATION ALGORITHM

The yield stress σ_y is defined by Eq. 5, $\sigma_y = \sigma$, which takes into account strain hardening, strain rate sensitivity and temperature. Thus in general loading conditions, the yield surface is defined as follows:

$$f(\epsilon_{ij}, \bar{\epsilon}^p, \dot{\epsilon}^p, T) - \bar{\sigma} - \sigma_y(\epsilon^p, \dot{\epsilon}^p, T) = 0 \quad \text{with} \quad \bar{\sigma} = \sqrt{\frac{3}{2} s_{ij} : s_{ij}} \quad (7)$$

where $\bar{\sigma}$ is the equivalent stress, $\bar{\epsilon}^p$ is the equivalent plastic strain, $\dot{\bar{\epsilon}}^p$ is the equivalent plastic strain rate and s_{ij} is the deviatoric part of the stress tensor σ_{ij}

In this approach, the total strain tensor ϵ_{ij} is a sum of the elastic strain tensor ϵ_{ij}^e , the plastic strain tensor ϵ_{ij}^p and the thermal strain ϵ_{ij}^0 . To define the plastic flow, the normality rule is used allowing to relate plastic strain rate $\dot{\epsilon}_{ij}^p$ to the stress. The last is defined as follows:

$$\dot{\epsilon}_{ij}^p = \lambda \frac{\partial f}{\partial \sigma_{ij}} \quad \text{with} \quad \lambda > 0; \quad \dot{\bar{\epsilon}}^p = \sqrt{\frac{2}{3} \dot{\epsilon}_{ij}^p : \dot{\epsilon}_{ij}^p} \quad \text{and} \quad \bar{\epsilon}^p = \int \dot{\bar{\epsilon}}^p dt \quad (8)$$

where λ is the plastic multiplier. In standard Perzyna's overstress models [11], the consistency condition is not used and excursions of stress outside the yield surface are allowed. Several authors have proposed the so called "consistency viscoplasticity models" to include rate effects in the consistency condition, Eq. 9. Following the work of Winnicki et al. [12], who used the approach $\dot{\bar{\epsilon}}^p = \Delta \bar{\epsilon}^p / \Delta t$ to include viscoplastic effects in the consistency condition for the Hoffman yield surface, the present algorithm is developed for J_2 plasticity and thermal effects

$$\dot{f} \left(\sigma_{ij}, \bar{\epsilon}^p, \dot{\bar{\epsilon}}^p, T \right) = \frac{\partial f}{\partial \sigma_{ij}} \dot{\sigma}_{ij} + \frac{\partial f}{\partial \bar{\epsilon}^p} \dot{\bar{\epsilon}}^p + \frac{\partial f}{\partial \dot{\bar{\epsilon}}^p} \ddot{\bar{\epsilon}}^p + \frac{\partial f}{\partial T} \dot{T} = 0 \quad \text{with} \quad \dot{T} = \frac{\beta}{\rho C_p} \sigma_{ij} : \dot{\epsilon}_{ij}^p \quad (9)$$

where $\ddot{\bar{\epsilon}}^p$ is the equivalent plastic acceleration, ρ is the density of material, β is the Quinney-Taylor coefficient and C_p is the specific heat at constant pressure assumed constant during numerical simulation

The linearization of the consistency equation, Eq. (9), leads to Eq. (10) where k is an iterative index [2].

$$f_{k+1} \approx f_k + \frac{\partial f}{\partial \sigma_{ij}} : \left(-\delta \Delta \bar{\epsilon}_{(k)}^p 2G \frac{\partial f}{\partial \sigma_{ij}} \Big|_k \right) + \frac{\partial f}{\partial \bar{\epsilon}^p} \Big|_k \delta \Delta \bar{\epsilon}_{(k)}^p + \frac{\partial f}{\partial \dot{\bar{\epsilon}}^p} \Big|_k \frac{\delta \Delta \bar{\epsilon}_{(k)}^p}{\Delta t} + \frac{\partial f}{\partial T} \Big|_k \frac{\beta}{\rho C_p} \left(\Delta \bar{\epsilon}_{(k)}^p \bar{\sigma}_{n+1}^{trial} - 6G \Delta \bar{\epsilon}_{(k)}^p \delta \Delta \bar{\epsilon}_{(k)}^p \right) \approx 0 \quad (10)$$

In order to complete analysis and numerical scheme and to solve the set of equations in general case of loading a special integration scheme has been developed. The complete characterization of the algorithm is given in [2]. The solution of Eq. 10 is the following

$$\delta \Delta \lambda = \frac{f_k}{3G - \frac{\partial f}{\partial \bar{\epsilon}^p} \Big|_k - \frac{1}{\Delta t} \frac{\partial f}{\partial \dot{\bar{\epsilon}}^p} \Big|_k - \frac{\partial f}{\partial T} \Big|_k \frac{\beta}{\rho C_p} \left(\bar{\sigma}_{n+1}^{trial} - 6G \Delta \bar{\epsilon}^p \right)} \quad (11)$$

Concerning the unloading conditions, the Hooke's law is programmed causing an instantaneous unloading.

NUMERICAL SIMULATION OF DYNAMIC PROCESS

To verify and validate the new thermoviscoplastic algorithm coupled with the constitutive relation, numerical simulations of the Taylor test have been performed in 3D with the limit and initial conditions shown in Fig. 3. In the first time, the original subroutine has been implemented in the VUMAT Abaqus subroutine and compared with the direct results obtained with ABAQUS using Johnson-Cook relation (present initially in ABAQUS). The element used during the numerical simulations is a C3D8R with 46080 elements and density element non uniform along the specimen, Fig. 4-a. The numerical results obtained and compared between the two approaches for copper were in complete agreement (see appendix A7-a-b). In fact, the first approach was completed to validate the VUMAT subroutine or more precisely the new algorithm proposed in [2]. Actually, the constitutive relation proposed in this paper and developed in [1-7] has been also implemented in the VUMAT Abaqus subroutine.

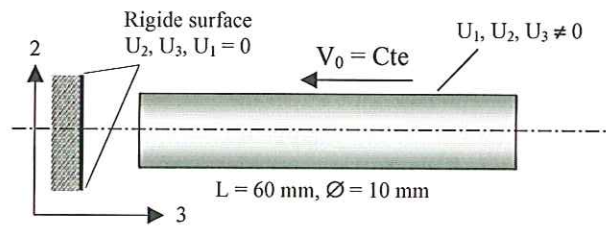


Fig. 3. Initial and boundary conditions used during numerical simulations of the Taylor's test.

The impacted surface has been defined as rigid without deformation, Fig. 3. Moreover, a friction has been introduced to define the contact condition between the rigid surface and the projectile, the Coulomb's coefficient is equal to 0.2 that is a dry contact steel-on-steel [1]. The numerical results obtained for the temperature distribution are shown in Fig. 4-b. We can observe in this figure the iso-temperature distribution, the apparition of a cone failure in the specimen due to the friction conditions applied during the numerical simulation. This failure mode is commonly observed during experiment due to limited sliding of the specimen interface which reduces the radial expansion of the cylinder.

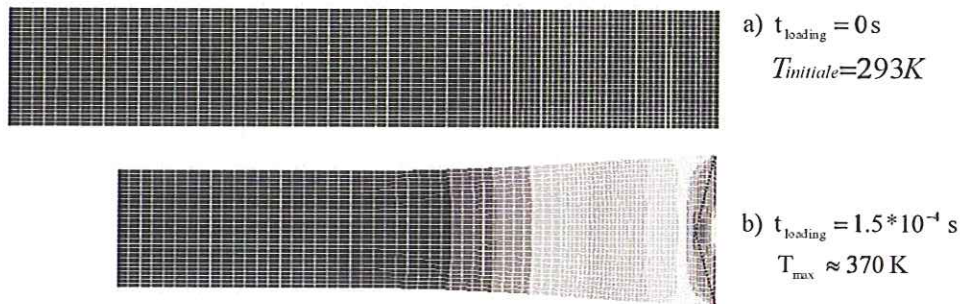


Fig. 4. a- Initial 3D mesh used during numerical simulations, b- Numerical results showing the temperature distribution for $V_0 = 150$ m/s

This first numerical result confirms the effectiveness and the robustness of the new algorithm [2] combined with the constitutive relations proposed previously [1-7]. It is necessary in the future to extend the numerical analyses to the dynamic problems of sheet deformation and compare experimental results and numerical simulations for different kinds of steels sheets.

CONCLUSIONS

The combination of the thermoviscoplastic model and a new integration scheme taking into account the strain hardening, strain rate sensitivity and temperature effects, allows to simulate and study variety of processes of dynamic loading and impact. In the past, the constitutive relation discussed in this paper were used without the new algorithm developed in [2] to study the problem of elastic-plastic wave propagation [1,13,14]. The constitutive relations may be also used in solving of analytical problems since all quantities may be defined as derivative of all orders (see Appendix, equations A1-A6).

References

- [1] Rusinek, A., Modélisation thermoviscoplastique d'une nuance de tôle d'acier aux grandes vitesses de déformation. Etude expérimentale et numérique du cisaillement, de la traction et de la perforation, Thèse de Doctorat de l'Université de Metz (2000)
- [2] Zaera, R. Fernández-Sáez, J., Navarro, C., A consistent algorithm for thermoviscoplastic hardening relations in adiabatic problems, *Int. J. Mechanical Sciences* (to be submitted 2004)
- [3] Rusinek, A., Klepaczko, J.R., Dynamic tension test : geometric effect on the arterial response and instability behavior, *Int. Journal of impact*, pp. 1-40 (to be submitted 2004)
- [4] Oussouadi, O., Klepaczko, J.R., An analysis of transition between isothermal and adiabatic deformation for the case of torsion of a tube, *J. Physique IV*, 1 (1999), pp. 323-327
- [5] Klepaczko, J.R., Thermally activated flow and strain history effects for some polycrystalline FCC metals, *Mat. Sci. and Engng*, 18 (1975), p. 121
- [6] Klepaczko, J.R., Modelling of structural evolution at medium and high strain rates, FCC and BCC metals, in : *Impact : Effects of fast transient loading*, A.A. Balkema, Rotterdam-Brookfield, Denmark (1988), pp. 3-35
- [7] Rusinek, A., Klepaczko, J.R., Shear testing of a sheet steel at wide range of strain rates and a constitutive relation with strain-rate and temperature dependence of the flow stress. *Int. J. of Plasticity*, 17 (2000), pp. 87-115
- [8] Kocks, U.F., Argon, A.S. and Ashby, M.F., *Thermodynamics and Kinetics of Slip*, Oxford, Pergamon Press (1975)
- [9] Mourou, P., Etude du comportement dynamique des tôles d'acier pour le calcul de crash, Thèse de Doctorat de l'Ecole Polytechnique de Paris (2002)
- [10] J.R.Klepaczko, Plastic shearing at high and very high strain rates, *Proc. Int. Conf. EURODYMAT'94, J. Physique IV*, 4 (1994), p. 35
- [11] Perzyna P., The Constitutive Equations for Rate-Sensitive Plastic Materials. *Q. Appl. Math.*, 20 (1963), pp. 321-332
- [12] Winnicki, A., Pearce, C.J., Bicanic, N., Viscoplastic Hoffman consistency model for concrete, *Computers & Structures*, 79 (2001), pp. 7-19

[13] Rusinek, A., Klepaczko, J.R., Effect of adiabatic heating in some processes of plastic deformation, Impact Engineering and Application, Akira Chiba, Shinji Tanimura and Kazuyuki Hokamoto (Eds), Elsevier Science Ltd, 2 (2001), pp. 541-546

[14] Rusinek, A., Klepaczko, J.R., Size Effects in Dynamic Tension Test, Numerical Approach, 14th DYMAT Technical meeting, Sevilla Espagne (2002), pp. 169-180

- Appendix -

$$\left. \frac{d\sigma_\mu}{d\epsilon} \right|_{\epsilon, T} = B(\dot{\epsilon}, T) n(\dot{\epsilon}, T) \epsilon_0 + \epsilon \quad (A1)$$

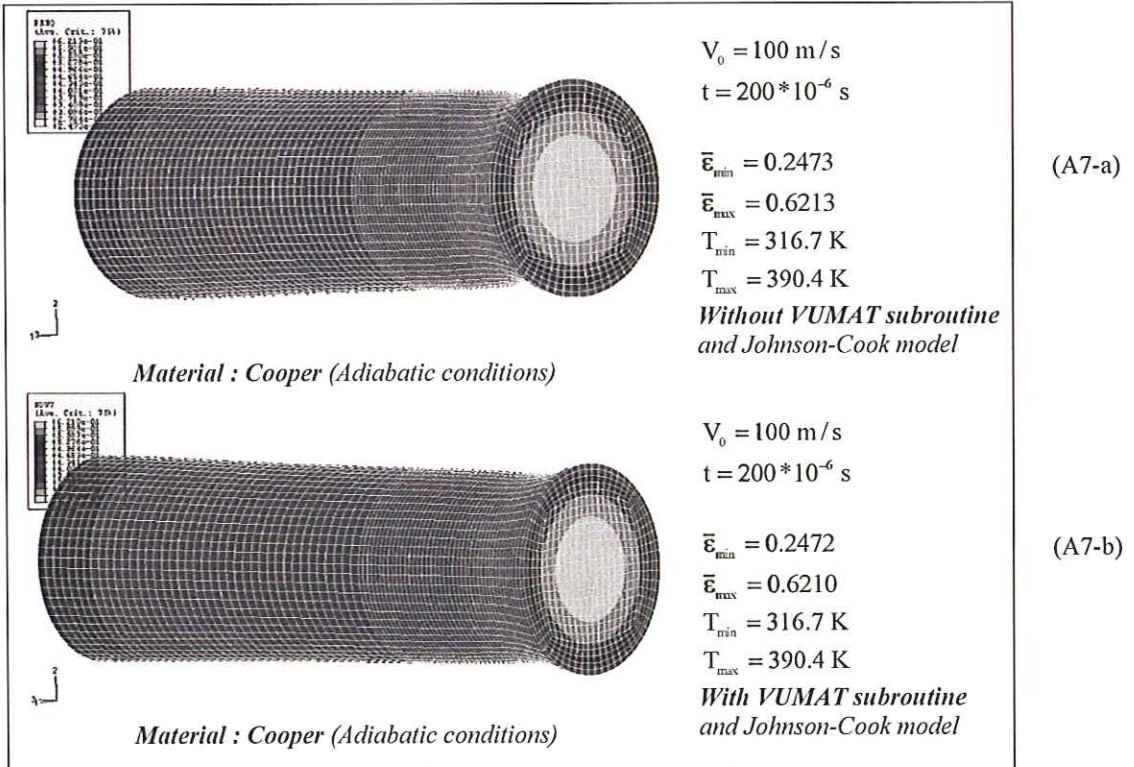
$$\left. \frac{d\sigma_\mu}{d\dot{\epsilon}} \right|_{\epsilon, T} = B(\dot{\epsilon}, T) \epsilon_0 + \epsilon \left[\frac{v \epsilon_0 + \epsilon}{\dot{\epsilon} \log\left(\frac{\dot{\epsilon}_{max}}{\dot{\epsilon}}\right)} - \frac{n_0 D_2 \ln \epsilon_0 + \epsilon}{\dot{\epsilon} T_m} \right] \quad (A2)$$

$$\left. \frac{d\sigma_\mu}{dT} \right|_{\epsilon, \dot{\epsilon}} = -B(\dot{\epsilon}, T) \epsilon_0 + \epsilon \left[\frac{v}{T} + \frac{n_0 D_2}{T_m} \log\left(\frac{\dot{\epsilon}}{\dot{\epsilon}_{min}}\right) \ln \epsilon_0 + \epsilon \right] \quad (A3)$$

$$\left. \frac{d\sigma'}{d\dot{\epsilon}} \right|_{\epsilon, T} = \frac{m D_1}{\dot{\epsilon} \ln(10)} \left(\frac{T}{T_m} \right) \sigma'_0 \left[1 - D_1 \frac{T}{T_m} \log\left(\frac{\dot{\epsilon}_{max}}{\dot{\epsilon}}\right) \right]^{m'-1} \quad (A4)$$

$$\left. \frac{d\sigma'}{dT} \right|_{\epsilon, \dot{\epsilon}} = -\frac{m D_1}{T_m} \log\left(\frac{\dot{\epsilon}_{max}}{\dot{\epsilon}}\right) \sigma'_0 \left[1 - D_1 \frac{T}{T_m} \log\left(\frac{\dot{\epsilon}_{max}}{\dot{\epsilon}}\right) \right]^{m'-1} \quad (A5)$$

$$\frac{dE}{dT} = -E_0 \exp\left[\theta' \left(1 - \frac{T}{T_m}\right)\right] \left(\frac{1}{T_m} + \frac{\theta'}{T}\right) \quad (A6)$$



THE IMPERFECTIONS IN PLASTIC STRAIN LOCALIZATION OF DYNAMICALLY LOADED SPECIMEN

Adam Glema, Tomasz Lodygowski

Poznan University of Technology, Institute of Structural Engineering, ul.Piotrowo 5, Pl 60-965 Poznan, Poland
Adam.Glema@put.poznan.pl, Tomasz.Lodygowski@put.poznan.pl

Summary: The problem of plastic strain localization in metals is taken into account. The phenomena is investigated from the theoretical and numerical points of research interests. The material is defined in elastic regime, plastic hardening/softening and is described by constitutive model with elastic, plastic and viscous properties. Viscosity introduces the mathematical regularization of initial-boundary value problem. This way of regularization does not need the introduction of the imperfections (material, geometrical, thermal nor numerical) to start and continue the computations up to considered time. The wave nature of physical phenomenon is crucial for mathematical formulation and numerical solution. The fast dynamic (impact) tension of the set of metal specimen with different geometry, initial and boundary conditions are considered. The velocity of order 10-50 m/s is applied to the boundary of the specimen. The results of equivalent plastic strain and the field of material point velocities are presented. The place of localization and the pattern of the following material failure are easily recognized. The place and intensity of localization significantly depend on initial imperfections. The solutions, without imperfection and other with proposed irregularities of material and geometry model, give the different places and/or patterns of localization zones. Introducing the imperfections does change the solutions and should be verified by the experiments and implemented in engineering design.

PLASTIC STRAIN LOCALIZATION PROBLEM

In the work the thermomechanical problem of advanced deformation driving to plastic strain localization phenomenon in ductile materials is studied. The specimens are under dynamic, impact loading. Particularly, the influence of the imperfections — geometrical (in the form of additional internal boundaries, exclusions) and specially material imperfections (in the form of inclusions) — on the placement and pattern of localization zone are elaborated and documented in the numerical examples. The knowledge on the influences of any type of imperfections (geometrical, external and internal shape changes, values and distribution of material properties) on the dynamic response of the specimen is crucial. It allows for better design and optimisation of mechanical elements and whole structure.

The description of plastic strain localization phenomena is in focus of scientific research from at least two decades. The phenomenon is clearly observed in ductile as well as in brittle materials. Localization as a precursor of failure is usually accompanied by other phenomena like for example heat generation in zones of localized deformations. When trying to propose the adequate description of the phenomena the most important point is to choose the constitutive structure which would be the closest to the observed properties but still formulated in the frame of continuum mechanics. The careful experimental observations proof that the plastic strain localization observed on the level of continuum is a complex phenomenon. In many cases under consideration the localization of plastic strains results from the material softening which could be the source of difficulties that arises in the process of solution. The crucial question that has to be answered is the well-posedness of the system of governing equations (for discussions see [1, 4, 5, 6, 7, 10, 12]).

There are different approaches to the solution of the problem in the frame of plasticity and continuum formulation. All of them introduce implicitly or explicitly internal length scale and are viewed as regularization methods. Depending on the ductile or the brittle properties of material, the static or dynamic character of the processes and necking or shear bands type of localization the different methods and constitutive models can describe the phenomena. The material under consideration exhibits strain softening as a result of temperature rise or/and evolution of porosity. Both of these effects for classical rate independent plastic strain formulation with negative stress-strain constitutive relation lead to ill-posed problems and in consequence to not unique results in numerical applications [6, 7, 12]. In computations, the attention is focused on assigning the place, time and the width of localization zones. All of them strongly depend on geometry of the specimens, boundary and initial conditions and the loading characteristic. The important feature which differs the treatment, and what follows the computations, the static cases versus dynamic is the necessity of introducing any geometric, material, thermal, numerical imperfections which are the sources of appearing the first plastic strain localization. For dynamic processes (impact) in computations one can avoid these imperfections. The place of the localization, its width (shear band) depends then only on waves interaction which in natural way introduce the heterogeneity and properly describes the merit of the phenomenon. The formulation of initial-boundary value problem and detailed discussion were presented in [12]. Following Perzyna's constitutive model [1, 4, 7] we postulate the elastic-viscoplastic associative model allowing for finite deformations with the use of the evolution equations for problem variables: displacements, velocities, stresses, mass densities and porosities. There are two different alternative hardening/softening factors: thermal decreasing of plastic capacity and porosity increasing separated into nucleation and grow parts. Whole physical and mathematical structure of analytical and numerical model has the wave nature [6, 8, 12, 17].

MOTIVATION - EXPERIMENTAL EVIDENCE

The experimental study to observe the localization phenomena in metals was reported in numerous papers [2, 3, 5, 10, 13, 14, 15]. The main results that were presented focus on placement, forms of localization and the widths of localization zones. The results prove even, for assumed symmetries, that for the real processes the non-symmetric forms of final patterns of localization are followed by failure and material separation in every single laboratory case. In Fig. 1 there are two examples of experimental results. The first one shows the localization for rectangle plate specimen under tension along the longer edge (Fig. 1a). The second one presents the results of localization for crystals. Here (Fig. 1b), the localization observed at the smaller space level, exhibits also the non-symmetrical form. One can see the non-symmetric failure, observed not only as the final destruction, but also in earlier time instances of the process. There can be different reasons for non-symmetric localization and failure states, for which generally symmetry conditions (specimen geometry, support and loading) are fulfilled. In details, there is no chance to have mathematically ideal case, because of material non-homogeneity, inexactness of supports and loadings. Even if mostly during the process of deformation the structural behaviour is symmetric, the final failure has one of the non-symmetric patterns selected among the set of possibilities. The failure is not obvious, but its character can be concluded from a series of experiments for the same kind of conditions. It is worth to mention that, the process velocity resulting from external loadings, described by deformation rate, influences very much the placement and pattern of the state at the end of the process.

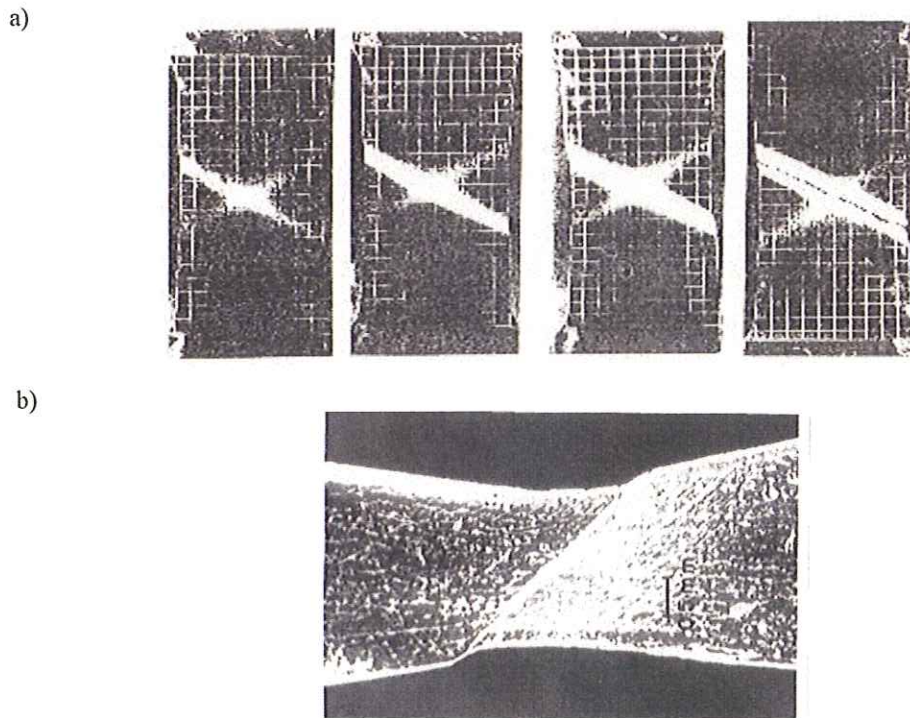


Fig. 1. a – Localization zone and shear band in plate specimen under tension (Chakrabarti i Spretnak [2]),
b – Deformation of aluminium-2.8%Cu cristal under tension (Lisiecki, Nelson & Asaro [3])

TENSION OF RECTANGULAR METAL SPECIMEN

In the presentation we do not insert the formal derivation of the governing equations which were presented and carefully discussed in previous papers [7, 12, 17]. Now, we focus the attention on the problem with initial imperfections. The examples of analysis for the numerical problems without any imperfections (structural element is perfect) were solved and results can be found in mentioned papers [12, 17], and also in the other works which already present the subject on role of imperfections in plastic strain localization [16, 17, 18]. There were studied the cases, when one single imperfection was applied to show, what is the difference between the solution for the model with and without imperfections. The single imperfection was introduced by definition of the small hole inside the specimen (central position) or another group with material inclusions: single inclusion defined by the change of material property (elasticity modulus). The case of material inclusion was verified in a set of solutions obtained for different positions of imperfections.

There was not only observed the influence of the imperfection position on the placement of localization zone but also the history of deformations could be quite different. The change was also observed when looking at the history of energy dissipation: its evolution and amount depend on the initial imperfections. There are two fundamental aims of the presented study. The first is the knowledge on the role of imperfection existence and the way how to solve the problem without imperfection (mostly for dynamic problems under consideration there is not any necessity of imperfection introduction to obtain the solution). The second very important and in future promising is to answer the question how we can actively influence on the shape of elements/specimens to obtain the expected properties of thermo-mechanical behaviour of specimen/element or finally the whole structure.

NUMERICAL EXAMPLES

The numerical examples of dynamic tension of steel rectangular plates are now presented for the problems composed of more than one material inclusion (only material inclusions are studied in the work). We restrict our attention to the initial boundary value problems for which the time scale covers only the fraction of a second, mostly for the same model data as in previous solutions. The thin plate loaded by dynamic impulse is taken into computations. The dimensions of the plate are as follows: length 25.4 mm and width 12.7 mm. The thickness of the specimen is 0.33 mm. The constitutive relation incorporates the thermal softening of yield stress or/and the evolution of porosity.

The constitutive parameters used in computations are: Young's modulus $E=200,000$ MPa (material for inclusion 15,000 MPa), Poisson ratio $\nu=0.3$, yield stress $\sigma^p=1634$ MPa, initial mass density $\rho_0=7850$ kg/m³. The inelastic heat fraction $\chi^*=0.9$ and specific heat $k=460$ J/kg K define the part of thermally dissipated energy. The strength stress decreases nonlinearly to the value of $\sigma^l=1016$ MPa when temperature grows up to 610 °C. Density evolution describes softening character of the material in the range of void volume ratio from $\xi^0=0.004$ up to $\xi^k=0.3$. The relaxation time of mechanical disturbances is $T_m=2.5\mu s$. The time of elongation process is short $t=50\mu s$ (results from external action, the dimensions of the specimen, material viscosity and velocity of wave propagation).

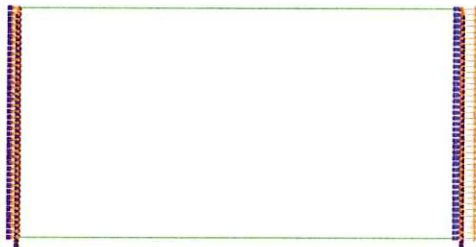


Fig. 2. The rectangular plate specimen with supported left edge and loading (constant velocity) applied to the right edge

Two dimensional shell model is applied. The space discretization consists of finite element mesh of square elements: 80 along the length and 40 along the width. The left side of the specimen was fixed and constant longitudinal velocity of 20 m/s is applied at all nodes of the right edge (see Fig. 2). Both horizontal boundaries are free, without any constraints. The whole process time is discretized for increments of order 0.01/s. The stability criteria for explicit procedure and physical requirements for wave propagation are satisfied. The achieved zones of localization are insensitive to the finite element mesh accepted for computations.

Specimen with different material inclusions. There are several examples with models containing considered imperfections in the different number of imperfection places and/or different sizes. In the following examples, we study four models with material inclusions. The inclusion is defined by material with changed constitutive properties - smaller Young's modulus (more flexible material) - associated with usually six finite elements. All other parameters remind the same. For first case there is the imperfection in the centre of specimen. In the case under consideration the imperfection does not brake the symmetry of the IBV problem. For the second case, the inclusion is located at the centre of specimen. For the next, third case, the imperfections are placed on the top edge and lie on the boundary. In the last case, the imperfections are placed at the top and bottom edges and in the middle of the specimen. In Fig. 3 on the left figures the imperfection schemas are shown while the right side figures present the adequate plastic strain localization zones by the contour plots of plastic equivalent strains distributions at the end of the process. The places of localization and its intensity allow to recognize the pattern of the material failure. The animations of the plastic equivalent strains and material point velocity fields which enrich the results presentation will be presented during the conference.

For each case of imperfection when comparing with the perfect specimens [16, 17, 18] one can clearly see that the imperfection influences both; velocity history and plastic deformation and finally the localization pattern. The single and multiply inclusions influence the solution, through the reflection and interaction of waves. The pattern and placement of localization became different from computed without imperfections. The changes in the localization patterns and the amount of energy that is dissipated during the whole process of deformations were in focus of authors' interests. The dissipation and its amount has various distribution, is more or less concentrated and covers greater or smaller part of specimen.

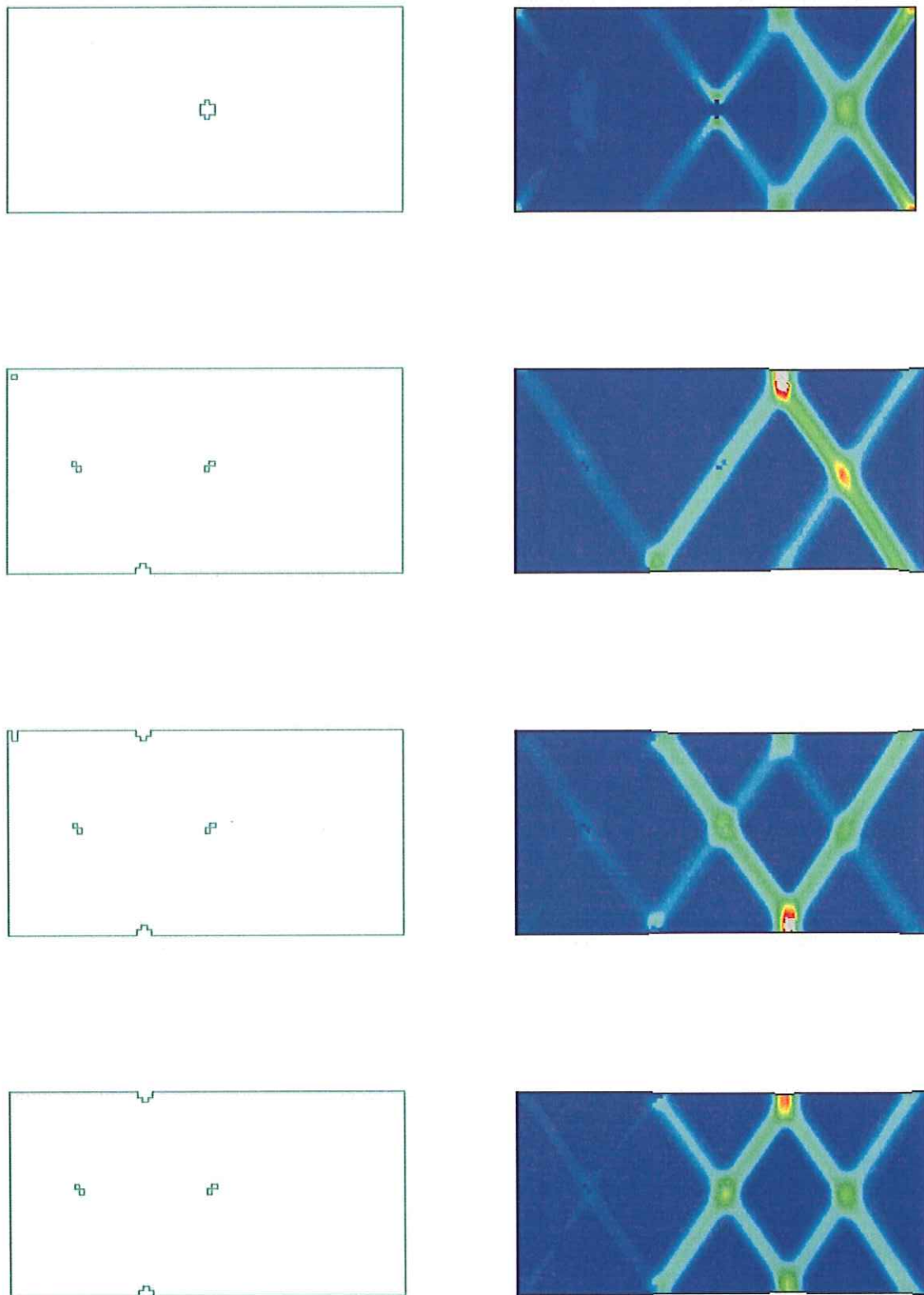


Fig. 3. The placements of initial imperfections (left) and contours of final state of plastic equivalent strain

CONCLUSIONS

The work proves that the final results (places, widths and intensity of localization patterns) depend significantly on introduced initial imperfections. The solutions with proposed irregularities of material properties give the different places and/or patterns of localization zones. The introduction of the imperfections determines the initial state, the evolution of the deformation process and the final state of strains and stresses. Finally, it leads to the different failure modes. The results of numerical analysis of plastic strain localization are in agreement with experiments and the variety of imperfections can be related to the real conditions, which induced final state of the deformation, fracture and failure for particular laboratory test. The knowledge on the imperfection influence is useful in the design process of structures. There is the possibility to control the deformation and energy dissipation. The decision on initial imperfection has the crucial influence on the pattern, the position and the shear band characteristic. The result of this assumption is always strongly dependent on the imperfections. One can expect the different form of localization for every single imperfection. For dynamic processes, when using rate dependent constitutive form, even for symmetric problems the localization pattern is finally achieved as a result of waves interaction. In these cases, the process of localized deformations will appear and grow up without any artificial accelerators. In the studied cases the symmetry in the behaviour of the specimen was obtained and also compared the results with those where the inclusions were consciously introduced. The importance of imperfection consequences has the brought influence in different single scale and multiscale analysis. The challenge in the design of structural elements via inclusions (material, geometrical, thermal and other physical fields) and exclusions arises as interesting opportunity.

Acknowledgements The support of Poznan University of Technology Grant 11-554-DS are gratefully acknowledged. The computations has been performed also in Poznan Supercomputing and Networking Center.

References

- [1] Perzyna P., The Constitutive Equations for Rate Sensitive Plastic Materials. *Quart. Appl. Math.*, 20, (1963), pp. 321-332
- [2] Chakrabarti A.K., Spretnak J.W., Instability of plastic flow in the directions of pure shear I: Theory, II: Experimental, *Metallurgical Transactions*, 6A, (1975), pp. 733-747
- [3] Lisiecki L.L., Nelson D.R., Asaro R.J., Lattice rotations, necking and localized deformations in f.c.c. single crystals, *Scripta Metallurgica*, 16, (1982), pp. 441-449
- [4] Perzyna P., Constitutive modelling of dissipative solids for postcritical behaviour and fracture, *ASME J. Eng. Materials and Technology*, 106, (1984), pp. 410-419
- [5] Cho K., Chi Y.C., Duffy J., Microscopic observations of adiabatic shear bands in three different steels, *Brown University Report No. DAAL03-88-K-0015/3*, (1988).
- [5] Bigoni D., Huckel T., Uniqueness and Localization, Part I and II, *Int. J. Solids and Structures*, 28, (1991), pp. 197-213
- [6] Sluys L.J., Wave propagation, localisation and dispersion in softening solids, *TU Delft*, (1992)
- [7] Perzyna P., Instability phenomena and adiabatic shear band localization in thermoplastic flow processes, *Acta Mechanica*, 106, (1994), pp. 173-205
- [8] Perzyna P., Interactions of elastic-viscoplastic waves and localization phenomena in solids, *IUTAM Symposium on Nonlinear Waves in Solids*, Victoria, Canada, August 15-20, 1993. Eds. Wegner J.L. and Norwood F.R., *ASME*, (1995), pp. 114-121
- [9] Glema A., Kakol W., Lodygowski T., Numerical modelling of adiabatic shear band formation in a twisting test, *Eng. Transactions*, 45, (3-4), (1997), pp. 419-431.
- [10] Liao S.C., Duffy J., Adiabatic shear bands in a Ti-6Al-4V titanium alloy, *Journal of Mechanics and Physics of Solids*, 46, (1998), pp. 2201-2231
- [11] Perzyna P., Constitutive modelling of dissipative solids for localization and fracture, in: *Localization and fracture phenomena in inelastic solids*, CISM Courses and Lectures No 386, Springer, Wien New York, (1998)
- [12] Glema A., Lodygowski T., Perzyna P., Interaction of deformation waves and localization phenomena in inelastic solids, *Comp. Meth. Appl. Mech. Eng.*, 183, (2000), pp. 123-140
- [13] Li S., Liu W.-K., Qian D., Guduru P.R., Rosakis A.J., Dynamic shear band propagation and micro-structure of adiabatic shear band, *Comp. Meth. Appl. Mech. Eng.*, 191, (2001), pp. 73-92
- [14] Nowacki W.K., Dynamic simple shear of sheets at high strain rates, in: *New experimental methods in material dynamics and impact*, Eds. Nowacki W.K., Klepaczko J.R., Warsaw, IPPT, (2001), pp.309-336
- [15] Field J.E., Proud W.G., Walley S.M., Goldrein H.T., Review of experimental registration of microparticles penetration into barriers, in: *New experimental methods in material dynamics and impact*, Ed. Nowacki W.K., Klepaczko J.R., Warsaw, IPPT, (2001), pp. 109-177
- [16] Glema A., Lodygowski T., On importance of imperfections in plastic strain localization problems in materials under impact loading, *Arch. Mech.*, 54, 5-6, (2002), pp. 411-423
- [17] Glema A., Wave Propagation in Elasto-Viscoplastic Solids for Advanced Impact Deformation with Softening. *Proceedings of the Fifth World Congress on Computational Mechanics (WCCM V)*, July 7-12, 2002, Vienna, Austria, Eds: Mang, H.A.; Rammerstorfer, F.G.; Eberhardsteiner, J., Publisher: Vienna University of Technology, Austria, (2002)
- [18] Glema A., Lodygowski T., The Consequences of Imperfections Introduction to the Analysis of Plastic Strain Localization in Solids. *IV European Congress on Computational Methods in Applied Sciences and Engineering*, 24 - 28 July, 2004, Jyväskylä, Finland, (2004)

NUMERICAL SIMULATION OF THE STRETCH FORMING PROCESS FOR PREDICTION OF FRACTURE AND SURFACE DEFECT

O. Jaspert, A. François, L. D'Alvise

CENAERO, Bât. Mermoz 1, 30 Av. J. Mermoz, B-6041 Gosselies, Belgium

URL: www.cenaero.be e-mail: olivier.jaspert@cenaero.be;

arnaud.francois@cenaero.be;

laurent.dalvise@cenaero.be

Summary: This paper focuses on the complete simulation of the cold stretch forming process heavily used in the aerospace industry to manufacture parts of aircraft fuselage or leading edge of wings. The objective is to numerically predict the risks of fracture during forming, surface defects (especially the Portevin-Le Chatelier effect), as well as spring-back phenomenon at the end of the process. The accurate kinematics of the machine and all the stages of the process are simulated : installation of the sheet, buckling, drawing, spring-back and cutting. The sheet is modelled by shell finite elements with elasto-plastic material behaviour using the SAMCEF code developed by SAMTECH. Forming Limit Curves (FLC) are employed to define a fracture criterion. A similar method is currently studied in order to verify that the appearance of surface defects can be numerically detected. Experimental validation of the model is carried out for flat drawing and for an industrial sheet forming.

Key words: Stretch forming, PLC effect prediction, finite element simulation, FLD

INTRODUCTION

The cold drawing process is often used in aluminium sheet forming by the aerospace industry to manufacture parts of fuselage or leading edge of the wings. During forming, some undesirable phenomena can occur such as the following :

- tearing of the sheet or fracture;
- appearance of surface defects due to plastic material instabilities. In particular, we focus on the analysis of the PLC effect which materializes as bands developing on the surface of the sheet [4];
- elastic discharging, resulting in a springback at the end of the process and during the post-process operations (cutting, chemical machining, etc.).

The mastering of the process requires the determination of the accurate prediction of these phenomena. The goals are to avoid forming of defective parts and enabling optimisation of the process operating parameters. A finite element model allowing the complete simulation of the process is employed to accurately predict the behaviour of the stretched metal plate and hence achieve these objectives.

DESCRIPTION OF THE PROCESS

Global process

The stretch forming process involves several stages (Fig. 1):

- (a) the sheet is installed by consecutive clamping in the two jaws of the forming machine;
- (b) the jaws approach each other to give an initial deformed shape to the sheet by bulking;
- (c) the sheet is bent and stretched on the forming block;
- (d) it is then released and spring-back can be observed due to the presence of residual stresses;
- (e) the sheet is cut causing sometimes a second spring-back.

All these stages must be accurately simulated by the model in order to predict the whole strain-stress history in the sheet material.

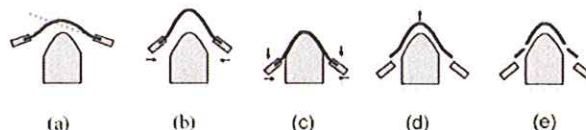


Fig. 1. Stages of the process : (a) installation (b) bulking (c) stretching (d) release (e) cutting

Forming Limit Diagram

The Forming Limit Diagram (FLD) characterises the formability of a material at defined conditions (temperature, thickness, strain rate...).

The Forming Limit Curve of the FLC are defined in the principal strains domain : ϵ_1, ϵ_2 . The parameters ϵ_1 and ϵ_2 correspond to the strain in the stretch direction and its orthogonal respectively. These curves define the onset of localised necking in the drawing domain ($\epsilon_2/\epsilon_1 < 0$), and the onset of diffuse necking in the stretching domain ($\epsilon_2/\epsilon_1 > 0$). A safe process domain is found below these curves, while any other regions correspond to unstable strain configurations which could lead to fracture (Fig. 2).

Experimental Forming Limit Curves

Approximate FLC are obtained by performing three types of experiments that correspond to three specific points of the FLC (Fig. 2): the limit uniaxial strains (a: $\epsilon_2/\epsilon_1 = -0.5$), the limit plane strains (b: $\epsilon_2 = 0$) and the limit biaxial strains (c: $\epsilon_2/\epsilon_1 = 1$). This results in an approximation of the FLC by two straight lines, which in practice reveals sufficiently accurate.

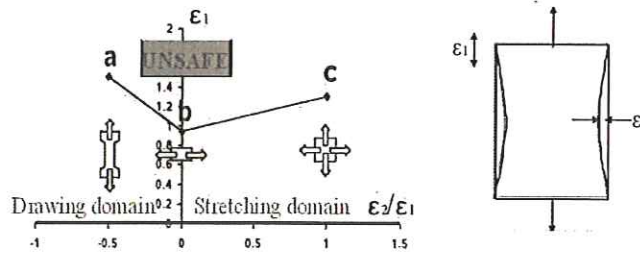


Fig. 2. Experimental Forming Limit Diagram

Analytical Forming Limit Curves

Another method to determine FLC using material law parameters was developed [2] and is described in § Fracture criterion : FLD. The method is based on an analytical determination which can be combined with experimental data to provide more accurate FLD.

NUMERICAL MODEL

Forming tool and sheet model

The complete model of the forming tool is required to apply realistic boundary conditions on the sheet. A set of rigid bodies and kinematical joints is used to represent the kinematical skeleton of the moving parts of the machine. The base frame of the machine is deformable and is modelled by shell elements.

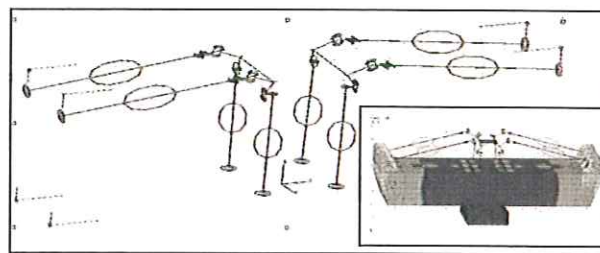
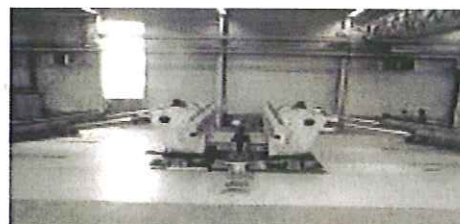


Fig. 3. Forming machine : kinematical skeleton and full model (including base frame model)

The virtual machine provides the same moving capabilities than the real one and thus the numerical control of the eight hydraulic actuators can be introduced into the model to impose realistic forming moves.



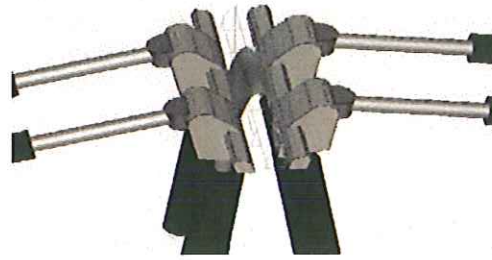


Fig. 4. Forming machine : the real machine and the SAMCEF FIELD model

The sheet is modelled by shell elements using an elasto-plastic material based on the Swift stress-strain curve. The forming block is assumed to be a rigid surface extracted from its CAD model. The contact is simulated between the sheet and the block and between the sheet and the jaws. The model is highly parameterised, the dimensions and position of the sheet, the forming block geometry and the numerical control set can be indeed easily changed.

Fracture criterion : FLD

For each step of the process, couples of principal strains are introduced in a FLD. The distances between these points of the diagram and the FLC give a criterion evaluating the risk for fracture.

An analytical determination of FLC is found using the material law parameters according to [1] which is only based on the hardening coefficient of the material. The latter is calculated on the (Swift) stress-strain curve.

The curve of the onset of localised necking is represented in figure 7 based on the following :

$$\varepsilon_1^* = \frac{n_{incr}}{1 + \rho} \quad (2)$$

where n is the hardening coefficient and ρ is the principal strains ratio:

$$n_{incr} = \frac{\partial \ln \sigma}{\partial \ln \varepsilon} \quad \rho = \frac{\varepsilon_2}{\varepsilon_1} \quad (3)$$

In addition, the curve defining diffuse necking is defined as follows:

$$\varepsilon_1^* = \frac{2n_{incr}(\rho^2 + \rho + 1)}{(\rho + 1)(2\rho^2 - \rho + 2)} \quad (4)$$

RESULTS

Strains and stresses distribution

The evolution and the distribution of the strains and stresses are accessible for any time step of the process. This knowledge of the strain history is very useful to predict fracture, spring-back and surface defects. Figure 6 represents the final plastic strain distribution of a typical industrial forming case and in the quasi plane stretching test. In the case of plane stretch, the largest strains are located along the edges of the sheet (Fig. 8), while they are present in the centre of the sheet in the "industrial" case.

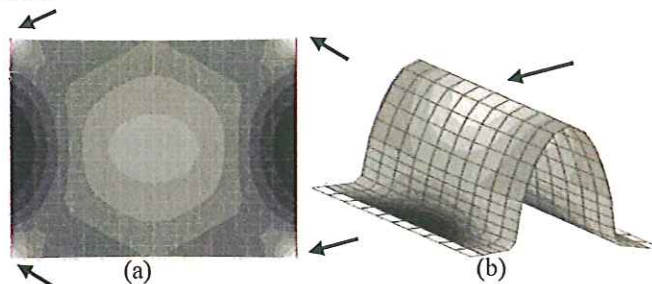


Fig. 5. Sheet model : first principal strain distribution for (a) plane stretching (b) stretching on a block (white color indicates largest strains)

Risk of fracture

The risk of fracture is evaluated using the forming limit diagram. Figure 7 presents the analytical FLD showing clouds of points corresponding to the principal strains couples on the upper and lower skin of the sheet. The fracture risk computed as the distance to the FLC for each finite element of the sheet is presented on figure 8. In the case of plane stretching, the model show that fracture will start on the edges of the sheet.

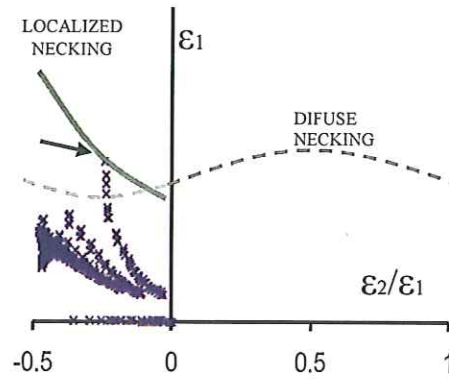


Fig. 6. Analytical Forming Limit Diagram

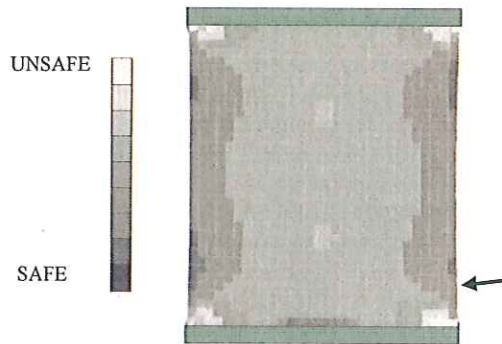


Fig. 7. Fracture risk (distance to the Forming Limit Curve)

VALIDATION

Kinematical validation

The accuracy of the model kinematics has been verified by comparing displacements of the real and virtual machines for the same control set (Fig.10).

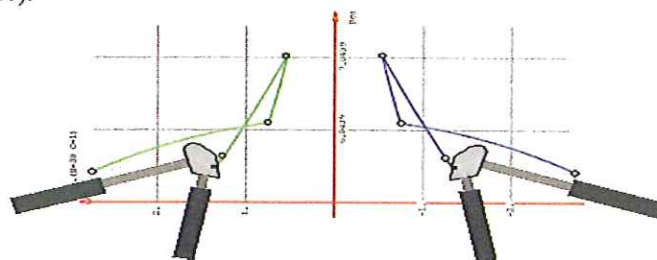


Fig. 8. Kinematical validation : comparison between model (solid line) and measured (dots) trajectories

Strains and fracture criterion validation

Two experimental plane stretching experiments were performed, one being carried out until fracture. A grid was drawn on the sheet in order to measure the strain distribution. The used material is an aluminium alloy. The results of the model are very similar to the experimental one : the differences between the numerical and experimental total deformation on the plate width and length are of the order of 5%. The error on local strain value are smaller than the experimental measurement precision, other experimental tests with precise measurement system are needed to validate more accurately the model. The material model has also to be improved. Experimental tests of the used material are currently conduct at SONACA to characterize it more accurately.

The FLC based fracture criterion correctly predicts the onset of fracture on the sheet edges, just after the clamped part of the sheet. This is observable by comparison of figure 7 and figure 9.

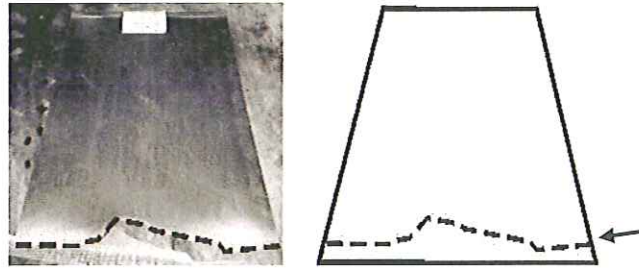


Fig. 9. Fracture in experimental test
(to be compared with figure 7)

Additional tests are planned in order to further validate the model in the whole working range for some typical industrial forming cases.

CONCLUSION

The mastering of the cold stretch forming process requires the accurate prediction of the stress/strain history of the sheet. A finite element model of the whole process capable of providing all the necessary information was constructed. A fracture criterion (FLD) implemented in this model giving appropriate predictions. The model has been validated for fracture prediction by comparing simulation results with experiments for planar sheet stretching. Further experimental validations are needed with other alloys and other forming cases.

A Portevin-Le Chatelier effect [3,4] prediction model is currently under development. The used method is similar to the FLD : per material, a PLC effect range is determined (experimentally or analytically [3,4]) in the stain-strain rate domain (instead of principal strains domain in the FLD case). A first PLC criterion is already implemented in our model, but need to be validated. Another approach is to completely simulate the PLC effect. Modelling the dynamical behaviour of the material by introducing in the Finite Element simulation a specific model based on the physics of the phenomena : PLC effect is due to Dynamic Strain Ageing (DSA) which consists in dynamical interactions between dislocations and solute atoms. Such models have already been developed [3,4] but the spatial coupling has to be improved (especially 2D and 3D generalisation).

Acknowledgements

The authors wish to thank SONACA for providing experimental facilities, results and helpful comments as well as SAMTECH for providing the SAMCEF code.

This research project is funded by the Wallon Region and FEDER European funds under contract n°EP1A122030000102.

References

- 1 W. Hosford, M. Caddell, *Metal forming, Mechanics and Metallurgy*
- 2 X. Mencaglia, *Rapport de Stage*, CENAERO juin 2003
- 3 E. Rizzi, P. Hähner, *On the Portevin-Le Chatelier effect: theoretical modelling and numerical results*, International Journal of Plasticity 20 (2004) 121-165
- 4 Y. Estrin, L.P. Kubin, *Spatial Coupling and propagative Plastic Instabilities*

DYNAMIC ANALYSIS INCLUDING SPECIAL CONSTITUTIVE MODEL FOR PVC-COATED FABRICS

Andrzej Ambroziak^{*}, Paweł Kłosowski^{*}

^{*}*Department of Structural Mechanics, Faculty of Civil Engineering, Gdańsk University of Technology,
Narutowicza 11/12, PL 80-952 Gdańsk*

Summary: The aim of the work is to present the basis of a special model for description of PVC-coated fabrics called the dense net model. This model belongs to the group of continuum models, in which the woven fabric is treated as a continuum without explicit reference to its discrete microstructure. An example of dynamic calculations of a hyperbolic paraboloid hanging roof is presented, as well as the possibilities of the material model implementation into commercial MSC.Marc system. The results obtained from the MSC.Marc software are compared with those from the self-developed Finite Element Method (FEM) code. A good correlation of the results between both computations which has been obtained, confirms the proper application of the model. Additionally, the elastic and viscoplastic variant of constitutive models are compared.

INTRODUCTION

One of the materials encountered frequently in civil engineering for hanging structures are the PVC-coated fabrics. In general the tensile membrane, air supported tents, sail and inflatable constructions belong to group of such structures. These constructions are light, elegant and effective (see e.g. [4]). However, the behavior of the PVC-coated woven fabric has not been completely clarified yet, whereas its advantage from the viewpoint of high specific strength widely induces progressive application in various fields. The architectural applications for fabric structures are still developed. The PVC-coated woven fabrics consist of threads' net and are coated from both sides with the PVC (polyvinyl chloride). In the threads' net usually two families of fabrics (two sets of interlaced yarns) can be distinguish. The lengthwise set is called the warp, and the crosswise set is called the weft. In the present paper, the complex nonlinear behavior of this material is described by the dense net model. It makes possible to implement elastic, viscoplastic or viscoelastic type of material behavior. The basis of fabric and another lightweight constructions calculation is proper determination of loads changeable in the time domain. The main role plays here the wind loading. This paper describes the elementary rules of the wind loading determination and discusses the behavior of the chosen hanging roofs on the blast of wind loading.

CONSTITUTIVE MODELS – BRIEF CHARACTERIZATION NOTE

This chapter is devoted to brief characterization of the constitutive models which are the most often used for the material modeling of the coated woven fabric. Karayka & Kurath [9] presented the micromechanical composite material model for woven fabrics based on mixed boundary conditions: iso-strain, iso-stress and homogenization technique. The fibers in interlaced cells are assumed straight. This model with nonlinear stress-strain relations was extended by Tabiei & Jiang [21], and Ivanov & Tabiei [8]. Within the model a representative volume cell is assumed. Using the iso-stress and iso-strain assumption the constitutive equations are averaged along the thickness direction. The cell is divided into many subcells and an averaging is performed again by assuming the uniform stress distribution in each subcell to obtain the effective stress-strain relations of the subcell. The stress and strain within the subcells are combined to yield the effective stress and strains in the representative cell. A computational micro-mechanical material model is developed to simulate failure by Tabiei & Ivanov [20]. Micro-mechanical failure criteria determine the stiffness degradation for the constituent materials. The pseudo-continuum model is proposed to calculate the three-dimensional deformation of membrane structures made of woven fabrics by Kuwazuru & Yoshikawa ([15] – [18]). The relationship between deformations of a thread and a unit cell is homogenized by a new strain displacement relationship obtained from a uniform strain model with consideration of threads finite rotation. In this model, the deformation of plain-weave fabric is categorized into three kinds of effects based on the thread deformation, that is: skewing, straightening and extension. Assuming that the out of plane strains are negligibly small, we derive the axial and transverse strains of the warp and weft threads by means of the principle of virtual work in the total Lagrangian description, in which the covariant base vectors are used for consideration of the three-dimensional finite rotation of the unit cell. The non-orthogonal constitutive model for characterizing the woven composite behavior under large deformation is proposed by Xue, Peng & Cao [23]. On the basis of stress and strain analysis in the orthogonal or non-orthogonal coordinates and the rigid body rotation matrices, the relationship between the stresses and strains in the global coordinates is obtained. The equivalent material properties are then determined by fitting the numerical load vs. displacement curves obtained from experimental results under biaxial tension and pure shear conditions. This model can be used to efficient prediction of material responses under various loading paths for woven composites with different weave architectures. Kato et al., in [10] and [11], proposed and discussed a new formulation of the continuum constitutive equations for fabric membranes. The formulation is based on the fabric lattice model where the structure of the membrane is replaced by an equivalent structure composed of truss bars representing yarns and a coating material. The equations consider the material nonlinearities of yarns and coatings and include crimp interchange between the warp and weft.

The papers [2] and [3] elaborated by Argyris et al. concerned the numerical analysis of membrane structures made of PVC-coated fabrics. The paper [2] devoted to the mechanical and numerical modeling of viscoelastic materials, has proposed novel schemes for the integration of the rheological relations in the time domain. The following paper [3] concentrated on the application of the developments from [2] to the constitutive description of a specific PVC-coated fabric and includes also comparison with the results of experimental testing. Among the modern approaches, the dense net model used in this paper can also be mentioned.

DENSE NET MODEL

The dense net model has been worked out by Branicki in [6], and afterwards extended by Branicki & Kłosowski in papers [5], [12], [14]. This model belongs to the group of continuum models, in which the woven fabric is treated as a continuum without explicit reference to its discrete microstructure. The advantage of this model is that it considers the change of the angle between thread families during deformation. On the other hand this approach has a drawback, i.e. the force in a given family of threads depends on the strain in the same direction only and the influence of PVC coating is generally neglected. The derivation of the elasticity matrix is based on the assumption that one family of threads ξ_1 is parallel to x_1 axis of the local coordinate system, and the second family ξ_2 is sloped by the angle α with reference to the first family (Fig.1).

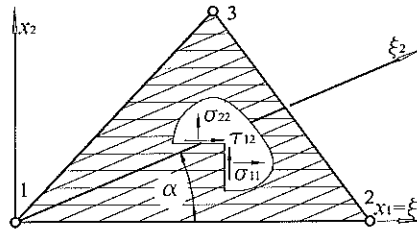


Fig. 1. The dense net model of three nodes finite element

The relation between strains \mathbf{g} along threads' families ξ_α and strains \mathbf{e} in the local coordinates x_α is defined as:

$$\mathbf{g} = \begin{Bmatrix} \gamma_{11} \\ \gamma_{22} \end{Bmatrix} = \begin{bmatrix} 1 & 0 & 0 \\ \cos^2 \alpha & \sin^2 \alpha & \sin \alpha \cos \alpha \end{bmatrix} \begin{Bmatrix} \varepsilon_{11} & \varepsilon_{22} & \varepsilon_{12} \end{Bmatrix}^T = \mathbf{C} \mathbf{e} \quad (1)$$

The threads forces (specific forces) \mathbf{T} in fibres depend on elongation in the same direction only, hence:

$$\mathbf{T} = \begin{Bmatrix} T_{11} \\ T_{22} \end{Bmatrix} = \begin{bmatrix} F_1 \gamma & 0 \\ 0 & F_2 \gamma \end{bmatrix} \begin{Bmatrix} \gamma_{11} \\ \gamma_{22} \end{Bmatrix} = \mathbf{F} \mathbf{g} \quad (2)$$

where: $F_1 \gamma$ and $F_2 \gamma$ are the components of the elasticity matrix of each threads' family, which are experimentally determined from the uniaxial tension tests. Several constitutive relations can be used to define these functions. In the present paper two variants: elastic and viscoplastic relations are used. The description of the identification process of these material parameters for the technical fabric "Panama" produced by Settler Company we can find in the paper [14]. The fabric is manufactured from polyester fibres (PES) and is double-side coated with polyvinyl chloride (PVC). In Table 1 the elastic properties of the fabric in the warp and weft direction are given. Among many types of viscoplastic constitutive approaches the Chaboche model has been selected for $F_1 \gamma$ and $F_2 \gamma$ description. In Table 2 this model's parameters are presented. The material characteristics and mechanical properties of several technical woven fabrics used for membrane constructions have been presented in details by Houtman & Orpara in [7].

The relation between components of the membrane forces in the plane stress state \mathbf{s} in the local coordinates and obtained from (2) threads forces \mathbf{T} can be calculated from the equation:

$$\mathbf{s} = \begin{Bmatrix} \sigma_{11} \\ \sigma_{22} \\ \tau_{12} \end{Bmatrix} = \begin{bmatrix} 1 & \cos^2 \alpha \\ 0 & \sin^2 \alpha \\ 0 & \sin \alpha \cos \alpha \end{bmatrix} \begin{Bmatrix} T_{11} \\ T_{22} \end{Bmatrix} = \mathbf{C}^T \mathbf{T} \quad (3)$$

Consequently, the relation between the membrane forces \mathbf{s} and the strains \mathbf{e} has the form:

$$\mathbf{s} = \mathbf{C}^T \mathbf{F} \mathbf{g} \mathbf{C} \mathbf{e} = \mathbf{D} \mathbf{e} \quad (4)$$

Therefore, the elasticity matrix can be expressed as:

$$D = \begin{bmatrix} F_1 \gamma + F_2 \gamma \cos^4 \alpha & F_2 \gamma \sin^2 \alpha \cos^2 \alpha & F_2 \gamma \sin \alpha \cos^3 \alpha \\ F_2 \gamma \sin^2 \alpha \cos^2 \alpha & F_2 \gamma \sin^4 \alpha & F_2 \gamma \sin^3 \alpha \cos \alpha \\ F_2 \gamma \sin \alpha \cos^3 \alpha & F_2 \gamma \sin^3 \alpha \cos \alpha & F_2 \gamma \sin^2 \alpha \cos^2 \alpha \end{bmatrix} \quad (5)$$

Table 1. Elasticity modulus of the "Panama" fabric

$F_1 \gamma$ (warp)	$F_2 \gamma$ (weft)		Unit
$0 \leq \gamma_{11}$	$0 \leq \gamma_{22} \leq 0.035$	$0.035 \leq \gamma_{22}$	-
932000	122000	253000	N/m

Table 2. Chaboche model parameters of the "Panama" fabric

Parameter	Unit	Parameter value
k	N/m	8600
K	N/m	14700
n	-	3.8
a	N/m	136000000
c	-	9600
b	-	4.0
R_1	N/m	16600
γ	s^{-1}	1.0

Application of this model has been extended in [1], by Ambroziak & Klosowski, by taking the layering of the fabric cross-section into account. In the discussed model the fabric is idealized by the threads net (core layer), symmetrically sandwiched by the coating films of small uniform thickness. Behaviour of the core layer is described by the traditional dense net model described above, where threads can have elastic, viscoelastic or viscoplastic properties. It is assumed that the both coating films are made of the same isotropic, linear elastic material and the strain tensor components at any point of the fabric cross-section are the same. Details of that approach will be presented during the Conference.

DESCRIPTION OF APPLIED PROGRAMS

In the numerical analysis two computer programs have been used. The first one is the Marc program licensed by MSC.Software. It is a multi purpose, finite element program for advanced engineering simulations. A great advantage of the system is possibility of user-subroutines introducing. The standard MSC.Marc system does not support the fabric material models and has no options for the automatic wind loading generation. To apply the dense net models and wind loading the user-defined subroutines HOOKLW [22] and FORCEM [22] were used. The second program is the self-made FEM code (OFC) for membrane structures analysis based on the three node finite element presented in the previous section. The theoretical description and application limits of this code are discussed in [13].

IMPLICIT INTEGRATION ALGORITHM

The non-linear equations of motion in the present paper are integrated with the Newmark algorithm [19]. The method basis on two principal numerical equations:

$$\begin{aligned} \dot{q}_{t+\Delta t} &= \dot{q}_t + [1 - \delta \ddot{q}_t + \delta \ddot{q}_{t+\Delta t}] \Delta t \\ q_{t+\Delta t} &= q_t + \dot{q}_t \Delta t + [0.5 - \alpha \ddot{q}_t + \alpha \ddot{q}_{t+\Delta t}] \Delta t^2 \end{aligned} \quad (6)$$

where: δ and α are method parameters satisfy the conditions $\delta \geq 0.5$, $\alpha \geq 0.25$ $0.5 + \delta^2$

The non-linear equations of motion should have the form:

$$M \Delta \ddot{q} + C \Delta \dot{q} + K_1 + K_2 \Delta q = R_{t+\Delta t} - M \dot{q}_t - C \dot{q}_t - Q_t \quad (7)$$

where : $\Delta \ddot{q} = \ddot{q}_{t+\Delta t} - \ddot{q}_t$, $\Delta \dot{q} = \dot{q}_{t+\Delta t} - \dot{q}_t$, $\Delta q = q_{t+\Delta t} - q_t$.

Application of the Newmark algorithm in nonlinear analysis requires iterations at each step. It is necessary also to construct and reverse the stiffness matrix at each time step. Nevertheless, the Newmark method is effective due to good stability, therefore relatively long integration step for elastic problems can be applied. On the other hand, when viscoplastic constitutive equations are taken into account, and the same time step is applied in the constitutive

equations' integration, much smaller integration step is required. Therefore the explicit algorithms (e.g. the central difference method), which need less time consuming matrix operations, can lead to more effective calculations.

DESCRIPTION OF HANGING ROOF MODEL

Let us consider the hyperbolic paraboloid hanging roof of square $2A \times 2A$ orthogonal projection (Fig. 2). The structures of this shape are more and more often used nowadays, due to their constructional properties merit (Fig. 3). The vertical coordinates of the initial roof surface were computed from the following equation:

$$Z = H_1/A^2 X^2 + H_1 - H_2/A^2 Y^2 - H_1 \tag{8}$$

where: $H_1 = 2.045\text{m}$ and $H_2 = 3.546\text{m}$ are the vertical coordinates at centre and maximum height points, $2A = 30.0\text{m}$ is the diagonal horizontal span.

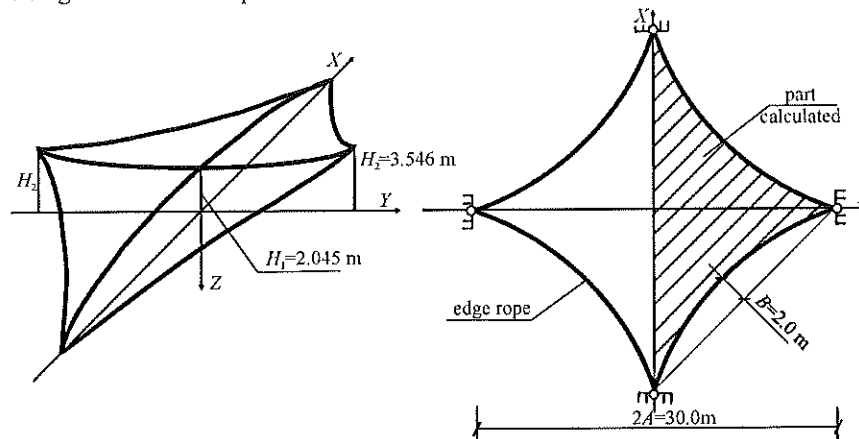


Fig. 2. Three-dimensional hanging roof visualization



Fig. 3. Restaurant near Great Canyon, USA

In the analysis it was assumed that surface edges are bounded with the steel edge ropes (they are modeled by elastic truss finite elements). The roof is subjected to the deadweight loading, initial pretension and wind loading acting along the X axis direction. Due to the symmetry of the geometry and loadings, it is sufficient to analyze only the half of the roof with proper symmetry boundary conditions at $Y = 0$ coordinates. For the rope elements the cross section of $A = 7.3\text{cm}^2$ and Young modulus of $E = 200\text{GPa}$ was accepted. In the initial configuration the threads have the global coordinate system XY directions (warp – Y and weft – X direction). Therefore, the initial angle between thread families is $\alpha = 90^\circ$. Before the wind loading imposing, the roof was loaded by the deadweight loading and then the stretching of membrane and rope elements. In the initial configuration for the membrane elements the pretension forces of $T_x = 55.0\text{kN/m}$ and $T_y = 40.0\text{kN/m}$ in the warp and weft directions are assumed respectively. The initial ropes force of $F = 20\text{kN}$ has been used. The process of the rope stretching was realized in three increments. In each step the internal rope element force has been increased by 30kN . Finally, in the operational configuration, the roof has been

subjected to the wind impulse which parameter's α_c value depends on the angle between normal to the finite element surface and horizontal surface. The current value of the nodal wind force W_i is calculated from the formula:

$$W_i = p(t) \cdot \alpha_c \cdot \bar{\Delta} / n \tag{9}$$

where: $p(t)$ is the time dependent pressure value calculated according to the graph in Fig. 4B; α_c is the reduction coefficient which depends on the element normal vector slope (Fig. 4A); $\bar{\Delta}$ is the current finite element area; n is the number of nodes in the finite element.

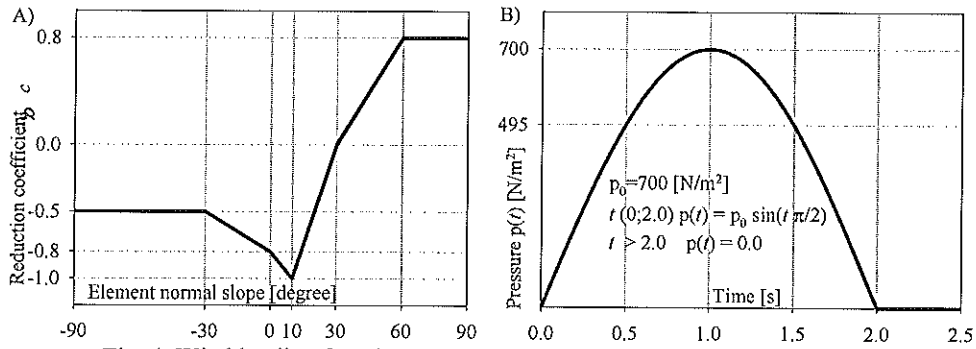


Fig. 4. Wind loading functions: A) reduction coefficient; B) pressure value

EXAMPLE OF DYNAMIC CALCULATIONS

The static loading cases were analysed in [1]. In this work it was found that both MSC.Marc and OFC programs gives almost the same response in all calculated static variants. In this chapter the results of dynamic, geometrically non-linear calculations of the roof from the previous chapter will be presented. Due to lack of data for damping coefficients only free vibrations are considered. In the research two constitutive models of PVC-coated fabrics elastic and viscoplastic are compared. The elastic computations have been done using both finite element programs (OFC and MSC.Marc), while all viscoplastic results were obtained from the OFC program only.

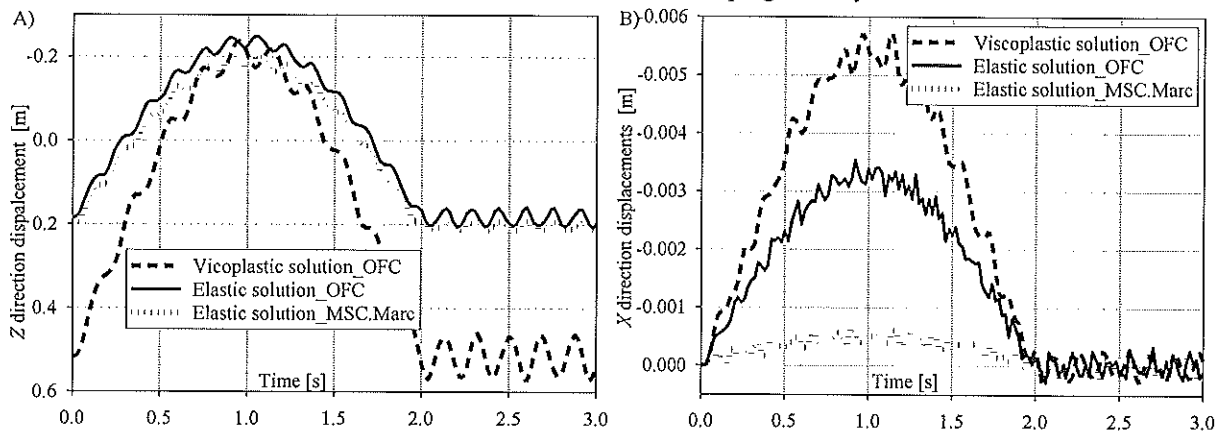


Fig. 5. Middle point deflection

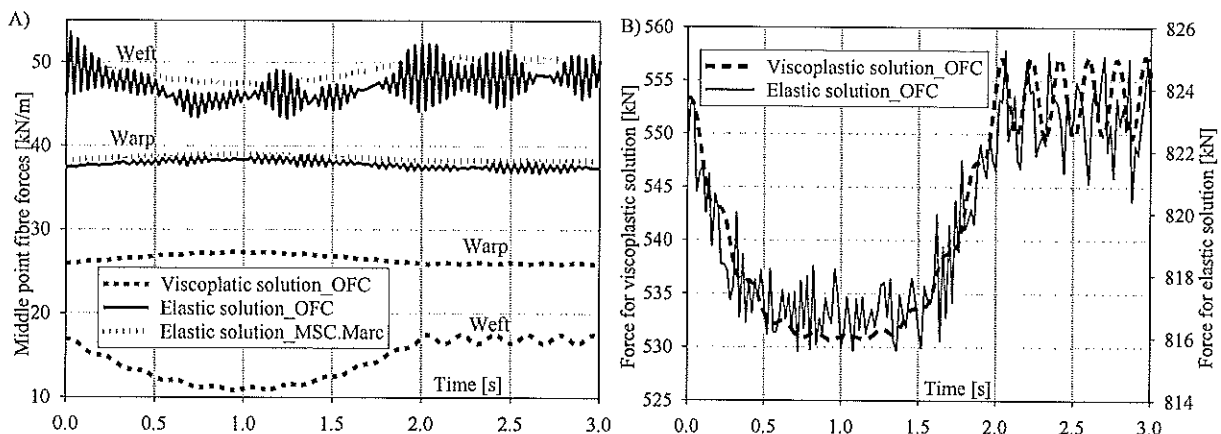


Fig. 6. Time functions: A) of the warp and weft forces at the middle of the roof, B) of the maximum rope force

In Fig. 5 the time functions of middle point displacements are given. In spite of different initial configurations (in the elastic case the maximum static deflection was about 0.20 m, in the viscoplastic about 0.50 m) the maximum displacements, related to the maximum impulse value, are the same (about – 0.20 m). After 2 seconds when the impulse is over the hanging roof is coming back to the configuration close to the initial one, but the free vibration have bigger amplitude in the viscoplastic case. Due to symmetry of static loading there are no horizontal displacements of the roof middle point at the beginning of dynamic calculations. During the wind blast their maximum value is about 0.006 m, in the case viscoplastic and 0.006 m or 0.003 m in the elastic one¹. Both values are very small in comparison with vertical deflections, that confirms proper pretensioning of the structure. The time functions of the tension warp and weft forces are analysed in Fig. 6A. In the elastic case values of the forces are much higher, but they do not change during deformation process. In the viscoplastic case distribution of the forces in the warp and weft is more unique and constant, but the weft threads express about 20% reduction of the force for maximum loading. In Fig. 6B, where the maximum rope forces are analysed. Both approaches give different values of the force but shape of the time function is similar.

CONCLUSIONS

The dense net model proposed for numerical analysis of hanging roofs has been successfully applied in the dynamic analysis. In the calculations geometrical and physical nonlinearity of the problem can be taken into account. Application of the model into commercial code enables application of different types of finite elements and simplified input and output procedures. The minor differences between OFC and MSC.Marc calculations are still investigated. In the dynamic calculations still the damping coefficients are necessary to obtain the results which can be compared with laboratory tests or with real structures behavior. In the viscoplastic approach the main problem is the small time step which is necessary for constitutive relations' integration by the trapezoidal rule. If the same time step is used for integration of equations of motion, the explicit methods seem to be promising. Further developments will include to static and dynamic analysis the effects of temperature and extension of viscoplastic approach to damage effects behavior of the PVC-coated woven fabrics.

References

- [1] Ambroziak A., Kłosowski P.: Constitutive Modelling and Computation of Technical Woven Fabric Using MSC.Marc. VIII Scientific-Technical Conference MSC Software, Rynia Poland (2003), (CD publication)
- [2] Argyris J., Doltsinis I.St., Silva V.D., Constitutive Modelling and Computation on Non-linear Viscoelastic Solid. Part I: Rheological Models and Numerical Integration Techniques, Computer Methods in Applied Mechanics and Engineering, 88 (1991), pp. 135–163
- [3] Argyris J., Doltsinis I.St., Silva V.D., Constitutive Modelling and Computation on Non-linear Viscoelastic Solid, Part II: Application to Orthotropic PVC-Coated Fabric, Computer Methods in Applied Mechanics and Engineering, 98 (1992), pp. 159–226
- [4] Berger H.: *Light Structures – Structures of Light*. Birkhäuser Verlag, Basel, 1996.
- [5] Branicki Cz., Kłosowski P., Statical Analysis of Hanging Textile Membranes in Non-linear Approach, Archives of Civil Engineering, 29 (1983), pp. 189–220
- [6] Branicki Cz., Some Static Problems of Hanging Nets, PhD Thesis Gdańsk University of Technology (1969)
- [7] Houtman R., Orpara M., Materials for Membrane Structures, Bauen mit Textilien, 4 (2000), pp. 27–32
- [8] Ivanov I., Tabiei A., Three-Dimensional Computational Micro-Mechanical Model for Woven Fabric Composites, Composite Structures, 54 (2001), pp. 489–496
- [9] Karayaka M., Kurath P., Deformation and Failure Behaviour of Woven Composite Laminates, Journal of Engineering Material Technology, 116 (1994), pp. 222–232
- [10] Kato S., Pongpo P., Takeda F., Yoshino T., Matsumoto E., Formulation of Nonlinear Constitutive Equations for Fabric Membranes on Schock Model, In: Research Report on Membrane Structures '94, Membrane Structures of Japan, 8 (1994), pp. 11–26
- [11] Kato S., Yoshino T., Minami H., Formulation of Constitutive Equations for Fabric Membranes Based on the Concept of Fabric Lattice Model, Engineering Structures, 21 (1999), pp. 691–708
- [12] Kłosowski P., Numerical Problems of Calculations of Hanging Roofs, Proc. Int. Conf. on Lightweight Structures in Civil Engineering, Warsaw 25-29 September 1995. vol. 1, pp. 661–669
- [13] Kłosowski P., Statics and Dynamics of Cable-Membrane Hanging Roofs in Materially and Geometrically Non-linear Approach [in Polish], PhD thesis, Gdańsk University of Technology, (1983)
- [14] Kłosowski P., Zagubień A.: Analysis of Material Properties of Technical Fabric for Hanging Roofs and Pneumatic Shells. Archive of Civil Engineering, 49 (2003), pp. 277–294
- [15] Kuwazuru O., Yoshikawa N., New Concept of Pseudo-Continuum Model for Plain-Weave Fabric, Proc. 33rd Int. SAMPE Tech. Conf., Seattle, SAMPLE, 33 (2001), pp. 564–573
- [16] Kuwazuru O., Yoshikawa N., Pseudo-Continuum Model for Structural Analysis of Plain-Weave Membranes, International Conference on Textile Composites and Inflatable Structures, Barcelona – Spain, (2003), pp. 355–340
- [17] Kuwazuru O., Yoshikawa N., Theory of Elasticity for Plain-Weave Fabrics (1st Report, New Concept of Pseudo-Continuum Model), JSME International Journal, Series A, 47 (2004), pp. 17–25
- [18] Kuwazuru O., Yoshikawa N., Theory of Elasticity for Plain-Weave Fabrics (2nd Report, Finite Element Formulation), JSME International Journal, Series A, 47 (2004), pp. 26–34
- [19] Newmark N.M., A Method of Computation for Structural Dynamics, Journal of the Engineering Mechanics Division, 85 (1959), pp. 67–94
- [20] Tabiei A., Ivanov I., Materially and Geometrically Nonlinear Woven Composite Micro-Mechanical Model with Failure for Finite Element Simulations, International Journal of Non-Linear Mechanics, 39 (2004), pp. 175–188
- [21] Tabiei A., Jiang Y., Woven Fabric Composite Model with Material Nonlinearity for Nonlinear Finite Element Simulation, International Journal of Solids Structures, 36 (1999), pp. 2757–2771
- [22] Users handbook: MSC.MARC Volume D: User Subroutines and Special Routines, Version 2003. MSC Software Corporation 2003.
- [23] Xue P., Peng X., Cao J., A non-orthogonal constitutive model for characterizing woven composites, Composites, Part A, 34 (2003), pp. 183–193 Acknowledgment Calculations presented in the paper have been made at the Academic Computer Centre in Gdańsk (TASK).

¹ Deferece can be caused by different type (different horizontal stiffness) of finite elements applied in both programs.

EXPERIMENTAL STUDIES OF THE TENSILE BEHAVIOR AT HIGH STRAIN RATES OF UNFILLED AND FILLED POLYPROPYLENES

Nadia Temimi*, Noëlle Billon

*Center for material forming (CEMEF), Ecole des Mines de Paris, UMR CNRS 7635,
Rue Claude Daunesse, BP 207, 06904 Sophia – Antipolis, France*

** This research is conducted with the financial support provided by Faurecia Interior Systems, Visteon and Renault*

Summary: In this work, the thermomechanical behavior of unfilled and filled polypropylenes was studied in tension at low and high strain rates (10^{-4} to 10^2 s⁻¹) with a rapid hydraulic tensile testing machine. A high-speed video camera (2500 frames/s) combined with image analysis and image correlation systems made possible measuring the 3D-strain field as a function of time. In parallel, temperature was measured using a non-contact infrared pyrometer with a large range of spectral settings (4-12 μ m) and a high sampling rate.

Thus, the stress-strain response of each material was analysed without any restrictive hypotheses during data processing. Experimental studies showed that both unfilled and filled polypropylenes was sensitive to strain rate and temperature. It was found, in addition, that plasticity of these materials does not obey incompressibility assumption. Voiding damage process was evidenced by SEM observations. This results in equivalent volume change for both polypropylenes. However, the morphology of voids is different. Moreover, an increase in the temperature of more than 10 °C was observed and is likely to modify the behavior of each material. Heat dissipation increases with increasing strain rates and induced disturbance is important with respect to temperature sensitivity of both materials.

It is concluded that experimental characterisation on polymers should be performed in a very cautious manner revisiting most of the usual assumptions used in classical analysis.

INTRODUCTION

Engineering plastics are used in a variety of applications such as automotive exterior and interior systems and fuel tanks. Among the various materials used today for these applications, polypropylene is one of the least expensive and is therefore one of the most attractive. This material encounters large strains over very short periods of time in its common use. Knowledge of material behavior under rapid deformation is then of prime importance when designing polymer-components.

One important mechanism, which can lead to plastic deformation in polymers, is shear banding [1]. However, additionally to this cohesive phenomenon, several damage processes such as voiding or crazing [2] can play a significant role in the deformation of polymers.

Mechanical behavior of polymers was traditionally analysed under the simplistic assumption of isochoric deformation. Although experimental evidence have proved the important role of non-cohesive mechanisms in the deformation of semicrystalline polymers and blends, to date, very few data have been published concerning the quantitative contribution of damage mechanisms to large strain plasticity. Thanks to an experimental device implying a high-speed camera and an image correlation system, we have analysed the influence of damage mechanisms in two semicrystalline polymers over a wide range of strain rate.

EXPERIMENTAL PROCEDURES

Photomechanical methods are more and more used and developed for mechanical characterisation of materials (for example [3]). However, these investigations are often performed under low velocity loading conditions.

In this work, a commercial photomechanical algorithm is coupled to a rapid hydraulic tensile testing machine. A high-speed video camera (2500 frames/s) combined with image analysis and image correlation systems made possible measuring the 3D-strain field as a function of time. Experiments were run at room temperature with a constant cross head velocity ranging from 0.08 to 900 mm/s. In parallel, temperature was measured using a non-contact infrared pyrometer with a large range of spectral settings (4-12 μ m) and a high sampling rate. Thus, the stress-strain response of each material was analysed without any restrictive hypotheses during data processing over a large strain rate range (10^{-4} to 10^2 s⁻¹ according to our geometry).

Two commercial grades of polypropylene were investigated in this work. The first one was an unfilled copolymer. The second material was a 20 w% mineral-filled copolymer polypropylene. The specimens were machined out from injection-moulded plates having a constant 3mm-thickness. The specimens were hourglass shaped (Fig.1). This geometry included a small rectilinear zone that aimed at localising the deformation in the zone where all the mechanical variables were determined while the triaxial effects, which could result from a small radius of curvature, were limited. Experimental studies showed that plasticity of these materials does not obey incompressible assumption. Voiding damage process was evidenced by SEM observations. This resulted in an increase of the volume during tensile testing.

Experimental protocol allowed determining strain field on the surface of the sample ((X, Y) plane on Fig. 1). It was found that, in any case, strain could reasonably be assumed to be homogeneous in the X-direction. Due to thickness, in the Z-direction the only possible measurement was an average value of the strain. It was then assumed that homogeneity assumption remained valid in the Z-direction. Obviously, strain was not homogeneous in the Y-direction. Thus, strain and stress were deduced from local measurement in the smallest section assuming that variables were constant across a lateral section ((X, Z) plane on Fig. 1).

Nevertheless, SEM observations indicated that the phenomenon of voiding was heterogeneous and varied from the core to the skin of the plate. One has to keep in mind that the assumption of homogeneity through the thickness should be untrue. This could result from usually core-skin laminate structure of injection-moulded polymers. However, hydrostatic pressure effects could not be totally ignored. Whatever the causes of such heterogeneity, we have to neglect it due to a lack of insight measurements.

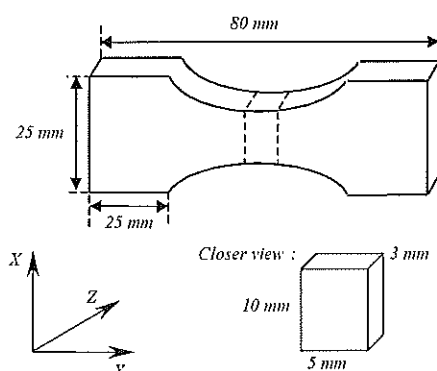


Fig. 1 Geometry of the hourglass shaped sample used for tensile tests.

DAMAGE BY VOIDING

Plastic deformation in polymers can be induced by cohesive (shear banding) or non-cohesive mechanisms (crazing, cavitation). These latter can result in volume expansion of the deformed specimens as suggested by recent investigations under low strain rates stretching conditions (for example [4] [5]). They point out that that volume changes are significant for glassy as well as for semicrystalline polymers.

In order to reveal the mechanisms of plastic damage, series of observations using a scanning electron microscope were performed on transversal surfaces of samples at different strain levels. Nucleation of voids took place in the early stage of deformation (strain of 0.2, Fig. 2). As the strain increased (up to 0.6) the number and size of voids increased significantly. Compared to the filled polypropylene, voids were smaller and more numerous in the unfilled polymer.

Resulting from the measurement of the three components of strain, the volume change during tensile test can be calculated (Fig. 3). It could be concluded that dilatation phenomenon was significant even for low strains for both materials. The main effect was the considerable monotonic increase of volume up to rupture. More interesting was the fact that volume change mechanism was not sensitive neither to strain rate nor to the presence of fillers. Fig.4 depicts the effect of erroneous isochoric assumption on stress-strain curves in our case.

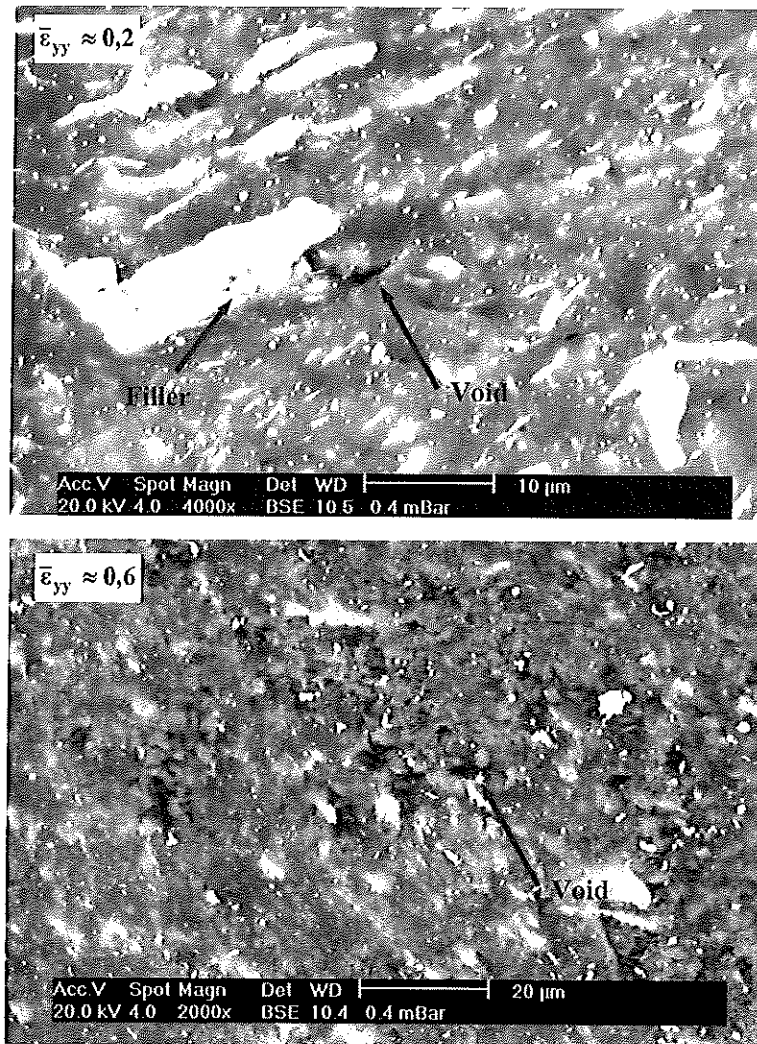


Fig. 2 Scanning electron micrographs of voids in a cross section of a filled polypropylene under uniaxial tension for two values of strain.

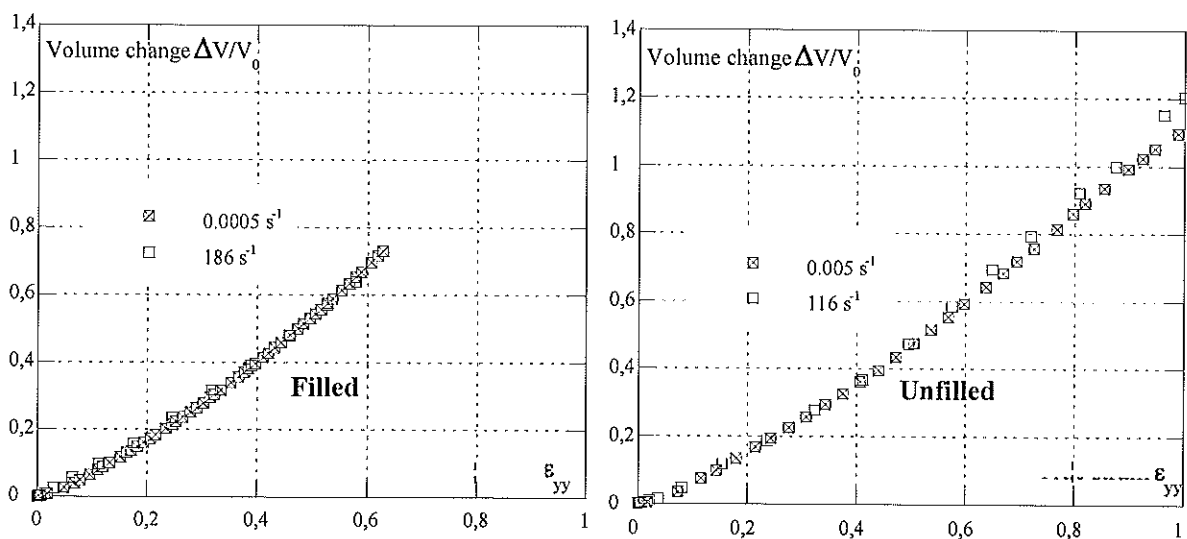


Fig. 3 Volume changes under uniaxial tension of unfilled and mineral-filled polypropylenes at different strain rates and at room temperature. Last point corresponds to rupture.

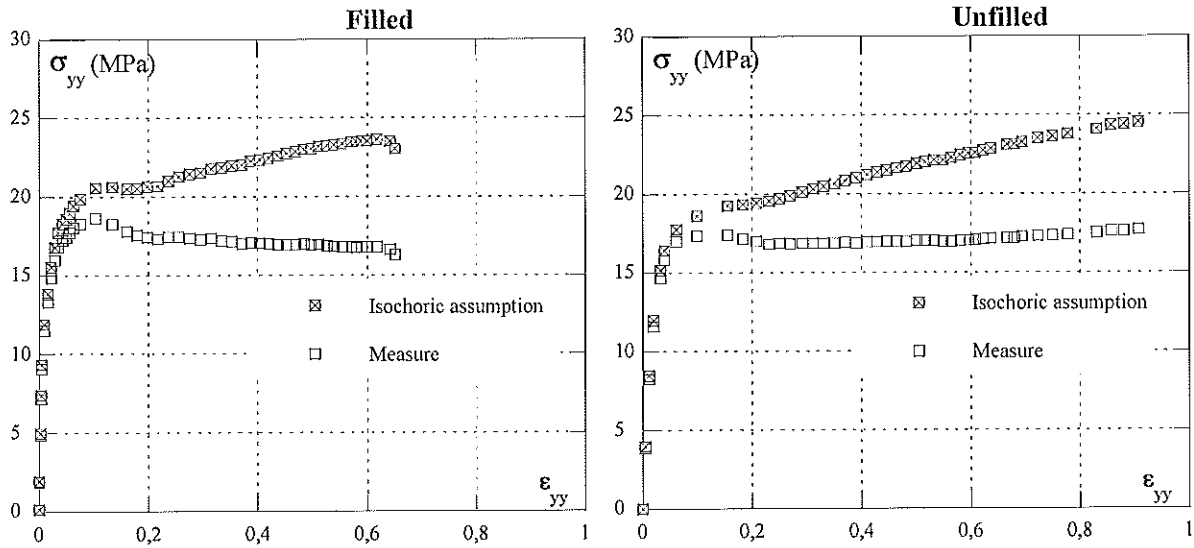


Fig. 4 Effect of isochoric assumption on the mechanical response of unfilled and mineral-filled polypropylenes under uniaxial tension tests performed at an average strain rate of 2 s⁻¹ and at room temperature.

HEAT GENERATION

Plastic deformation coupled to low thermal conductivity of polymers leads, at high strain rates, to an important heat dissipation phenomenon. Moreover, self-heating can disturb apparent mechanical behavior depending on the thermal setting and on the temperature sensitivity of each material [6] [7] [8].

Experimental measurements show significant thermal dissipation during mechanical testing of polymers even at 10⁻² s⁻¹ strain rate (for example [9]). The present study investigates the importance of this phenomenon thanks to an infrared pyrometer having a high sampling rate. Temperature increases during tensile tests are recorded for various strain rates. The corresponding temperature changes are depicted in Fig. 5 for both polypropylenes. Temperature evolution within both polymers is equivalent. Due to a higher ductility, unfilled polypropylene exhibits a higher final temperature. Temperature sensitivity of both materials obeys Arrhenius relationship (equation 1). Thus, the thermal softening can be estimated. One can calculate a kind of isothermal stress (equation 2) that should had been obtained in the case where no dissipation occurred. The disturbance of the apparent mechanical behavior related to heat dissipation is shown in Fig. 6. Softening phenomenon visible on the stress-strain curves of both materials is closely related to thermal effects. It is obvious that temperature rise become noticeable once yield occurs. Then, thermal softening overtakes eventual strain hardening during deformation leading to potential erroneous estimation of constitutive equation.

$$\sigma = \sigma_0 \times \exp\left(\frac{a}{T}\right) \times f(\epsilon, \dot{\epsilon}) \quad (1) \quad \sigma_{\text{isotherm}} = \sigma \times \left(1 + \frac{a}{T^2} \Delta T\right) \quad (2)$$

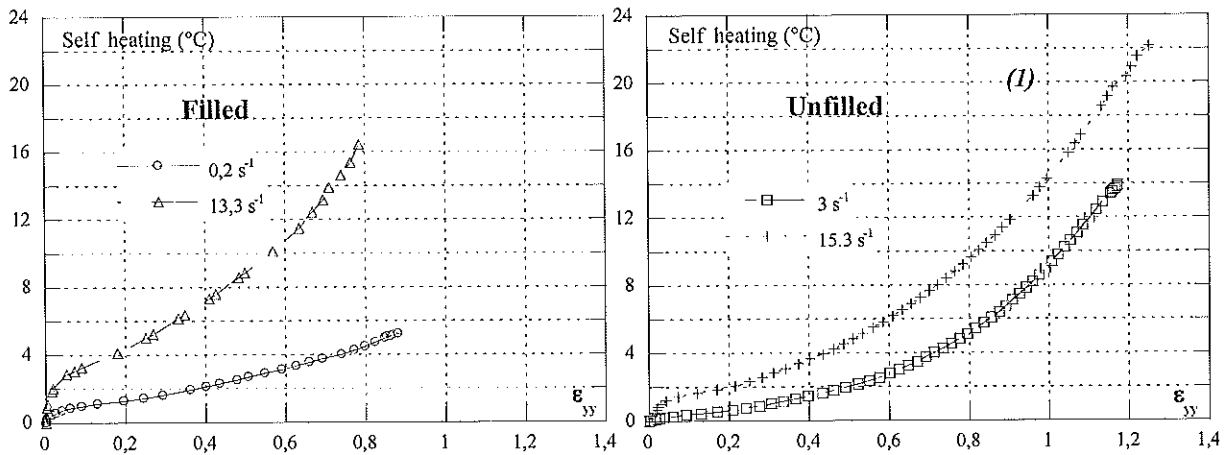


Fig. 5 Self-heating measurements under uniaxial tension tests performed on unfilled and mineral-filled polypropylenes at room temperature.

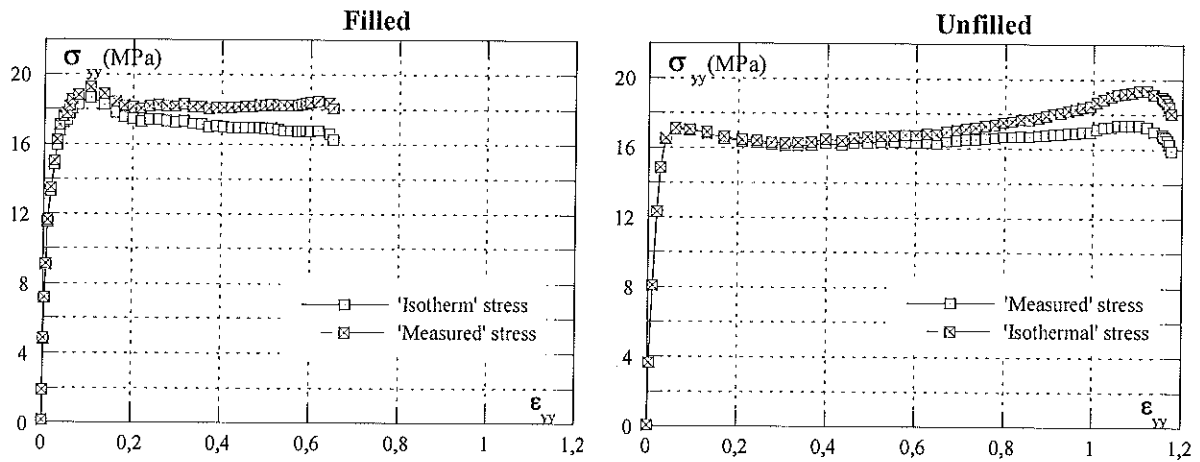


Fig. 6 Effect of self-heating on the mechanical response of unfilled and mineral-filled polypropylenes under uniaxial tension tests performed at an average strain rate of 2 s^{-1} and at room temperature.

STRAIN RATE SENSITIVITY

Tensile stress-strain curves of unfilled and mineral-filled polypropylenes over a wide range of strain rates are shown in Fig. 7. The mechanical behavior of both materials is strongly non-linear even at stresses lower than apparent yield stress. A 15%-stress-softening after yielding is observed. It should be noticed that this decrease corresponds to the intrinsic softening of the polymer as the geometrical effects are avoided by the use of local measurements and as thermal effects have been accounted for. The strain rate sensitivity of these materials appears through the increase of apparent tensile yield stresses (maximum of stress) with strain rates. According to yield stress versus strain-rate curves (Fig. 8), the strain rate sensitivity of both materials is identical and significant.

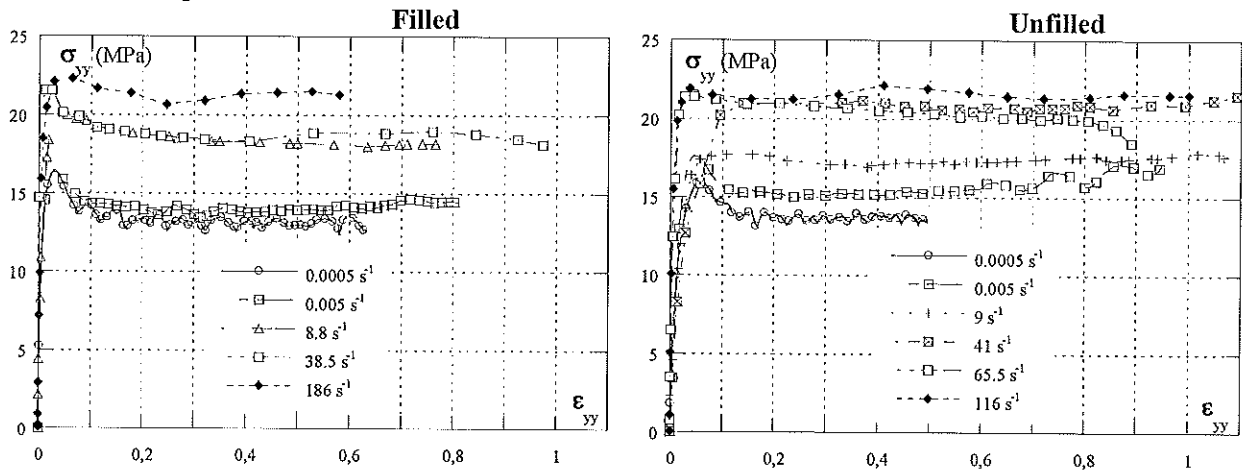


Fig. 7 Mechanical behavior of unfilled and mineral-filled polypropylenes under uniaxial tension tests at room temperature.

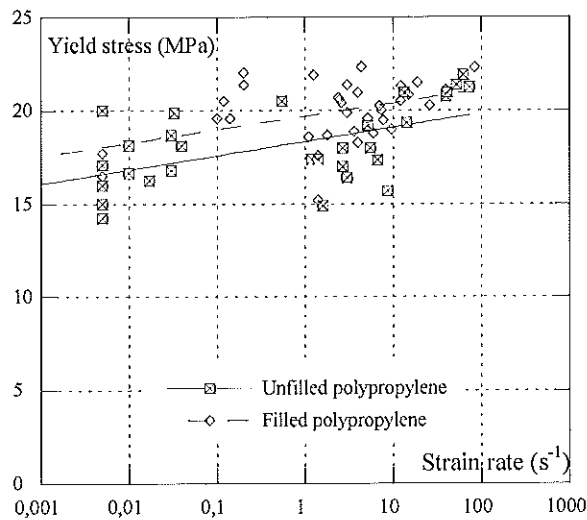


Fig. 8 Effect of strain rate on yield stress under uniaxial tension tests at room temperature.

CONCLUSIONS

An experimental technique was developed for assessing the importance of volume change and self-heating during deformation of solid polymers upon stretching at high strain rates. Based on image correlation and temperature measurements, this technique allowed measuring the three components of strain and the temperature at the sample surface. Thus, the relevance of homogeneity, incompressibility and isothermy assumptions during deformation could be validated.

It must be emphasised that classical isochoric assumption should be avoided. This implies that experimental protocol has to be improved when studying polymer.

The procedure used in this work allowed pertinent characterisation of filled and unfilled polypropylenes. According to detailed examination of the experimental data, the classic theory of plastic instability in polymers, originally established under the simplifying assumptions of isochoric and isotherm deformation, must be revisited to take into account the important effect of volume change and self-heating.

References

- [1] Kinloch A.J. and Young, R.J.; "Fracture behavior of polymers", 5^{ème} édition. London : Chapman & Hall, 1995, 491 p.
- [2] Schirrer R.; "Les craquelures dans les polymères", In : Introduction à la mécanique des polymères 1^{ère} édition, G'Sell C. et Haudin J.M., France, 1995, p.395-404.
- [3] Tie Bi G., "Etudes expérimentales des couplages thermomécaniques par méthodes optiques et par thermographie infrarouge, applications aux polymères". Thèse de Doctorat 2000, Université de Poitiers.
- [4] G'sell C., Hiver J.M., Dahoun A., "Experimental characterisation of deformation damage in solid polymers under tension, and its iteration with necking". International Journal of solids and structures 39 (2002) p.3857-3872.
- [5] Bai S.L., Wang M., "Plastic damage mechanisms of polypropylene/polyamide6/polyethylene-octene elastomer blends under cyclic tension". Polymer 44 (2003) p.6537-6547.
- [6] Rittel D., "An investigation of the heat generated during cyclic loading of two glassy polymers". Mechanics of Materials 32 (2000) p.131-147.
- [7] Billon N., "Effet de couplage thermomécanique dans la caractérisation du comportement de polymères solides". Mécanique & Industries 4 (2003) p.357-364.
- [8] Li Z., Lambros J., "Strain rate effects on the thermomechanical behavior of polymers". International Journal of solids and structures 38 (2001) p.3549-3562.
- [9] Tillier Y. "Identification par analyse inverse du comportement mécanique des polymères solides ; applications aux sollicitations multiaxiales et rapides". Thèse de Doctorat 1998, Ecole des Mines de Paris.

IDENTIFICATION OF FOAM BEHAVIOR UNDER DYNAMIC LOADING BY THE USE OF PARTICLE IMAGING TECHNIQUES

Philippe Viot, Pierre Vacher*

*LAMEFIP, ENSAM de Bordeaux
Esplanade des arts et métiers, 33405 Talence Cedex France
*LMECA ESIA
Domaine Universitaire, BP 806, 74016 Annecy Cedex France*

Summary : Structures used in impact-absorbing applications have to be modelled in order to improve the mechanical performances of these applications. This approach requires the characterisation of the whole of the structure materials and particularly foams used to absorb shock energy. The identification of foam behaviour by high strain rate tests is necessary in order to identify parameters of rheological models commonly implemented in FE code. For this study, tests were achieved on polypropylene foams under high strain rate compression loading. The material behaviour has been determined as a function of two parameters, density and strain rate. Samples (at several values of volumic mass 70, 80, 90 and 100 Kg/m³) were impacted on a fly wheel. A new mechanical device was developed on the fly wheel in order to achieve stopped compression tests on foam sample. This test consists in compressing the sample by a hammer fixed on the metallic wheel (diameter 1 m, mass 617 kg) turning at high speed. When the compressive force reaches a threshold value, a mechanical fusible is sheared and the compression device is ejected, the test is stopped. With this testing machine, the dynamic compressive behaviour has been evaluated in the strain rate up 100 s⁻¹.

During these tests, force and hammer displacement are measured as a function of time. These data enable to calculate the stress-strain responses of polypropylene foam sample which were finally defined as a function of density and strain rate. Typical result curve shows three regimes: an elastic behaviour followed in a second step by a stress plateau and finally, a phase corresponding to foam densification.

However, the foam structure being complex, it was necessary to study with finesse displacement and strain field during impact in order to better understand the foam behaviour. Gage measurements can not be used on this porous material, therefore, particle imaging techniques are more relevant. These methods enabled to obtain information on the strain field (with picture correlation techniques). The first difficulty has been to film high quality pictures of foam sample during dynamic compression. The pictures analysis shows strong strain localizations which reveal local damage of the structure.

INTRODUCTION

Polypropylene foams are used in passive safety applications such as electronic material packing, helmet... In order to improve the performances of these products, they have to be modelled in dynamic. The numerical simulation requires the behaviour identification of materials used in these structures. The objective of this work was the characterization of the polypropylene foam in dynamic compression.

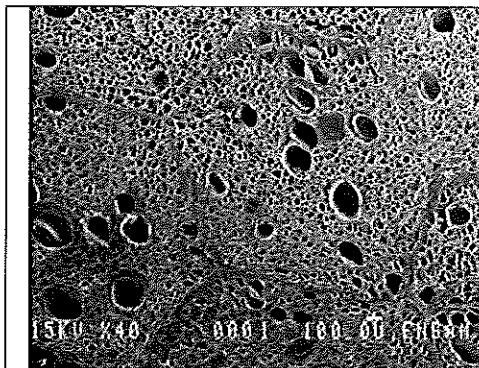


Figure 1a : micrography of polypropylene foam showing grain structure

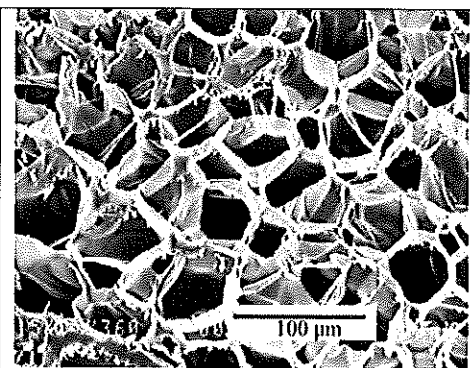


Figure 1b : micrography of polypropylene foam showing closed cells

The studied foams consist of glued macroscopic grains with the size varies between 2 and 3 mm (figure 1a). The grain structure is constituted by small closed cells organized in a random way (figure 1b). The cells size is non-uniform (diameter 60 μm, wall thickness lower than 1μm) and the structure does not present particular orientation.

During a static compression (axis y), the evolution of the stress σ_{yy} as a function of strain ϵ_{yy} includes three behaviour steps, a linear elastic response, next a plastic behaviour characterized by a plateau stress σ_{pl} followed by a densification phase [1]. Furthermore, first tests achieved on electromechanical testing machine, at low strain rate, have shown the great heterogeneity of strain ϵ_{yy} . Collapse starts in a sample layer and is propagated near this initial zone.

If the layer position is random, the stress threshold σ_{pl} to obtain the beginning of the ruin is a characteristic parameter of material behaviour and depends on foam density as well as imposed strain rate during the test.

Two experimental devices were used in order to study the influence of these two parameters on the foam behaviour and particularly to estimate the plateau stress evolution : an electromechanical testing machine MTS (maximum force 100 kN) used for lower strain rate and a new compression device fixed on a fly wheel (used to obtain displacement speeds higher than 1m/s) . Lastly, test films obtained with a high speed cam were analysed by image correlation techniques to visualize strain field during the compression.

DYNAMIC COMPRESSION DEVICE

Fly wheel (figure 2) is a shock generator machine developed at the laboratory LAMEFIP (see Lopez [2]), It consists in a wheel (diameter 1m, mass 617 kg, inertia moment 77 kg.m²) carrying a hammer and putted in rotation by an asynchronous motor. So, the rotation velocity can be controlled precisely during the test. This device was initially designed to carry out dynamic tensile tests on light metal alloys. The pendular system (figure 3) is in pivoting joint with the mounting and is operated by a pneumatic jack. When the hammer is detected by an optical sensor, the jack pushes the pendular system against the wheel and the anvil fixed at the low end of the sample is then grabbed by the hammer [3].

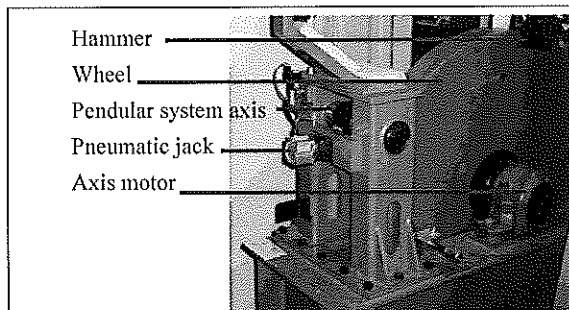


Figure 2 : fly wheel

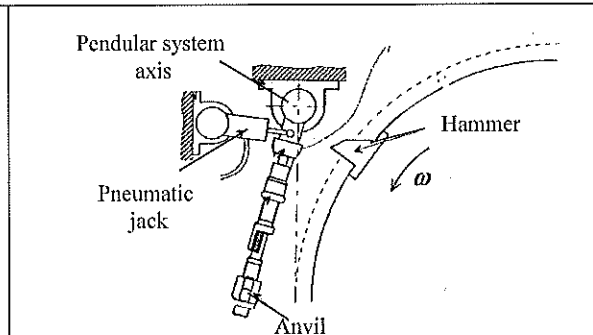


Figure 3 : Diagram of the pendular device

This device was modified to be able to carry out dynamic compressions. A new mechanical device was designed in order to achieve stopped dynamic compression tests on polymeric foam [4]. With it, the uni-axial pressing of a sample can be stopped with a predetermined loading for two mainly reasons : it is interesting to visualize the shape of foam sample after the test (for a rate of damage) and it is also necessary to limit the maximum effort of compression to avoid any damage on the parts of the testing apparatus.

The new device includes two subsets (figure 4) : the module of compression and the positioning module. This last one consists of tubular parts assembled by threading to adjust the position of the sample. Moreover, one tube (A) is instrumented by 4 gauges to determine only the compressive force. The compression module consists of an anvil (B) and a compression block (C). The anvil is guided in translation by tube (A) and the compression block (C) is fixed on the same tube (A) via a fusible pin (D). The foam sample is compressed between these two parts. During the test, the anvil is grabbed by the wheel hammer and compresses the sample on the lower plate. When the compressive force reaches a threshold value, the fusible pin is sheared and the subset of compression is ejected. The pin is out of polycarbonate, two diameters (8 and 10 mm) are used to reach two maximum values of compression (3000 and 4500 N).

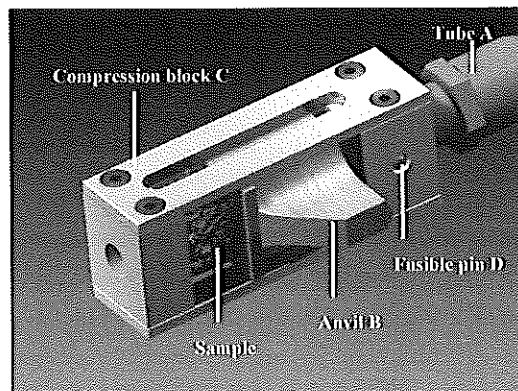


Figure 4 : scheme of the compression device

The measured parameters are the force F and the rotation speed ω of the wheel. The force $F(t)$ is estimated from the measurement of the deformation of tube (A) equipped with strain gauges. Calibration of this sensor enables to obtain the relation between the effort applied and the measurement of the gauges bridge stuck on the tube. At the instant t , the stress $\sigma(t)$ applied to the sample is calculated by dividing the force $F(t)$ by the area $S(t)$. On this device, it is very delicate to measure with precision the evolution of the section during dynamic loading. However, works of Gibson and Ashby [1], Zhang [5] and Avalle [6] showed that the Poisson's ratio of a polymeric foam can be considered as null. One can thus estimate the stress $\sigma(t)$ from the initial surface $S(t_0)$.

At macroscopic scale, the strain ϵ and strain rate $\dot{\epsilon}$ are calculated from the rotation speed ω and the instantaneous height of the sample h . At one instant t , there is:

$$\epsilon \approx \ln\left(\frac{h}{h_0}\right) = \ln\left(\frac{h_0 - R\omega t}{h_0}\right). \quad (1)$$

With R the radius of the wheel and h_0 the initial height of the sample.

RESULTS

The foam behaviour has been identified at different strain rates with the conventional testing machine (at three speed of upper punch : 1 mm/min, 100 mm/min and 500 mm/min) and with the fly wheel by imposing several impact speeds (1 m/s, 2.5 m/s and 5 m/s). So, the compressive behaviour has been evaluated in the strain rate from $6,7.10^{-4} \text{ s}^{-1}$ up to 100 s^{-1} . The volumic mass of tested polypropylene foam was 70, 80, 90 and 100 Kg/m^3 .

Influence of the foam density

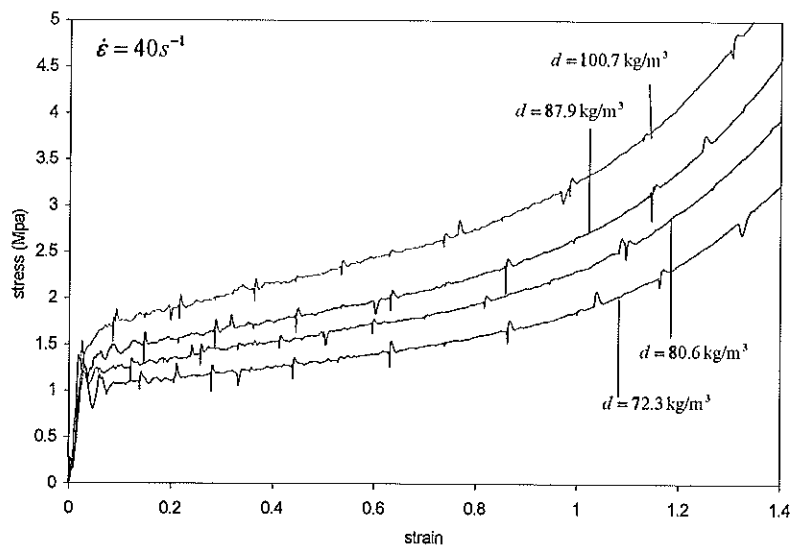


Figure 5 : stress – strain responses for four densities – flywheel.

The effect of the parameter density on the foam behaviour has been evaluated at different strain rate. Results presented figure 5 - for an impact speed of 1m/s corresponding to a initial strain rate $\dot{\epsilon} = 40 \text{ s}^{-1}$ - are representative of the whole of the tests obtained on the flywheel. These curves, obtained on two different testing machines, present a similar evolution. Anyway, it appears that the increase in density involves a rise in the plateau stress σ_{pl} .

It is more difficult to evaluate the influence of density on the Young modulus. The dynamic compression device was designed to measure the uni-axial stress as a function of large strain of the porous material. Complementary tests have to be defined to identify with precision the elastic behaviour of foam by adding an optical dynamic extensometer on the compression device. Moreover, the results obtained on the press seem to validate the observations of Gibson and Ashby [1] who detect a rise in the Young modulus with the density. One notes that curves obtained with the fly wheel present a cyclic perturbations. Preliminary tests had shown that it was due to the electromagnetic noise generated by the asynchronous motor.

Influence of the strain rate

The influence of the strain rate on the material behaviour was studied on samples (of same density) by using the two testing machine. Figure 6 shows the stress – strain curves of the tests carried out on samples of density 90 kg/m^3 and reveals an increase in the plateau stress with the rise in strain rate. This influence is verified for the four densities.

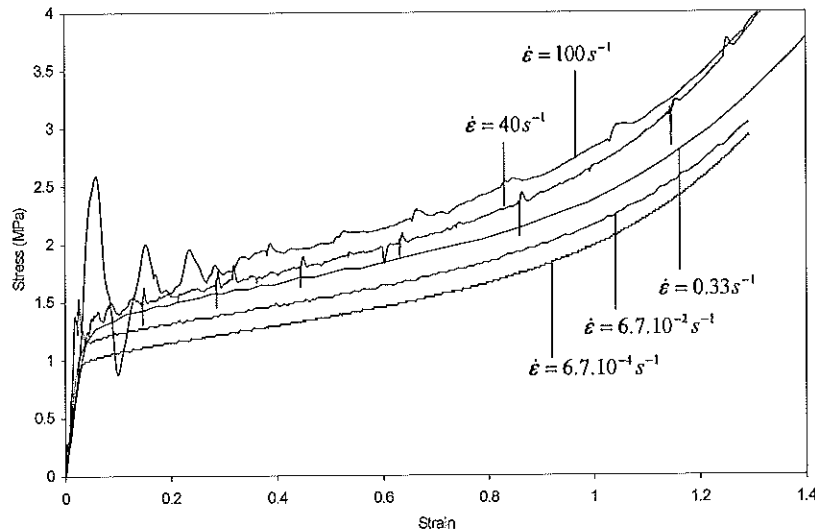


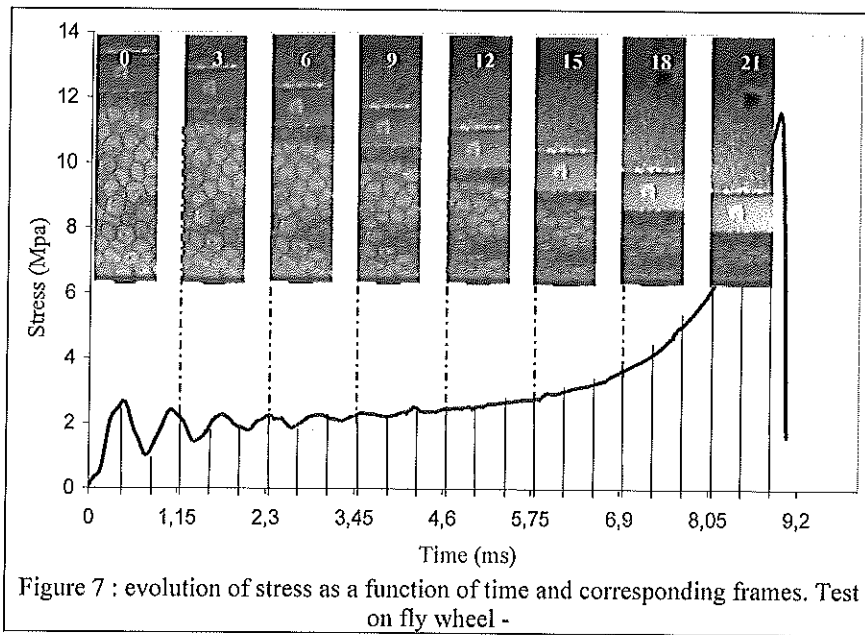
Figure 6 : stress – strain curves for five strain rates. Volumic mass : 90 kg / m^3

Curves obtained from fly wheel tests (at speed higher than 100 s^{-1}) have strong oscillations at the beginning of the compression. This phenomenon, inherent in impact loading and already observed on other machines such as falling towers, is due to the propagation of the shock wave in the test device (sample and machine). The tests carried out with the flywheel, at strain rate of 200 s^{-1} and more, have oscillations such as it is difficult to obtain the value of the plateau stress. This device is now improved in order to reduce these oscillations and to evaluate the foam behaviour at higher strain rate

High speed video device

To the compression mechanical device was added a high speed colour camera Phantom V4 which the maximum resolution is 512×512 pixels (at 1000 images per second, coded in 10 bits). For these tests, the speed setting was of 2600 frames per second and the resolution was of 128×512 pixels. The main difficulty of this video recording lies in the good adjustments of several settings (depth of field, obturation time, lighting...) to obtain clearest images of foam sample compressed inside the pendular device –thus mobile during the test-. The whole of settings was adjust when the fly wheel is stopped and with the compression pendular in impact position (against the wheel).

Exposition time being of $167 \mu\text{s}$, (to avoid blur due to the deformation and displacement of the sample), a power lighting of the dark polypropylene foam was necessary : two projectors (1500 Watts each one) and two additional spots with optical fibre were installed in order to obtain a homogeneous luminosity and the better contrast. This high lighting power was necessary to obtain a sufficient depth of field with a very weak exposition time. The whole of the spots is switch on just before the compression in order to limit the increase in temperature of the sample.



The high speed cam enables to obtain 24 frames during the impact loading (figure 7). The first image (number 0 on figure 7) corresponds at the uncompressed state of material. The second image is taken roughly at the end of the elastic phase, if one refers to the stress curve as a function of. So, from image 3 to image 18, one can visualize the deformation state of sample during the plastic plateau. On these images, it is easy to identify the zone where the damage started (darker zone closed to the sample center). A strong localization of the deformations is visible in this area, whereas the polypropylene grains located in the higher part of sample does not seem deformed. The use of images correlation technique achieved to verify these first visual remarks [6],[7].

Evaluation of strain field

The strain field ϵ_{yy} (along the compression axis y) is calculated by image correlation techniques between two successive frames. The video speed setting being of 2600 images per second, the calculated strain corresponds to the variation of sample deformation state during 384 μ s. The strain cartographies ϵ_{yy} (figure 8) are the results of these calculations at different steps of compression; These maps completed by the stress- strain curves of the figure 5 and 6 enable to better understand the foam behaviour and to describe the collapse mechanisms.

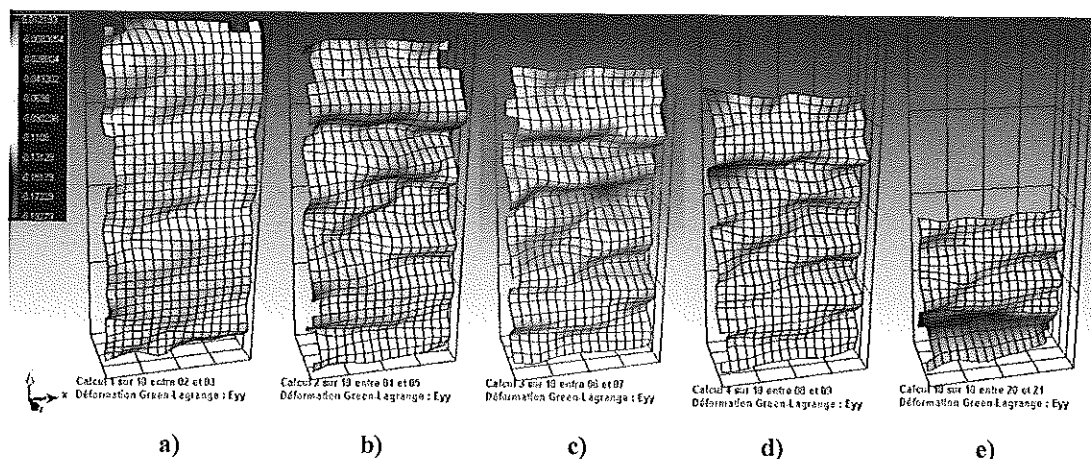


Figure 8 : Strain field ϵ_{yy} during compression test

The strain field ϵ_{yy} (figure 8a) is calculated during the initial step, when the material behaviour is still elastic, the strain seems homogeneous. The figure 8b shows the state of strain calculated at the beginning of plateau plastic. Layers where ϵ_{yy} is high appear clearly. The material damage –mainly by buckling of the foam cells walls- is localised on these layers.

On the whole of the dynamic compression tests, the direction of these collapse layers is usually perpendicular to the direction of loading - in the case of quasi static compression (or at low strain rate) , this remark can not be establish , the bands orientation seems random -.

The damage goes on near these horizontal bands (figure 8c and 8d) and the strain gradient is less marked. Hence, during the densification (figure 8e), the state of strain becomes again more homogeneous. Foam is completely compressed, the whole of foam cells are crushed, and the foam behaviour tends towards the one of dense material.

CONCLUSION

The new dynamic compression device installed on the fly wheel enables to estimate the evolution of the axial stress as a function of imposed axial strain. The tests carried out on electromechanical testing machine and fly wheel have shown effects of strain rate and foam density on the expanded polypropylene behaviour. More precisely, it was observed that a higher density involves an increase in the plateau stress. The influence of the strain rate on this plastic stress threshold was also highlighted.

This macroscopic mechanic study was completed by the analyse of images correlation obtained during the compression with a high speed cam. The numerical treatment of these images enables to show the evolution of the state of strain and reveals the damage mechanisms. In dynamic loading, collapse is initiated brutally in a fine layer perpendicular to the direction of compression, the damage is propagated from this band. These optical measurements also showed the strong gradients of deformation which appear by layers during compression.

This experimental study shows that the usual presentation of expanded material performances in the form of stress-strain curves is insufficient; it is necessary to identify more finely stress and strain fields. The final objective of this research is the effect evaluation of the foam structure on the material behaviour.

References

- [1] Gibson L. and Ashby F. : « Cellular solids. Structures and properties », Edition : Cambridge Solid State Science Series, 1988
- [2] J.M. Lopez « Conception et réalisation d'une machine à choc pour l'étude de la déchirure à grandes vitesses de tôle en composites ». mémoire de diplôme d'ingénieur du Centre National des Arts et Métiers. 1992.
- [3] M. Lambert and al. "high strain rate testing of aluminium alloy and high speed photography", dymat 2003, Porto
- [4] P. Viot, F. Beani. "Polypropylene Foam behavior under compressive loading at high strain rate" 8e international conference on structures undershock and impact, Crete, Greece, 2004.
- [5] : Zhang J., Kikuchi N., Li V., Yee A. Nuscholtz G. : « Constitutive modeling of polymeric foam material subjected to dynamic crash loading ». International Journal of Impact Engineering, vol.21. 1998.
- [6] M. Avalle and al. "characterization of polymeric structural foam under compressive impact loading by means of energy absorption diagram". International journal of Impact Engineering, vol 25 455- 472 2001.
- [7] P.Viot, A. Vagnon, P. Vacher. "Identification du comportement viscoplastique de matériaux poreux par analyse d'image" Journée scientifique AFM "Identification des propriétés mécaniques de matériaux et de structures à partir de mesures de champs » 29 avril 2002, Clermont Ferrand.
- [8] Vacher, Dumoulin, Morestin, Mguil-Touchal. « Bidimensional deformation measurement using digital images ». Proc instr. Mech. Engrs, vol. 213, part C ImechE (1999)

ON THE DYNAMIC FRAGMENTATION OF A HIGH-PERFORMANCE CONCRETE

Pascal Forquin, François Hild* and Laurent Rota

DGA/CTA-Département MSP, 16 bis avenue Prieur de la Côte d'Or, F-94114 Arcueil Cedex, France

*LMT-Cachan, ENS de Cachan / CNRS-UMR 8535 / Université Paris 6, 61 avenue du Président Wilson, F-94235 Cachan Cedex, France

Summary: The degradation and failure of a high-performance concrete is analyzed. The main emphasis is put on the discrimination between discrete and continuum approaches to describe damage and fracture. The derived model is used to analyze the fragmentation of a high-performance concrete impacted by an aluminum projectile.

SINGLE AND MULTIPLE FRAGMENTATION OF A HIGH PERFORMANCE CONCRETE

High performance concrete is analyzed in the sequel. This material (powder reaction concrete, commercial name: DUCTAL[®]) has a very fine microstructure made of components of different sizes (Fig. 1a), namely, fine quartz sand aggregates, cement, crushed quartz and silica fume [1]. For the sake of simplicity, the results reported herein only concern fiber-free matrices for which a high compressive strength can be achieved but with a ductility comparable to conventional mortar. These materials can achieve values of the order of -200 MPa to -800 MPa in uniaxial compression [2], and when reinforced by fibers the ductility is significantly increased. A residual porosity of the order of 2% is obtained in the present case (i.e., when containing short fibers, the compressive strength is equal to -200 MPa). The latter is the likely cause of failure in three-point flexure experiments (Fig. 1b).

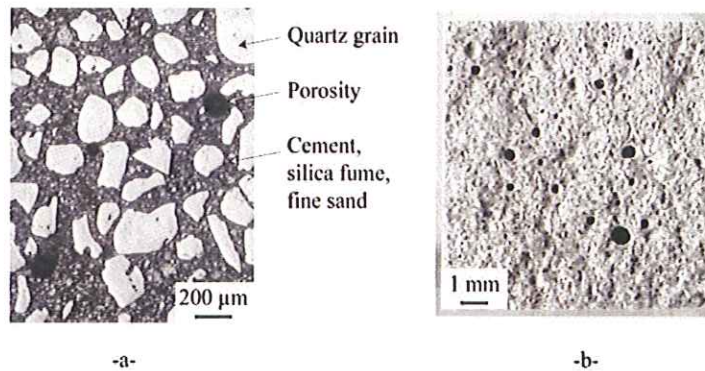


Fig. 1. a- Microstructure of the high performance concrete studied herein. b- Fractured surface after a three-point flexural test.

Under quasi-static loading condition, the behavior is elastic-brittle and the failure stress is scattered. A weakest link hypothesis can be made [3] and a Weibull model [4,5] is used to fit experimental data

$$P_F = 1 - \exp \left[-Z_{eff} \lambda_l(\sigma_F) \right] \text{ with } \lambda_l(\sigma_F) = \lambda_0 \left(\frac{\sigma_F}{\sigma_0} \right)^m \quad (1)$$

where P_F denotes the failure probability, σ_F the failure stress (i.e., the maximum value of any suitable equivalent stress), Z_{eff} the effective volume, surface or length [6], λ_l the corresponding defect density, m the Weibull modulus,

σ_0 a scale parameter relative to a reference density λ_0 . The constant σ_0^m / λ_0 is the Weibull scale parameter. In the following, when no special mention is made, the development is valid for any space dimension n (i.e., 1, 2 or 3). Otherwise, it will be clearly stated for which space dimension the results are valid. 18 experiments on samples of size $11.2 \times 10.2 \times 150 \text{ mm}^3$ submitted to three-point flexure (outer span: 130 mm) were performed. A Weibull modulus of 9.5 is obtained and $\sigma_0 = 23 \text{ MPa}$ when $1/\lambda_0 = 59 \text{ mm}^3$ (i.e., identical to the effective volume).

Tensile cracking, one of the major degradation mechanisms during impact, can be observed by using so-called Edge-On Impact (EOI) configurations instead of a real configuration where the degradation is 'hidden' in the bulk of the material. These configurations are developed by the Ernst-Mach-Institute (EMI) in Germany [7,8] and more recently by the Centre Technique d'Arcueil (CTA) in France [9,10]. It can be shown that the same damage mechanism (i.e., damage in tension) is observed in EOI and in real impact configurations [11]. To avoid damage induced by the compressive wave close to the impact zone, a special EOI setup is used (Fig. 2). It consists in creating an additional dynamic confinement obtained by using a steel ring containing a tungsten cylinder whose radius is greater than that of the projectile.

This system creates an additional confinement during 12 μ s (i.e., time duration for the wave to propagate back and forth in the steel ring) that prevents damage to develop in these zones by increasing the hydrostatic stress and reducing the deviatoric stress (i.e., less than 240 MPa for a distance greater than 12 mm from the impact point) to levels below the threshold of damage under confined conditions (i.e., of the order of 400 MPa). When using a 2024 aluminum alloy projectile, this setup allows one to analyze fragmentation with no prior confined damage (i.e., hoop stresses greater than 35 MPa for a distance less than 80 mm from the impact point). Figure 3 shows a post-mortem observation when the tile is put in a sarcophagus to prevent the fragments to move too much. In this configuration, a blunt projectile (20 mm in diameter and 50 mm in length) impacts at 88 m/s a concrete plate of size 300 x 150 x 10 mm³. After impact, the tile is coated in an epoxy resin and polished for macroscopic (and microscopic) analyses.

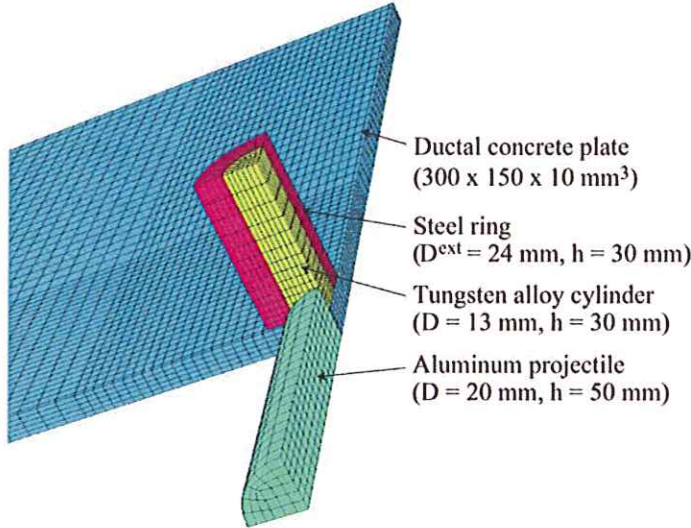


Fig. 2. One quarter of an edge-on impact configuration with dynamic confinement.

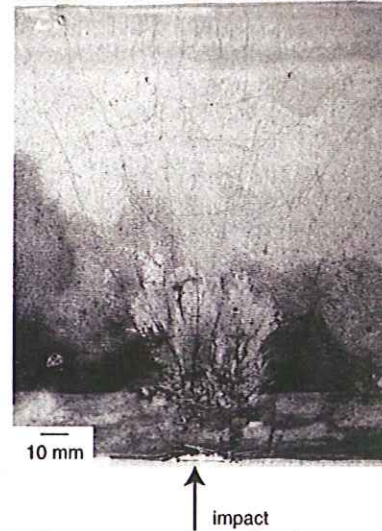


Fig. 3. Post-mortem view of an impacted high performance concrete tile.

FRAGMENTATION MODEL

When a dynamic fracture is initiated in mode I, the local stress state is modified around the crack by a stress relief wave which is a complex function of time, crack velocity and stress wave celerity. To understand why a crack nucleates, one has to model the interaction of the zone (i.e., volume, surface or length) affected by the stress relief and other defects that would nucleate. The behavior of a flaw around a nucleated crack can be described by two different cases: namely, the flaw is far from the nucleated one and the microscopic stress state is not affected, the flaw is in the interaction zone and the microscopic tensile stress is decreasing, i.e., no cracks are emanating from this potential initiation site. A third case may occur in which the flaw is in the affected zone but the local tensile stress increases, i.e., initiation may occur. It is assumed that this case is insignificant in this problem. The direction of the microscopic maximum principal stress is assumed to be constant (i.e., proportional loadings), which allows one to use $\sigma = (\sigma_1, \sigma_2, \sigma_3)$ instead of the stress tensor as an equivalent failure stress. The flaw distribution can be split into two parts and the average density of cracks can be written as

$$\lambda_b(\sigma) = \lambda_t(\sigma) - \lambda_{obs}(\sigma) \quad (2)$$

where $Z\lambda_t(\sigma)$ denotes the mean number of flaws that may break in a zone of measure Z (i.e., volume ($n = 3$), surface ($n = 2$) or length ($n = 1$)) for a stress less than or equal to σ . The subscripts indicate the crack density (b), the obscured flaw (obs), and the total density of flaws able to break (t). Furthermore, we assume that the distribution of total flaws is modeled by a Poisson point process of intensity λ_t . New cracks will initiate only if the defect exists in the considered zone and if no cracks exist in its horizon so that [12]

$$\frac{d\lambda_b}{dt}(T) = \frac{d\lambda_t}{dt}(T) [1 - P_o(T)] \text{ with } \lambda_b(0) = 0 \quad (3)$$

where $1 - P_o$ is the probability that no cracks exist in the horizon. The variable $1 - P_o$ can be split into an infinity of events defined by the probability of finding at t a new crack during a time step dt in an obscuration zone $\Omega_o(T - t)$. This probability increment is written by using a Poisson point process of intensity $d\lambda_t / dt$. Those independent events can be used to provide an expression for P_o

$$P_o(T) = 1 - \exp\left(-\int_0^T \frac{d\lambda_t}{dt}(t) Z_o(T-t) dt\right) \quad (4)$$

where $Z_o(T-t)$ is the measure of the obscuration zone at T for a defect that would break at t . At the beginning of loading, no interactions occur and $\lambda_b(T) \approx \lambda_t(T)$ and as more and more cracks nucleate $\lambda_b(T) \ll \lambda_t(T)$. It is expected that the crack density saturates when $T \rightarrow +\infty$ even though the total density of flaws able to break may approach infinity. Usually, the obscuration zone cannot be assumed as a time-constant variable and since no analytical expressions are available for $Z_o(T-t)$, an approximation will be proposed. The shape of the interaction zone is supposed to be constant, i.e., all the interaction zones are self-similar [13,14] and $Z_o(T-t)$ can be written as

$$Z_o(T-t) = S [C(kC-t)]^{-n} \quad (5)$$

where S is a shape parameter, $k \in]0,1[$ is a constant, C the longitudinal stress wave velocity so that $kC(T-t)$ is a representative length of the relaxation zone around a crack.

When dynamic loadings are considered with a constant stress rate $\dot{\sigma}$ one can define a dimensionless flaw density ($\tilde{\lambda} = \lambda/\lambda_c$), time ($\tilde{T} = T/t_c$), space measure ($\tilde{Z} = Z/Z_c$) and stress ($\tilde{\sigma} = \sigma/\sigma_c$) from the condition

$$\lambda_c Z_c = 1 \text{ with } \lambda_c = \lambda_c(t_c) \text{ and } Z_c = Z_o(t_c), \quad t_c = \left(\frac{\sigma_0^m}{\lambda_0 \dot{\sigma}^m S (kC)^n}\right)^{1/m+n}, \quad Z_c = \left(\frac{\sigma_0 (kC) S^{1/n}}{\lambda_0^{1/m} \dot{\sigma}}\right)^{mm/m+n} \quad (6)$$

where the subscript c denotes characteristic quantities. A characteristic stress can be defined by $\sigma_c = \dot{\sigma} t_c$. Equation (6) expresses the fact that the characteristic zone of measure Z_c contains a unique flaw that may break at the characteristic time t_c . By using Eqs. (1), (4) and (5) an analytical solution is given for the differential equation (3) in the case of a constant stress rate $\dot{\sigma}$

$$\tilde{\lambda}_b(\tilde{T}) = \frac{m}{m+n} \left[\frac{(m+n)!}{m!n!} \right]^{m+n} \gamma\left(\frac{m}{m+n}, \frac{m!n!}{(m+n)!} \tilde{T}^{m+n}\right) \quad (7)$$

where γ is the incomplete gamma function. The crack density at saturation $\tilde{\lambda}_b(\infty)$ can be derived from Eq. (7) and is only dependent on the Weibull modulus m and the space dimension n when normalized by λ_c .

DAMAGE MODEL

The variable P_o can be used to define a damage variable in the framework of Continuum Damage Mechanics, even if P_o describes a non-homogeneous stress-field due to the randomness of fragmentation [15]. By averaging over a representative zone (to be specified later on), P_o is equal to the damage variable D , with $D = 0$ for the virgin material and $D = 1$ for the fully broken one. It is interesting to notice that the first order approximation of Eq. (3) leads to the differential equation proposed by Grady and Kipp [16] to describe the kinetics of a damage variable. By using Eqs. (4) and (5), the kinetic law of the damage variable D can be written as

$$\frac{d^{n-1}}{dt^{n-1}} \left(\frac{1}{1-D} \frac{dD}{dt} \right) = \lambda_t [F(t)]^{-n} S (kC)^n. \quad (8)$$

An expression for the damage parameter D can be derived by integrating Eq. (8) for a constant stress rate $\dot{\sigma}$

$$D = 1 - \exp\left(-\frac{m!n!}{(m+n)!} \tilde{T}^{m+n}\right). \quad (9)$$

Equation (9) shows that $D(\tilde{T}=1) \approx 0$ and $D(\tilde{T}=2) \approx 1$ (i.e., most of the damage change occurs during a time interval equal to the characteristic time t_c). During t_c , the measure of the horizon is limited by Z_c so that the *minimum* measure of the representative zone is Z_c . By noting that the applied stress $\bar{\sigma}$ is related to the local (or effective) stress σ by $\sigma = \bar{\sigma}/(1-D)$, the ultimate strength ($d\bar{\sigma}/d\sigma = 0$) is denoted by $\bar{\sigma}_{\max}$ and is expressed as

$$\frac{\bar{\sigma}_{\max}}{\sigma_c} = \left(\frac{(m+n-1)!}{e m!n!} \right)^{1/m+n} \quad (10)$$

The normalized ultimate strength only depends upon the Weibull parameter m and the space dimension n . The ultimate strength $\bar{\sigma}_{\max}$ is then proportional to $\dot{\sigma}^{n/(m+n)}$. This result is in agreement with experimental data of oil shale [16] and microconcrete [17,18].

DISCRETE VS. CONTINUUM APPROACH, PROBABILISTIC VS. DETERMINISTIC DESCRIPTION

Different failure regimes are observed. Under quasi-static loading conditions, a weakest link hypothesis is made. It follows that the first fracture event leads to the complete failure of a structure made of brittle materials. Conversely, under dynamic loading conditions, multiple fragmentation is observed and a damage model can be derived. The aim of the present section is to get the conditions of applications of the previous results. Figure 4 shows the change of the tensile strength with the stress rate for an effective volume V_{eff} ($n=3$) equal to $1/\lambda_0$. The lines represent analytical solutions while the dots and error bars are Monte-Carlo simulations (500 realizations per point). For a dimensionless stress rate less than 0.5, the ultimate strength is not modified by the loading rate and follows a classical Weibull model [see Eqn. (1)]. When $\dot{\sigma}$ increases by approximately one order of magnitude, the ultimate strength follows the analytical solution (10). The standard deviation significantly decreases in the multiple fragmentation regime. Even if the ultimate strength has to be defined for static and dynamic loadings by a mean and a standard deviation, one can see that dynamic loadings lead to a more ‘deterministic’ behavior.

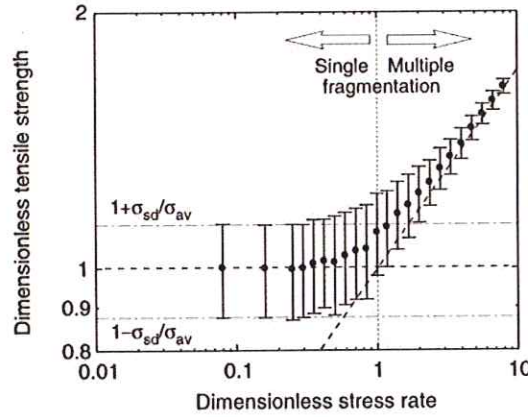


Fig. 4. Normalized tensile strength $\sigma_{ts} / \sigma_{av}$ vs. normalized stress rate $\dot{\sigma} / \dot{\sigma}_t$ when $m = 10$. Solid circles (average) and bars (standard deviates) are given by the Monte-Carlo simulations (500 realizations for each point).

The transition between single and multiple fragmentation can be estimated by the following condition [19]

$$\sigma_{av} = \bar{\sigma}_{\max}(\dot{\sigma}) \quad \text{with} \quad \sigma_{av} = \sigma_0 \left(Z_{eff} \lambda_0 \right)^{1/m} \Gamma \left(1 + \frac{1}{m} \right) \quad (11)$$

The transition between quasi-static and dynamic descriptions defined by Eq. (11) leads to the following inequalities

$$\dot{\sigma} \begin{cases} < \dot{\sigma}_t & \text{single fragmentation} \\ \geq \dot{\sigma}_t & \text{multiple fragmentation} \end{cases} \quad (12)$$

with the transition stress rate $\dot{\sigma}_t$ defined by

$$\dot{\sigma}_t = \sigma_0 k C (\lambda_0 S)^{1/n} (Z_{eff} \lambda_0)^{(m+n)/mn} \left(\frac{e n! m!}{(m+n-1)!} \Gamma^{m+n} \left(\frac{m+1}{m} \right) \right)^{1/n} \quad (13)$$

This transition does not only depend on material parameters but also involves the measure Z_{eff} of the considered element. The response of a large structure can be considered as ‘dynamic’ for low stress rates even if the material follows a weakest link hypothesis for the same loading applied on a smaller volume.

For each principal stress direction \underline{d}_i , an anisotropic damage variable D_i is defined so that the principle strains $\bar{\epsilon}_i$ are related to the principal stresses $\bar{\sigma}_i$ by

$$\bar{\epsilon}_i = \bar{K}_{ij}(D_1, D_2, D_3) \bar{\sigma}_j \quad (14)$$

where the usual index summation is used. The compliance tensor \bar{K} is defined by

$$\underline{\underline{K}}(D_1, D_2, D_3) = \frac{1}{E} \begin{pmatrix} \frac{1}{1-D_1} & -\nu & -\nu \\ -\nu & \frac{1}{1-D_2} & -\nu \\ -\nu & -\nu & \frac{1}{1-D_3} \end{pmatrix}_{(d_1, d_2, d_3)} \quad (15)$$

where E is the Young's modulus and ν the Poisson's ratio of the undamaged material. In 3D configurations ($n = 3$), the kinetic law for D_i is expressed in a differential form [see Eq. (8)]

$$\frac{d^2}{dt^2} \left(\frac{1}{1-D_i} \frac{dD_i}{dt} \right) = 6\hat{\lambda}_i(\sigma_i) S(kC)^3 \quad (16)$$

when $\sigma_i > 0$ and $\dot{\sigma}_i > 0$ (the effective principal stress σ_i is related to the macroscopic principal stress $\bar{\sigma}_i$ by $\bar{K}_{ij}(D_1, D_2, D_3)\bar{\sigma}_j = \bar{K}_{ij}(0,0,0)\sigma_j$). The defect density $\hat{\lambda}_i$ associated with the Weibull model is defined so that the damage model is used only if at least one defect is broken in the considered finite element Ω_{FE} of volume V_{FE} [20]

$$V_{FE}\hat{\lambda}_i(\sigma_i) = \begin{cases} 0 & \text{if } \sigma_i < \sigma_k \\ \max \left[V_{FE}\lambda_0 \left(\frac{\sigma_i}{\sigma_0} \right)^m, 1 \right] & \text{otherwise} \end{cases} \quad (17)$$

where σ_k a random failure stress obeying the Weibull law (1). For low stress rates, the first defect breaks and relaxes the stresses in Ω_{FE} . It follows that the quasi-static Weibull properties are recovered. For a high (tensile) stress rate, the zone relaxed by the first defect to break has a weak influence and a deterministic (damage) approach applies. The behavior of a FE cell is therefore not deterministic and numerous calculations have to be performed when average values are awaited [e.g., average macroscopic ultimate stress $\bar{\sigma}_{\max}(\dot{\sigma})$].

PREDICTION OF THE DYNAMIC FRAGMENTATION

In the following, the capability of the damage model is evaluated to reproduce observed degradation patterns. The velocity of a single crack is estimated to be about 1875 m/s (i.e., the value of the parameter k is equal to 0.4). The simulation is performed on the confined EOI configuration with an impact velocity of 88 m/s. The random stress to failure is computed by using Eq. (1) for a FE volume of 1 mm³.

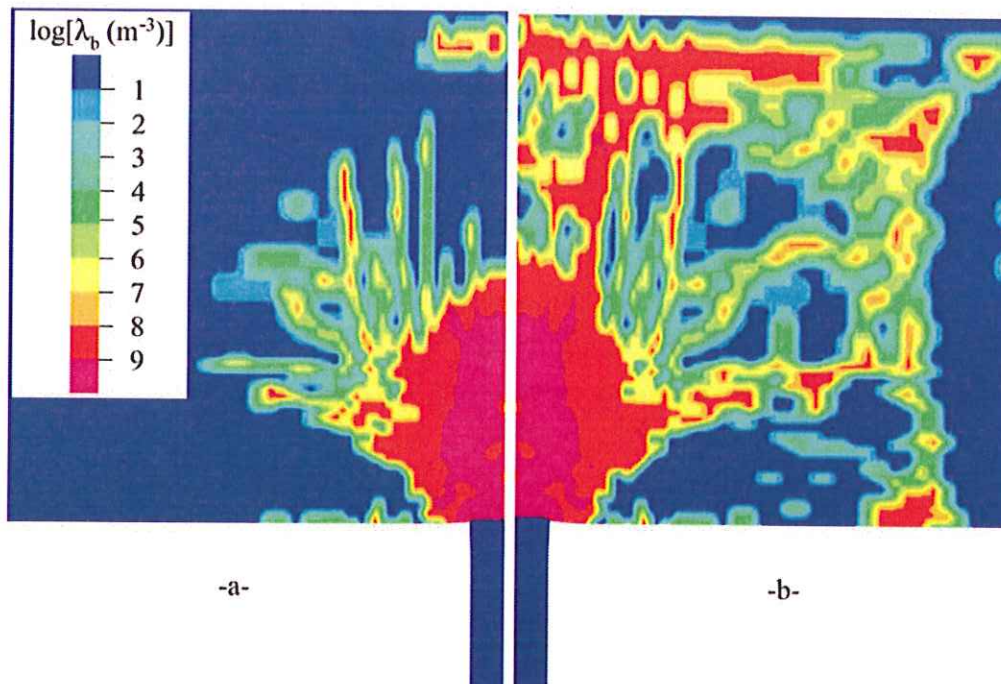


Fig. 5. Contour of crack density associated to the first principal direction 35 μ s (a) and 50 μ s (b) after impact in a confined EOI experiment on Ductal[®].

Figure 5 shows the crack density associated to the first principal stress direction 35 μ s after impact and at the end of the fragmentation process. For high stress rates (i.e., in front of the projectile and in the Hertz-like cone crack), many cracks nucleate in a FE cell. Failure of an element set, which can be compared to macroscopic cracks, can be observed in addition to the continuous degradation generated close to the impact zone. However, there are some difficulties in handling macroscopic cracks. When a crack is created, there is a tendency to follow the direction of the FE mesh. This result may be improved by refining the mesh and the model [21]. Overall, the prediction is in reasonable agreement with the experimental observations (Fig. 3), namely, a fine fragmentation in the first part of the plate followed by long radial cracks in the second half.

SUMMARY

A probabilistic (Weibull) model was used in different situations discussed herein. First, a weakest link hypothesis was made. Under this assumption, a single (discrete) event leads to the complete failure of a structure. Then multiple cracking was discussed. A deterministic formulation can be used within the framework of Continuum Damage Mechanics, provided there are numerous local events occurring almost simultaneously. However, strain-softening may lead to strain localization (i.e., macrocrack initiation) which is a discrete phenomenon again. Some solutions have been proposed, viz. non-local damage models [21] or discrete models [22,23]. Last, the developed damage model was applied to predict in a reasonable way the dynamic fragmentation experienced by a high performance concrete.

References

- [1] Richard P., Cheyrezy M., « Composition of reactive power concretes », *Cement Conc. Res.*, vol. 25, no. 7, 1995, p. 1501-1511.
- [2] Dugat J., Roux N., Bernier G., « Mechanical properties of reactive powder concretes », *Mat. Struct.*, vol. 29, 1996, p. 233-240.
- [3] Freudenthal A.M., « Statistical Approach to Brittle Fracture », *Fracture*, Academic Press, New York (USA), vol. 2, 1968, p. 591-619.
- [4] Weibull W., A Statistical Theory of the Strength of Materials, Roy. Swed. Inst. Eng. Res. Report 151, 1939.
- [5] Weibull W., « A Statistical Distribution Function of Wide Applicability », *ASME J. Appl. Mech.*, vol. 18, no. 3, 1951, p. 293-297.
- [6] Davies D.G.S., « The Statistical Approach to Engineering Design in Ceramics », *Proc. Brit. Ceram. Soc.*, vol. 22, 1973, p. 429-452.
- [7] Hornemann U., Kalthoff J.F., Rothenhäusler H., Senf H., Winkler S., Experimental Investigation of Wave and Fracture Propagation in Glass - Slabs Loaded by Steel Cylinders at High Impact Velocities EMI report E 4/84, Weil am Rhein (Germany), 1984.
- [8] Strassburger E., Senf H., Rothenhäusler H., « Fracture Propagation during Impact in Three Types of Ceramics », *J. Physique IV*, vol. coll. C8, no. suppl. IV, 1994, p. 653-658.
- [9] Denoual C., Cottenot C.E., Hild F., « Analysis of the Degradation Mechanisms in an Impacted Ceramic », *Shock Compression of Condensed Matter*, 1998, AIP Press, New York (USA), p. 427-430.
- [10] Riou P., Denoual C., Cottenot C.E., « Visualization of the Damage Evolution in Impacted Silicon Carbide Ceramics », *Int. J. Impact Eng.*, vol. 21, no. 4, 1998, p. 225-235.
- [11] Denoual C., Cottenot C.E., Hild F., « On the Identification of Damage during Impact of a Ceramic by a Hard Projectile », *16th International Conference on BALLISTICS*, 1996, APDS, Arlington (USA), p. 541-550.
- [12] Denoual C., Barbier G., Hild F., « A Probabilistic Approach for Fragmentation of Ceramics under Impact Loading », *C. R. Acad. Sci. Paris*, vol. 325, no. Série IIb, 1997, p. 685-691.
- [13] Bluhm J.I., « Fracture Arrest », *Fracture*, Academic Press, New York (USA), vol. V, 1969, p. 1-63.
- [14] Freund L.B., « Crack Propagation in an Elastic Solid Subjected to General Loading - Constant Rate of Extension », *J. Mech. Phys. Solids*, vol. 20, 1972, p. 129-140.
- [15] Denoual C., Hild F., « A Damage Model for the Dynamic Fragmentation of Brittle Solids », *Comp. Meth. Appl. Mech. Eng.*, vol. 183, 2000, p. 247-258.
- [16] Grady D.E., Kipp M.E., « Continuum Modeling of Explosive Fracture in Oil Shale », *Int. J. Rock Min. Sci. & Geomech. Abstr.*, vol. 17, 1980, p. 147-157.
- [17] Brara A., Klepaczko J.R., « An Experimental Method for Dynamic Tensile Testing of Concrete by Spalling », *Int. J. Impact Eng.*, vol. 25, 2001, p. 387-409.
- [18] Hild F., Brajer X., Denoual C., Forquin P., « On the Probabilistic-Deterministic Transition Involved in a Fragmentation Process of Brittle Materials », *Comput. Struct.*, vol. 81, no. 12, 2003, p. 1241-1253.
- [19] Denoual C., Hild F., « On the Characteristic Scales involved in a Fragmentation Process », *J. Phys.*, vol. IV, no. 8, 1998, p. 119-126.
- [20] Denoual C., Hild F., « Dynamic Fragmentation of Brittle Solids: A Multi-Scale Model », *Eur. J. Mech. A/Solids*, vol. 21, no. 1, 2002, p. 105-120.
- [21] Brajer X., Hild F., Roux S., Gy R., « Behavior of soda-lime glasses impacted by a soft bullet: experimental and numerical investigations », *14th Dymat Technical Meeting*, 2002, EURODYMAT, p. 35-44.
- [22] Camacho G.T., Ortiz M., « Computational Modelling of Impact Damage in Brittle Materials », *Int. J. Solids Struct.*, vol. 33, no. 20-22, 1996, p. 2899-2938.
- [23] Mastilovic S., Krajcinovic D., « High-Velocity Expansion of a Cavity within a Brittle Material », *J. Mech. Phys. Solids*, vol. 47, 1999, p. 577-600.

DYNAMIC TESTING OF CONCRETE WITH SPLIT HOPKINSON PRESSURE BARS

Sébastien Richomme*, Patrice Bailly*, Franck Delvare*, Guy Mavrothalassitis**

*Laboratoire Energétique Explosions Structures (LEES), ENSI de Bourges (Ecole Nationale Supérieure d'Ingénieurs de Bourges)
10 Bd Lahitolle, 18020 Bourges Cedex, France

**Institut National de l'Environnement industriel et du RISque (INERIS), 10 Bd Lahitolle, 18020 Bourges Cedex, France

Summary : This article presents the experimental results of compressive and bending dynamical tests on concrete and reinforced concrete specimens. Dynamical tests were carried out with Split Hopkinson Pressure Bars and were coupled with static ones. The strength and the difference of response were compared in both cases (rate sensitivity). The influence of the specimen's length for compressive tests was studied. For bending tests, we looked at the strain rate effect, the influence of distance between the supports, of reinforcement and of boundary conditions.

INTRODUCTION

The failure and collapse of reinforced concrete structures are studied in order to be used in vulnerability analyses. These phenomena are complex and even in simple cases, it is not always possible to solve the problem with analytical methods. The use of numerical tools requires a precise knowledge of dynamical behaviour. The purpose of this study is to identify macroscopic models of reinforced concrete behaviour thanks to experiments.

This article presents the experimental results of compressive and bending dynamical tests on concrete and reinforced concrete specimens. Dynamical tests were carried out with Split Hopkinson Pressure Bars (SHPB) either in the usual configuration or in a more original one to carry out dynamical bending tests.

EXPERIMENTAL SYSTEMS

Dynamic testing system

To carry out a dynamical test with SHPB [1], a specimen is inserted between two bars. A longitudinal wave is induced in the incident bar after the impact of a projectile. On the bar-specimen interface, the wave is divided into two parts. A part is reflected and the other part is transmitted through the specimen and induces an elastic wave in the transmitter bar. Strain gauges are stuck on the bars and measure the elastic strains of the bars.

The following relations based on a one dimensional wave assumption relations, may be obtained:

$$\begin{aligned} \sigma &= E \cdot \epsilon \\ v(x, t) &= -C_0 \cdot \epsilon \end{aligned} \tag{1}$$

where σ denotes the stress, ϵ the strain, E the Young modulus, C_0 the speed of elastic waves in bars and v the mass velocity.

Thanks to the following well-known relation, it is possible to obtain the displacement of input interface U_a and of output interface U_b , the input force F_a , the output force F_b , the input velocity V_a and the output velocity V_b .

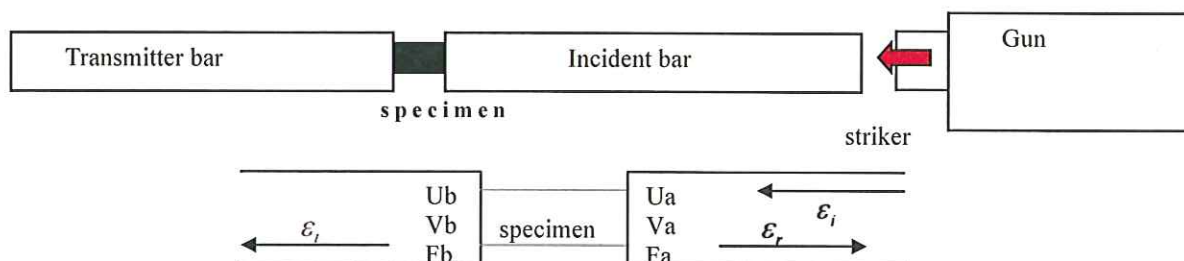


Fig. 9-Simplified schema of SHPB

$$V_a(t) = C_0(\epsilon_i(t) - \epsilon_r(t)) \quad (2)$$

$$V_b(t) = C_0(\epsilon_t(t))$$

$$F_a(t) = S.E.(\epsilon_i(t) - \epsilon_r(t)) \quad (3)$$

$$F_b(t) = S.E.(\epsilon_t(t))$$

where S , E denote the cross section and the Young modulus of bars, and ϵ_i , ϵ_r , ϵ_t are respectively the incident, the reflected and the transmitted strain.

The main difficulty of this analysis lies in the wave shifting problem. The strains used in equations (2) and (3) are assumed to be known at the specimen-bar interface but they are measured respectively at 1.5 meters on the incident bar and 40 centimetres at the transmitter bar. This distance is significant especially for the incident bar because the incident wave and the reflected wave are measured with the same strain gauges. The waves must be virtually shifted in time or in space. It is important to consider the wave dispersion and the relative time shift of the three waves. For the correction of dispersion [2][3] we used the Pochhammer and Chree ([4][5]) wave dispersion model which was applied by Davies [6]. The origin of the three waves must be shifted in a precise way to the time origin corresponding to the arrival of the incident wave at the first interface. The correction technique is based on the initially elastic response at the specimen-bar interface.

In order to carry out dynamical bending tests, we used the SHPB in a different configuration. In this case, the transmitter bar was replaced by two transmitter bars (fig.2). Two transmitter waves were measured and they were identical. The analysis of signals was standard. These tests were carried out at LMS laboratory (Laboratory of Solids Mechanics, Ecole Polytechnique, Palaiseau, France).

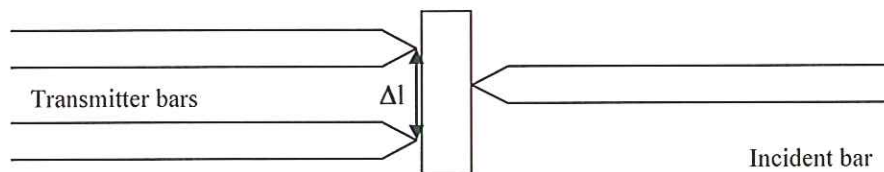


Fig. 10-System of dynamical bending tests (LMS,X)

To obtain more information about the response of concrete and reinforced concrete during a dynamic loading, we modified (fig.3) the dynamical three-point bending test system (fig.2). We wanted to modify the boundary conditions, for example fixing the specimen at both ends.

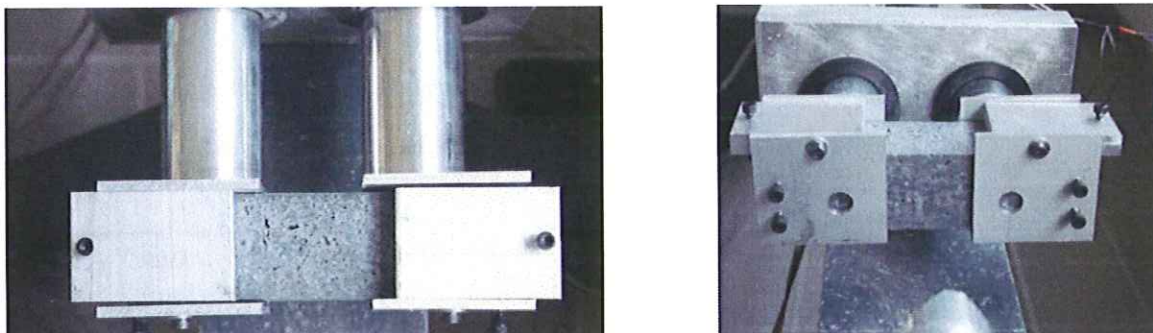


Fig. 11-Modified dynamical bending system((a) topview, (b) front view)

Static testing system

The static tests were carried out on a traditional testing machine with a 100 kN force meter.

For compressive tests, the boundary conditions were the same as for dynamical tests. The interfaces between the testing machine and the specimen were two cylindrical pieces (diameter 40mm) of aluminium alloys (fig.4), similar to the SHPB bars. Figure 5 shows the three-point bending test used for the static bending tests and figure 6 shows a modified bending test.

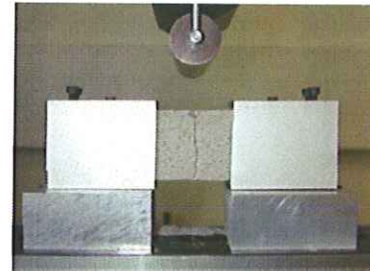
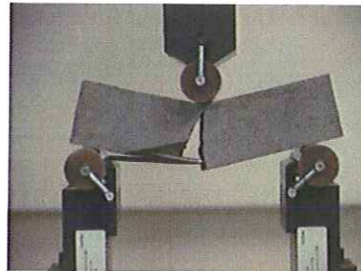
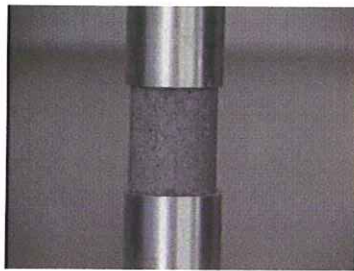


Fig. 12- Static compressive system

Fig. 13- Three-point bending test

Fig. 14- Modified bending test

Specimens

Concrete specimens are cylindrical (fig.4). Their diameter is 35 mm and the range of their length is 10 mm to 200 mm. (10 mm, 20 mm, 40 mm, 80 mm, 100 mm, 160 mm, 200 mm).

For bending tests and modified bending tests, small size beam specimens (fig.4 and 5) are made of concrete or reinforced concrete. They are 160 millimetres long, 40 mm wide and 40 mm deep.

The composition of concrete is the same for all specimens (tab.1).

Components	Mass Percentage
Sand 0 /2	51.6
Finest sand	9.2
Silica fume	5.5
Cement 52.5	22.1
Water	11.5
Concrete fluidifying	0.23% of cement mass

Table 1-Components of concrete

EXPERIMENTAL RESULTS

Compressive tests

The object of these tests is to show the influence of the slenderness ratio.

Figure 6 gathers all the results for static and dynamical tests and compares them to Hansen's static results [7]. The relative resistance is plotted versus the length/diameter ratio. The relative resistance of a specimen is the ratio of specimen resistance to the resistance of a L/D=2 specimen. We may underline that the curves decrease and reach a plateau. We observe this phenomenon both in static and dynamical tests.

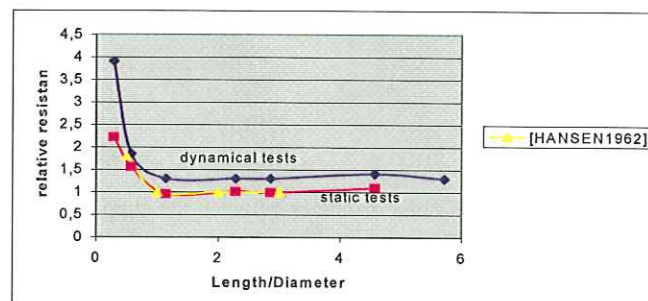


Fig. 7-Relative resistance versus ratio L/D (Comparison Static/Dynamic)

A stronger the resistance is observed for dynamical tests, this is obviously a strain rate effect [8,9,10]. Figure 6 clearly shows that the dynamical resistance to static resistance ratio depends on the specimen's length. This ratio varies from 2 for a 10 mm long specimen to 1.25 for a longer one. Bischoff and Perry [11] give us a value of 2 for a similar strain rate. This value may be the result of tests on small size specimens.

The ratio decreases with longer specimens and reaches a plateau for a length between 40 and 80 mm ($1 < L/D < 2$). The observation of the cracking profile of specimens after the test confirms the existence of a “characteristic length”. Specimens that are less than 80 mm long are completely broken while the longer specimens still have a safe part and the broken one is between 70 and 90 mm long.

To conclude, the resistance values (static and dynamic) decrease when the specimen’s length increases and remain constant it reaches once a characteristic length value. A rate effect is observed and the dynamic/static resistance ratio is dependent on the specimen’s length. The L/D ratio in concrete resistance studies is a significant parameter.

BENDING TESTS

Observations on three-point bending test

The SHPB system gives us the forces at the specimen-bar interfaces. The sensitivity of different testing parameters on input and output forces are studied. The parameters are the strain rate, the distance between the supports, the reinforcement and the boundary conditions.

Strain rate influence

The maximum forces are higher during dynamical tests. Table 2 shows the ratio for concrete and reinforced concrete specimens and for the distance between the supports.

Material	Concrete		Reinforced concrete
Distance between the supports (in mm)	60	140	140
Maximum Forces Ratio (FM _{dyn} /FM _{stat})	2,5	5,5	2,8

Table 2- Maximum Forces Ratio (FM_{dyn}/FM_{stat})

Sensitivity to distance between supports

The bending tests were carried out with two different distances between the supports, Δl=14cm and Δl=6cm (fig.2). Figures 7 and 8 show the input and output forces in both cases.

In the case of a concrete specimen with a distance between each support of 140mm, the input force reaches about 10000 N while the value of the output force remains low (900N). When the distance between the supports decreases, the maximum value of the input force does not change (about 10000N) and the maximum value of the output force is about 5000N, i.e. half that of the input force. It is also possible to assume a quasi static balance of forces.

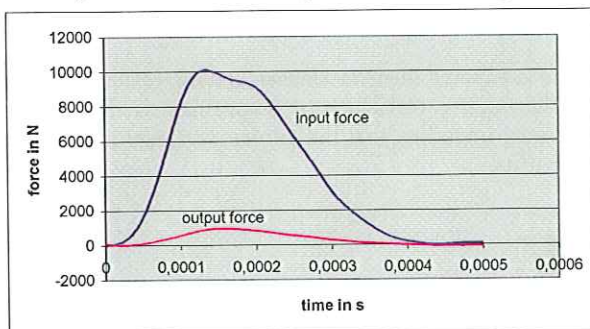


Fig. 15-Test with distance Δl=14cm

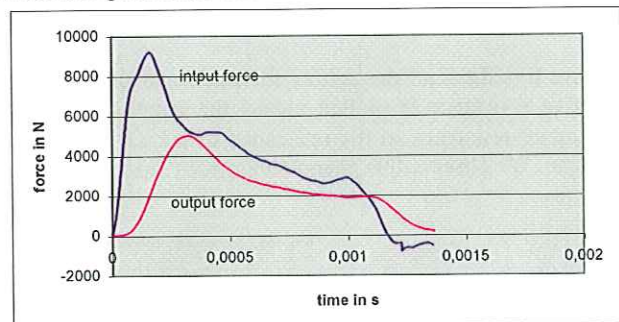


Fig. 16-Test with Δl=6cm

The static bending tests were carried out with the same distances between the supports. The highest value of the force was multiplied by 2.1 when we moved the supports together. This ratio was equal to the length ratio ($l=140/l=60$). The bending moment at the middle of the beam ($M_f = (FL)/4$) was also identical.

Sensitivity to reinforcement

Reinforcement with steel gave a plastic behaviour to the specimen. We observed for static and dynamical tests that the forces remained constant after reaching their maximum values. For static test this value was 1.8 higher for a reinforced concrete specimen than for one in concrete while there was no difference for dynamical tests.

Test’s film showed the influence of steel in concrete (fig.9). During the test, a crack appeared at the center of both beams but its propagation was stopped by steel while the other specimen was broken into two parts.

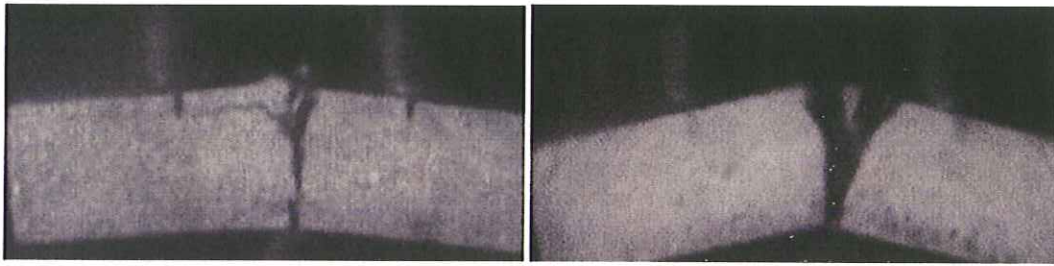


Fig. 17-Final state after a dynamical bending test ((a) reinforced concrete, (b) concrete)

Sensitivity to boundary conditions

The modified bending system developed in LEES laboratory permits to observe the influence of the boundary conditions. For dynamic cases this new system could enable us to distinguish two failures modes (shear failure and bending failure) on concrete specimens.

A static loading causes a single crack at the center of the beam (fig.10) but in dynamical tests, two types of failures are observed (fig.10, fig.11). In dynamic cases (fig.11 and 12) we observed the same crack, denoted by 1, as in static case. Other cracks denoted by 2 which only appear in dynamic case are at right angles (about 45°) to the loading direction. The film (1000/s) cannot indicate the order of appearance of the cracks. Figure 11 shows two consecutive pictures.

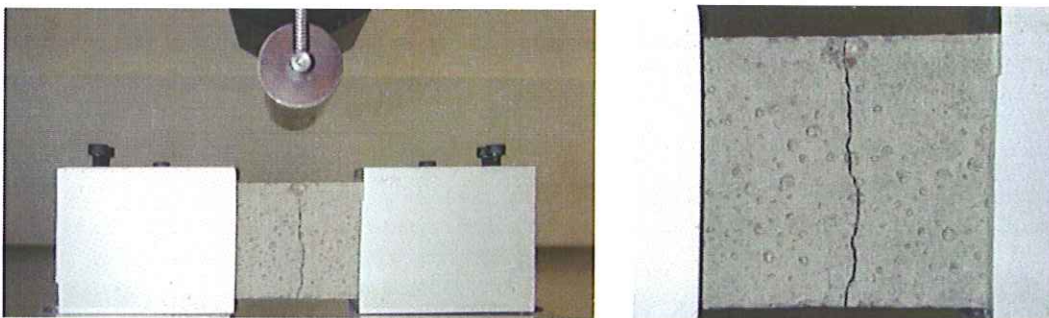


Fig. 18-Crack on specimen after a static test

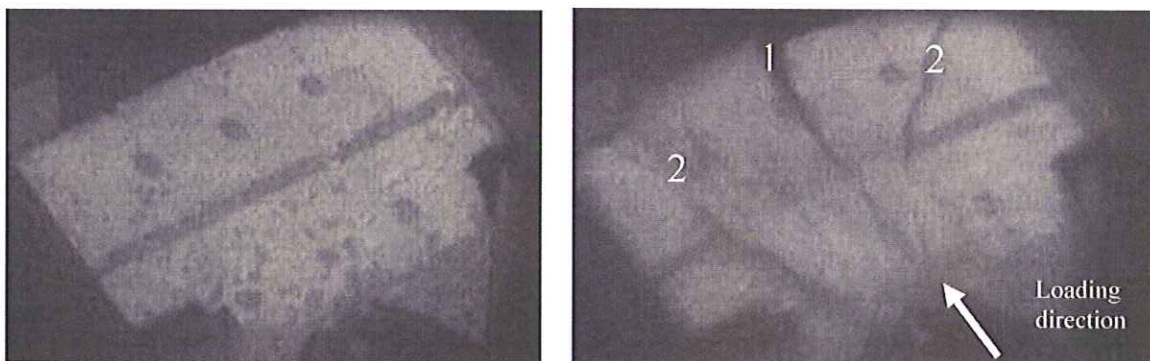


Fig. 19-Consecutive pictures ($\Delta t=1ms$)

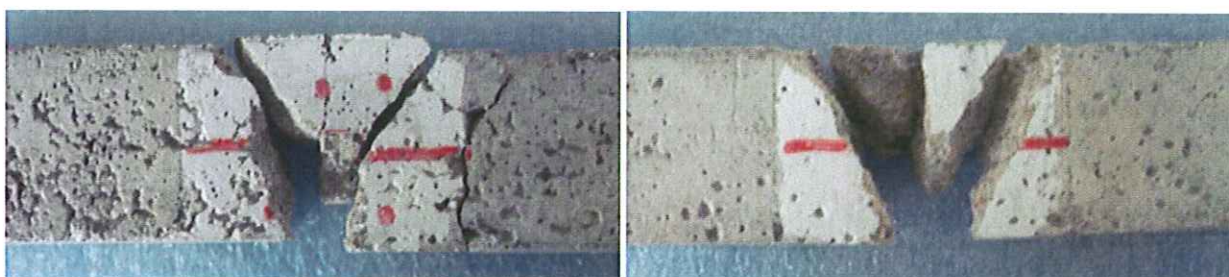


Fig. 20- Crack on specimen after dynamical tests

CONCLUSION

We have presented in this paper static and dynamical tests of concrete and reinforced concrete with SHPB. These experimental studies have resulted in several interesting findings. The compressive tests highlight the strain rate effect of concrete and a structural effect for small size specimens. Bending tests highlight the strain rate effect of concrete, its sensitivity to reinforcement and to boundary conditions.

At this point, several issues still need to be investigated. First, modelisation and numerical simulations could be useful to validate the bending tests. Second, it would be interesting to understand the failure modes obtained with the modified bending system. Last, all these experiments could be useful to identify macroscopic models of concrete and reinforced concrete behaviour.

References

- [1] Hopkinson B., A method of measuring the pressure in the deformation of high explosive by impact of bullet, Phil. Trans., Royal Soc. of London, 1914
- [2] Gary G., Klepaczko J.R. et Zhao H., Correction de dispersion pour l'analyse des petites déformations aux barres d'Hopkinson, DYMAT 91, pp 403-410, Strasbourg-ED.Phys, France, 1991
- [3] Zhao H., Gary G. et Rota L., Utilisation des barres d'Hopkinson pour le comportement dynamique des matériaux fragiles, Actes du 11ème congrès Français de Mécanique, pp 413-416, Lille France, 1993
- [4] Pochhammer L., J. für die Reine und angewandte Mathematic, vol.81, 1876, p 324
- [5] Chree C., Trans. 14, Cambridge Phil. Soc., 1889, p155
- [6] Davies R.M., Phil.Trans. A240, 1948, p155
- [7] Hansen H., Compressive strength of concrete-cube or cylinder ?, Bulletin RILEM, n°17, 1962
- [8] Toutlemonde F., Résistance au choc des structures en Béton, Thèse de l'ENPC, 1995
- [9] Rossi P., A physical phenomenon which can explain the mechanical behaviour of concrete under high strain rates, Materials and structures, vol. 24, pp 422-424, 1991
- [10] Bailly P., Une modélisation d'un matériau fragile avec prise en compte d'effets dynamiques, C.R. Acad. Sci. Paris, t.318, Série II, 1994
- [11] Bischoff P.H., Perry S.H., Compressive behaviour of concrete at high strain rates, Materials and Structures, 1991

INDIRECT MEASUREMENT OF DYNAMIC CUTTING FORCES

Sébastien Auchet, Pierre Chevrier, Paul Lipinski

*Laboratoire de Physique et Mécanique des Matériaux, Ecole Nationale d'Ingénieurs de Metz -CEPGV,
Ile du Sauley, 57045 Metz, France*

Summary: Milling tests have been performed on 5-axis machine fitted out with an electro-spindle with active magnetic bearings (AMB). These bearings are not affected by friction and wear. An experimental approach has been developed to determine the cutting forces in function of the measured control voltages of the milling spindle's magnetic bearings. The spindle is treated as a "black box", where the transfer functions linking the unknown cutting forces with control voltages are established experimentally. The validity of the cutting force calculation method was firstly established for slotting [1] and extend to the case of peripheral milling operation [2]. This indirect method of cutting force determination provides a useful way to estimate tool wear and monitor on-line product quality in high-speed milling.

The aim of this paper is to describe dynamic components of cutting forces in the case of slotting and peripheral milling operation. Moreover, a comparison between cutting forces measurements obtained by using a Kistler dynamometer and from analysis of AMB command voltage underlines the less of accuracy on cutting forces measurements of Kistler dynamometer 9225B in high speed machining.

However, gyroscopic effects of the rotor motion limit the use of this method for instable conditions. Transfer functions between magnetic bearing and tool are measured using an impact hammer without rotation of the rotor. When milling, gyroscopic effects modify transfer functions around flexural modes of the rotor. Moreover, regenerative chatter creates spectral arrays of high amplitude at frequencies that are close to the flexural modes of the rotor. Consequently, reaction forces applied to the rotor by magnetic bearings are not properly transferred at the end of the tool to give cutting forces. Transfer functions are actually incorrect at frequencies close to the flexural modes of the rotor, where spectral arrays of high amplitude appear due to regenerative chatter vibrations.

CUTTING FORCES MEASUREMENT METHODS

The use of high-speed milling allows an increase of productivity by reducing the machining time, but additional tool costs reduce economic gains of this technology. The tool wear decreases with decreasing cutting forces, which are, moreover, the most important indicator of machining state and quality. Consequently, many methods of measuring cutting forces have been developed. Principal investigations have been focused on in-process force measurement systems because knowing cutting forces allows to reduce tool wear, to control continuously quality of the milling operation and to detect tool breakage.

The most frequently used sensor is the piezoelectric dynamometer that provides the accurate measurement of cutting forces. However, the use of this method is limited by the dynamic responses of the sensor, each dynamometer being characterized by its bandwidth. Recently, Lapoujouade et al. [3] and [4] and Tounsi and Otho [5] have proposed an accelerometer-based method to compensate signal distortions of piezoelectric dynamometer due to its self-dynamic behaviour. Their method allows the measurement of dynamic cutting forces, such as high speed milling forces, with a high frequency bandwidth up to 5 kHz. However, this device is expensive and the size of work pieces, on which it is possible to measure cutting forces during machining, is limited by the size of the dynamometer cover plate, typically of a few hundred millimeters. To avoid these limitations, indirect cutting force measurement methods have been developed [6], [7], [8], and [9]. However, the relatively low bandwidth of these sensors limits the use of all indirect cutting force measurements that can be found in literature to the case of low-speed milling.

In this paper, a new method exploiting command voltages of the magnetic bearing of the S2M's spindle is proposed. A short description of S2M's spindle is presented in the next paragraph. Then, force measurement method based on the command voltages analysis is exposed. In the last part of this paper, a comparison with measurements obtained using a Kistler dynamometer for full and partial immersion milling operations underlines limitations of piezoelectric based sensors.

DESCRIPTION OF THE MILLING SPINDLE

This spindle is composed of two radial active magnetic bearings, AMB 1 and AMB 2, and one axial AMB 3, (Fig. 1a). The milling tool (4) is fixed at the rotor by the way of the tool holder (5). A part of the length of the spindle's rotor forms the rotor of the drives motor (6).

A magnetic bearing is composed of two pairs of electromagnets exerting radial forces on the shaft and maintaining it in equilibrium position, as shown in Figure 1.b. The design of this magnetic bearing introduces two main orthogonal directions defined by axes V and W. Forces applied to the shaft by the magnet are proportional to the coils' current, which can be modulated.

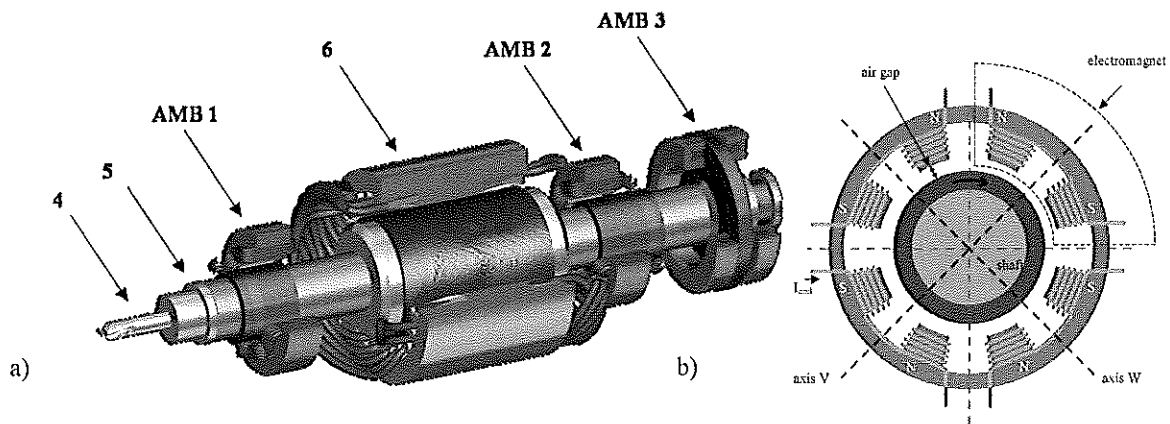


Fig. 1 : a - view of the milling spindle developed by S2M, b - main axes of a magnetic bearing

This specificity is used to maintain the shaft's rotation axis at the centre of the bearing in reacting to any load variation such as external disturbance forces or mass unbalance of the rotor. Position sensors measure the shaft displacement. When a position error is detected, the control loop system modulates the current in each coil to vary the force of the electromagnets in order to bring back the rotor to the required central position. Each pair of electromagnets is controlled independently.

As explained previously, axis V and axis W are the two main perpendicular directions of magnetic bearings. Radial cutting forces are commonly decomposed according to the coordinate system of the milling machine (X and Y axes), which are different from the AMB's V-W axes. For the studied spindle, the X-axis of the milling machine was rotatively positioned 150° from the V-axis of the electro-magnetic bearings.

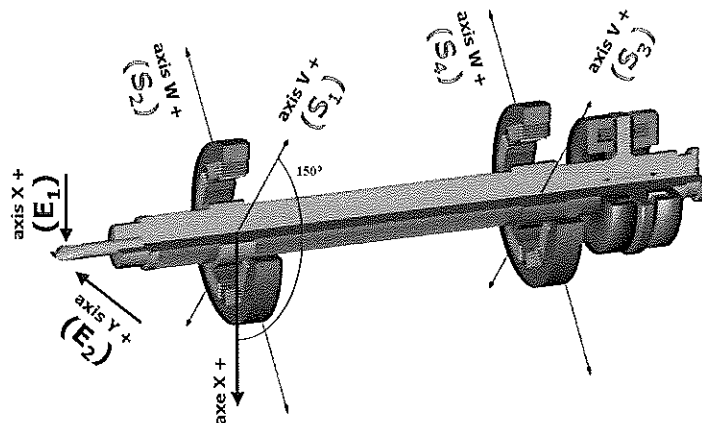


Fig. 2 : systems of axes of the AMB (V-W) and of the milling machine (X-Y)

CUTTING FORCE MEASUREMENTS FROM COMMAND VOLTAGES OF THE AMB

The milling force components F_x and F_y are the input quantities denoted E_1 and E_2 . The four command voltages of the electromagnets constitute the output quantities denoted S_1 , S_2 , S_3 and S_4 . They constitute six degrees of freedom of the "black box". Eight complex transfer functions have to be determined linking each input parameter with four outputs.

Measurement of command voltages of AMB's

Command voltage S_1 , S_2 , S_3 , and S_4 are measured during the milling operation. S_i indicates the command voltage of the electromagnet that causes forces on the rotor in dof_{i+2} ($i=1$ to 4). When a position error of the shaft is detected, the control loop system modulates the command voltage in the range $-10 < U < 10$ V. Depending on the sign of the command voltage, only one electromagnet in each pair of electromagnets varies its attraction force applied to the shaft in order to bring back the rotor to the required position. Figures 4, 6 and 8 illustrates the evolution of the command voltage S_1 during a typical milling operations. Command voltages are measured in the temporal domain by using an eight channels spectral analyzer Pimento developed by LMS. The sampling frequency is 10 kHz and the total measurement time is 4 seconds. The Fast Fourier Transform (FFT) is applied using a Mathematica's notebook to the four signals $S_1(t)$ to $S_4(t)$, where t represents the time. $S_1(j\omega)$, $S_2(j\omega)$, $S_3(j\omega)$ and $S_4(j\omega)$ are the frequential spectra obtained, where ω indicates a frequency in Hertz.

Transfer functions magnetic bearings - tool

To determine the cutting force components from the command voltages, two impulse loadings were applied to the tool extremity in X and Y directions, successively. For each impulse, denoted respectively $E_1(t)$ and $E_2(t)$, four responses $S_1(t)$ to $S_4(t)$ were measured. Impulses and responses are measured in the temporal domain by using the eight channels' analyzer Pimento and transformed to the spectral space using one of the Mathematica Fast Fourier Transform techniques. Eight complex transfer functions are determined in this way. These functions are defined by the expression :

$$H_{ij}(j\omega) = \frac{S_i(j\omega)}{E_j(j\omega)} \quad (1)$$

where $i=1$ to 4 indicates one of the fourth output parameters of the rotor and $j = 1, 2$ points to one of the two input degrees of freedom of the tool. So, the functions $H_{11}(j\omega)$, $H_{21}(j\omega)$, $H_{31}(j\omega)$, $H_{41}(j\omega)$ are obtained simultaneously by measuring command voltages variations (S_1 to S_4 in Volts) due to impulses applied at the end of the tool by an impact hammer in the X direction (E_1 in N). Impulses at the end of the tool in the Y direction (E_2 in N) are used to determine experimentally the functions $H_{12}(j\omega)$, $H_{22}(j\omega)$, $H_{32}(j\omega)$, $H_{42}(j\omega)$. A typical transfer function is presented in figure 3.

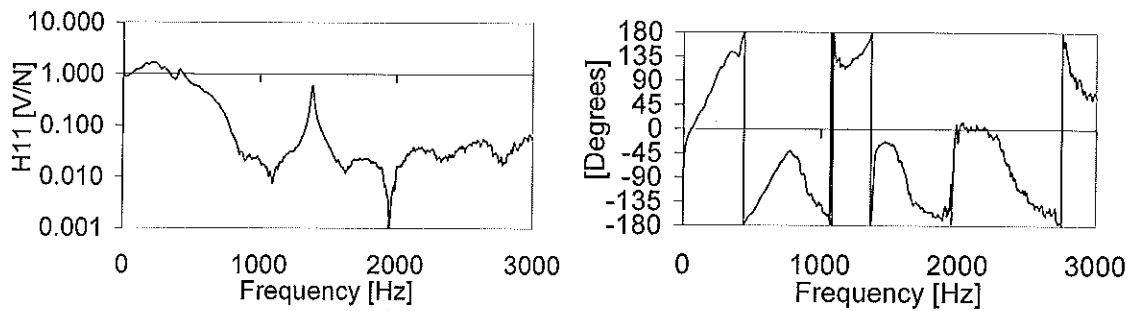


Fig. 3 : transfer function H_{11} (amplitude and phase)

Determination of cutting forces from electromagnets command voltages

In this section, method of calculation of cutting forces, combining the eight transfer functions of the two bearings, is presented. As mentioned earlier, the complex transfer functions link command voltages to cutting forces. Consequently, the expression relating two inputs and four outputs parameters can be written:

$$\begin{pmatrix} S_1 \\ S_2 \\ S_3 \\ S_4 \end{pmatrix} = \begin{bmatrix} H_{11} & H_{12} \\ H_{21} & H_{22} \\ H_{31} & H_{32} \\ H_{41} & H_{42} \end{bmatrix} \begin{pmatrix} E_1 \\ E_2 \end{pmatrix} \quad (2)$$

To circumvent the difficulty consisting in the inversion of a rectangular matrix, the least square method applied to the system of complex functions should be used, as exposed in [1]. In our case, the solution of Eq. (2) gives the cutting forces E_1 and E_2 :

$$\begin{aligned} E_1 &= \frac{de - bf}{ad - bc} \\ E_2 &= \frac{af - ce}{ad - bc} \end{aligned} \quad \text{where} \quad \begin{aligned} a &= \overline{H_{11}}H_{11} + \overline{H_{21}}H_{21} + \overline{H_{31}}H_{31} + \overline{H_{41}}H_{41} \\ b &= \overline{H_{11}}H_{12} + \overline{H_{21}}H_{22} + \overline{H_{31}}H_{32} + \overline{H_{41}}H_{42} \\ c &= \overline{H_{12}}H_{11} + \overline{H_{22}}H_{21} + \overline{H_{32}}H_{31} + \overline{H_{42}}H_{41} \\ d &= \overline{H_{12}}H_{12} + \overline{H_{22}}H_{22} + \overline{H_{32}}H_{32} + \overline{H_{42}}H_{42} \\ e &= \overline{H_{11}}S_1 + \overline{H_{21}}S_2 + \overline{H_{31}}S_3 + \overline{H_{41}}S_4 \\ f &= \overline{H_{12}}S_1 + \overline{H_{22}}S_2 + \overline{H_{32}}S_3 + \overline{H_{42}}S_4 \end{aligned} \quad (4)$$

where the conjugate term of the complex function H_{ij} is written $\overline{H_{ij}}$.

The cutting force $E_1(t)$ and $E_2(t)$ are obtained by applying an inverse FFT to functions $E_1(j\omega)$ and $E_2(j\omega)$ and by dividing temporal signals by the window of Hanning.

EXPERIMENTAL RESULTS

The aim of this paper is to determine dynamic components of cutting forces in the case of slotting and peripheral milling operation. Moreover, a comparison between cutting forces measurements obtained by using a Kistler dynamometer and from analysis of AMB command voltage underlines the less accuracy on cutting force measurements by Kistler dynamometer 92225B in high speed machining. All measurements presented in this section have been repeated three times to verify their consistency, and very close values have been obtained.

Cutting force measurements for slotting and peripheral milling under stable conditions

The validity of the above cutting force calculation method was firstly established for slotting [1] and extend to the case of peripheral milling operation [2] up to an excitation frequency of 4 KHz, which is twenty times the widest bandwidth of others methods that can be found in literature [9]. Two flute cylindrical tools have been used to machine slots and peripheral milling operations in aluminum AU4G. Command voltage S_1 , S_2 , S_3 , and S_4 are measured during the milling operations. Typical measurement of S_1 is represented during full immersion milling with a 32 mm diameter tool (Fig. 4) and during peripheral milling with a tool of $\Phi=40$ mm (Fig. 5).

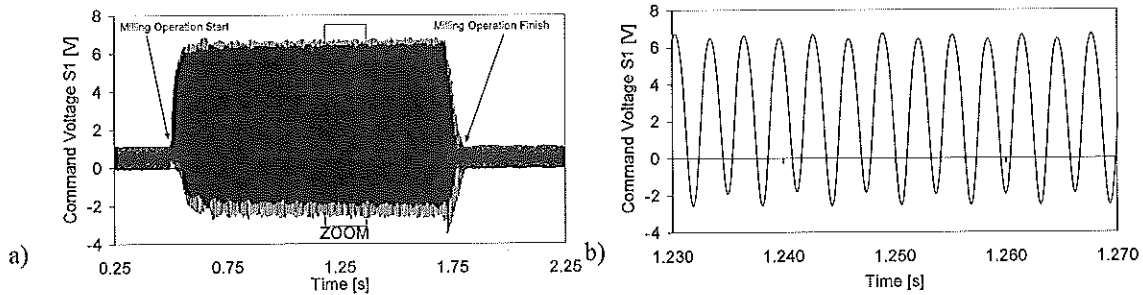


Fig. 4 : full immersion milling S_1 (cutting conditions : $Fr = 0.36$ mm/tooth, d.o.c. = 4 mm, $\omega=14\ 000$ rpm) a) before, during and after milling, b) during the milling operation

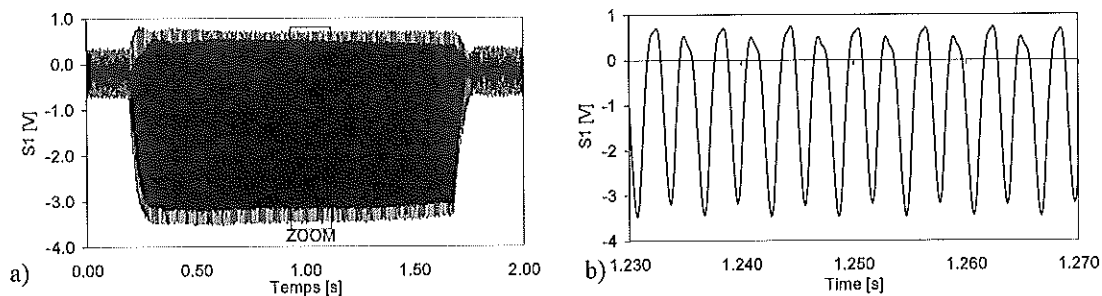


Fig.5 : peripheral milling (cutting conditions : $Fr = 0.5$ mm/tooth, d.o.c. = 3 mm, $\omega=10\ 000$ rpm) a) before, during and after milling, b) during the milling operation

The analysis of FFT of command voltage measurements shows clearly dynamic characteristics of each type of milling operation. On each spectrum of the command voltage S_1 for a slot operation, three spectral arrays appear as shown in Figure 6.a : the first one corresponds to the shaft rotation frequency (166.7 Hz), the second to the tooth passing frequency (333.3 Hz), and the last appears at twice the tooth passing frequency (666.7 Hz). For a peripheral milling operation, the array at the shaft rotation frequency and the tooth passing frequency appear, as in the case of a full immersion operation, but seven harmonic rays at the tooth passing frequency are also present, as shown on figure 6.b. The high number of harmonic rays in the case of peripheral milling can be explained by the discontinuity of the cutting force functions caused by nil chip thickness when the cutting edge goes out from workpiece during up milling and come in workpiece for down milling.

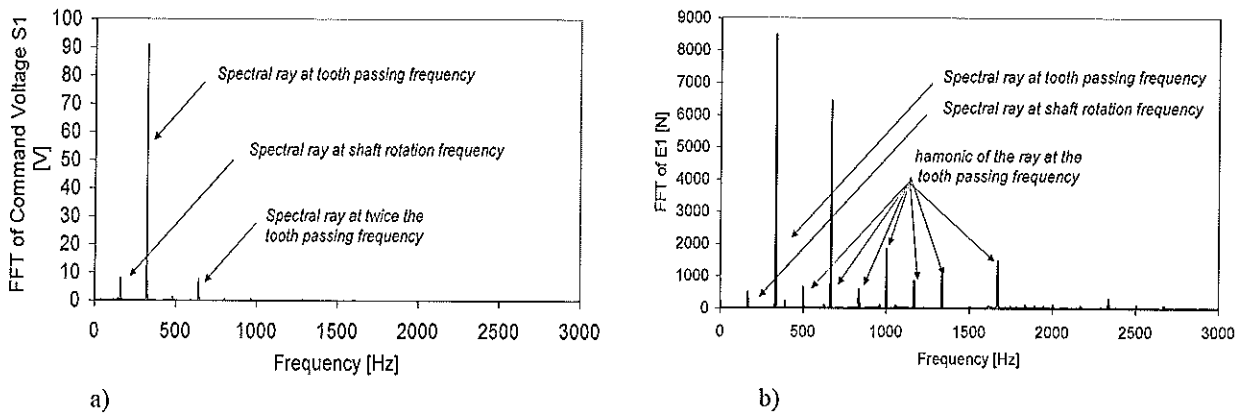


Fig.6 spectrum of command voltage S_1
 a) full immersion milling, b) peripheral milling

The forces of machining calculated from command voltages of the magnetic bearing measurements have been compared with those given by the Kistler 4-components dynamometer for the each cutting test. For the slot operation, see Figure 7.a, both F_x and F_y cutting forces calculated using the least square method are in good agreement with measurements obtained with the Kistler dynamometer.

But, it seems that the bandwidth of the Kistler dynamometer is too low to detect the secondary oscillations, which appear at four times the tooth passing frequency, recorded by the indirect method ($f \approx 1290$ Hz). The two curves exhibit the same tendency but the amplitudes of the secondary oscillations recorded by the Kistler dynamometer are less pronounced.

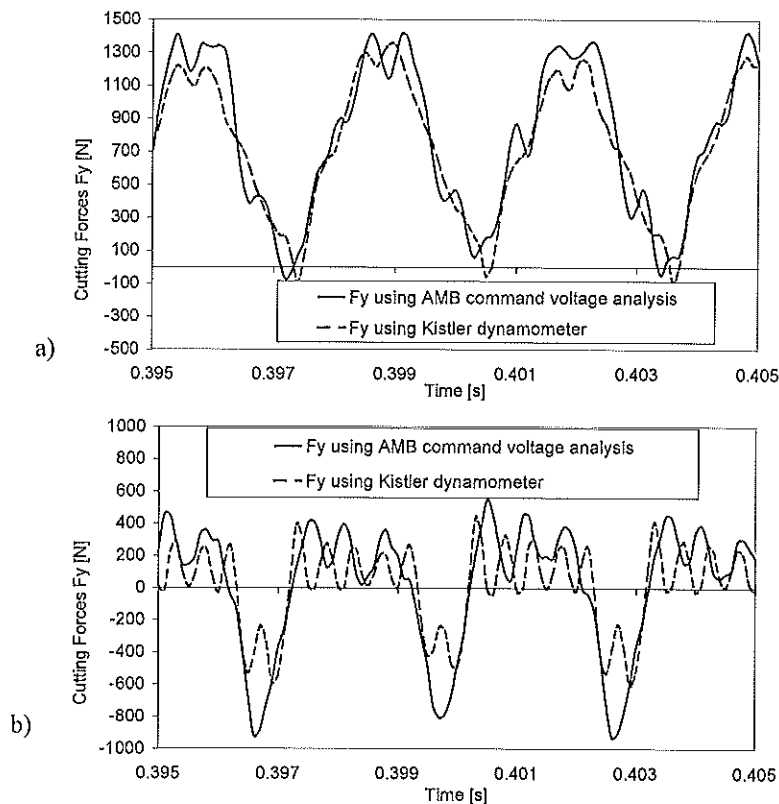


Fig.7 : comparison between cutting force F_y calculated from command voltages of magnetic bearings measurements and F_y measured with the Kistler 4-components dynamometer
 a) full immersion milling, b) peripheral milling

However, F_x and F_y cutting forces measured for the peripheral operation with the Kistler dynamometer are very different from those calculated using AMB command voltage analysis, as shown Figure 7.b. In fact, harmonic rays of the ray at the tooth passing frequency are not detected the Kistler dynamometer. High frequency excitations make vibrating the Kistler dynamometer. It measures its own vibrations and not the cutting forces anymore.

Case of unstable milling

For full immersion milling tests with a speed of rotation of 12 000 rpm (200 Hz) and 13 000 rpm (216.7 Hz), chatter regenerative vibrations distort the measured signal of cutting forces. The Kistler dynamometer measurements are very different from the cutting force calculated using the least square method as shown in figure 8, and both measuring methods give incorrect results.

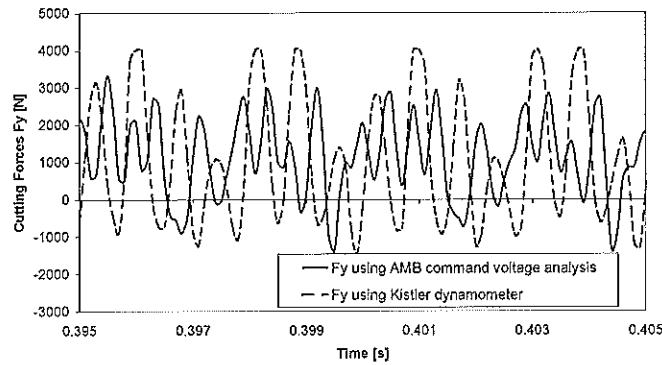


Fig.8 : cutting force measurements distorted by regenerative vibrations

Spectral rays of frequency which are not a multiple of the tooth passing frequency appears on FFT of cutting force signals as shown in Figure 9. A ray at the frequency of first flexural mode (1050 Hz) always appears when the milling operation becomes unstable. It seems that the Kistler dynamometer failed to detect vibrations of frequency greater than 1500 Hz.

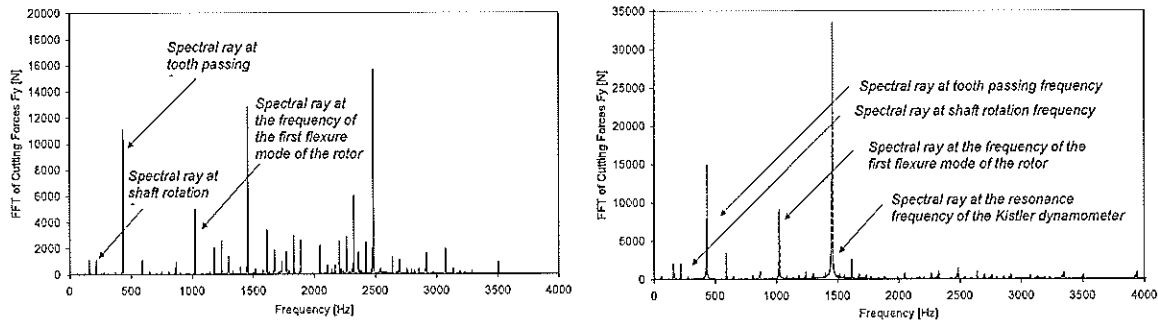


Fig.9 : spectral array of cutting force Fy during unstable milling
 a- Fy calculated from command voltages of magnetic bearings measurements
 b- Fy measured with the Kistler 4-components dynamometer

Regenerative chatter induces the Kistler dynamometer vibrations and the influence of dynamic vibrations dominates the signal of chip forming force due to cutting.

For the magnetic bearings based method, transfer functions between magnetic bearing and tool were measured using an impact hammer without rotation of the rotor. When milling, gyroscopic effects modify transfer functions around flexural modes of the rotor. Moreover, regenerative chatter creates spectral arrays of high amplitude at frequencies that are close to the flexural modes of the rotor. Consequently, reaction forces applied to the rotor by magnetic bearings are not properly transferred at the end of the tool to give cutting forces. Transfer functions are actually incorrect at frequencies close to the flexural modes of the rotor i.e. where spectral arrays of high amplitude appear due to regenerative chatter vibrations.

CONCLUSIONS

The experimental results presented above show that dynamic components of cutting forces in the case of slotting are different from those of peripheral milling operation. On the FFT of cutting forces measurement for peripheral milling operation, the array at the shaft rotation frequency and the one at the tooth passing frequency appear, as in the case of a full immersion operation, but equally seven significant harmonic rays of the ray at the tooth passing frequency when only one harmonic ray appears for the slotting case. The high number of harmonic rays in the case of peripheral milling can be explained by the discontinuity of the cutting forces functions caused by nonzero thickness of the chip when the cutting edge come out workpiece the up milling and come in workpiece for down milling.

Moreover, a comparison between cutting force measurements obtained by using a Kistler dynamometer and from analysis of AMB command voltage underlines the less accuracy on cutting forces measurements of Kistler dynamometer 9225B.

The low bandwidth of the Kistler dynamometer (about 650 Hz) limits the use of this sensor in the case of high-speed milling, because significant excitation frequency is two times and seven times the tooth passing frequency respectively in the case of slotting and peripheral milling.

However, gyroscopic effects of the rotor motion limit the use of the current version of this method to stable conditions. A semi analytical approach allowing the indirect determination of cutting forces including the Coriolis effect is in development.

References

- [1] S. Auchet, P. Chevrier, M. Lacour, P. Lipinski, A new method of cutting force measurement based on command voltages of Active Electro-Magnetic Bearings, *under submission*, International Journal of Machine Tools & Manufacture
- [2] S. Auchet, P. Chevrier, M. Lacour, P. Lipinski, Mesure indirecte de la puissance de coupe, in : Proc. 3^{ème} assises UGV, Clermont-Ferrand, Mars 2004; pp. 51-58
- [3] F. Lapujoulade, Measuring of cutting forces during fast transient periods, in : Proc. First French and German Conference on High Speed Machining, Metz, Juin 1997, pp. 372-376.
- [4] F. Lapujoulade, G. Coffignal, J. Pimont, Cutting forces evaluation during high speed milling, in : Proc. Second Conference International IDMME'98, Compiègne, Mai 1998, Vol. 2 pp. 541-549.
- [5] N. Tounsi, A. Otho, Dynamic cutting force measuring, International Journal of Machine Tools & Manufacture, 40 (2000) 1157-1170.
- [6] Y. Altintas, Prediction of cutting forces and tool breakage in milling from feed drive current measurement, ASME, Journal of Engineering for Industry, 114 (1992) 386-392.
- [7] T.-Y. Kim and J. Kim, Adaptive cutting force control for a machining centre by using indirect cutting force measurements, International Journal of Machine Tools & Manufacture 36 (1996) 926-937.
- [8] Y.-H. Jeong, D.-W. Cho, Estimating cutting force from rotating and stationary feed motor currents on a milling machine, International Journal of Machine Tools & Manufacture, 42 (2002) 1559-1566.
- [9] I. Korkut, A dynamometer design and its construction for milling operation, Materials & Design, 24 (2003) 631-637.

EXPERIMENTAL METHOD FOR CONCRETE TESTING AT HIGH STRAIN RATE TENSILE LOADING

J. R. Klepaczko and A. Brara *

*Associate Professor, National Center of Integrated Research in Building Engineering (CNERIB); Algiers, Algeria
Professor Emeritus, Laboratory of Physics and Mechanics of Materials, Metz University, France

Summary: The understanding of concrete responses to short-lived stresses and high amplitude impulse loads are of vital importance in design and analysis of protective structures. However, under such loading the strength data of most brittle materials, amongst other concrete, are very limited. For instance, the data concerning the dynamic tensile behavior of concrete beyond the strain rate of about 20 s^{-1} are practically non-existent. The shortage of the information on this subject might be attributed primarily to an insufficiently developed base for dynamic tests applicable for brittle materials.

An original experimental method for investigating the dynamic tensile strength of brittle materials such as concrete is developed in the Laboratory of Physics and Mechanics of Materials of Metz. The experimental method suggested by Klepaczko is based on a judicious combination of the Hopkinson bar principle and the spalling technique. This method allowed for reaching very high loading rates of about 5000 GPa/s (corresponding to strain rate up to 120 s^{-1}).

An experimental program on concrete was performed with this new equipment. The mean trends of the dynamic tensile behavior found in the literature for high loading rates are confirmed by the experimental results obtained, specially the continuation of the drastically strong increase of the tensile strength beyond the strain rate threshold of 1 s^{-1} . Those additional results permit for better estimation of the concrete strength in tension and are used by many authors to model the concrete behavior within the following range of strain rates: 20 s^{-1} to 120 s^{-1} .

INTRODUCTION

In the engineering practice, it is known that concrete inherently weak in tension is generally used as compressive member material in most structures. However, tensile behavior is a more intrinsic characteristic of concrete material. For a more accurate analysis and design optimization of some modern protective structures, account must be taken of the tensile strength of this material. Despite the important research effort devoted during the past several decades, the experimental and as well as the theoretical knowledge with regard to the tensile dynamic behavior of concrete are however still quantitatively limited. More emphasis is typically placed on the compressive behavior, for which more data is available (at strain rates in the order of 10 s^{-1} to 1000 s^{-1}), and less on the tensile response. In experiment the maximum strain rate reached in tension is less than 20 s^{-1} and the physical mechanism governing the dynamic tensile failure is not well understood. The lack of such experimental data is essentially due to the difficulty of accurate measurement of tensile strength for brittle or quasi-brittle materials like ceramics, rock and concrete. This difficulty is strongly exacerbated when it concerns dynamic experimentation, for which all parameters could possibly affect the experimental results, and their subsequent interpretation. During the last decade, a vast research program devoted to the interaction between geo-materials, environment and civil engineering works, GEO [1], was conducted by the French laboratory network. One group of these laboratories was in charge of the investigation axis concerning the 'behavior of concrete structures at high strain rates', with the main objective to provide experimental data and to model the crushing phenomenon and spalling of concrete under impact loading. The research project attributed to the Laboratory of Physics and Mechanics of Materials (LPMM, Metz University, France) was the experimental characterization of tensile behavior of concrete. In this framework, a new experimental method based on the Hopkinson bar is developed under the direction of Klepaczko, for estimating the tensile strength of concrete in strain rate ranged from 20 s^{-1} to 120 s^{-1} . In this paper the existing dynamic tensile testing techniques of concrete and their results are succinctly reported, followed by the description of the original method developed in the LPMM. Some results obtained by means of this method are presented and compared with those existing in the literature.

DYNAMIC TENSILE TESTING METHODS OF CONCRETE AND RESULTS

Experimental methods and results

The dynamic tensile experiments on concrete reported in the literature are performed in various test configurations. Nevertheless, the major test methods can be categorized globally as follows: the Constant Strain Rate Test, adapted to tension mode in SHPB (Split Hopkinson Pressure Bar) test, and finally all tests based on "the Stress Wave Technique", as described in [2]. The constant strain rate test constitutes an ideal test suitable for strain softening materials such as concrete, which can be done in tension and bending. Tests are carried at a certain strain rate that remains constant throughout the whole experiment. It should be noted that high strain rates are not always possible to reach when such type of tests is applied, because the difficulty to control the boundary conditions and to ascertain the uniformity of stress along the specimen due to the wave propagation. Higher strain rates up to about 20 s^{-1} can be reached with the conversion into tension of the SHPB apparatus, [3]. The first adaptation was developed in Delft University of Technology, [4]. This test set up consists of two coaxial elastic aluminum bars between which concrete specimen is

sandwiched. Tensile stress pulses are generated by a weight hitting vertically an anvil fixed at the end of the incident vertical bar. Another adaptation of SHPB called the Splitting Tensile Test consisted application the load along the specimen diameter, in "Brazilian test" configuration, [5]. The principal problem of the techniques based on the Hopkinson bar principle in compression is to find the optimal compromise between the size of the bars and the strain rate threshold, which are antagonistic parameters in the wave propagation theory. The same loading rate range was reached also by the use of the so-called "Stress Wave Technique", [6]. In this experiment, typical cylindrical or prismatic specimens are impacted at one end with high-velocity strikers. When the wave reaches the other end of the cylinder it is reflected as tensile wave, which causes the concrete to spall. For the stress measurements, the specimens are instrumented with strain gauge resistance.

The experimental results of the last decades obtained by these various test methods are gathered in several reviews, [7,8]. In those retrospectives, the material studied was generally dry and wet micro- or mini-concrete (with approx. 10 mm maximum aggregate size), in the form of cylindrical and prismatic specimens with relatively small size. The concrete tested was from few days to several months aged and with compressive strength varying from 14 MPa up to about 70 MPa. The experimental database of the last decades concerning the dynamic tensile behavior of concrete pointed clearly on "the rate effect", that is the increase of the tensile strength with strain rate. This effect of strain rate on the tensile strengths is typically reported as dynamic increase factor (DIF), i.e. the ratio of dynamic to quasi-static strength versus strain rate on a semi-log or log-log scale. The enhancement is characterized by a slight continuous increase of the maximum recorded strength in the range between static loading and strain rate of about $1/s$ and thereafter a steep increase of this strength for highest strain rate.

For strain rates lower than about $1 s^{-1}$, the observed phenomena is attributed to the presence of excess moisture in concrete, [9,10]. The relatively higher strengths in dynamics can be due to micro-inertia or viscous-type forces acting on microcracks at the meso-level. Nevertheless, at strain rates higher than $1 s^{-1}$ both wet and dry concretes exhibit almost the same significant strain rate sensitivity and the physical reasons of this phenomenon pose an open question.

The analysis of the existing experimental methods presented above and observation of the current trends in testing of concrete in dynamic tension leads to the conclusion that the best configuration to reach high strain rates in tension is the arrangement of cylindrical striker, instrumented Hopkinson bar and a cylindrical, relatively long specimen. Such arrangement permits for many different variations in geometry and measurements. For example, the specimen can be instrumented or not. In the case of instrumentation, it will play a role of Hopkinson bar as well. The level of the wave analysis may be also very different. This conclusion conducted to develop the new experimental method in the Laboratory of Physics and Mechanics of Materials of Metz University. This efficient method of simple use combining the Hopkinson bar principle and the stress wave technique allowed for reaching strain rate in tension above $100 s^{-1}$.

THE EXPERIMENTAL METHOD

Test setup and loading procedure

The setup consists of an air launcher of cylindrical projectiles and a Hopkinson bar as measuring tool in tight contact colinearly with a concrete specimen. The cylindrical bars arrangement is shown schematically in Fig. 1. The Hopkinson bar of is instrumented with three SR stations and made of hard aluminium alloy (6065-T5). Projectiles are made of the same alloy and with different lengths. The specimens tested are not instrumented.

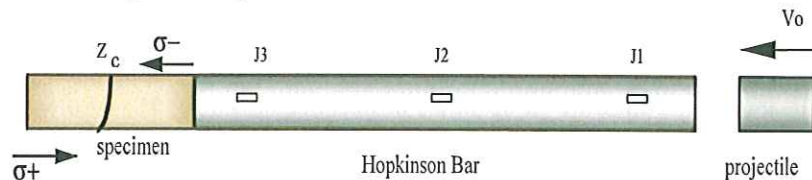


Fig.1: Scheme of the experimental arrangement and the loading principle.

When the projectile impacts the measuring bar a longitudinal compressive incident stress wave σ_I is induced. The compressive pulse propagates along the measuring bar. When arrived at the interface bar-specimen, part of the incident stress will be transmitted as compression wave σ_T into the specimen and a small part will be 15^{th} reflected as σ_R as tension wave, back of the measuring bar. The partitioning of the incident stress results from

the difference of the effective impedances between the measuring bar and the specimen. The compressive pulse σ_T transmitted into the specimen propagates along upon its arrival at the free end, and is reflected as a tensile pulse σ^+ and superposed upon the still arriving tail σ^- . The resulting stress distribution leads to tensile stresses increasing with the distance from the free end and fast growing in time. Wherever the peak value of the resulting stress distribution reaches the level of the tensile strength, the spalling of material occurs. The relatively short length of the striker bars (80 mm, 120 mm and 160 mm) allows for reaching elevated loading rates.

Data acquisition system

The recovered data after each test are the recorded pulses σ_I and σ_R at the three measuring stations and the fracture profile of the specimen. This latter accurately measured and digitalized, gives the spalling sites reported from the free end of the reconstituted specimen. The propagating pulses are recorded by means of three pairs of strain gages cemented to the bar surface. Two of these gages (J1 and J2) are situated each at 120 mm from the Hopkinson bar ends, and one (J2) is cemented in the middle of the bar. These gages are connected to amplifiers (band pass 1.0 MHz), then to four channel oscilloscopes with high sampling rates (1.0 GHz), recording at the same time the signals respectively in (J1, J2), and (J2, J3). These signals are visualized and stored under numerical format by PC's connected to the oscilloscopes, Fig. 2.

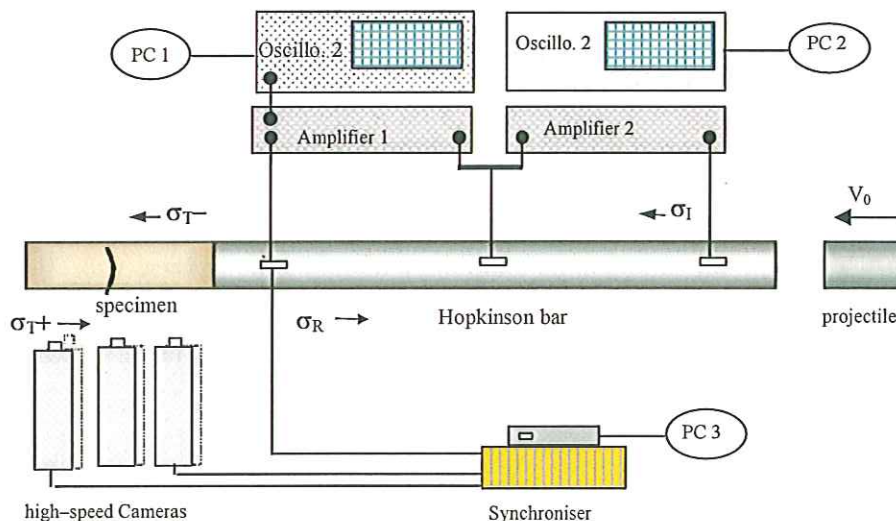


Fig. 2. Schematic of data acquisition system with six high-speed CCD cameras

The wave propagation in the Hopkinson bar is considered by taking into account the geometrical dispersion, as well as the recent theoretical developments concerning the signal processing, see [11]. The incident and reflected pulses are corrected for the geometrical dispersion by time shifting to bar-specimen interface, where the transmitted pulse into specimen is determined. At the bar-specimen contact surface, the force equilibrium during the contact time as well as the propagation of the transmitted pulse are based on the unidimensional theory. The superposition of the transmitted pulse numerically simulated gives the chronological and also spatial evolution (assuming a constant longitudinal wave velocity C_0) of the maximum tensile stress along the specimen. Considering an instantaneous and local fracture, the accurate measurement of the site of spall Z_c , when confronted with the numerically evaluated resulting tensile stress evolution in the specimen, allows for determination of the spall strength σ_F .

It should be noted that application of high amplitudes of the incident wave leads to a consecutive multiple fracturing of the specimen, in such situation the chronology of spalling is very important. When a multiple spalling occurs only the first one is analyzed. In order to find the chronology of spalling, as well as to observe development of failure, a coupled arrangement of six fast CCD cameras has been applied. These cameras with a framing rate up to 10^6 frames per second, are triggered successively with a chosen time interval (from 1 μ s to 10 ms.) thanks a set an electronic cards named the synchronizer. The numerical pictures are stored by fast memory units connected to each camera and recovered by means of a demultiplexer in a PC, using an adapted program. For more details concerning the new experimental technique, the reader may be interested in [12].

Concrete and specimen

The mechanical characteristics and the composition of the tested concrete are given in Table 1. The method of preparation of this concrete consists in preparation of homogeneous large blocks and next trepanation of the cylindrical specimens of diameter 40 mm and length 120 mm. Both faces of each specimen were machined to achieve parallel and flat surfaces. The specimens were protected in the wet state by a plastic foil and aluminum cover. The composition of the concrete is a compromise between a standard concrete with larger aggregate and the heterogeneity in relation to the specimen dimensions.

TABLE 1: Composition and mechanical characteristics of the studied concrete

Mix proportions	
Water	200 kg/m ³
Portland cement HP	400 kg/m ³
Fine aggregate 0-2 mm	1783 kg/m ³
Mechanical characteristics	
Density	2395 kg/m ³
Young's Modulus	35 GPa
Quasi-static compressive strength	42 MPa
Quasi-static tensile strength	4 MPa

EXPERIMENTAL RESULTS

Several series of tests on wet micro-concrete specimens were performed with an impact velocity varying between 7 and 15 m/s, corresponding for mean values of transmitted compression stresses amplitudes ranged from 30 to 90 MPa. For each impact velocity, 3 to 5 specimens have been tested, for which one and sometimes two or even three fractures have been obtained. The failure profiles of the specimens are almost flat. Indeed, the measured failure position show a weak scattering from only 1 to 3%, which leads to confirm the uniformity of the loading stress profiles and the specimens homogeneity, justifying thus the hypothesis of the unidimensional wave propagation in the specimen. The mean values of the loading rates for the experimentally determined spalling sites are very high and varied from 800 up to about 5000 GPa/s.

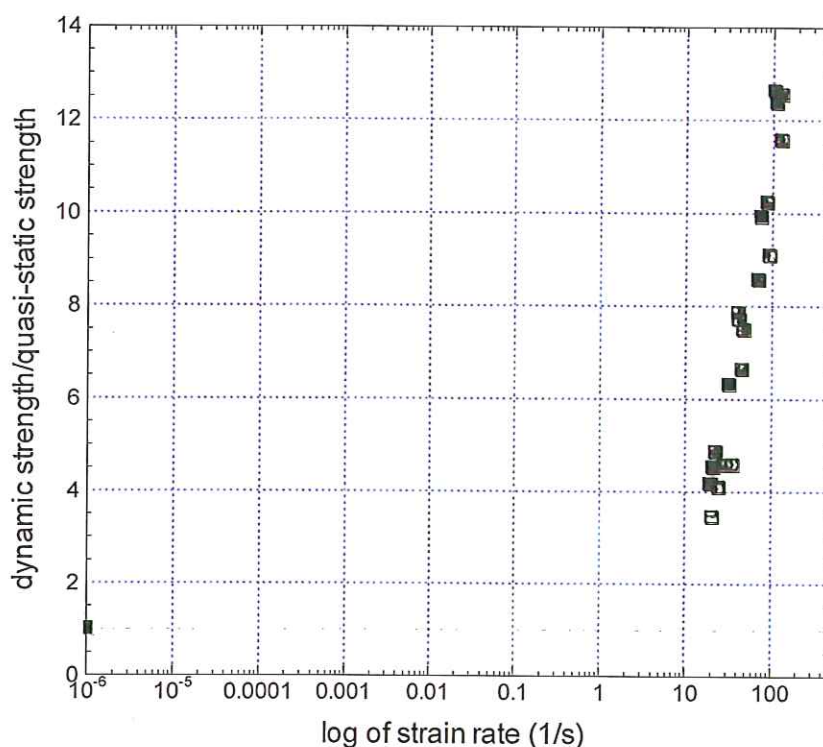


Fig. 3. Tensile strength ratios for wet concrete as function of (log) strain rate

For constant dynamic Young's modulus assumed as $E = 41.5 \text{ GPa}$, the corresponding strain rates are ranged from 20 s^{-1} to 120 s^{-1} . The obtained results reveal a substantial increase of the tensile strength as a function of the strain rate for the wet mini-concrete, Fig. 3. In the strain rate range studied, the DIF varies from 4 up to 10.

These critical stresses of spalling obtained analytically by wave analysis were confronted to those determined through the velocity of ejected specimen fragments during the fracture process, measured by means of the CCD cameras. The considerable increase of the tensile strength is corroborated by the velocity measurement via the sequence of framing camera photographs of the tests. Some images of the CCD cameras with consecutive stages of the specimen ejection are shown in Fig. 4. The specimen is broken into two pieces with relatively flat fracture surface. The critical stress evaluated by the ejection velocity in case of the test shown in Fig. 4 is $\sigma_F = 57 \text{ MPa}$, very close to the critical fracture stress obtained by the wave analysis which is 53 MPa . This test was performed with the mean strain rate of about 112 s^{-1} .

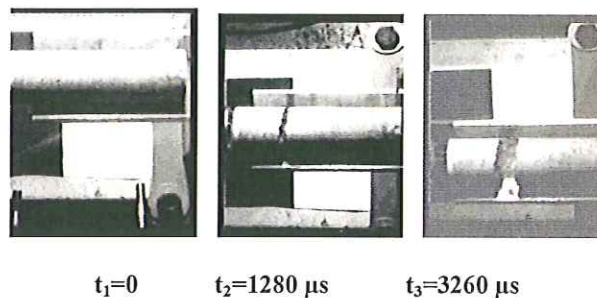


Fig.4. Camera photographs sequence of a specimen fracture process

The results obtained with the new experimental method are compared to those found in the literature. Nevertheless, some authors reported results of experiments conducted at strain rates higher than 1 s^{-1} , see [6,8] and all references therein. The evolution of the relative tensile strength versus the logarithm of strain rate of the experiment reported in this paper and those obtained by other authors are gathered in Fig. 5. It appears clearly that the relative strength increases continuously without saturation when the strain rate is increased.

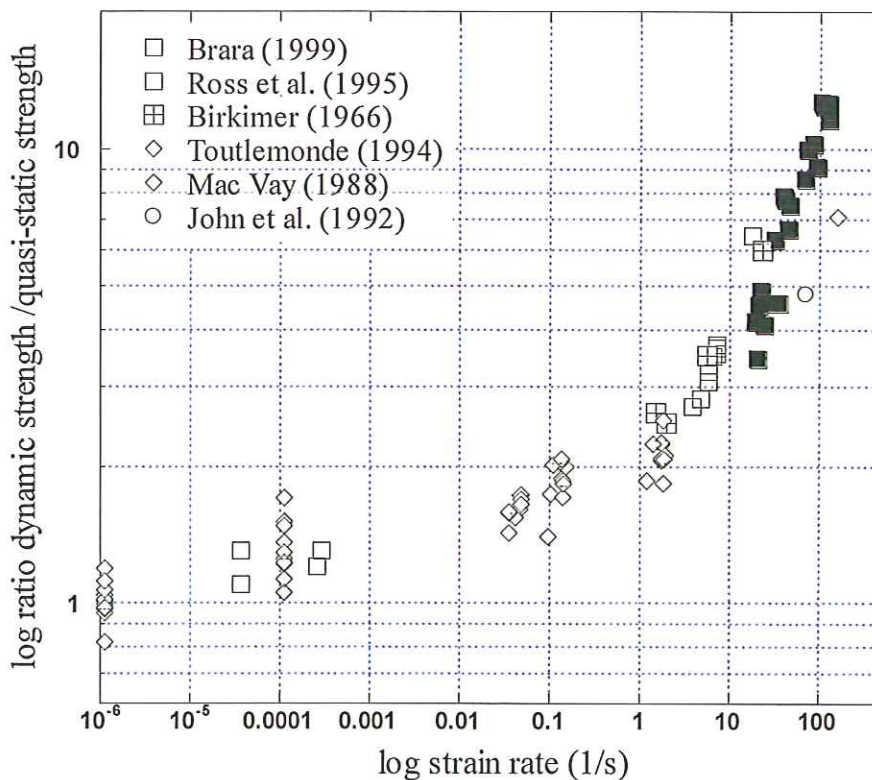


Fig. 5. Comparison of various experimental data, after [6,8]

A direct observation of the fractured surfaces by the stereographic microscope confirmed that the surfaces are very flat. Further, some pictures were taken with the optical microscope, they clearly shown that at short loading times majority of aggregates were cleaved. At very short loading time even very small aggregates were also cleaved. This confirms observations reported by different authors, for example [13], about domination of the intra-granular separation at high strain rates in tension.

These results were used by many researchers to model successfully the dynamic tensile behavior of concrete with different numerical codes (Discrete Element Method, Finite Element Method), amongst others [14,15, 16].

CONCLUSION

The dynamic tension tests completed with the new experimental arrangement, have shown a possibility to reach very high strain rates in tension for concrete and perhaps also for brittle materials like ceramics. In the range of strain rate from 20 s^{-1} to 120 s^{-1} , data on dynamic tensile strength of concrete are practically non existent in the literature.

The experimental investigation conducted by means of this technique permitted to produce additional data and better define the concrete tensile strength at high strain rates. The mean trends of the dynamic tensile behavior of concrete found in the literature are confirmed by the experimental results obtained, specially the substantial increase of the tensile strength with at high strain rates. At strain rates of about 100 s^{-1} , the dynamic tensile strength of concrete can reach ten times the quasi-static one. The steep increase of the tensile strength at high strain rates could be explained by the inertia of micro-cracking and an extensive micro-cracking forced to propagate throughout stronger areas of the material notably the aggregates. The obtained results constitutes an appreciable reference and are used successfully by many researchers to model the dynamic failure of concrete.

References

- [1] Bailly P., Final Scientific Report, behavior of structures at high strain rates - concrete dynamic behavior, Laboratories Network, Geomateriaux – Environment - Ouvrage (GEO), 1999 (in French).
- [2] Abbott, B. W., and Cornish, R. H., , A Stress-Wave Technique for Determining the Tensile Strength of Brittle Materials, *Experimental Mechanics*, (1965), pp. 148-153.
- [3] Kolsky, H., An investigation of the mechanical properties of materials at very high rates of loading, *Proceedings, Physical Society of London, Section B*, V. 62, (1949), pp. 676-704.
- [4] Körmeling, H.A., Zielinski, A.J. and Reinhardt, H.W. Experiments on concrete under single and repeated uniaxial impact tensile loading, *Stevin Report 5-80-3*, Delft University, Nederland, (1980).
- [5] Ross, C. A., Thompson, P.Y. and Tedesco, J. W., , Split Hopkinson Pressure Bar Tests on Concrete and Mortar in Tension and Compression, *ACI Material Journal*, V.86, N°5, (1989), pp. 475-481.
- [6] Mellinger, F. M., Birkimer, D. L., Measurement of stress and strain on cylindrical test specimens of rocks and concrete under impact loading, *Technical report 4-46*, U.S. Army Corps of Engineers, Ohio River Division Laboratories, Cincinnati, Ohio, (1966), pp. 71.
- [7] Brara, A., Klepaczko, J.R., and Kruszka, L., , Tensile testing and modeling of concrete under high loading rates, *Proceedings, Brittle Matrix Composites 5 (BMC5)*, A. M. Brandt, V. C. Li and I. H. Marshall eds, Warsaw, Poland, (1997), pp. 281-290.
- [8] Malvar, L. J., and Ross C. A., , Review of Strain Rate Effects for Concrete in Tension, *ACI Material J.* , V. 95, N°6, 1998), pp. 735-739.
- [9] Toutlemonde, F., and Rossi, P., Major Parameters Governing Concrete Dynamic Behavior and Dynamic Failure of Concrete Structures, *DYMAT journal*, V. 2, N°1, (1995), pp. 69-77
- [10] Ross, C. A., Jerome, D. M., Tedesco, J. W., and Hugues, M. L. , Moisture and Strain Rate Effects on Concrete Strength, *ACI Materials Journal* , V. 93, N°3, (1996), pp.293-300.
- [11] Klepaczko, J. R., and Brara, A., An Experimental Method for Dynamic Tensile Testing of Concrete by Spalling, *International Journal of Impact Engineering*, V. 25, (2001), pp. 387-409.
- [12] Brara, A., Experimental Study of Dynamic Tension of Concrete via Spalling, PhD Thesis, Laboratory of Physics and Mechanics of Materials, Metz University, France (1999).
- [13] Bishoffs P. H., Perry S. H., Compressive behaviour of concrete under high strain rates, *Materials and Structures*, 24, (1991), pp. 425-450.
- [14] Brara A., Camborde F., Klepaczko J. R., Mariotti C., , Experimental and numerical study of concrete at high strain rate in tension, *Mechanics of Materials*, V. 32, pp. 33-4T *Journal*, 2, n°1, (2001), pp. 69-77.
- [15] Hild, F., Denoual, C., Forquin, P., and Brajer, X., On the probabilistic-deterministic transition involved in a fragmentation process of brittle materials, *Computers and structures*, V. 81, Issue 12, (2003), pp. 1241-1253.
- [14] Gatuignt F., Pijaudier-Cabot G., Coupled Gurson Plasticity and Damage Model for Concrete Structures in Dynamics, 15th ASCE Engineering Mechanics Conference, Columbia University, New York, USA (2002).

A METHOD FOR IDENTIFICATION OF MATERIAL BEHAVIOUR FROM HIGH SPEED COMPRESSION TEST USING A SERVO-HYDRAULIC PRESS

Stéphanie Diot, Adinel Gavrus, Dominique Guines and Eric Ragneau

*Laboratoire de Génie Civil et Génie Mécanique (LGCGM, EA 3217-3218),
Insa de Rennes, 20 Av des Buttes de Coësmes, 35043 Rennes, France*

Summary: Numerical simulations of dynamic material forming processes require accurate constitutive models describing the materials behaviour at large plastic strains (50%-150%), at high strain rates (up to 10^2 - 10^3 s⁻¹) and taking into account adiabatic heating and thermal softening. The major difficulty is that few experimental tests are enabled to reach all these criteria. For a few years, several studies have been carried out on hydraulic machines provided with a dynamic jack. However, for high strain rates, the load measurement is disturbed by the elastic response of the experimental set-up, proved by the important oscillations with appear on the load-displacements variation. This contribution proposes to improve the experimental dynamic compression test analysis and present a new method to convert experimental data into a true stress-strain relationship. The method is based on a finite element model of the experimental set-up and use the inverse analysis principle.

INTRODUCTION

Several industrial applications, such as dynamic material forming or machining processes, require to improve the analysis of material behaviour in order to describe correctly the material flow corresponding to high speed loadings. The choice of the constitutive model and the determination of its parameters should be made from tests generating such severe conditions: elevated strain rates, large strains and important rise of the temperature. Sometimes it is very difficult to find a mechanical test that enables to reach simultaneously all the requirements. For machining and dynamic material forming it is general consented that the axis-symmetrical compression is the most suitable experimental test. The plastic strain can reach 100% and a large range of the strain rate can be obtained from different upsetting velocities and using a special specimen shape. However, for conventional machines, the strain rates are limited to a few tens of s⁻¹, whereas one would like to characterise materials up to 10^3 – 10^4 s⁻¹. To obtain higher strain rates (more than 10^3 s⁻¹), a special experimental set-up, named Split Hopkinson Pressure Bars [1,2] can be used, but the plastic strain reached during the test is limited at 25%-50% and is not sufficient for a dynamic material forming characterisation. A suitable upsetting test, giving both large strain and large strain rates requirements, can be obtained from a servo-hydraulic machine provided with a dynamic hydraulic jack that can reach 10 m/s. If a classical load cell is used, the experimental tests showed that the load/times curves are disturbed by important oscillations. Several researches highlighted this phenomenon and different approaches were explored. The first one concerns the use of a filtering method to convert the load /displacement variation into the true stress-strain curves [3]. The second one search to analyse the dynamic phenomena and to avoid the load oscillations increasing the first eigen frequency of the experimental set-up via a shape optimisation method [4,5]. The principal aim of this work is to propose a new method to analyse and identify the material behaviour from high speed compression tests.

A first analysis concerns the dynamic response of the experimental set-up using a finite element model taking into account the elastic and inertia effects of the whole experimental structure and starting from a well-known elastic-plastic behaviour given from a standard specimen. The obtained numerical load-times variation and the corresponding eigen frequencies are compared with the experimental ones. The good correlation between the numerical results and the experiment valid the relevance of numerical description, especially concerning the observed dynamic phenomena. Because the analysis of rheological behaviour for high temperatures requires a special experimental equipment, a shape optimisation of the whole experimental set-up in order to reduce the load oscillations seems very difficult. Therefore a parameter calibration of the elastic set-up model (via an optimisation tool) is sufficient to insure the quantitative capability of the building numerical model to describe real dynamic phenomena.

The second part is focused on the identification of the material behaviour by mean of a two-step sequential identification method. In a first step the variation of the load on the specimen interfaces is estimated from the global responses of the load cell. Using the numerical model, which describe the whole structure existing between specimen and load cell, an inverse problem can be then formulated, regarding the load/times variation on the specimen interface as an unknown boundary condition. Knowing all the loading data at the contact surfaces of the specimen with the tools: impact velocity on the upper surface and variation of the load on the low surface, the constitutive behaviour of the specimen material can be obtained from a thermo-elasto-viscoplastic finite element computation. Finally, behaviour of a XC10 steel, submitted to different compression speeds (between $3 \cdot 10^{-4}$ and 3 m/s) and heated at different temperatures (200°C – 400°C) will be presented.

NUMERICAL DYNAMIC ANALYSIS OF THE EXPERIMENTAL SET-UP

The dynamic compression tests are carried out on a computer-controlled servo-hydraulic testing machine provided with a dynamic jack allowing to obtain a maximum impact velocity of 9 m/s. A classical load cell fixed on the equipment rack is used to measure the time load variation and a LVDT displacement sensor, set on the top of the jack, measure the corresponding displacement. The experimental measurement signals are acquired at a frequency of 5 MHz to avoid all problems caused by electronic equipment. For high temperature tests a furnace is set on the machine and a water coolant part is put between the sensor and the heated parts in order to protect the load cell from heating. An upper tool is chosen out of the furnace so as to protect the jack from high temperatures. The whole experimental compression set-up is illustrated in Fig. 1-a. As the inertia effects generated by the dynamic tests are quite important, special specimens were designed in order to avoid an overload of the sensor and to control the impact velocity [6]. The obtained specimen geometry is shown in Fig1-b and has been used successfully in quasi-static or dynamic loading.

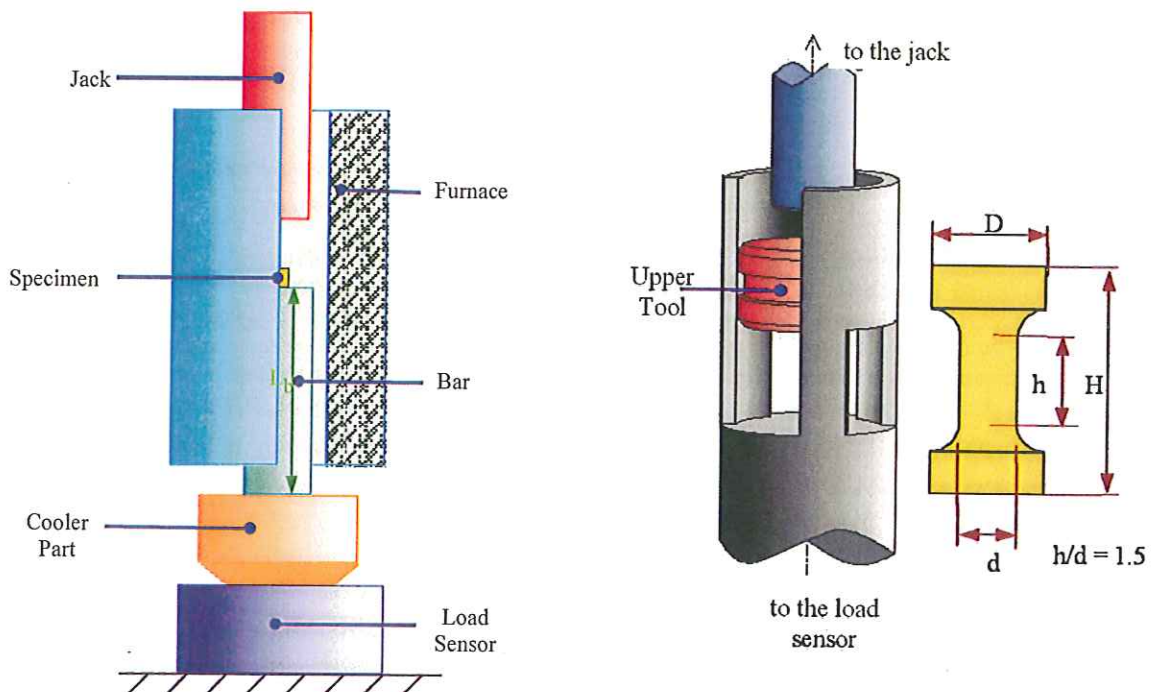


Fig. 1. a- Experimental set-up of servo-hydraulic compression machine, b- Specimen assembly and optimal geometry

According to a maximum load of 25 KN, the following optimal dimensions are recommended for a steel specimen: heights of $H = 16\text{mm}$, $h = 6\text{mm}$ and diameters of $D = 8\text{mm}$, $d = 4\text{mm}$. Moreover a numerical FE model of classical compression tests was shown an independence of the load with respect to the friction on the specimen-tools interfaces, consequently the influence of friction phenomenon can be neglected [7]. Actually, the principal problem on experimental characterization of high speed dynamic tests is the appearance of important oscillations on the load-displacement curves. However, it is generally assumed that for a dynamic loading, the most important mechanical characteristics are represented by inertia effect, elastic properties and shape of the structure [8]. A precise comprehension of these phenomena requires to analyse rigorously the dynamic behaviour of whole experimental structure, essentially represented here by the assembly of the lower bar, water cooler part and load sensor (Fig. 2-a). Concerning the impact velocity on the upper specimen surface, it can be controlled by an electro-hydraulic regulation of the jack speed and can be regarded as an well-known boundary condition for the specimen. It is then possible to use a dynamic FE model starting from the structure mesh (Fig. 2-b). As the dynamic behaviour of the experimental assembly can't be analysed from a direct impact of the chosen structure, which leads to an overload of the cell measure, a specimen with a lower yield stress must be added. A first study has been performed for a 50CrMo4 steel specimen using a known elasto-plastic behaviour, previously identified from other experimental tests, varying the strain rates from 0.05 s^{-1} to 5 s^{-1} . The behaviour of all others parts is considered only as elastic. More details on the numerical results obtained with CASTEM2000 software have been already presented by Diot, S. [8]. Analysis of the Eigen frequencies has shown a very good agreement between the computed values and the experimental ones. Concerning the load-displacement variation, a comparison between the experimental and numerical model, for a compression test carried out at 3 m/s and at a temperature of 25°C, is presented in Fig. 2-c.

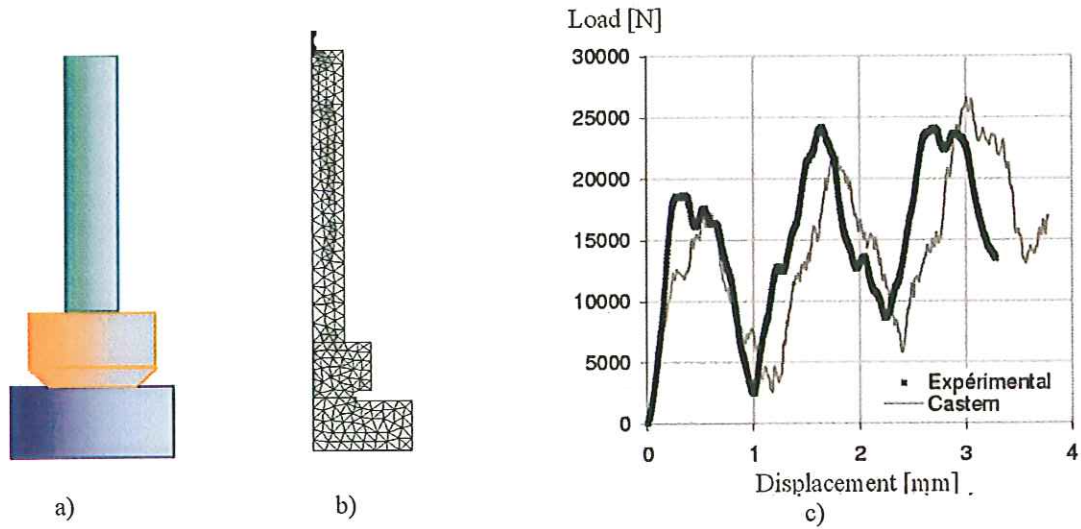


Fig. 2. a- Experimental structure ($L_b = 244$ mm), b- Finite Element model, c- Comparison between experiment and computation for a compression of a 50CrMo4 steel at 3 m/s.

The good correlation, obtained especially for the oscillations shape, shows that a dynamic FE model, based only on an inertia phenomenon and elastic behaviour, allows to reproduce the observed experimental dynamic effects. These results permits to confirm that the principal phenomenon of impact loadings is the propagation of an elastic deformation, named elastic strain or elastic stress wave. Because the numerical model requires to define the elastic properties characterising the structure rigidity, it is possible to consider that the load magnitude is essentially sensitive with respect to the following parameters: Young modulus E_b and material density ρ_b of the bar and of the cooler part (E_c, ρ_c), equivalent stiffness K_s and equivalent mass c for the load sensor. Concerning the small deviation of the computed curve as compared to the experimental one, caused by the difference between the delay of the elastic wave propagation, an offset time Δt_d can be add as a additional unknown parameter. Consequently the global elastic dynamic behaviour of the experimental set-up can be completely defined by the set of the following structural parameters $P_S = \{\Delta t_d, E_b, \rho_b, K_s, K_S\}$.

PARAMETER CALIBRATION OF THE NUMERICAL MODEL

On a computational point of view, to obtain a correct prediction of the proposed numerical model, first is necessary to perform a parameter calibration. To find the optimal values of structural parameters it is then necessary to use an optimisation method, minimizing the deviation between the observed experimental data and the corresponding numerical results.

Structural Parameters	Initial Values	Identified Values
K_s [KN/mm]	5000	6051.049
M_s [Kg]	4.3	3.896
E_b [MPa]	211000	217984
ρ_b [Kgm ⁻³]	8190	7884.571
Δt_{d1} [s]	7.00E-5	7.8644E-5
Δt_{d2} [s]	6.00E-5	6.7236E-5
Δt_{d3} [s]	4.00E-5	3.4989E-5
Δt_{d4} [s]	3.00E-5	2.3183E-5
Deviation [%]	33.8	21.3

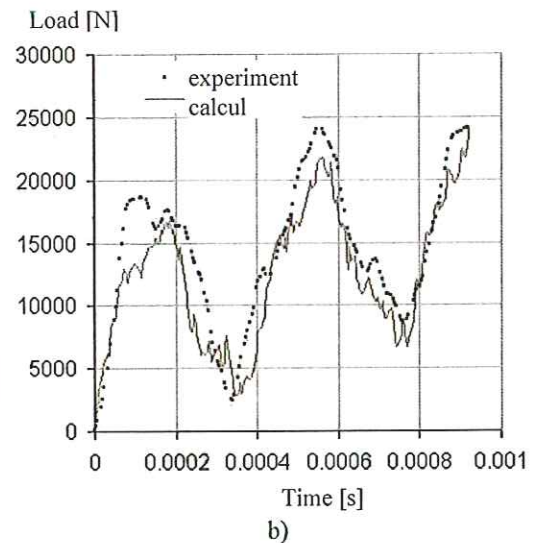


Fig. 3. a-Identified values of structural parameters (OPTPAR software), b- Comparison between the numerical model and experiment after structural parameter calibration (configuration I : $L_b = 244$ mm, with the cooler part)

To increase the parameter sensitivity and the quality of the parameter identification, four different design of the experimental structure have been chosen, starting from two different lengths of the bar ($L_b = 244$ mm and $L_b = 56$ mm) and using two options for the mechanical assembly: a first one which introduce the cooler part and a second one without this part. Choosing a non-linear least-squares method, the cost function which must to be minimized with respect to the structural parameter is defined here by :

$$Q(P_s) = \sum_{i=1}^{N_c} \sum_{l=1}^{N_i} \left[F_{i,l}^c(P_s, t + \Delta t_{d_i}) - F_{i,l}^e(t) \right]^2 / \sum_{i=1}^{N_c} \sum_{l=1}^{N_i} \left[F_{i,l}^e(t) \right]^2 \quad (1)$$

where N_i represents the number of the measured data corresponding to each structure configuration i , N_c is the number of experimental structures ($N_c = 4$), F^e is the experimental loads and F^c the computed ones.

Concerning the parameters values and the load variation, the obtained results are presented in Fig. 3. A good agreement is obtained between the experimental and numerical predictions, so the proposed numerical model can be used to analyse material behaviour undergoing impact loadings.

IDENTIFICATION ALGORITHM OF MATERIAL BEHAVIOUR

Thermo-elasto-viscoplastic behaviour of metallic materials undergoing a dynamic compression impact requires to convert the measured load-displacement variation into the true stress-strain curves. For an isotropic and homogeneous material these ones must to be estimated using an available constitutive equation, expressing the equivalent Von-Mises stress $\bar{\sigma}$ as a function of the cumulated plastic strain $\bar{\epsilon}$, generalized strain-rates $\dot{\bar{\epsilon}}$ and temperature T :

$$\bar{\sigma} = \sigma_0(P_c, \bar{\epsilon}, \dot{\bar{\epsilon}}, T) \quad (2)$$

The previous dynamic analysis of the experimental test has shown that it is very difficult to obtain directly this material behaviour information and a method based on the inverse analysis principle must be used. Firstly, we can search to evaluate the variation of the load on the low bar-specimen interface $F_s^e(\Delta l)$, regarded as an unknown boundary condition, starting from the load-sensor measurements $F^e(\Delta l)$ (Fig. 4-a).

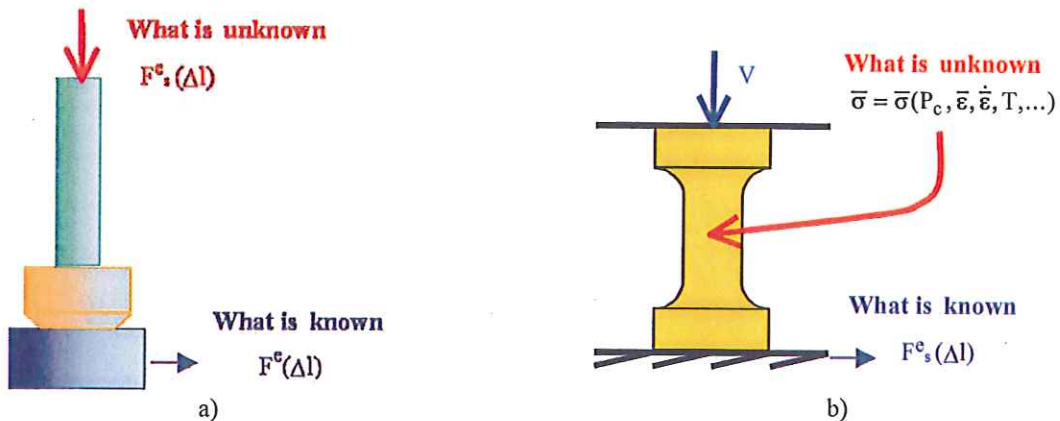


Fig. 4. a- Definition of the first inverse problem, b- Model of the rheological identification problem

If a numerical finite element simulation is used for elastic deformation of the structure part, an inverse problem can be formulated: *What is the load function F_s^e , applied on the upper interface, which permits to obtain the observed experimental values F^e on the load sensor?* In order to obtain a classical identification problem, a parametric formulation of the $F_s^e(\Delta l)$ is needed, using a piece-wise linear interpolation method or an approximate relationship given by:

$$F_s^e = a_1 \Delta l^{a_2} \exp(a_3 \Delta l) \quad (3)$$

The main advantage of the last one is the reduced number of the unknown parameters $P_a = \{a_1, a_2, a_3\}$ which allows to a smallest computing times of the identification procedure. The identification problem is then defined by:

$$\text{find } P_a \text{ which minimizes } Q(P_a) = \frac{\sum_{i=1}^{N_e} \left[\left(\int_{s_i}^e (P_a) - F_i^e \right)^2 \right]}{\sum_{i=1}^{N_e} \left[\int_{s_i}^e \right]} \quad (4)$$

Material behaviour can be now obtained from a second numerical analysis, limited only on the specimen deformation, defining the boundary conditions as a constant impact velocity V on the upper surface and as a sticking condition on the lower surface (Fig. 4-b). The very small displacement of the specimen-bar interfaces is neglected as compared to the upper surface one. Starting from a chosen constitutive law it is then possible to obtain the constitutive parameters P_c from a rheological identification problem: *What is the parameters values P_c defining the constitutive behaviour which permits to obtain the close values of the observed loads F_s^e on the specimen interface?* formulated as:

$$\text{find } P_c \text{ which minimizes } Q(P_c) = \frac{\sum_{i=1}^{N_e} \left[\left(\int_{s_i}^{e_c} (P_c) - F_{s_i}^e \right)^2 \right]}{\sum_{i=1}^{N_e} \left[\int_{s_i}^e \right]} \quad (5)$$

where $F_s^{e_c}$ represents the finite element estimation of the specimen loads.

This method is essentially based on a rigorous computation of the loads applied at the specimen interfaces and his main advantage is the possibility to estimate the material constitutive parameters, in a similar way, for a static and/or a dynamic compression loading. A complete numerical analysis of the robustness and feasibility of the proposed identification procedure is presented in [9].

APPLICATION

To verify and validate the proposed two-step sequential identification algorithm, real experimental compression tests for a XC10 steel specimen are considered. Starting from different compression velocities (corresponding approximately to 0.05, 5 and 500 s⁻¹) and different initial temperatures of the material (20°C, 200°C and 400°C), the experimental load-displacement curves are pictured in Fig. 5.

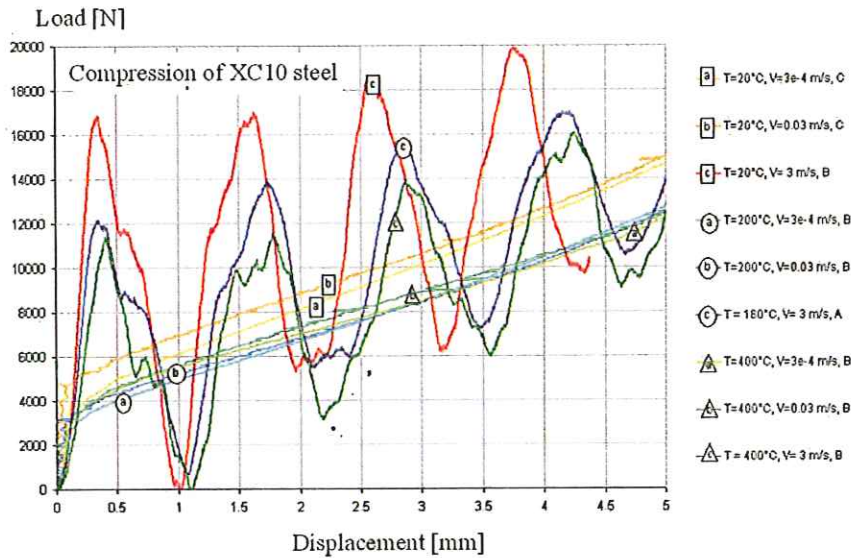


Fig. 5. Experimental load measured by the load-sensor (static and dynamic compression of a XC10 steel)

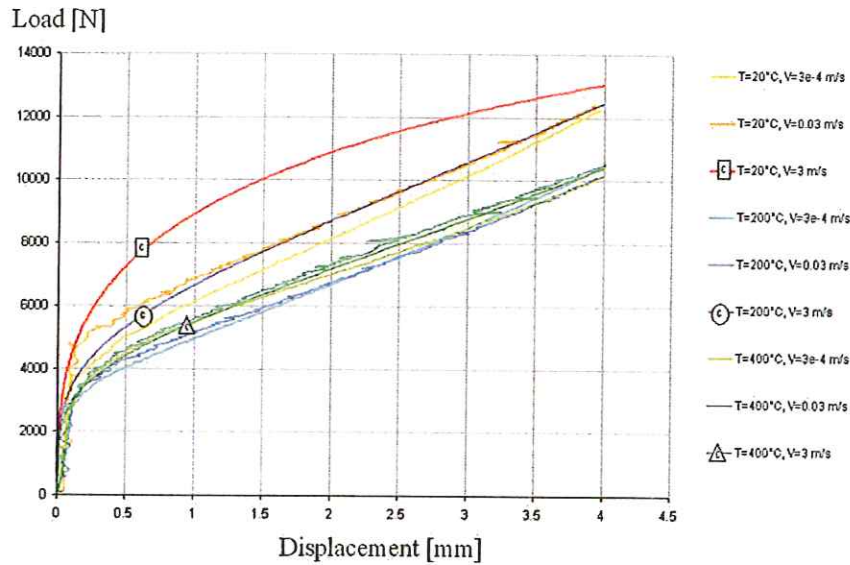


Fig. 6. New experimental data characterising the load-displacement variation on the specimen interface.

In the first time, the load variation on the specimen interface is estimated by solving numerically the inverse finite element model outlined above. The results are shown in Fig. 6 and can be regarded as the new experimental data, able to be convert into a constitutive relation expressing the true stress in terms of plastic deformation variables. According to previous works on the field of dynamic thermo-elasto-viscoplastic behaviour the following constitutive equation is proposed to be identified:

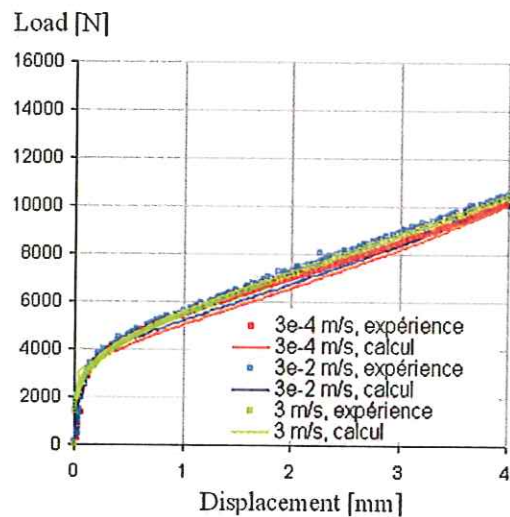
$$\sigma_0 = K \bar{\epsilon}^{n(T)} \text{sinh}^{-1} \left[1.3591 \left(\dot{\epsilon} / \dot{\epsilon}_0 \right)^{m(T)} \right] \exp \left(\beta / T \right) \tag{6}$$

$$n(T) = n_0 + n_1 T, \quad m(T) = m_0 + m_1 T$$

Figure 7 shows the numerical results concerning the identified values of the constitutive parameters (Fig. 7-a) and the comparison between the experimental curves and the computed ones (Fig. 7-b). We can observe a good agreement between the real and the predicted behaviour (global error of 7.8%).

Rheological Parameters	Initial Values	Identified Values
K [MPa]	275.380	320.087
n_0	0.134	0.228
n_1 [K ⁻¹]	4.05E-5	-1.15E-4
m_0	0.066	0.089
m_1 [K ⁻¹]	-9.1E-5	-1.15E-4
β	114.3	189.7
$\dot{\epsilon}_0$	1.	1.
Deviation [%]	26.6%	7.8%

a)



b)

Fig. 7. a- Identified values of the rheological parameters, b- Comparison between the model predictions and experiment (for a initial specimen temperature $T_0 = 400^\circ\text{C}$)

CONCLUSIONS

The proposed two steep sequential identification algorithm permits to identify rigorously the material constants from dynamic compression tests. Obviously, this method requires an a priori formulation of the constitutive relationship used by the finite element model, nevertheless it can be successfully employed to determine the material constants and to analyse different constitutive models *via* a posterior comparison between the numerical results and the observed experimental data. His main advantage is the possibility to treat both the quasi-static and the dynamic tests, using a same computational method. In the future, different constitutive equations will be analysed using the proposed algorithm, principally to describe the change on the strain-rate sensitivity during the transition between quasi-static loading and the dynamic one.

References

- [1] Zhao, H. , Analyse de l'essai aux Barres d'Hopkinson – application à la mesure du comportement dynamique des matériaux, Thèse de Doctorat, Ecole Nationale des Ponts et Chaussées, France (1992).
- [2] Klepaczko, J. R., Recent progress in testing of materials in impact shearing“, ASME/ISME Conf. on pressure vessels and piping, vol. 300, pp. 165-173 (1995).
- [3] Kopp, R. and al., Flow stress measuring by use of cylindrical compression test and special application to metal forming processes, Steel Research, 72 (10), pp. 394-401 (2001).
- [4] Haugou, G. and al., Mise en oeuvre d'une méthode originale pour l'identification des modes propres et la conception d'un montage d'essais dynamiques, Int. Conf. on multidisciplinary design in engineering, CSME-MDE 2001, 21-22 novembre 2001.
- [5] Haugou, G., Fabis, J., Langrand, B., Deletombe, E. and Markiewicz, E. "Iterative experimental/numerical procedure for improvement of dynamic experimental facilities". *Structures Under Shock and Impact*. 2002., pp. 113-122.
- [6] Diot, S., Gavrus, A., Guines, D. and Ragneau, E., Identification of a forging steel behaviour from dynamic compression tests, 15th ASCE Engineering Mechanics Conference, Columbia University, New-York, 2-5 June, 2002
- [7] Diot, S., Gavrus, A., Guines, D., Ragneau, E., Identification of a steel compression behaviour: from quasi static approach to dynamic one, *Mécanique & Industries* 2003, 4 (5), pp. 519-524.
- [8] Diot, S., Gavrus, A., Guines, D., Ragneau, E., Model of dynamic compression tests on hydraulic test machines: influence of dynamic phenomena, *Journal de Physique IV* 2003, 110, pp. 391-396.
- [9] Diot, S., Caractérisation expérimentale et numérique du comportement dynamique des matériaux, Thèse de Doctorat, Institut National de Sciences Appliquées, Rennes, France (2003).

NUMERICAL SIMULATION OF SMOOTH TIME-SPACE DECOMPOSED IMPACT ON A CONCRETE STRUCTURE WITH A VISCOPLASTIC VISCODAMAGEABLE BEHAVIOUR.

G.Hervé, F.Gatuingt and A. Ibrahimbegović

Laboratoire de Mécanique et de Technologie, 61, avenue du Président Wilson,
94235 Cachan Cedex, FRANCE,

Summary: The purpose of this paper is to present our way of conducting crash simulations of smooth striker like commercial aircraft onto concrete structures. We first upgraded the implementation of a behaviour initially developed by F. Gatuingt [4] in order to make it more efficient, then we developed a time-space decomposition of the impact signal computed with an elastic mesh of the structure, the signal is then interpolated following some reference functions and applied on the structure with a mesh that may have a different geometry and that could be coarser and that has the viscodamageable and viscoplastic implemented behaviour. All the computations were conducted with the FE code LS-Dyna 3D. Hence, we first present the behaviour and its implementation then we expose the way we build the equivalent impact loading. The examples are provided in the oral presentation of the paper.

INTRODUCTION

In the impact phenomenon that occurs on the studied structure, high stresses may happen : this leads to the compaction of concrete associated with a volume decrease over 10 %. In the present paper, we present a constitutive relation for concrete in dynamics based on viscoplasticity combined with rate dependent continuum damage. This relation is restricted to cases with moderate strain rates in concrete, corresponding typically to impacts of projectiles at a velocity less than 350 m/s , yielding an hydrostatic pressure in the material which is less than 1 GPa.

In the following section, we will detail the constitutive relation where three mechanisms are combined: compaction which is modelled with an homogenisation technique, tensile damage which is described with a rate dependent damage model and compression failure which is modelled with viscoplasticity combined to damage. We present also the numerical implementation of the developed model.

DESCRIPTION OF THE CONSTITUTIVE RELATION

There are two mechanisms which induce a variation of the elastic moduli of the material: microcracking in tension and the crushing of the cement or mortar matrix in hydrostatic compression. For the first phenomenon, we use a classical rate dependent damage model [7], which uses two damage variables in order to provide a realistic response of the material in uniaxial compression while preserving a good description of what occurs in tension, which is a characteristic of damage models. Rate effects are necessary in order to represent dynamic experiments (mostly dynamic tensile tests). In addition, rate dependency preserves well posedness of the equations of motion when strain softening occurs [8].

The second phenomenon is captured by using a modified Gurson yield function in which the porosity of the material f^* is governed by the plastic flow (the porosity always decreases because in tension microcracking occurs first). In addition, we use a homogenisation technique to have elastic properties of material functions of the variation of porosity, especially during hydrostatic loadings. The method due to Mori-Tanaka is selected because it provides explicit expressions of the shear and bulk moduli of (uncracked) concrete function of the porosity.

These two mechanical effects are combined in the final relationships which relate the stresses to the elastic strains:

$$\sigma_{ij} = (1 - D) \left[K \varepsilon_{kk}^e \delta_{ij} + 2G \left(\varepsilon_{ij}^e - \frac{1}{3} \varepsilon_{kk}^e \delta_{ij} \right) \right] \quad (1)$$

where the shear G and bulk moduli K are obtained using Mori-Tanaka's expressions [10] with the moduli of the cementitious matrix without pores K_M and G_M and the porosity f^v :

$$\begin{aligned} K &= \frac{4K_M G_M (1 - f^v)}{4G_M + 3K_M f^v} \\ G &= \frac{G_M (1 - f^v)}{1 + \frac{6K_M + 12G_M}{9K_M + 8G_M} f^v} \end{aligned} \quad (2)$$

The damage model is issu of the works of Mazars [9]. We can obtain a rate dependent form of this model, similar to the equations used by Dube *et al.*[7], using the following definition of the damage rate:

$$\dot{D} = \left(\frac{\langle \bar{\varepsilon}^e - \varepsilon_{D0} - \frac{1}{\alpha} \left(\frac{D}{1-D} \right)^{(1/\alpha)} \rangle}{m_D} \right)^{m_D} \quad (3)$$

where $\bar{\varepsilon}^e = \sqrt{\sum_i (\varepsilon_i^e)^2}$ is the equivalent strain which permit to have a good representation of damage growth with the loading path.

Colantonio and Stainier proposed a similar viscoplastic model in which the definition of the plastic multiplier accounts for the variation of porosity of the material. We follow here the same approach and define the viscoplastic multiplier as :

$$\dot{\lambda} = \frac{f^v}{(1 - f^v)} \left\langle \frac{F_{NT}}{m_{vp}} \right\rangle \quad (4)$$

where m_{vp} is a material parameter.

The viscoplastic strains are obtained following Perzyua's approach:

$$\varepsilon_{ij}^{vp} = \dot{\lambda} \frac{\partial F_{NT}}{\partial \sigma_{ij}} \quad (5)$$

F_{NT} is the modified Gurson's yield function proposed by Needleman and Tvergaard :

$$F_{NT}(\sigma_{ij}, \sigma_M, f^v) = \frac{3J_2}{\sigma_M^2} + 2q_1 f^v \cosh \left(q_2 \frac{I_1}{2\sigma_M} \right) - (1 + (q_3 f^v)^2) = 0 \quad (6)$$

where σ_M is the stress in concrete without voids and q_1, q_2, q_3 are scalars parameters.

IMPLEMENTATION WITH A RETURN MAPPING ALGORITHM

Given the complexity of the constitutive relations and their aim, which is to model concrete in fast transient dynamics, the model has been implemented in the finite element code DYNA3D. The objective of the numerical implementation of the model is to be able to calculate the new state of stress at time $t + \Delta t$ knowing the increment of strain $\Delta \varepsilon$ and the state of material at time t .

If we consider the constitutive equations previously presented (for the case where the damage is constant), we can rephrase the equations using the additive decomposition of the strains and obtain an elastic predictor of a return mapping algorithm [5]:

$$\begin{aligned} \dot{\varepsilon}_{ij} &= \dot{\varepsilon}_{ij}^e \\ \dot{\sigma} &= (1 - D) \left[K \dot{\varepsilon}_{kk}^e \delta_{ij} + 2G \left(\dot{\varepsilon}_{ij}^e - \frac{1}{3} \dot{\varepsilon}_{kk}^e \delta_{ij} \right) \right] \\ \dot{\varepsilon}_{ij}^{vp} &= 0 \\ \dot{f}^v &= 0 \\ \dot{\sigma}_M &= 0 \end{aligned} \quad (7)$$

and a viscoplastic correction:

$$\begin{aligned}
 \dot{\varepsilon}_{ij} &= \dot{\varepsilon}_{ij}^e + \dot{\varepsilon}_{ij}^{vp} = 0 \\
 \dot{\sigma} &= -(1-D) \left[K \dot{\varepsilon}_{kk}^{vp} \delta_{ij} + 2G \left(\dot{\varepsilon}_{ij}^{vp} - \frac{1}{3} \dot{\varepsilon}_{kk}^{vp} \delta_{ij} \right) \right] + (1-D) \left[\dot{K} \varepsilon_{kk}^e \delta_{ij} + 2\dot{G} \left(\varepsilon_{ij}^e - \frac{1}{3} \varepsilon_{kk}^e \delta_{ij} \right) \right] \\
 \dot{\varepsilon}_{ij}^{vp} &= \dot{\lambda} \frac{\partial F_{NT}}{\partial \sigma_{ij}} \\
 \dot{f}^* &= k(1-f^*) f^* \dot{\varepsilon}_{kk}^{vp} = \dot{\lambda} k(1-f^*) f^* \frac{\partial F_{NT}}{\partial \sigma_{kk}} \\
 \dot{\sigma}_M &= \dot{\lambda} \frac{E_L}{(1-f^*) \sigma_M} \frac{\partial F_{NT}}{\partial \sigma_{ij}} \sigma_{ij}
 \end{aligned} \tag{8}$$

Substituting equations 8c, 8d and 8e in equation 8b we obtain:

$$\dot{\sigma} = -\dot{\lambda} [c(t)] \tag{9}$$

where $c(t)$ is constant at time t :

$$\begin{aligned}
 c(t) &= (1-D) \left[K \cdot \frac{\partial F_{NT}}{\partial \sigma_{kk}} \cdot \delta_{ij} + 2G \cdot \left(\frac{\partial F_{NT}}{\partial \sigma_{ij}} - 1/3 \cdot \frac{\partial F_{NT}}{\partial \sigma_{kk}} \cdot \delta_{ij} \right) \right] \\
 &\quad - (1-D) \left[\frac{\partial K}{\partial f^*} \cdot k \cdot (1-f^*) \cdot f^* \cdot \frac{\partial F_{NT}}{\partial \sigma_{kk}} \cdot \varepsilon_{kk}^e \cdot \delta_{ij} \right. \\
 &\quad \left. + 2 \frac{\partial G}{\partial f^*} \cdot k \cdot (1-f^*) \cdot f^* \cdot \frac{\partial F_{NT}}{\partial \sigma_{kk}} \cdot \left(\varepsilon_{ij}^e - 1/3 \cdot \varepsilon_{kk}^e \cdot \delta_{ij} \right) \right]
 \end{aligned} \tag{10}$$

If we considered equation 4 we can write:

$$\begin{aligned}
 \frac{d\sigma}{dt} &= -\frac{f^*}{(1-f^*)} \left\langle \frac{F_{NT}}{m_{vp}} \right\rangle [c(t)] \\
 \frac{df^*}{dt} &= \frac{f^*}{(1-f^*)} \left\langle \frac{F_{NT}}{m_{vp}} \right\rangle k(1-f^*) f^* \frac{\partial F_{NT}}{\partial \sigma_{kk}} \\
 \frac{d\sigma_M}{dt} &= \frac{f^*}{(1-f^*)} \left\langle \frac{F_{NT}}{m_{vp}} \right\rangle \frac{E_L}{(1-f^*) \sigma_M} \frac{\partial F_{NT}}{\partial \sigma_{ij}} \sigma_{ij}
 \end{aligned} \tag{11}$$

In the time derivative of the yield function:

$$\frac{dF_{NT}}{dt} = \frac{\partial F_{NT}}{\partial \sigma} \cdot \frac{d\sigma}{dt} + \frac{\partial F_{NT}}{\partial f^*} \cdot \frac{df^*}{dt} + \frac{\partial F_{NT}}{\partial \sigma_M} \cdot \frac{d\sigma_M}{dt} \tag{12}$$

We obtain an ordinary differential equation to solve to compute the position of the stress point on the return path:

$$\frac{\partial F_{NT}}{\partial t} = -\Lambda \left\langle \frac{F_{NT}}{m_{vp}} \right\rangle \tag{13}$$

with:

$$\begin{aligned}
 \Lambda &= \frac{1}{m_{vp}} \times \frac{f^*}{1-f^*} \left\{ \frac{\partial F_{NT}}{\partial \sigma_{ij}} : [c(t)] \right. \\
 &\quad \left. - \frac{\partial F_{NT}}{\partial f^*} \cdot k \cdot (1-f^*) \cdot f^* \cdot \frac{\partial F_{NT}}{\partial \sigma_{kk}} - \frac{\partial F_{NT}}{\partial \sigma_M} \cdot \frac{E_L}{(1-f^*) \sigma_M} \cdot \frac{\partial F_{NT}}{\partial \sigma_{ij}} : \sigma_{ij} \right\}
 \end{aligned} \tag{14}$$

If we have simultaneously an evolution of the damage, the correction is modified:

$$\begin{aligned}
 \dot{K}^{dam} &= (1-D) \frac{\partial K}{\partial f^*} \dot{f}^* - \dot{DK} \\
 \dot{G}^{dam} &= (1-D) \frac{\partial G}{\partial f^*} \dot{f}^* - \dot{DG}
 \end{aligned} \tag{15}$$

We can then write, in the iterative scheme, the different corrections:

$$\begin{aligned}
 \lambda &= \frac{f^{*(i)}}{1 - f^{*(i)}} \cdot \frac{F_{NT}^{(i)}}{m_{exp}} \\
 \sigma_{n+1}^{(i+1)} &= \sigma_{n+1}^{(i)} + \dot{\sigma}_{n+1}^{(i)} \cdot \frac{1}{\Lambda^{(i)}} \\
 \dot{\sigma}_{n+1}^{(i+1)} &= \dot{\sigma}_{n+1}^{(i)} + \ddot{\sigma}_{n+1}^{(i)} \cdot \frac{1}{\Lambda^{(i)}} \\
 f_{n+1}^{(i+1)} &= f_{n+1}^{*(i)} + \dot{f}_{n+1}^{*(i)} \cdot \frac{1}{\Lambda^{(i)}} \\
 t^{(i+1)} &= t^{(i)} + \frac{1}{\Lambda^{(i)}} \cdot \log \left(\frac{F_{NT}^{(i)}}{F_{NT}^{(i+1)}} \right)
 \end{aligned} \tag{16}$$

the iterative scheme end when we have $t^{(i+1)} = \Delta t$.

TIME-SPACE DECOMPOSITION AND BUILDING OF THE IMPACT LOADING

In a first step, we need to have the loading function due to the impact on each finite element node of the concrete structure concerned with the impact phenomenon. We will then assume that all the loading signals can be decomposed considering the following equation:

$$F(x, y, t) = H(d(x, y), D(x, y), P(x, y)) * f(t) \tag{17}$$

In this part, we focus only on an axisymmetric case of projectile. As shown in Figure 1, we use a refined mesh in the impacted area and a coarse one in the other parts of the slab.

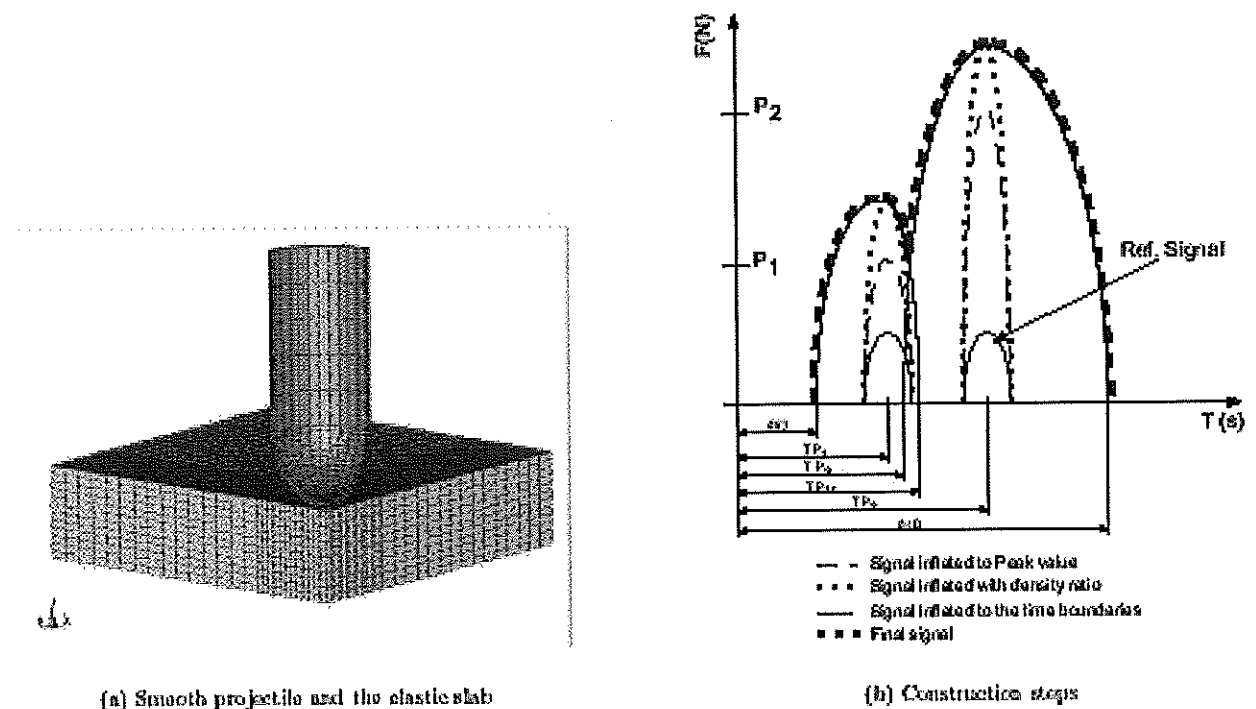


Figure 1: Elastic mesh and equivalent loading building steps

The load-time function in the impact direction of the projectile is picked up at the impacted nodes following one radius. In a systematic perspective we wanted to generalize the method even to very noisy signals, so we apply a Savitsky-Golay filter on the signal that has been picked at each node, see [6].

On each node we decompose the signal in the following representative functions : r = radius from the axis of the projectile

$d(r)$: the delay function is the delay between the very first time of impact ($t = 0$) and the time the signal begins at the considered node

$D(r)$: the duration function is the duration of the load-time signal at the considered node

$P_k(r)$: the k^{th} peak observed on the signal, i. e. local maxima on the full signal

$tp_k(r)$: the time at which the k^{th} peak is considered

$f(t)$: the force-reference function as : $f(t) = \sin(\pi\sqrt{t})$

We can then finally write that at each node :

$$F(r, t) = \text{Sup} [H(d(r), D(r), P_k(r), tp_k(r)) * f(t)] \quad (18)$$

Those functions are known at every nodes of the refined elastic mesh, we make a Hermite polynomial interpolation between those points. With these interpolations, we can obtain the functions at every nodes of a coarse non-linear mesh for the impacted structure. We use what we can call a "local Hermite polynomial", this means that we build the interpolation for each $[x_i, x_{i+1}]$ of the global $[x_0, x_n]$. As we build it on two points we get a fourth order polynomial, this avoids us to have high degree polynomial because of our refined mesh and then to be confronted to runge phenomenon near the boundaries of the interval due to the high degree. If we consider a g function known at x_i and x_{i+1} and interpolating it into $r \in [x_i, x_{i+1}]$, we build \tilde{g} as follows :

$$\tilde{g} = g(x_i) + (x - x_i)g'(x_i) + \chi(x - x_i)^2 + \psi(x - x_i)^2(x - x_{i+1}) \quad (19)$$

where:

$$\chi = \frac{\frac{f(x_{i+1}) - f(x_i)}{x_{i+1} - x_i} - f'(x_i)}{x_{i+1} - x_i} \quad (20)$$

$$\psi = \frac{f'(x_{i+1}) - \frac{f(x_{i+1}) - f(x_i)}{x_{i+1} - x_i} - \chi}{x_{i+1} - x_i} \quad (21)$$

As we know the several interpolated time-space decomposition functions of the signal, we can rebuild the full signal at the nodes of the non-linear coarse mesh. The rebuilding of the full signal is presented both in the following lines and in the Figure 1.

Step 1 : Due to the \tilde{d} , \tilde{D} and \tilde{tp}_k functions the beginning of load-time history, its end and the time of each peaks are placed.

Step 2 : The reference function $f(t)$ is placed on every peak-time of the signal.

Step 3 : Each $f(t)$ is inflated or deflated following the vertical reaching the $\tilde{P}(r_i)$, we have then a $f_v(t)$.

Step 4 : The $f_v(t)$ function is multiplied by the local mesh density ratio between refined and coarse mesh on the considered node, this means that we write :

$$\hat{f}_v(t) = f_v(t) * \frac{P_{coarse}}{P_{refined}}$$

Step 5 : Each vertically inflated $\hat{f}_v(t)$ is inflated or deflated following the horizontal on the left and right sides of the considered tp_k reaching the following values :

$$(t_k)_l = tp_k - \frac{(tp_k - tp_{k-1})P_k}{P_k + P_{k-1}} \text{ and } (t_k)_r = tp_k + \frac{(tp_{k+1} - tp_k)P_{k+1}}{P_{k+1} + P_k}$$

$$(\hat{t}_k)_l = (t_k)_l - \frac{P_k}{P_{k-1} + P_k} \text{Min} [(tp_k - (t_k)_l); ((t_k)_l - tp_{k-1})] \quad (22)$$

$$(\hat{t}_k)_r = (t_k)_r + \frac{P_k}{P_{k+1} + P_k} \text{Min} [(t_k)_r - tp_k]; (tp_{k+1} - (t_k)_r)] \quad (23)$$

If the peak is the first or the last of the interval we inflate or deflate $\hat{f}_v(t)$ respectively to \tilde{d} and $\tilde{D} + \tilde{d}$.

Step 6 : Then we build the final signal in taking the $\text{Sup}[(\hat{f}_{v,h})_k(t)]$.

The final signal is then reported on the nodes of the coarse non-linear mesh.

CONCLUSION

A constitutive relation aimed at describing the response of concrete in dynamics has been presented. It contains a description of microcracking in tension and compression, and of compaction due to hydrostatic compression. The model combines viscoplasticity with a rate dependent damage model. Compaction is described with a homogenisation technique, assuming that concrete is a homogeneous material with voids. Its implicit numerical implementation using the Ortiz and Simo return mapping algorithm have also been presented.

The time-space decomposition method of the impact loading we propose here is an alternative to several methods like Riera's model [1] for it takes care of the response of the structure in the load-time history and of the spatial repartition in time of the loading. Indeed the other methods [2] do not use a spatial repartition of the loading. The method presented here has been developed and used in axisymmetric cases, but we must notice that it is possible to adapt it to any symmetric projectile. We must put the stress on the fact that whereas the very first signal is extracted with a refined mesh, it can be applied on every kind of mesh even more refined or coarser ones. Some simulations have been conducted and will be presented in the oral presentation of this paper.

References

- [1] J. D. Riera. A critical reappraisal of nuclear power plant safety against accidental aircraft impact. *Nuc. Eng. Design*, **57**, 193–206, 1980.
- [2] M. Y. H. Bangash. *Impact and explosion - Analysis and Design*. Blackwell Scientific Publications, 1993.
- [3] F. Gatuingt, G. Hervé and A. Ibrahimbegović. Local response of a concrete slab submitted to a smooth or a hard impact. *Complus VII - 7th International Conference on Computational Plasticity*, Barcelona (Spain), CIMNE, 2003.
- [4] F. Gatuingt and G. Pijaudier-Cabot. Coupled damage and plasticity modelling in transient dynamic analysis of concrete. *Int. J. Numer. Anal. Meth. Geomec.*, **26**, 1–24, 2002.
- [5] M. Ortiz and J. C. Simo. An analysis of a new class of integration algorithms for elastoplastic constitutive relations. *Int. J. Numer. Meth. Engng.*, **23**, 353–366, 1986.
- [6] Savitsky and Golay. *Analytical Chemistry*, **36**, 16–27, 1964.
- [7] J.F. Dubé, G. Pijaudier-Cabot and C. Laborde. A rate dependent damage for concrete in dynamics. *Journal of Engineering Mechanics ASCE*, **122**, 939–947, 1996.
- [8] L.J. Shyis and R. De Borst. Wave propagation and localization in a rate dependent cracked medium : Model formulation and one dimensional examples. *I.J.S.S.*, **29**, 2945–2958, 1992.
- [9] J. Mazars. Application de la mécanique de l'endommagement au comportement non linéaire et à la rupture du béton. *Ph. D. Thesis*, 1984.
- [10] Average stress in matrix and elastic energy of materials with misfitting inclusions. *Acta Metallurgica*, **21**, 571–574, 1973.

ON THE STRAIN RATE DEPENDENT BEHAVIOUR OF SHORT FIBRE REINFORCED COMPOSITES

Zouhaier Jendli*, Joseph Fitoussi*, Fodil Meraghni, and Didier Baptiste*

*LM3 UMR-CNRS 8006, ENSAM Paris, 151 bd. de l'Hôpital 75013 Paris, France; LMPF, JE-2381, ENSAM Châlons en Champagne, rue Saint Dominique, BP 508 51006 Châlons en Champagne, France.

Summary: Analysing the damaged elastic behaviour of composite materials under dynamic loading requires specific insights into the damage mechanisms evolution as a function of the strain rates. The comprehension relies upon the development of theoretical simulation approaches and an experimental methodology for strain rates up to 200 s^{-1} . The present work aims at investigating experimentally, at microscopic and macroscopic material scales, the effects of the strain rate on the damage behaviour of a sheet moulding compound composite material subjected to high-speed tensile tests. To this end, we used the interrupted tensile test technique. The applied experimental procedure has been optimised in an attempt to isolate the inherent inertial disturbances attributed to the test system. The optimisation aims at minimizing the amplitude of measurements perturbation in order to give rise to homogeneous stress/strain fields within the tested specimen. Using a servo-hydraulic machine, monotonic and interrupted tensile tests were performed at different strain rates and coupled to scanning electronic microscope observations. The developed approach has been applied at strain rates varying from the quasi-static 10^{-3} m/s to 20 m/s for SMC-R26 composite material. In this paper, experimental findings have established that the material macroscopic response is governed by the damage growth on the micro- and mesoscale levels. Finally, the obtained results shed light on the visco-damaged nature of the non-linear behaviour under a moderate dynamic loading.

INTRODUCTION

While metals have been studied extensively over a wide range of strain rates, limited information is available with regard to the effects of strain rate on composite mechanical performances. Mechanical response of fibre reinforced polymer composites under low and high-speed loading is not well understood. In fact, investigating dynamic behaviour of composites requires the development of an experimental methodology able to describe efficiently load-rate effects. Success with the high strain rate testing of polymer composites depends widely on the ability to isolate the inherent inertial disturbances attributed to the test system [1-6-8]. The primary objective of the present work is to set up and optimise an experimental approach aimed at characterising the mechanical behaviour of composite materials subjected to rapid loadings. The experimental methodology is built upon monotonic and interrupted rapid tensile tests and were coupled to microscopic observations using scanning electronic microscopic. Tensile testes were performed at different crosshead velocities yielding to strain rates from $\dot{\epsilon} = 2.10^{-4} \text{ s}^{-1}$ (quasi-static) to $\dot{\epsilon} = 200 \text{ s}^{-1}$. On the one hand, this study intended to quantify the strain-rate effects on the overall behaviour in terms of elastic properties, damage and ultimate characteristics. On the other hand, it contributes to investigate local processes involving damage initiation and growth. Nevertheless, high-speed mechanical testing of polymer composites arises specific difficulties inherent to inertial effects, non-uniform stress/strain distributions and measurements repeatability of the material composite materials behaviour. The use of a servo-hydraulic test machine raises some issues related to the test control variables, notably for interrupted tests [7-9]. Due to the stress-wave propagation, the strain and the stress are non-uniform and hence the strain-rate cannot be spatially constant into the tested specimen. To reduce this difficulty, numerical computations have led to an optimal design of the specimen geometry and the experimental damping system in terms of thickness and material. These simulations were achieved using ABAQUS finite element code [10] and are intended to model the stress wave propagation occurring for a high-speed tensile test. The developed experimental methodology is applied on a Sheet Moulding Compound (SMC-R26).

EXPERIMENTAL METHODOLOGY: PROCEDURE AND TESTING DEVICES

Material description

The tested composite material is a Sheet Moulding Compound noted SMC-R26. It consists of an unsaturated polyester resin reinforced by glass fibres and weakly filled with calcium carbonate fillers (CaCO_3). Glass fibres have a weight content of 26 % and are assembled in bundles in such a way that each one contains approximately 200 fibres. These packets of fibres are randomly oriented in the material compression plane and have a constant length ($L = 25 \text{ mm}$) with a fibre diameter of $15 \text{ }\mu\text{m}$. The random distribution of reinforcement confers to the material a microscopic heterogeneous aspect and an overall transverse isotropic mechanical behaviour. The SMC-R26 tested plates were prepared of thickness 2.7 mm and were cured at $140 \text{ }^\circ\text{C}$ with an applied pressure averaging between 7 and 8 MPa for 2 minutes [9]. High-speed tensile tests have been conducted upon a servo-hydraulic test machine. As specified by the manufacturer (Schenck), the test machine can reach a crosshead speed range from 10^{-3} m/s to 20 m/s . Moreover, the test force level is measured by a piezo-electric load cell of a 50 kN capacity. Strain rates have been estimated exclusively on the basis of strain gauge responses. Tensile tests were carried out at different strain rates according to two ways.

High-speed tensile tests until rupture

High-strain rates tensile tests were conducted using servo-hydraulic machine at different strain-rates until the composite specimen total failure. The test machine is equipped with a launching system. The composite specimen is positioned between the load cell (upper extremity) and the moving device (lower extremity) as sketched in figure 1. Prior to the contact between the sliding bar and the hydraulic jack, the latter is accelerated on a straight displacement of 135 mm in order to achieve the constrained crosshead velocity. Once the contact occurs, the specimen is then subjected to a tension at a constant load-rate. The damping joint placed between the slide and the hydraulic jack may attenuate partially the wave effects caused by the dynamic shock.

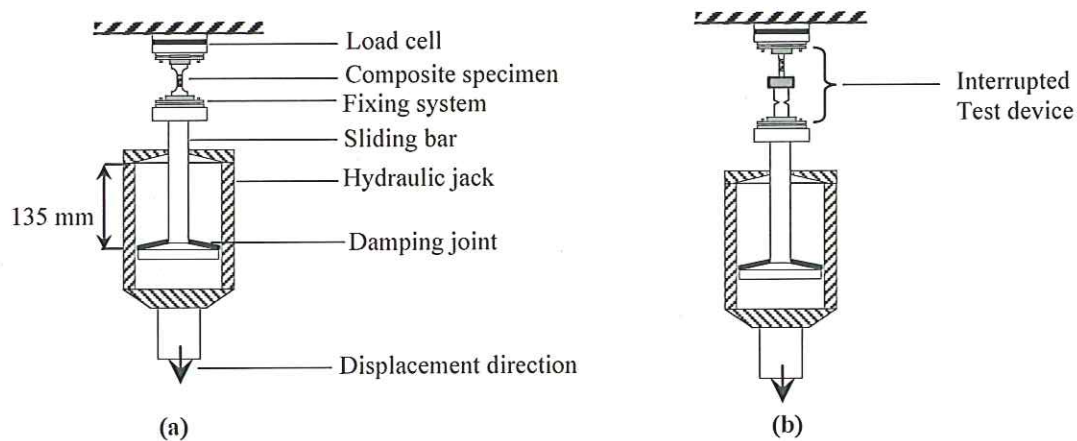


Fig. 1. Schema of the device used for high-speed tensile experiments until specimen rupture (a) and for interrupted high-speed tensile experiment (b) using servo-hydraulic machine.

Interrupted high-speed tensile tests

The originality of this experimental methodology, proposed by Lataillade et al. [7], consists of the capability to interrupt the specimen loading at fixed stress levels. Indeed, due to inertial effects of the launching system, a rapid tensile test cannot be interrupted until the total failure of the specimen. Accordingly, the specimen is loaded simultaneously with a double-notched fuse sample (Fig. 1-b) characterised by an elastic brittle fracture. The fuse ligament width is assigned to a suitable level load to be reached when interrupting the loading of the specimen. The above brings about then a stress release in the specimen. This procedure is repeated several times onto the same specimen by changing the fuse (width) before each a new re-loading. One can hence reach a load level greater than the previous.

OPTIMISATION OF HIGH-SPEED TENSILE EXPERIMENTS

Experimental optimisation procedure: Damping joint and specimen geometry

The damping joint inserted between the sliding bar and the tube of the hydraulic jack enables a partial absorption of the generated stress wave. Nevertheless, the damping joint must be able to attenuate the shock wave during the first stage of its elastic compression. It is obvious that the above affects the load rate. Consequently, an optimal design of the damping joint, in terms of constitutive material and thickness, may result in a constant strain-rate into the tested specimen. For different crosshead velocities, several geometries and materials of the damping joint have been experimentally tested so that gives rise to homogeneous strain/stress in the central zone of the composite specimen. This optimisation led to choose a damping joint consisting of a low impedance material: rubber nitrile of 1.5 mm thickness. Furthermore, composite specimen geometry has been optimised as a result of numerical computations using ABAQUS finite element code. The optimisation procedure relies upon coupling FE numerical results and experimental data. It falls into four stages:

- i. A tensile test is conducted at a fixed displacement-rate. The displacement induced at specimen extremities is measured. The damping joint, positioned between the sliding and the hydraulic jack, may limit the shock until its total elastic compression corresponding to a rise time noted hereafter (t_r). The latter is averaging between 2.10^{-4} s and 10^{-6} s as a function of the adopted joint thickness and the imposed velocity. Beyond this time, the composite specimen is therefore subjected to a dynamic loading. The first stage aims then at estimating experimentally the rise time (t_r).
- ii. Having estimated the rise time, boundaries conditions are applied on the specimen extremities in terms of imposed velocity, to compute numerically the dynamic response of the specimen.
- iii. On the basis of the FE simulations and assuming that the specimen behaves as an elastic solid, a recursive optimisation procedure results in the determination of optimal geometric parameters: L_1 , L_2 , L_3 and R .

These parameters are those of a dumbbell-shaped specimen and are optimised in such a way of reducing the stress wave effects in the overall response and generating homogeneous stress/strain field (Fig. 2).
 iv. Finally, high-speed tensile tests are achieved on SMC-R26 composite specimen to validate its optimised geometry. The optimised specimen dimensions are summarised in table 1.

	L ₁ (mm)	L ₂ (mm)	L ₃ (mm)	R (mm)
SMC-R26	6	80	30	7

Table 1. Specimen dimensions optimised for SMC-R26 composite material.

For interrupted high-speed tensile tests, the optimisation procedure is illustrated in the following sections. First, it aims at optimising the fuse and therefore the system consisting of the fuse sample in series with the composite specimen.

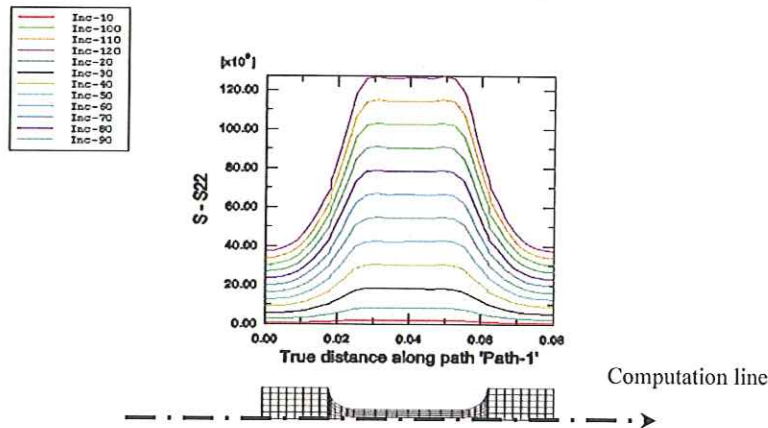


Fig. 2: Spatio-temporal profile of the longitudinal stress (σ_{22}) calculated along the central line of the SMC specimen.
 Loading conditions: Imposed velocity $V=1\text{ m/s}$ giving rise to a strain-rate $\dot{\epsilon}=20\text{ s}^{-1}$

Optimisation and validation of the fuse geometry

For interrupted high-speed tensile tests, the load level reached prior to an elastic release is assigned to the fuse ligament width. Hence, a preliminary experimental analysis intends to characterise the failure load evolution as a function of the ligament width (W). As abovementioned, the fuse must fail as a brittle material and exhibits a linear elastic mechanical response, which is insensitive to the strain-rate. Several experimental rapid tensile tests were conducted and have allowed retaining a double notched fuse that consisting of polymethylmethacrylate (PMMA). On the basis of the expected load levels, the fuse samples are double notched bars of thickness 4 mm, 80 mm length and 20 mm total width. These high-velocity tensile tests have contributed to establish experimentally the relationship between the interrupting load level and the fuse ligament width as illustrated in the Table 2.

Ligament width (mm)	7	10.5	12	13.5	14.5	15	15.5	16
Maximal load (N)	822	1059	1089	1314	1511	1635	1721	1842

Table 2. Correlation between maximal load levels and the ligament width of PMMA fuse. These load levels are estimated for tensile tests performed at 1 m/s crosshead displacement rate.

Using ABAQUS code, numerical simulations were carried out to assess the stress wave propagation involved into the fuse sample during high-velocity tensile tests. Boundary conditions applied for these numerical computations are those defined by experimental conditions and results. These are applied in terms of rise time ($t_r=10^{-4}\text{ s}$) and maximal velocity ($V_{\text{max}}=1\text{ m/s}$). The PMMA fuse is clamped at an extremity and subjected to a constrained displacement-rate. In what follows, numerical results for a velocity ($V_{\text{max}}=1\text{ m/s}$) are presented for the fuse specimen with a ligament width $W=7\text{ mm}$. Note that for the others ligament widths, numerical simulations provide similar results. Considering the different time increments, one notices that the front of longitudinal stress wave remains steady close to the fuse notch (Fig.3-a). For the whole time steps, FE analysis shows that the stress front is not shifted along the fuse longitudinal line. In addition, the stress distributions, produced during the dynamic event, are numerically estimated along the fuse line as well as along the ligament width. As reported by figure 3-a, these stress distributions exhibit a homothetic increase as a function of time increments. On the basis of these results, one can claim that, in terms of dispersion and perturbation, adopting experimental conditions minimizes stress wave effects.

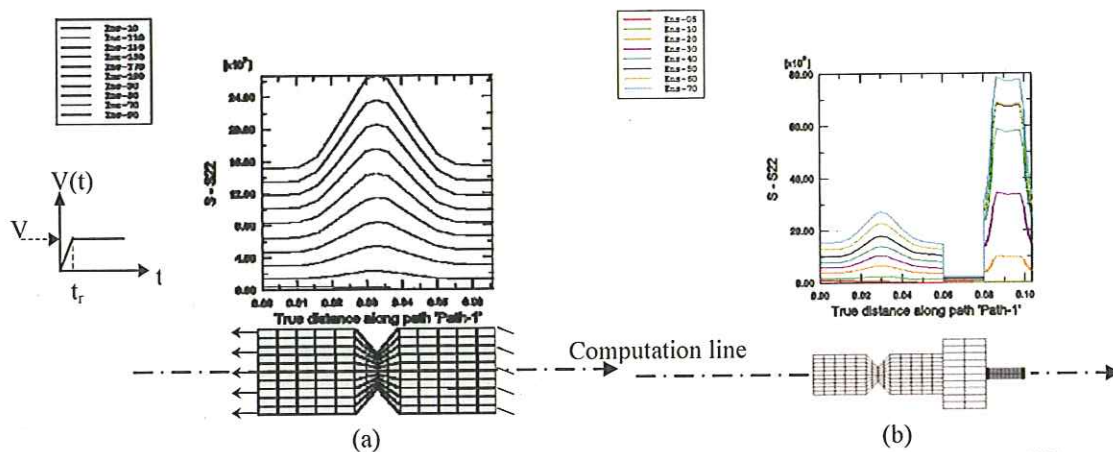


Fig. 3. (a) Numerical predictions of the stress distributions along the fuse line (σ_{22}) estimated for different calculation steps ($W=7$ mm). (b) Longitudinal stress profile calculated along the system fuse-specimen line. SMC-R26

Optimisation and validation of the system: fuse in series with the composite specimen

The optimisation of the whole system was conducted according to the same stages described in the previous section. In what follows, the composite specimen is perfectly clamped at the upper extremity and is in series with the PMMA fuse. The latter is fixed to the sliding bar (lower extremity). Numerical computations are performed upon this system subjected to boundary conditions described in a previous section. These conditions consist of a velocity curve defined by a rise time ($t_r=10^{-4}$ s) and maximal velocity ($V_{max}=1$ m/s). SMC composite test specimens are rectangular section tabbed ends bars and having the dimensions of $36 \times 6.5 \times 2.7$ mm³. Tabs with tapered ends are bonded on each side of the specimen. These tabs allow a progressive load introduction. They will reduce stress concentration and thus the shock wave stress effects. The adopted specimen geometry was chosen in order to carry out microscopic observations using a scanning electronic microscope (SEM) after each interrupted high-speed tensile test. Figure 3-b shows an example of the stress distribution calculated for different increments load and represented along the central line of the system: fuse-composite specimen.

EXPERIMENTAL INVESTIGATIONS AND VALIDATION

The developed optimisation methodology is based on experimental tests and coupled to the numerical simulations. It was validated at strain rates up to 200 s^{-1} for Sheet Moulding Compound (SMC-R26).

Effects of strain-rate on the overall tensile response

The application of the optimised methodology has contributed to investigate the sensitivity of the mechanical characteristics to the strain-rate, in terms of the linear, non-linear behaviour and ultimate properties. These high-strain rate tensile tests were conducted on SMC-R composite at different strain-rates until the specimen total failure. Note that for the investigated material the strain rates have been determined directly on the basis of strain gauges temporal responses. As shown in the Figure 4, stress-strain (σ - ϵ) tensile curves plotted for several strain rates show noticeably that the overall behaviour is load-rate dependent. Indeed, under rapid traction SMC-R composites exhibit typically a non-linear response. The beginning of the non-linearity is noticed around 30% of the maximum loading and corresponds to the first stages of the damage growth generated by the matrix micro-cracks leading to interface decohesions.

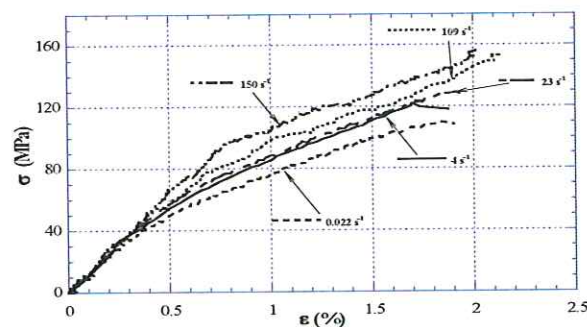


Fig. 4. Experimental strain-stress tensile curves for SMC-R26 composites obtained for testes carried out at strain rate: 0.022, 4, 23, 109 and 150 s^{-1}

An inflection point, commonly called knee-point, characterizes the latter. Tensile tests were achieved at crosshead velocities from quasi-static to 9 m/s corresponding to strain rates from 10^{-3} to 150 s^{-1} . Figure 4 shows that initial slopes of the stress-strain curves, estimated for a strain less than 0.3 %, are roughly identical for the different tested strain rates. Therefore, the above implies that the elastic modulus remain insensitive to the load rate for the tested velocity range. It has a rough average value of 13 GPa. However, the microstructure variability of this class of materials [9, 11] can bring about a slight discrepancy notably for dynamic loadings.

Additionally, figure 4 indicates that the non-linear stage of the overall response rises moderately as the strain rate increases. Furthermore, a mechanical behaviour accommodation is noticed for the high strain rates. The above arises through an increase of the ultimate strain and stress. Indeed, in terms of stress and strain, ultimate properties and the damage threshold increase significantly for high strain rate. As illustrated in figure 5, one can see that the strain rate effect is more noticeable and marked on the ultimate stress than the strain.

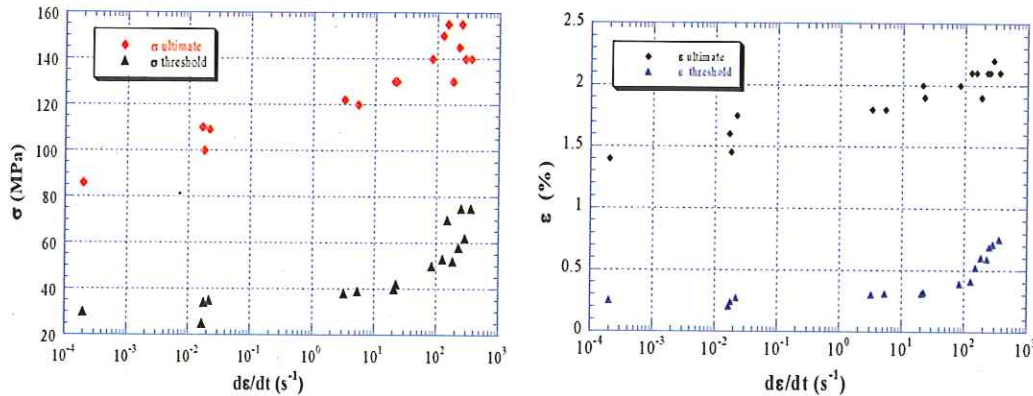


Fig. 5. Effects of strain-rate on the damage threshold and ultimate properties in terms of strain and stress.

These experimental findings are consistent with those obtained in other works [1-2]. These authors have pointed out that tensile strength increases with strain rate. In addition, one notes a shift of the damage by increasing the strain rate. Actually, when varying the strain rate from the quasi-static to 250 s^{-1} , the stress damage threshold is delayed from 30 MPa to 80 MPa (Fig. 5). While, the strain damage onset increases from 0.25 % to 0.77 %.

Effects of strain-rate on the damage onset and kinetic

Interrupted high-speed tensile tests have widely contributed to evaluate the rate dependence of the damage in terms of initiation and kinetic of the experimented composite. Damage analysis was conducted according to two ways. The first intends to estimate the macroscopic Young's modulus reduction (D_{macro}) whereas the second aims at quantifying the damage accumulation (d_{micro}) at the microscopic material scale. Macroscopic damage can be quantified by the tensile modulus reduction using the well-known damage mechanics [7-11]. The damage scalar parameter is thus expressed, Eq. (1) such as:

$$D_{\text{macro}} = 1 - \frac{E^D}{E^0} \quad (1)$$

E^0 and E^D , are respectively the Young's modulus of virgin and damaged material. (E^0) is determined by the initial slope of the stress-strain curve. The current modulus (E^D) is estimated by the slope of the reloading curve after to each tensile test interruption at a predefined load level.

Additionally, the local damage estimation aims at establishing a relationship between the micro-defects density, generated by the interface decohesions, and the macroscopic strain/stress applied level. After each interrupted tensile test, damage accumulation is investigated by means of SEM micrographs performed upon a representative element volume (REV). Specimen cartography is achieved using image-analysis. These contribute to characterizing the bundles degradation, in terms of matrix micro-cracks and fibre-matrix debonding. This investigation results in a quantitative damage evaluation by estimating defects effects. For that, one defines first a microstructural parameter describing the debonded fibres content (f_d). The microscopic damage state is then represented at the local scale as, Eq. (2):

$$d_{\text{micro}} = \frac{f_d}{f_v} \quad (2)$$

f_d is the volume fraction of debonded fibres and f_v is the fibre volume content in the (REV).

Interrupted high-speed tensile tests have been achieved on SMC-R26 composite for the following strain rates: 0.0002, 3, 8 and 20.5 s^{-1} . These correspond respectively to crosshead velocities of 2.10^{-4} , 0.2, 0.5 and 1 m/s. As reported in figure 6-a, the evolution of the macroscopic damage parameter is plotted against the strain level for three tested strain rates. Experimental findings from interrupted tensile tests confirm that increasing the strain rate leads to a delayed

macroscopic damage initiation. Indeed, for a strain rate of 3 s^{-1} , macroscopic degradation begins at a strain level of 0.25% when for a strain rate of 20.5 s^{-1} , the first stiffness reduction appears at a strain in the order of 0.43%.

Hence, it easily follows that the damage evolution is relatively reduced as the crosshead rate increases from quasi-static to intermediate. Thus, one can claim that the stiffness reduction is rate dependent

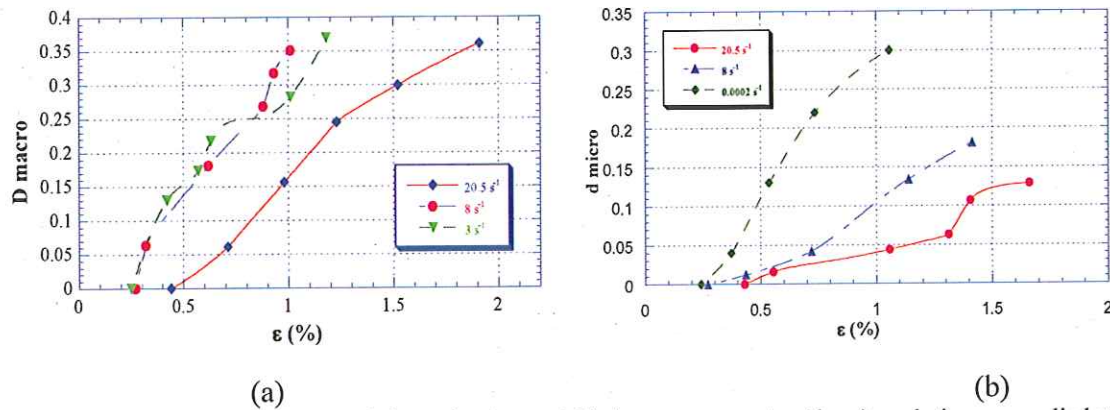


Fig. 6. (a) Longitudinal Young's modulus reduction and (b) damage parameter (d_{micro}) evolution vs. applied strain and plotted for different strain-rate. SMC-R26.

Figure 6-b illustrates the accumulation of micro-defects, generated by the interface decohesions, as a function of the macroscopic strain level. One observes that at the local scale, the damage growth is shifted in term of strain and exhibits a lessened kinetic due to the strain rate effect. Both aspects are related to the viscous effect generated by the delay of the dissipation occurring at interfacial zones. Consequently, one notices a lag in the macroscopic damage initiation coupled to a slight decreasing in term of its evolution.

CONCLUSIONS

The present work has proved that servo-hydraulic testing machine may be suitable to examine strain-rate effects on overall composite behaviour for a moderate rates up to 200 s^{-1} . Nevertheless, success with the high strain rate testing of polymer composites requires an experimental methodology able to isolate inertial disturbances attributed to the test system. To this end, an experimental methodology has been developed and optimised. It aims at minimizing the amplitude of measurements perturbation for giving rise to homogeneous stress/strain fields within the tested specimen. Experimental findings, obtained from monotonic and interrupted tensile tests performed at different strain rate, were inputted in numerical computations using ABAQUS FE code [10] for optimising iteratively the experimental conditions. The analysis of the stress wave propagation occurring for a high-speed tensile test has resulted in an optimal design of the specimen geometry and the experimental damping system: thickness and material characteristics. On one hand, the optimisation has contributed to generate uniform strain and stress fields yielding hence to a strain-rate spatially constant into the tested specimen. On the other hand, it has enabled to set up the interrupted high-speed tensile tests. These have provided the monitoring of the stiffness reduction evolution and the damage accumulation by interrupting the test at predefined load levels.

The developed experimental methodology based on dynamic tensile tests has contributed to emphasize the strain rate effects on overall behaviour of SMC-R26. As the strain rate increased, noticeable effects consist of a delayed damage onset followed by a slightly reduced damage accumulation. It was established that the strain rate brings about a viscous nature of damage evolution leading hence to the notion of the visco-damaged behaviour. Due to the time-dependant damaged-behaviour, the interface strengths are increased, which explains readily the accommodation exhibited at the macroscopic scale. As the strain rate increases, the damage viscosity reduces then the degradation and its kinetic.

References

- [1] Okoli O.I., Smith G.F., High strain characterization of a glass/epoxy composite. *J. Compos. Technol. Res., JCTRER*, 22-1 (2000), pp.3-11
- [2] Okoli O.I., The effects of strain rate and failure modes on the failure energy of fibre reinforced composites. *Composite Structure* 54 (2001), pp. 299-303
- [3] Harding J., Welsh L.M., A tensile testing technique for fibre-reinforced composites at impact rates of strain. *J. Mater. Sci.*, 18 (1983), pp.1810-1826
- [4] Rodney J. Clifton., Response of materials under dynamic loading. *International Journal of Solids and Structures* 37 (2000), pp. 105-113
- [5] Dear J.P., Brown S.A., Impact damage in reinforced polymeric materials *Composites. Part A: Applied Science & Manufacturing*, 34 (2003), pp. 411-420
- [6] H.M. Hsiao and I.M. Daniel, Strain rate behavior of composite materials. *Composites Part B* 29B (1998), pp. 521-533
- [7] Lataillade J-L., Delaet M., Collombert F., Wolff C., Effects of the intralaminar shear loading rate on the damage of multi-ply composites. *Int. J. Impact Engng.*, 18-6 (1996), pp. 679-699.
- [8] Pardo S., Baptiste D., Décobert F., Fitoussi J., Joannic R. Tensile dynamic behaviour of a quasi-unidirectional E-glass/polyester composite. *Composites Science and Technology*, 62-4 (2002), pp. 579-584
- [9] Jendli Z., Meraghni F., Fitoussi J., Baptiste D., Micromechanical analysis of strain rate effect on damage evolution in Sheet Molding Compound composites. (in-press) *Composites. Part A: Applied Science & Manufacturing*, (2004)
- [10] HKS Inc, ABAQUS Theory and Users Manuals V. 6.2.1, 2001
- [11] Krajcinovic D., Selection of damage parameter – Art or science? *Mechanics of Materials*, 28 (1998), pp. 165-179

SIMULATION OF COMPLEX IMPACT PROBLEMS WITH IMPLICIT TIME ALGORITHMS. APPLICATION TO CRASHWORTHINESS PROBLEMS

Ludovic Noels, Laurent Stainier and Jean-Philippe Ponthot

*LTAS-Milieux Continus & Thermomécanique, Department of AeroSpace, Mechanics and Materials, University of Liège,
Chemin des Chevreuils 1, B-4000 Liège, Belgium*

Summary: Recently, robust implicit energy and momentum conserving algorithms have been developed in the non-linear range. The authors extended these algorithms to hypoelasticity-based constitutive models and introduced numerical dissipation, opening the way to more complex simulations such as blade-loss in a turbofan.

INTRODUCTION

When studying impact problems, time integration of the equations of evolution occurs in the non-linear range. Usually, explicit algorithms are used in such a context. Nevertheless, due to its lack of stability in the non-linear range, and its limitation in the time step size, an implicit scheme could advantageously be used. The most widely used implicit algorithm is the Newmark algorithm [1]. Nevertheless, when this algorithm is used in the non-linear range, the conservation of the energy is no longer satisfied. To avoid divergence due to the numerical instabilities, numerical damping was introduced, leading to the generalized- α methods [2]. But these schemes can exhibit instabilities in the non-linear range too [3]. Therefore a new family of integration algorithms for structural dynamics has appeared that satisfies the mechanical laws of conservation (i.e. conservation of linear momentum, angular momentum and total energy) and that remains stable in the non-linear range.

The first algorithm verifying these properties was described by Simo and Tarnow [4]. They called this algorithm Energy Momentum Conserving Algorithm or EMCA. It consists in a mid-point scheme with an adequate evaluation of the internal forces. This adequate evaluation was given for a Saint Venant-Kirchhoff hyperelastic material. A generalization to other hyperelastic models was given by Laursen [5], who iteratively solved a new equation for each Gauss point to determine the adequate second Piola-Kirchhoff stress tensor. Another solution that avoids this iterative procedure, and leads to a general formulation of the second Piola-Kirchhoff stress tensor, was given by Gonzalez [6]. This formulation is valid for general hyperelastic materials. The EMCA was recently extended to dynamic finite deformation plasticity by Meng and Laursen [7]. The finite element discretization leads to high frequency modes that are purely numeric. To avoid the convergence problems resulting from these modes, Armero and Romero [8,9] introduced numerical dissipation in these conserving algorithms. This dissipation only affects the total energy but preserves the angular momentum. Moreover, it is proved to be stable in the non-linear range, contrarily to the α -generalized algorithms. It is called Energy Dissipative Momentum Conserving algorithm or EDMC. Besides, Armero and Petöcz [10,11] proposed a treatment of contact interactions in a consistent way in the non-linear range.

All the conserving methods described above were established for hyperelastic materials. We have recently [12,13] established a new expression of the internal forces for the hypoelastic materials using the final rotation scheme [14]. When associated with the mid-point scheme, this expression ensures the conservation laws of mechanics for a hypoelastic constitutive model. Moreover, we proved that this adaptation remains consistent with the Drucker postulate when plastic deformation occurs. Nevertheless, to be able to simulate complex impact problems, two improvements are necessary. The first one is to introduce numerical dissipation in a consistent way for such hypoelastic constitutive models [15]. This numerical dissipation avoids the numerical high frequency modes parasiting the physical solution. The second one is an enhancement of the contact formulation proposed by Armero and Petöcz to surfaces with discontinuous normal, as is the case when the two bodies in contact are deformable and are thus discretized by finite elements [16]. With such improvements, we are able to simulate complex problems of impact such as a blade-loss in a turbo engine.

DESCRIPTION OF THE MODEL

The turbo-engine is modeled with a shaft that has an imposed revolution motion on one extremity. At its other extremity, there is a disk with 24 blades. The shaft, the disk and the blades are part of the rotor, which is in rotation in a stator. The stator is composed of a casing and a bearing. The rotor has a cyclic symmetry of 15 degrees. Fig. 21 illustrates a 15-degree part of the rotor. The blade is defined from a ruled surface that has two splines for extremities. The blade is made of an alloy (density 3600 kg/m³, Young's modulus 88000 N/mm², Poisson's coefficient 0.31, initial yield stress 880 N/mm² and hardening parameter 26700 N/mm²). The disk and the shaft are composed of another alloy (density 6300 kg/m³, Young's modulus 165000 N/mm², Poisson's coefficient 0.31, initial yield stress 800 N/mm² and hardening parameter 271 N/mm²). The blade is discretized with 99 elements: 11 in length (elements at the head of the blade are 50% smaller than at the root), 9 elements in height and 1 element on the thickness.

The disk has 2 elements on the thickness and 72 elements on the circumference. The shaft has 1 element on its thickness and 11 elements on its length (8 for the constant section shaft and 3 for the conical part). The shaft has 72 elements on its circumference. The elements are 8-node bricks with constant pressure.

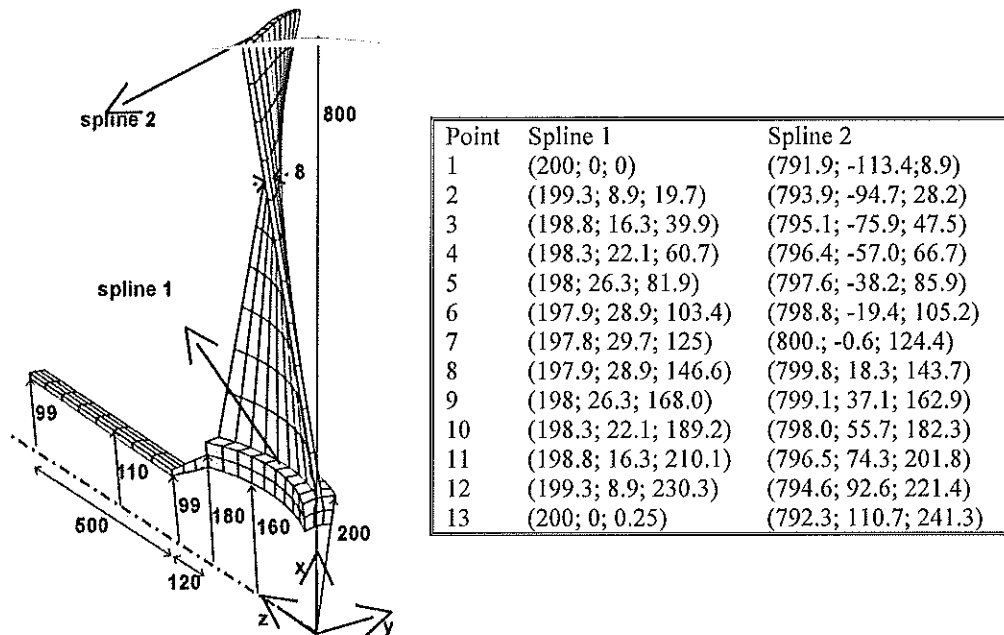


Fig. 21. model (dimensions in mm).

The casing is a cylinder made of an aluminium alloy (density 2710 kg/m³, Young's modulus 55200 N/mm², Poisson's coefficient 0.31, yield stress 550 N/mm² and hardening parameter 281 N/mm²). Its geometry is illustrated at Fig. 22a. The bearing has a conical geometry (Fig. 22b) and is made of an alloy (density 3600 kg/m³, Young's modulus 88000 N/mm², Poisson's coefficient 0.31, yield stress 550 N/mm² and hardening parameter 2600 N/mm²). The displacement of the shaft is restrained by the bearing thanks to a central node (Fig. 22b). There are springs between the central node and the extremity nodes of the bearing and there are springs between the central node and two rows on nodes of the shaft. Each spring has a stiffness of 10⁸ N/mm. A mass of 0.05kg is associated with the central node. The bearing and the casing have 1 element on the thickness. The casing has 36 elements on its circumference and 8 elements on its length. The bearing has 3 elements on its length and 20 on its circumference. The elements are 8-node bricks with constant pressure.

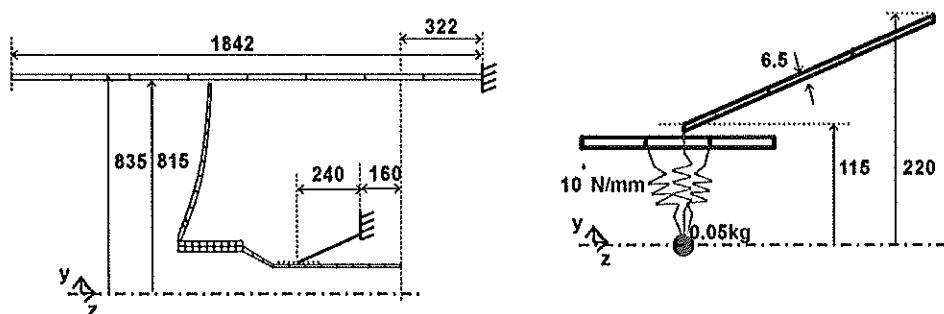


Fig. 22. Stator model, a- casing, b- bearing.

INITIAL CONFIGURATION

At time $t=0s$, the initial configuration of the rotor is computed for a rotation velocity of 4775 rpm. This initial configuration is computed with a Newton-Raphson scheme where the external forces are the analytical inertial forces computed from the nodes position and from the imposed rotation velocity. The von Mises stresses resulting from this uniform rotation velocity are illustrated at Fig. 23. The blade pointed by an arrow is independent from the disk. To evaluate the initial configuration, it is linked to the disk thanks to an adhesion law (normal penalty 10⁹, tangential penalty 10⁸). After the initial configuration is evaluated, this link is removed and the free blade interacts with the other blades and with the casing. The interaction between the blades and the casing is simulated with a Coulomb friction law (normal penalty 10⁹, tangential penalty 10⁷ and friction coefficient 0.1).

The interaction between the free blade and the other blades is simulated with the same law. Contact interactions between attached blades are simulated with a frictionless law (normal penalty 10^9).

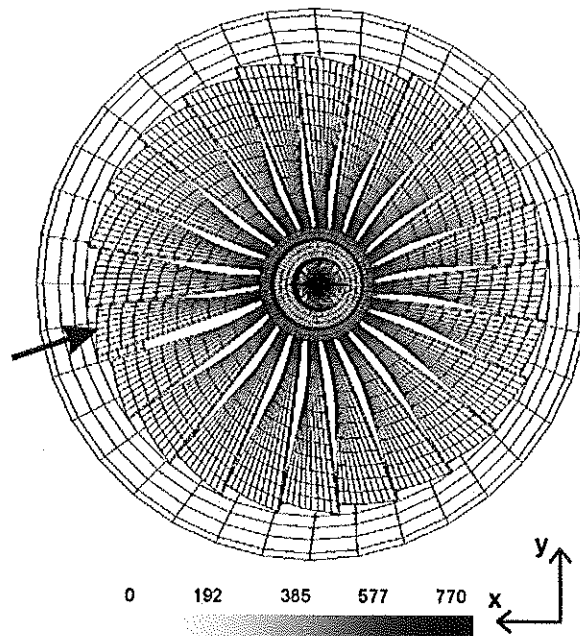


Fig. 23. Initial von Mises stress (Mpa) of the rotor (front view).

NUMERICAL SIMULATION OF THE FIRST REVOLUTION

Now we analyze the first revolution of the rotor after the blade loss. We use the EDMC (first order accurate) algorithm with a spectral radius equal at the infinity frequency 0.8. The time step size is computed from an automatic criterion [17] and with an accuracy of 10^{-4} on the integration error. The Hessian matrix is updated only when necessary [17]. Each time step is computed with a Newton-Raphson scheme (tolerance = 10^{-5}) enhanced by a line-search [18] (tolerance 10^{-3}).

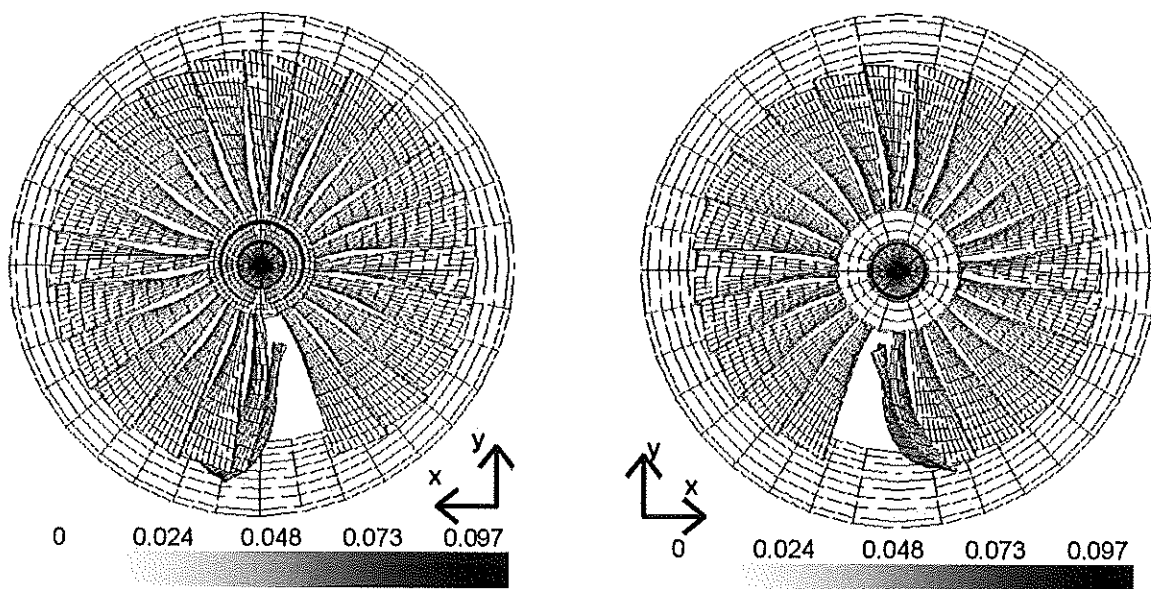


Fig. 24. Configuration and equivalent plastic strain after a quarter of revolution, a- front view, b- rear view.

Fig. 24a and Fig. 24b illustrate respectively the front and the rear view of the configuration after a quarter of revolution. The free blade interacts with the first next (attached) blade. Fig. 25a and Fig. 25b illustrate respectively the front view and the rear view of the configuration after half a revolution. The free blade remains between the linked blades and the casing. Due to the friction law, the attached blades bend. The head of the free blade enters into contact with the fifth linked blade. Fig. 26a and Fig. 26b illustrate respectively the front view and the rear view of the deformation after three

quarters of a revolution. The head of the free blade has led the fifth blade to bend significantly, and the free blade is pushed towards the rear of the casing. Fig. 27a and Fig. 27b illustrate respectively the front view and the rear view of the results after a revolution. The free blade was pushed away from the disk so that the remaining interactions only occur between the linked blades and the casing.

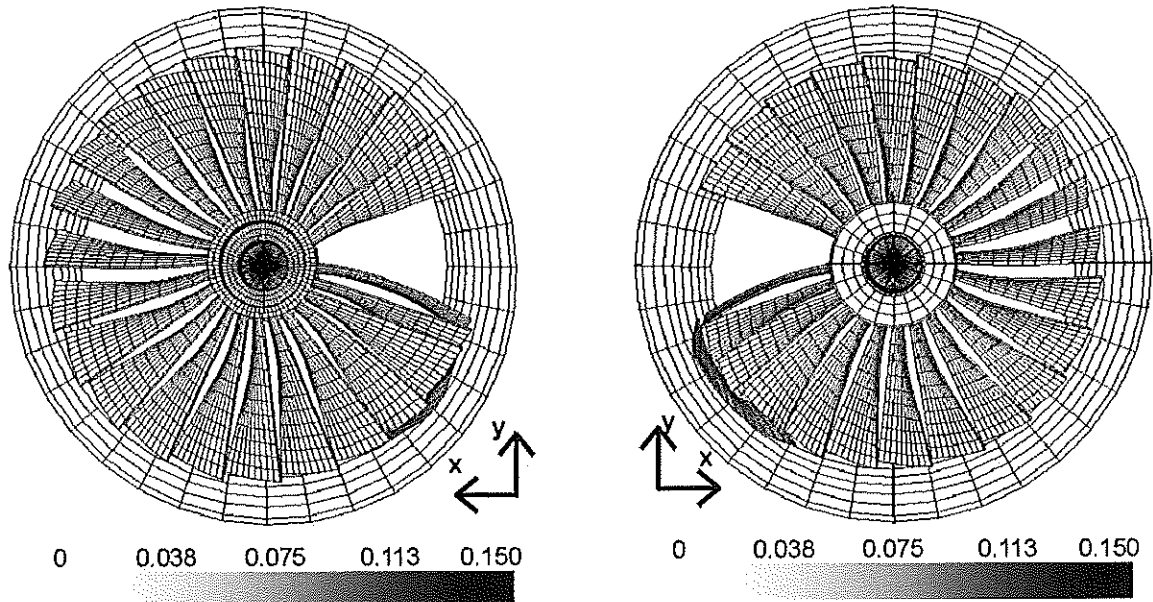


Fig. 25. Configuration and equivalent plastic strain after half a revolution, a- front view, b- rear view.

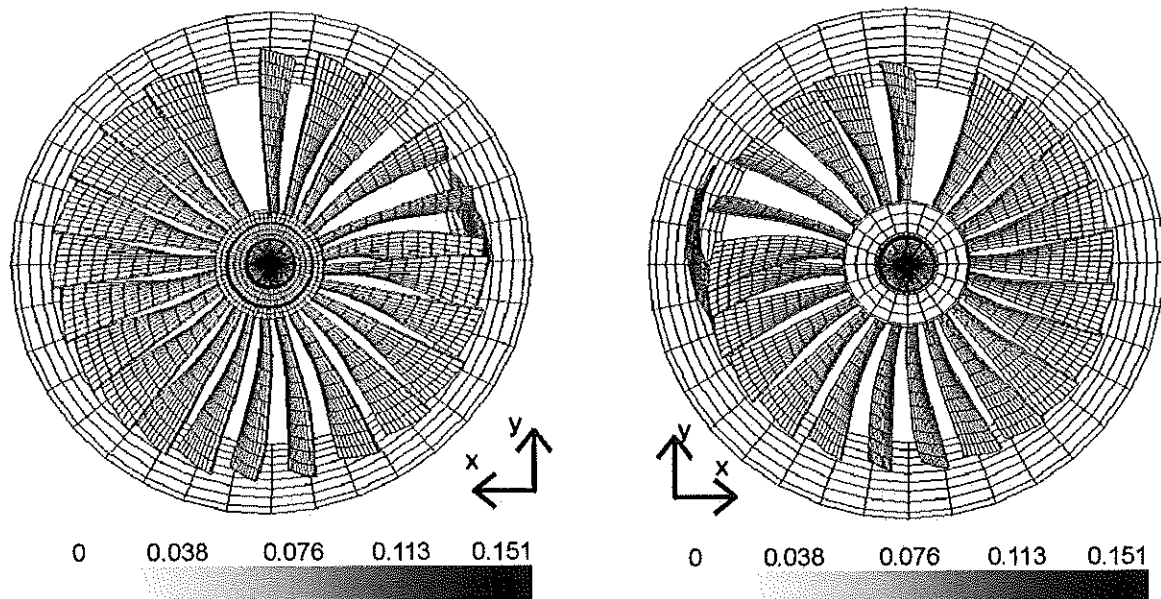


Fig. 26. Configuration and equivalent plastic strain after three quarters of revolution, a- front view, b- rear view.

The total force on the bearing is illustrated at Fig. 28a. It appears that this force is linear during the first instants, when the bearing reacts to the presence of an unbalanced shaft. But when the free blade interacts with both the linked blades and the casing, the force starts oscillating. The time evolution of the force on the casing (Fig. 28b) results from the interaction of the blades on the casing and the force oscillates during the whole simulation.

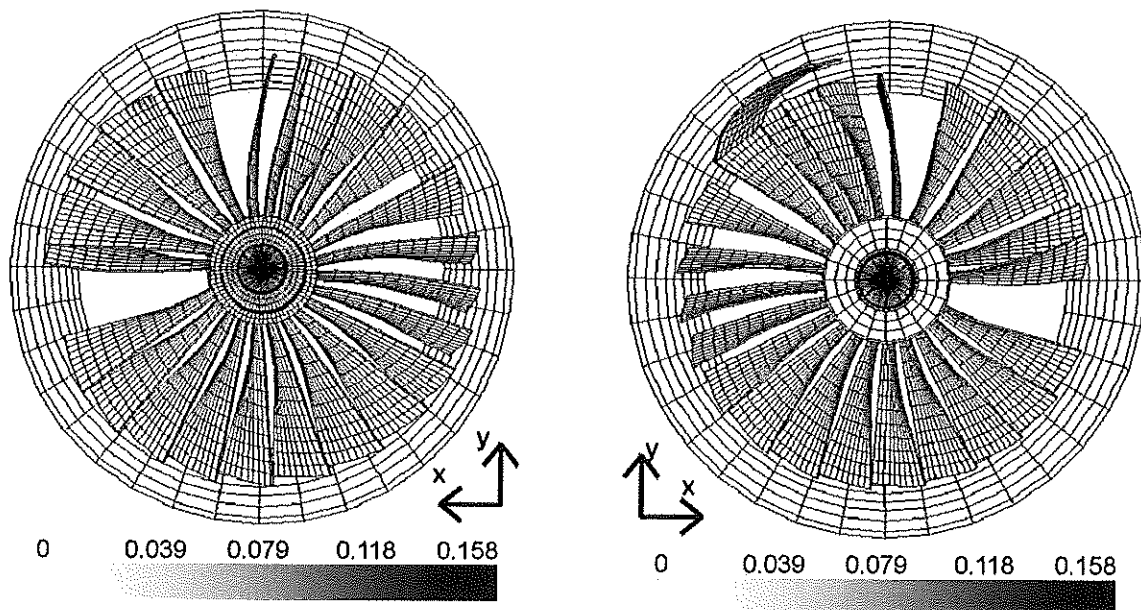


Fig. 27. Configuration and equivalent plastic strain after a quarter of revolution, a- front view, b- rear view.

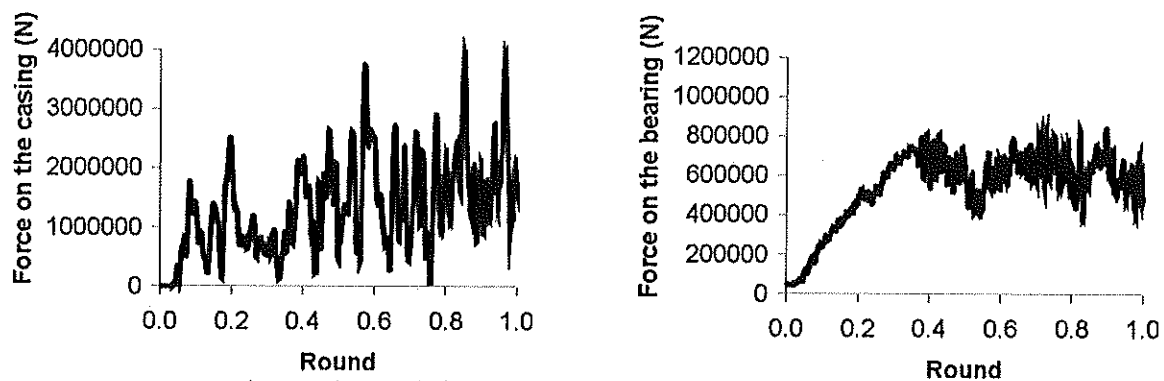


Fig. 28. Time evolution of the clamping forces, a- casing, b- bearing.

CONCLUSIONS

In this paper we proved that new developments in the study of the implicit schemes stability allow us to compute complex dynamics such as a blade loss problem. Advantages of the implicit scheme compared to the explicit one are its stability in the non-linear range that is mathematically proved and its ability to use large time step size. For the present simulation, the mean implicit time step size is equal to about $1.8 \mu\text{s}$ and the explicit critical time step is equal to $0.07 \mu\text{s}$. But thanks to the automatic Hessian matrix update and time step computation, the implicit steps are not much more expensive than the explicit ones. The implicit simulation is therefore twice cheaper than the explicit one.

References

- [1] Newmark, N., A method of computation for structural dynamics, *Journal of the Engineering Mechanics Division ASCE*, 85 (1959), pp. 67-94
- [2] Chung, J., Hulbert, G., A time integration algorithm for structural dynamics with improved numerical dissipation: the generalized- α method, *Journal of Applied Mechanics*, 60 (1993), pp. 371-375
- [3] Erlicher, S., Bonaventura, L., Bursi, O., The analysis of the α -generalized method for non-linear dynamic problems, *Computational Mechanics*, 28 (2002), pp. 83-104
- [4] Simo, J., Tarnow, N., The discrete energy-momentum method. Conserving algorithms for nonlinear elastodynamics, *ZAMP*, 43 (1992), pp. 757-792
- [5] Laursen, T., Meng, X., A new solution procedure for application of energy-conserving algorithms to general constitutive models in nonlinear elastodynamics, *Computer Methods in Applied Mechanics and Engineering*, 190 (2001), pp. 6309-6322
- [6] Gonzalez, O., Exact energy and momentum conserving algorithms for general models in nonlinear elasticity, *Computer Methods in Applied Mechanics and Engineering*, 190 (2000), pp. 1763-1783
- [7] Meng, X., Laursen, T., Energy consistent algorithms for dynamic finite deformation plasticity, *Computer Methods in Applied Mechanics and Engineering*, 191 (2001), pp. 1639-1675
- [8] Armero, F., Romero, I., On the formulation of high-frequency dissipative time-stepping algorithms for non-linear dynamics. Part I: low-order methods for two model problems and nonlinear elastodynamics, *Computer Methods in Applied Mechanics and Engineering*, 190 (2001), pp. 2603-2649

- [9] Armero, F., Romero, I., On the formulation of high-frequency dissipative time-stepping algorithms for non-linear dynamics. Part II: second order methods, *Computer Methods in Applied Mechanics and Engineering*, 190 (2001), pp. 6783-6824
- [10] Armero, F., Petőcz, E., Formulation and analysis of conserving algorithms for frictionless dynamic contact/impact problems, *Computer Methods in Applied Mechanics and Engineering*, 158 (1998), pp. 269-300
- [11] Armero, F., Petőcz, E., A new dissipative time-stepping algorithm for frictional contact problems: formulation and analysis. *Computer Methods in Applied Mechanics and Engineering*, 179 (1999), pp. 151-178
- [12] Noels, L., Stainier, L., Ponthot, J.-P., Energy-momentum conserving algorithm for non-linear hypoelastic constitutive models, *International Journal for Numerical Methods in Engineering*, 59 (2003), pp. 83-114
- [13] Noels, L., Stainier, L., Ponthot, J.-P., On the use of large time steps with an energy-momentum conserving algorithm for non-linear hypoelastic constitutive models, *International Journal of Solids and Structures*, 41 (2003), pp. 663-693
- [14] Ponthot, J.-P., Unified stress update algorithms for the numerical simulation of large deformation elasto-plastic and elasto-viscoplastic processes, *International Journal of Plasticity*, 18 (2002), pp. 91-126
- [15] Noels, L., Stainier, L., Ponthot, J.-P., On Simulation of complex impact problems with implicit time algorithm. Application to a blade-loss problem, *International Journal of Impact Engineering*, (in preparation 2004)
- [16] Noels, L., Stainier, L., Ponthot, J.-P., Simulation of crashworthiness problems with new improvement in implicit time integration of non linear dynamical systems, *International Journal of Impact Engineering*, (in preparation 2004)
- [17] Noels, L., Stainier, L., Ponthot, J.-P., On Self-adapting time integration management in crash-worthiness and sheet metal forming computations, *International Journal of Vehicles Design*, 30 (2002), pp. 67-114
- [18] Crisfield, M., *Non-linear finite element analysis of solids and structures*, John Wiley and Sons (2001)

MESODYNAMICS OF A 3D C/C COMPOSITE UNDER SHOCK LOADING: A DEDICATED COMPUTATIONAL MULTI-SCALE APPROACH

Jayant Sen Gupta*, Olivier Allix*, Pierre-Alain Boucard*, Alain Fanget† and Pierre-Louis Hérell†

* : Laboratoire de Mécanique et de Technologie
E.N.S. de Cachan / C.N.R.S. / Université Paris VI
61, avenue du Président Wilson, 94230 Cachan
e-mail: sengupta@lmt.ens-cachan.fr
†: Centre d'Études de Gramat
46500 GRAMAT

Summary: This paper deals with the dynamic behavior of a three-dimensional carbon/carbon composite (3D C/C) up to fracture. The *LMT-Cachan* and the *Centre d'Études de Gramat*, a research centre of the French Ministry of Defense, carried out this study jointly. In a previous collaboration, a modeling of the material at the mesoscale (scale of the matrix blocks, yarns sections, interfaces) had been built and identified (see [3], [6], [2]). The 3D computation of the behavior at such a scale leads to computations of huge size. This work deals with a domain decomposition strategy in order to decrease the cost of an analysis, make it parallel and have a specific treatment of the interfaces. In this paper, we present the first results obtained with this dedicated mesoscale computational strategy, which is described briefly.

INTRODUCTION

This work is motivated by the simulation of the behavior of a 3D C/C under shock loading (see figure 1 or 4(a) for the description of the material). The difficulties that have to be overcome in order to achieve this goal are double. The first is the fact that the mesoconstituents (matrix blocks, fibre yarns sections, interfaces) are highly nonlinear (plasticity, damage, compaction). The second is that the 3D modeling at the mesoscale implies to take into account the geometry of the mesoconstituents, which leads, even for simple structures, to problems with a great number of dof (about 10,000 dof per mm³). The most natural way to deal with these problems is to use domain decomposition techniques which are suitable for parallel computing. It is quite natural also to identify the substructures with the mesoconstituents. This particular choice gives a great importance to the interfaces between the substructures because they correspond to the physical interfaces between the mesoconstituents. In Cachan, a domain decomposition approach has been developed which is adapted for nonlinear interface behaviors. This approach has been presented in [8] and [5] for the statics and the quasistatics and adapted to dynamics in [4] and [9].

In this work, the substructure nonlinearities are very important because they modify greatly the dynamics of the structure, especially the wave velocities. Thus, we had to extend the previous approach that has been mainly developed for linear substructures behavior to the case of nonlinear substructures.

In the first part, the method is briefly presented as well as a few numerical applications in the second part.

THE LATIN METHOD APPLIED TO DOMAIN DECOMPOSITION

Splitting of the difficulties The first step of the method is to define two different entities: the substructures and the interfaces. In figure 2(a), two substructures are shown (Ω_E et $\Omega_{E'}$) and the interface between these two substructures ($\gamma_{EE'}$). These two entities exchange data defined at the

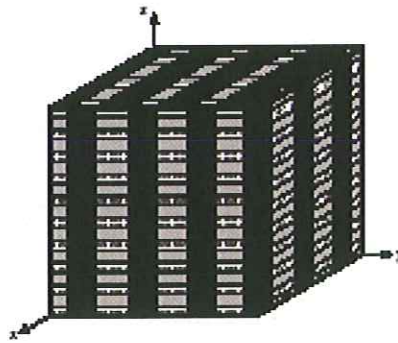


Figure 1: Mesostructure of the 3D C/C

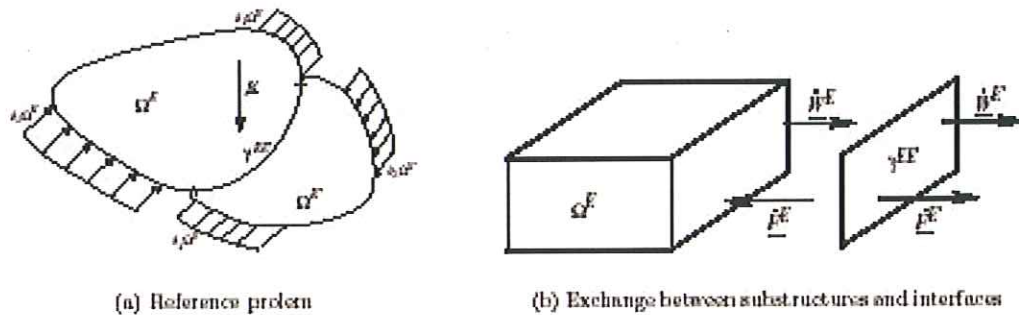


Figure 2: Splitting of the difficulties

interface: velocities and forces, as can be seen in figure 2(b). The velocities and forces coming from the substructure are projected on the edge $\gamma_{EE'}$, using an operator π .

Two spaces are defined :

- The first one, called **Ad**, is constituted by the fields $s = (\underline{V}(M, t), \sigma(M, t))$ defined on $(\Omega_E \times [0, T])$ verifying :
 - the dynamical equilibrium of Ω_E with \underline{F}_E and \underline{f}_t (volumical forces);
 - the kinematical admissibility with \underline{W}_E ;
 - the initial conditions;
- The second one, called Γ , is constituted by the fields $\hat{s} = (\hat{s}^1, \hat{s}^2)$ with $\hat{s}^1 = (\dot{W}_E(M, t), \hat{F}_E(M, t), \underline{W}_{E'}(M, t), \hat{F}_{E'}(M, t))$ defined on $\Gamma_{EE'} \times [0, T]$ and $\hat{s}^2 = (\hat{V}(M, t), \hat{\sigma}(M, t))$ defined on $\Omega_E \times [0, T]$ so that :
 - \hat{s}^1 satisfies the constitutive relation of $\Gamma_{EE'}$.
 - \hat{s}^2 satisfies the constitutive relation of Ω_E ;

Iterative algorithm The principle is to search for a field alternatively in **Ad** and Γ . Two steps may be defined in this process :

- Local step

During the local step, a solution s_n in **Ad** is supposedly known. We look for $\hat{s}_{n+1/2} = (\hat{s}_{n+1/2}^1, \hat{s}_{n+1/2}^2)$ in Γ such that $(\hat{s}_{n+1/2}^1 - \pi s_n, \hat{s}_{n+1/2}^2 - s_n)$ is in a linear space E^+ . This can be translated by :

$$\mathbf{L}_n^E - \hat{\mathbf{L}}_{n+1/2}^E = h^+ \left(\dot{\mathbf{W}}_n^E - \dot{\mathbf{W}}_{n+1/2}^E \right) \quad (1)$$

$$\sigma_n^E - \hat{\sigma}_{n+1/2}^E = \mathbf{H}^+ \left(\varepsilon_n^E - \hat{\varepsilon}_{n+1/2}^E \right) \quad (2)$$

where h^+ and \mathbf{H}^+ are parameters of the method called the search directions. h^+ is usually a constant scalar and \mathbf{H}^+ has been chosen in order to have an explicit expression of $\hat{\varepsilon}_{n+1/2}^E$, *i.e.* $\hat{\varepsilon}_{n+1/2}^E = \varepsilon_n^E$. This step is described in figure 3a.

- **Global step**

During the global step, a solution $\hat{s}_{n+1/2}$ in Γ is supposedly known. We look for s_{n+1} in Ad such that $(\pi s_{n+1} - \hat{s}_{n+1/2}^1, s_{n+1} - \hat{s}_{n+1/2}^2)$ is in a linear space E^- . This can be translated by :

$$\mathbf{L}_{n+1}^E - \hat{\mathbf{L}}_{n+1/2}^E = h^- \left(\dot{\mathbf{W}}_{n+1}^E - \dot{\mathbf{W}}_{n+1/2}^E \right) \quad (3)$$

$$\sigma_{n+1}^E - \hat{\sigma}_{n+1/2}^E = \mathbf{H}^- \left(\varepsilon_{n+1}^E - \hat{\varepsilon}_{n+1/2}^E \right) \quad (4)$$

where \mathbf{H}^- and h^- are the parameters of the method, also called the search directions. This step is described in figure 3b.

Depending on the way one chooses to go from Ad to Γ , that is to say the choice of the search direction, the method will slightly change. The search direction that concerns the interfaces is usually a scalar. The search direction that concerns the substructures is a bit more difficult to pick.

A first version was the simplest extension to the work in [9], choosing \mathbf{H}^- , in the substructures, as the initial elastic Hooke operator. Using a Newmark time integration scheme or a HHT scheme, the rigidity operators of the substructures are therefore constant and may be treated only once before any calculations are proceeded. During this step, one has to solve one global problem on each substructure but this problem is linear. The nonlinearities appear in the equations through a volumical term in the second part of the equilibrium equation. This term disappears if the behavior is satisfied by s_n . More details can be found in [10].

This simple method shows a good efficiency if the nonlinearities are small, *i.e.* if the variation of the tangent rigidity is small. The convergence rate of the method is close to the initial version dedicated to linear substructures. However, when the variation of the tangent rigidity is important, the convergence rate drops and this method is not efficient.

A second version has been conducted in order to treat highly nonlinear problems. The idea is to choose \mathbf{H}^- as the tangent behavior of the solution $\hat{s}_{n+1/2}$.

$$\hat{\sigma}_{n-1/2}^E = \mathbf{H}_{\text{NL}}^- \hat{\varepsilon}_{n-1/2}^E \quad (5)$$

Doing so, the global problems to solve are still linear but the operators change throughout the iterations of the method. After the application of a time integration scheme, the problem at each time step t_{n+1} may be written as:

$$\mathbf{K}_{\text{NL}} \dot{u}_{n+1} = F_{n+1}^{\text{dyn}} \quad (6)$$

\mathbf{K}_{NL} is a dynamic operator that depends on \mathbf{H}_{NL}^- , therefore it is non constant. To solve this problem, we use a preconditioned conjugate gradient algorithm. This allows us to solve it with a minimum number of iterations.

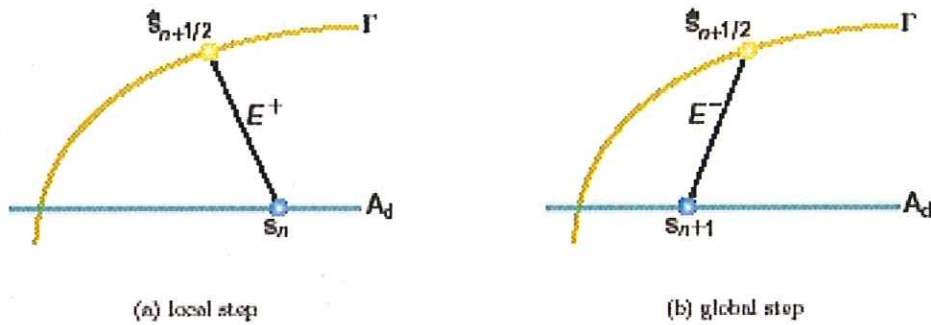


Figure 3: The two steps of the Latin method

FIRST 3D COMPUTATIONS

In order to test the potentiality of the method to solve huge computations, a 3D impact case with linear substructures has been conducted. This example was treated in the software CoFAST (developed by Laurent Champany). In the mesh of the figure 4(a), the impactor (aluminium), the sample (3D C/C), the buffer and the window (experimental devices made of PMMA in order to have a clean output signal) are represented from right to left. At $t = 0$, the impactor hits the sample with an initial velocity V_0 .

The memory cost of this example (about 150,000 DOFs and 400 time steps) showed the necessity to make this computation parallel. This allowed us to compute this example in less than one hour on an ORIGIN 2000 parallel machine. The longitudinal stress is shown in figure 4(b). In this figure, the longitudinal yarns in the direction \vec{y} are artificially removed to increase the comprehension of the figure. As shown, we observe that the longitudinal yarns come out. This phenomenon is observed also experimentally, inducing prints in the buffer.

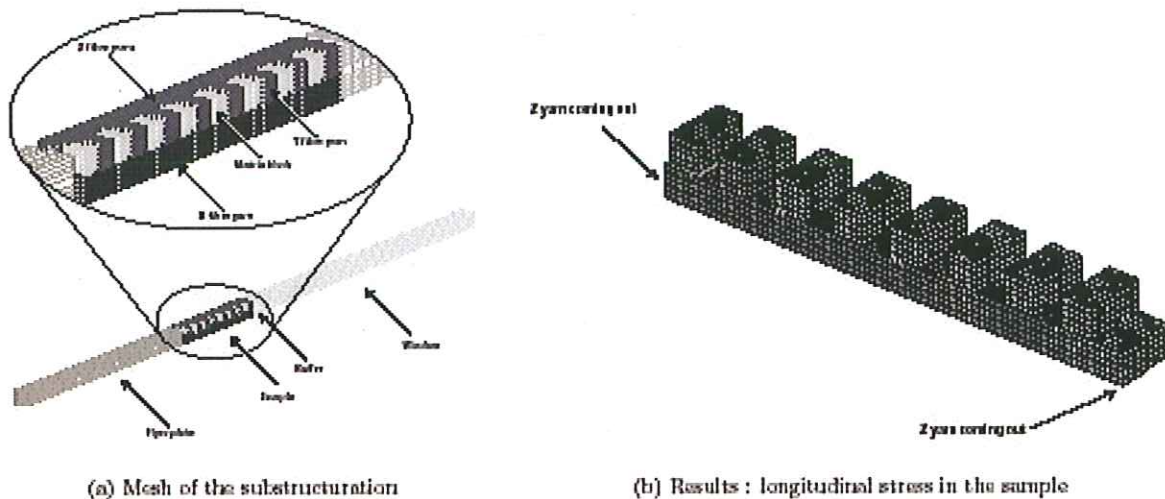


Figure 4: Substructured mesh and results

1D EXAMPLE WITH NONLINEAR SUBSTRUCTURES

In order to test the efficiency of the method to solve the nonlinear behavior of the substructures, the case of a bar submitted to a traction/compression loading is treated. In order to represent the complex behavior of the matrix blocks, the behavior of the bar is different in traction and compression. The models, recalled briefly in the following, are detailed in [1].

- **Delay damage in traction:** the idea here is to limit the damage rate by $1/\tau_c$.

$$\begin{cases} \rho\dot{\Psi} = \frac{1}{2} \left[\frac{\langle \sigma \rangle_-^2}{E} - \frac{\langle \sigma \rangle_+^2}{E(1-d)} \right] & \text{Free energy} \\ Y = \frac{1}{|\Omega|} \int_{\Omega} \left[\frac{\partial \rho\dot{\Psi}}{\partial d} \right]_{\sigma} d\Omega & \text{Damage force} \\ f(Y) = \left(\frac{Y}{Y_c} \right)^{1/2} & \text{Damage force} \\ \dot{d} = \frac{1}{\tau_c} \left(1 - e^{-\alpha (f(Y)-d)_+} \right) & \text{Damage rate} \end{cases} \quad (7)$$

- **Compaction in compression:** the material compacts until it reaches the dense material's Young modulus E_{max} .

$$\begin{cases} \sigma = \frac{E_0 \epsilon}{(1 + a \epsilon)^2} & \text{if } 0 > \epsilon > -\epsilon_{max} \\ \sigma = E_{max} (\epsilon - \epsilon_{max}) + \frac{E_0 \epsilon_{max}}{(1 + a \epsilon_{max})^2} & \text{if } \epsilon < -\epsilon_{max} \end{cases} \quad (8)$$

The example is described in figure 5a. The stress field is shown in figure 5b.

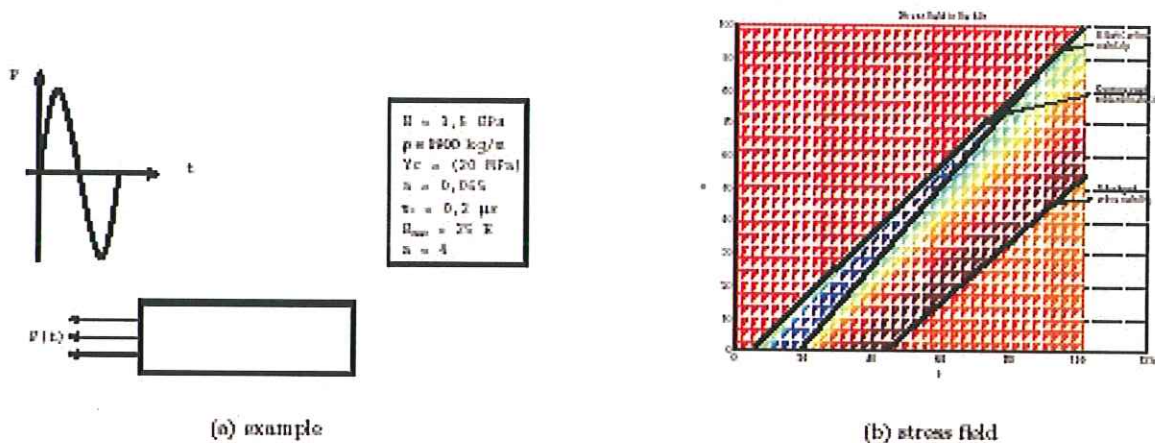


Figure 5: Numerical example

The results show that we are able to reproduce the different wave speeds in the material. In the first phase, the material is under compression and the waves propagating in the compressed material are faster than the waves propagating in the virgin material. As described in [7], we are also able to create shocks, or discontinuities, with a regular loading. The shock is created when the faster waves reach the slower ones.

On the other hand, when the material is in tension, the waves are slower than the elastic ones, which is in concordance with the physics.

CONCLUSION

The goal of the presented work is to build a method suitable to deal with a mesoscale description of a 3D C/C in dynamics. The solution is based on an mixed domain decomposition method, solved by the Latin method, which takes into account the nonlinear behavior of the substructures and interfaces. A preconditioned conjugate gradient algorithm is used to solve the linear problems. The nonlinearities treated are damage and compaction.

For the moment, computations on a large number of DOFs have been made on parallel computers but with linear substructures. On the other hand, in simple cases, we are able to deal with important structural nonlinearities. The perspective of this work is to be able to deal with both difficulties at the same time. This effort is in progress.

References

- [1] O. Allix, J. Sen Gupta 2001 Composite Damage Mesomodel for impact problems : Application to 3D C/C Material, *keynotes of ECCM-2001, Cracovia, Poland (2001)*.
- [2] O. Allix, M. Dommangeat, M. Gratton, P.L. Hérelil 2001 A multi-scale approach for the response of a 3D Carbon/Carbon Composite under shock loading, *Composite Science and Technology*, **61**, 409–415.
- [3] O. Allix, P.L. Hérelil, M. Gratton 1997 Comportement dynamique d'un composite 3D C/C: mésomodélisation et prévision de la rupture sous choc. *3e Colloque National en Calcul des Structures*, Giens (France), Presses Académiques de l'Ouest.
- [4] P.-A. Boucard, L. Champaney, P. Ladevèze and H. Lemoussu 1997 Une approche pour le calcul de choc avec contact unilatéral *13e Congrès Français de Mécanique Poitiers (France)*, AUM.
- [5] L. Champaney, J.-Y. Cognard, D. Dureisseix and P. Ladevèze 1997 Large scale applications on parallel computers of a mixed domain decomposition method *Computational Mechanics* **19**(4), 253–263.
- [6] P.L. Hérelil, O. Allix, M. Gratton 1997 Shock behavior of 3D carbon/carbon composite, *J. de Physique IV*, Colloque C3, **7**, 529–534.
- [7] A. Jaumotte 1971 Chocs et ondes de choc, *Ed. Masson et Cie*.
- [8] P. Ladevèze, Ph. Lorong 1992 A large time increment approach with domain decomposition technique for mechanical non linear problems *Computing Methods in Applied Sciences and Engineering INRIA* 569–578.
- [9] P. Ladevèze, H. Lemoussu, P.A. Boucard 2000 A modular approach to 3D impact computation with frictional contact, *Computers & Structures* **78**, 45–52.
- [10] J. Sen Gupta, O. Allix, P.-A. Boucard, A. Fangeat, P.-L. Hérelil 2003 Mésodynamique des 3D C/C : une première stratégie multiéchelle dédiée, *Proceedings of CFM2003, Nice, France (2003)*.

BEHAVIOR OF THE REINFORCED CONCRETE CIRCULAR PLATES SUBJECTED TO IMPULSIVE LOADING

Adam Zyskowski^{*}, Krzysztof Woznica, Patrice Bailly

Laboratory of Energetic, Explosions and Structures, ENSI de Bourges
10 Bld Lahitolle 18 000 Bourges, France

Summary: The aim of the study is to provide an adequate approach to dimension the reinforced concrete structures subjected to dynamic pressure loading. The work covers the numerical simulations of circular plates and focuses on multi-layered finite element method formulation. The impulsive loading applied on the plate has the characteristics of the pressure wave resulting detonation. To verify the influence on the results of biaxial stress distribution, the Mindlin theory together with corotational shell formulation and hexahedral elements' formulations are used. Among several constitutive laws of concrete, an equivalent softening diagram-based model with initial dynamic yield limit originally developed and applied for frame structures is chosen. The steel behavior is modeled by viscoplastic Perzyna model. Both constitutive formulations are supplied by the subroutine written in Fortran and implemented in Autodyn code.

INTRODUCTION

Nowadays, due to the extensive use of reinforced concrete material and the risk related to the terrorist menace, the methods of prediction of the behavior of reinforced-concrete structures subjected to impulsive loading focus the attention of civil engineers. Because of the deficiency in analytical methods, in order to evaluate the dynamic behavior of structure, the finite element method continues to be the predominant strategy. As distinct from analytical calculations, such approach accompanied with the explicit scheme makes possible to take into consideration both geometric (large displacements, deformations and rotations) and material non-linearities (plasticity, strain-hardening, softening and failure). The composition of reinforced concrete is, however, a major factor that renders difficult application of this approach. The geometry and location of reinforcement embedded in the concrete lead the mathematical formulation of an element quite complex [1, 9]. To overcome this problem some of the authors propose multilayered strategy with the steel material separated from the concrete [7, 8].

To conduct the dynamical structural analysis there are many software packages accessible on the market. Their implementation, however, is based on the various theories and different initial assumptions. For that reason, taking advantage of them is not a straightforward task. The main difficulty is the verification of the results obtained and their comparison to the experimental results.

The presented study is a part of the more global work that considers an ability of finite element codes to perform analysis of dynamically loaded reinforced-concrete members. The prime aim of this work is to verify two calculation approaches implemented in a general purpose finite difference, finite volume and finite element method presented in Autodyn 3D code for dynamically loaded reinforced concrete plates. The considered methods are the three-dimensional hexahedral elements expressed in Lagrange coordinates and the three-dimensional composite shell elements, formulated in corotational coordinate system that rotates with material. The secondary objective is the implementation of the constitutive models, which in the near future will serve as the basis for more generalized models.

THEORETICAL BASIS

From multiple analysis techniques presented initially in Autodyn v. 4.3 a Lagrange named and a 3D Shell formulations are selected as the basic platform for this study. To update the solution in successive time steps, an explicit central difference scheme is used.

For the hexahedral (brick) elements, the method of solution is founded on the approach derived by Wilkins [12] and is precisely described in [2]. Hence, only the comprehensive information is reviewed here. Fig. 1-a illustrates the computational algorithm.

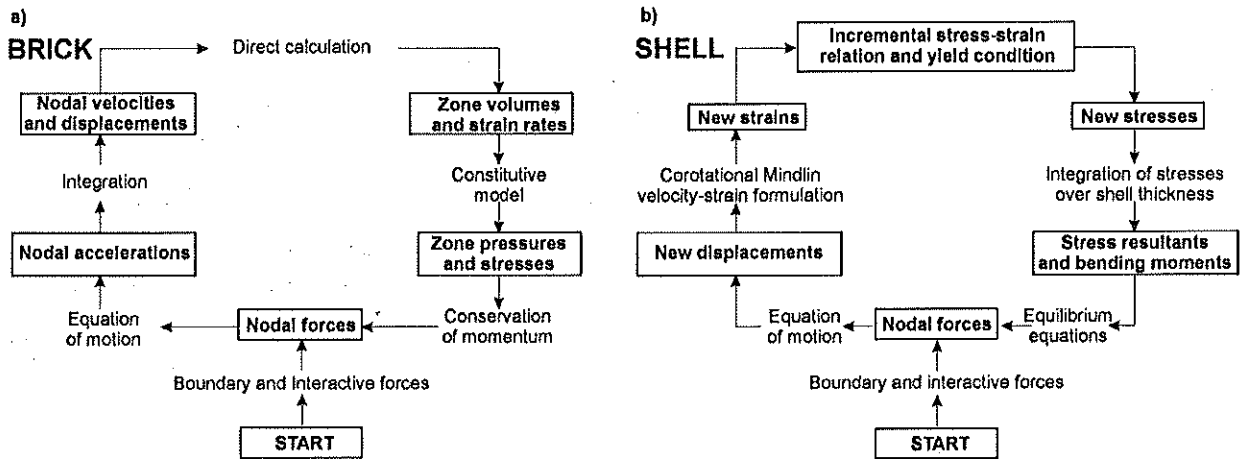


Fig. 1. Computational cycles for: a - hexahedral elements, b - shell elements [2]

As presented, the calculations begin with the computation of boundary and interactive forces. In the successive step, the obtained values are combined with the internal forces computed during the previous time cycle. Then from the consecutive integration of momentum equation the accelerations, velocities and positions are computed. From these values, the new zonal volumes and strain rates are calculated. With the use of a constitutive model together with the energy equation the zonal pressures, stresses and energies are computed, providing forces for use at the start of the next integration cycle [2].

The element implemented in Autodyn has a generalized hexahedral shape and consists of eight nodes. At each node positions, velocities and accelerations are defined. The other variables as pressure, internal energy, density, stress deviators, strain deviators, mass and temperature are calculated at an element center. An algorithm of hourglass forces is developed by Hallquist [6].

The relation between the strain rates $\dot{\epsilon}_{ij}$ and the velocities \dot{x} , \dot{y} , \dot{z} is expressed in the well-known form:

$$\dot{\epsilon}_{xx} = \frac{\partial \dot{x}}{\partial x}, \quad \dot{\epsilon}_{yy} = \frac{\partial \dot{y}}{\partial y}, \quad \dot{\epsilon}_{zz} = \frac{\partial \dot{z}}{\partial z}, \quad \dot{\epsilon}_{xy} = \frac{1}{2} \left(\frac{\partial \dot{x}}{\partial y} + \frac{\partial \dot{y}}{\partial x} \right), \quad \dot{\epsilon}_{yz} = \frac{1}{2} \left(\frac{\partial \dot{y}}{\partial z} + \frac{\partial \dot{z}}{\partial y} \right), \quad \dot{\epsilon}_{zx} = \frac{1}{2} \left(\frac{\partial \dot{z}}{\partial x} + \frac{\partial \dot{x}}{\partial z} \right). \quad (1)$$

In the case of the plate element the Mindlin-Reissner theory is applied. The bilinear four-node isoparametric elements with several quadrature points based on the resultant stress theory are used [3, 4]. Compared to the Lagrange formulations this approach noticeably simplifies the basic equations on an element level.

The geometry of the shell is defined by its midsurface, with coordinates denoted by x^m , y^m , z^m and its thickness h . The velocity of the midsurface v^m is given by:

$$\begin{Bmatrix} v_x^m \\ v_y^m \\ v_z^m \end{Bmatrix} = \begin{Bmatrix} \dot{x}^m \\ \dot{y}^m \\ \dot{z}^m \end{Bmatrix}. \quad (2)$$

The vectors tangent to the midsurface are e_1 and e_2 , and a fiber direction is defined by 1 . The fiber direction is initially coincident with e_3 , where:

$$e_3 = e_1 \times e_2 \quad (2)$$

and the angle between 1 and e_3 is assumed to remain small, so that:

$$|e_3 - 1| < \delta \quad (3)$$

where: the values of δ for most elastic-plastic calculations are in the order of 10^{-2} . The triad e_1, e_2, e_3 is defined to be corotational in the sense that it rotates with the material except that the vectors e_1 and e_2 remain tangent to the midsurface. If condition is met, the difference between the rotation of the material and the triad e_i should be small.

In the Mindlin theory of plates and shells, the velocity of a point in the shell is defined by the velocity of the midsurface v^m and the angular velocity vector θ by:

$$v = v^m - \hat{z}e_3 \times \theta \quad (4)$$

where: \hat{z} - is the local coordinate in the e_3 direction.

The corotational components of the strain rate \hat{d}_{ij} expressed in the local coordinates are given by:

$$\hat{d}_{ij} = \frac{1}{2} \left(\frac{\partial \hat{v}_i}{\partial \hat{x}_j} + \frac{\partial \hat{v}_j}{\partial \hat{x}_i} \right) \quad (5)$$

Substituting (5) into (6) the relations for the strain rates are obtained:

$$\hat{d}_{xx} = \frac{\partial \hat{u}_x^m}{\partial \hat{x}} + \hat{z} \frac{\partial \hat{\theta}_y}{\partial \hat{x}}, \quad \hat{d}_{yy} = \frac{\partial \hat{u}_y^m}{\partial \hat{y}} - \hat{z} \frac{\partial \hat{\theta}_x}{\partial \hat{y}}, \quad \hat{d}_{xy} = \frac{1}{2} \left[\frac{\partial \hat{u}_x^m}{\partial \hat{y}} + \frac{\partial \hat{u}_y^m}{\partial \hat{x}} + \hat{z} \left(\frac{\partial \hat{\theta}_y}{\partial \hat{y}} - \frac{\partial \hat{\theta}_x}{\partial \hat{x}} \right) \right] \quad (6)$$

$$\hat{d}_{yz} = \frac{1}{2} \left(\frac{\partial \hat{u}_z^m}{\partial \hat{y}} - \hat{\theta}_x \right), \quad \hat{d}_{zx} = \frac{1}{2} \left(\frac{\partial \hat{u}_z^m}{\partial \hat{x}} + \hat{\theta}_y \right) \quad (7)$$

The stress state in the shell is subdivided as follows:

$$\sigma = \begin{Bmatrix} \sigma' \\ \sigma'' \end{Bmatrix}, \quad \sigma' = [\hat{\sigma}_x, \hat{\sigma}_y, \hat{\sigma}_{xy}], \quad \sigma'' = [\hat{\sigma}_{xz}, \hat{\sigma}_{yz}] \quad (8)$$

The computational procedure is analogous to the algorithm for 3D brick elements (Fig. 1-b).

NUMERICAL EXAMPLE

The example chosen in the studies is founded on the work by Toutlemonde [11] and presented schematically in Fig. 2-a. The simulation of the reinforced concrete plate is conducted using the layered finite element method, as shown in Fig. 2-b. To avoid excessive computational times the considered problem is modeled by one quarter of the plate with planes of symmetry aligned with the x- and y-axes (Fig. 2-b). The decomposition of the plate is carried out by specifying 10x10 elements for the shell and 10x10x8 elements for the brick models, respectively in x, y and z directions. The shape of the mesh is illustrated in Fig. 2-a. The plate is divided into eight layers from which seven of 11.36 mm thick each is filled with the concrete material. The material in the last layer is defined as steel. The plate is loaded by the triangular pressure impulse as presented in Fig. 2-a.

To avoid very small numerical values of mass, volume and pressure within numerical cell the units of mm, mg and ms are used. Moreover, to limit the truncation error the 8 bytes definition of the user variables and double precision version of the code are utilized. The time increments are $\Delta t = 2.2E-7$ [s] for the shell and $\Delta t = 1.7E-8$ [s] for the hexahedral models. The time of the analyses is set to five ms. The computational time on Intel Pentium IV 1.7 GHz system varied from 70 minutes to 20 hours for shell and hexahedral models respectively.

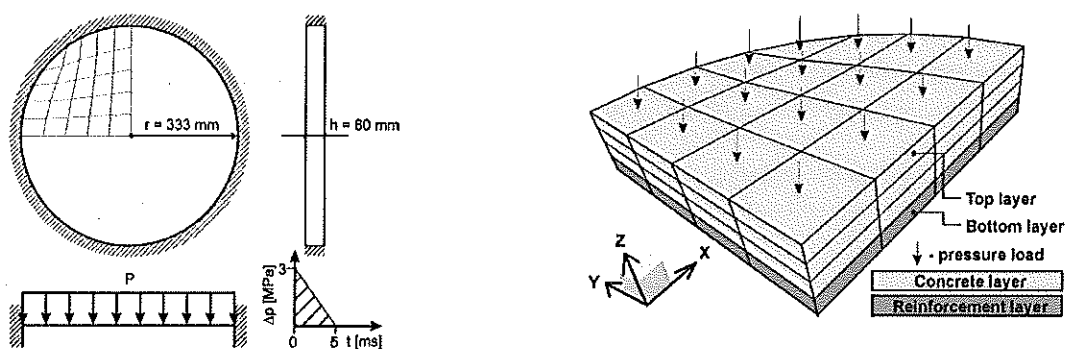


Fig. 2. a – Plate geometry and loading function, b - layers' convention

Concrete model

In the case of concrete modeling, the uniaxial model founded on the work by Bał and Stolarski [5] is simplified to represent the monotonous behavior of material. This model is based on an equivalent softening diagrams and is characterized by:

- linear - elastic segment up to the dynamic strength calculated by making use of Campbell's criterion:

$$\int_0^{t_d} \left[\frac{\sigma}{\sigma_0} t \right]^\alpha dt = t_0 \tag{9}$$

where: σ_0 - static yield stress, α , t_0 - material constants, σt - function of stress-strain for the dynamic elastic part, t_d - beginning time of dynamic yielding. Simplification of above equation results in:

$$\sigma_c^d = \sigma_0 \left[\alpha_c + 1 t_0 \frac{E_c \dot{\epsilon}}{\sigma_0} \right]^{\frac{1}{\alpha_c + 1}} \tag{10}$$

Therefore, the expression for dynamic elastic strain limit:

$$\epsilon_e = \frac{\sigma_c^d}{E_c} \tag{11}$$

- ideally plastic branch in the range specified by deformation $\epsilon_e - \epsilon_r$,
- and the linear degradation of material's strength $\epsilon_r - \epsilon_u$.

The material model together with relevant parameters is presented in the Fig. 3.

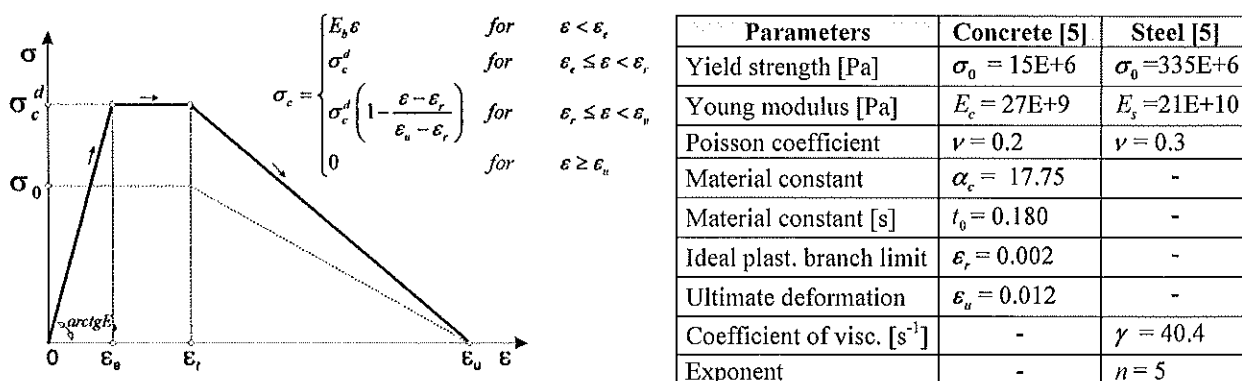


Fig. 3. a - uniaxial model of concrete – in compression, b – concrete and steel model parameters.

Steel model

During the deformation process, the state of stress in the reinforcement bars could be considered as uniaxial. Hence, the viscoplastic constitutive model of Perzyna [10] can be written as:

$$\sigma_0 = k \left(\frac{\dot{\epsilon} \operatorname{sgn} \sigma}{\gamma} \right)^{1/n} + k \tag{12}$$

where: σ_0 - instantaneous elastic limit, γ - viscosity coefficient, n - exponent.
 The parameters used in the studies are presented in Fig. 3-b.

Both concrete and steel models are implemented in the Autodyn code by the use of EXYLD user subroutine. The algorithm of principal stress calculation is realized through EXEDIT subroutine. All of the external procedures are written in Fortran. The EXYLD routine is called by main program at each cycle for each cell.

RESULTS

In Fig. 4 the principal stress 1 variation for the outer layers in the center of the plate are presented. Comparing Fig. 4-a and Fig. 4-b, it is observed that maximum stress amplitudes take place at the same time. As supposed, the concrete material is subjected to the compression state of stress while the steel to the tension. The stress values in the top layer are one order of magnitude smaller from those obtained in the bottom layer. From Fig. 4, it is clear that use of the shell elements cause the temporal variation of stress to be more quick and abrupt. In addition, their application reduces the maximum amplitudes.

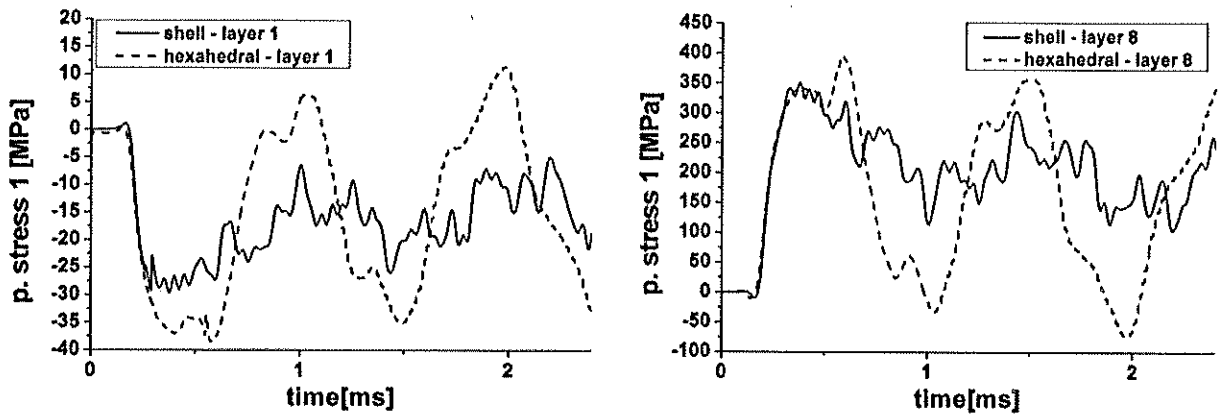


Fig. 4. Principal stress 1 for shell and hexahedral elements: a - layer 1 - concrete, b - layer 8 - steel

The introduction of the fictitious - forces such as hourglass damping forces, anti-tangle forces or pseudo-viscous forces preclude the conservation of the equilibrium equations. For that reason, to render the solution credible the results have to be accompanied by small energy error. In the conducted analyses, the maximum error expressed as the difference between the current energy of the system and work done on it, is set to 5 %. As presented in Fig. 5, the limit-error requirement is maintained and oscillates round zero.

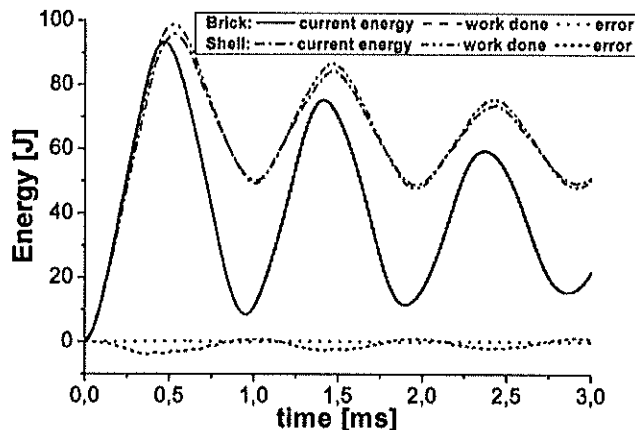


Fig. 5. History of the energy balance.

The vertical deflections of the middle point of the plate for various concrete strengths are presented in Fig. 6. The results show high dependence of the material strength. Comparing graphs, a significant difference in the amplitudes can be noticed. Increase of the static yield stress causes the amplitudes to be more pronounced what is particularly visible using the shell models. Regarding brick approach, only a slight variation between the results of considered models is observed. The differences between shell and brick formulations begin to appear just after the first maximum deflection and reduce with the increase of the concrete strength. For concrete strength equal to 45 MPa the response of the plate is independent of the model applied. Considering the frequency of vibration, it is observed that the periods of oscillation are almost identical.

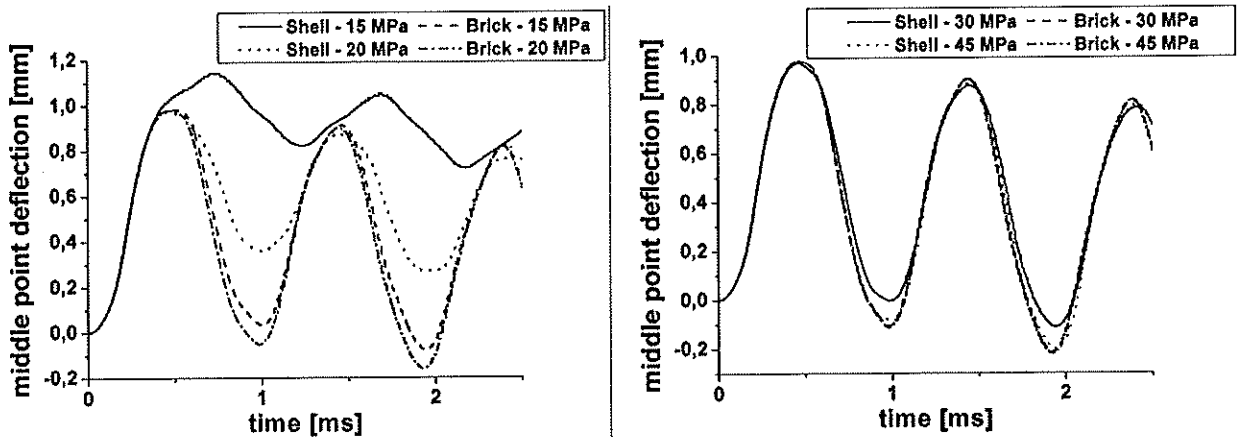


Fig. 6. Middle point vibrations of the plate for several strength configurations.

CONCLUSIONS

Despite the fact that hexahedral mesh is composed from the elements with large aspect ratios and the loss of accuracy would be expected, it is found, that the calculations with such approach result in less erroneous solution. Considering the computational time it is strongly advisable to use the shell elements. In that formulation, contrary to the brick elements where the full strain rate tensor is evaluated at each integration point, some of the strain rate components (\hat{d}_{yz} , \hat{d}_{zx}) are determined once per element (thickness). Besides, the shell formulation only requires a plane-stress constitutive equation, which effectively reduces the number of state variables associated and as effect leads the computations to be more efficient.

References

- [1] Abaqus v. 6.2. Electronic Documentation Library, HKS Inc, (2002)
- [2] Autodyn v. 4.3 Electronic Document Library, Century Dynamics Inc., (2003)
- [3] Belytschko, T., Lin J.J., Tsay C.-S., Explicit algorithms for the nonlinear dynamics of shells, *Comp. Meth. Appl. Mech. Eng.*, 42 (1984), 225-251
- [4] Belytschko, T., Wong, B.L., Chiang, H.-Y., Advances in one-point quadrature shell elements, *Comp. Meth. Appl. Mech. Eng.*, 96 (1992), 93-107
- [5] Bąk G., Stolarski A., Analiza nieliniowa prętowych ustrojów żelbetowych obciążonych impulsowo, *Komitet Inżynierii Lądowej i Wodnej PAN, Studia z Zakresu Inżynierii*, 30 (Warszawa 1990)
- [6] Hallquist, J. O., A theoretical manual for DYNA3D, LLNL Report UCID-19401, (June 1982)
- [7] Miyamoto A., King M. W., Fujii M., Nonlinear dynamic analysis of reinforced concrete slabs under impulsive loads, *ACI Struct. J.*, (July - August 1991), 411-419
- [8] Miyamoto A., King M. W., Fujii M., Analysis of failure modes for reinforced concrete slabs under impulsive loads, *ACI Struct. J.*, (September - October 1991), 538-545
- [9] MSC. Marc Documentation, MSC. Software Corporation (2003)
- [10] Perzyna, P., Fundamental problems in viscoplasticity. *Advances in Mechanics*, 9 (1966), 243-377
- [11] Toutlemonde F., Résistance au choc des structures en béton, Du comportement du matériau au calcul des ouvrages, *Rapport Laboratoire Central des Ponts et Chaussées*, (1995)
- [12] Wilkins, M. L., Blum, R. E., Cronshagen, E., Grantham, P., A Method for Computer Simulation of Problems in Solid Mechanics and Gas Dynamics in Three Dimensions and Time, *Lawrence Livermore Laboratory Report UCRL-51574*, (1974)

A STUDY OF DYNAMIC BEHAVIOR OF THE AUTOCLAVED AERATED CONCRETE

J.R. Klepaczko ** and R. Belouettar *

* Laboratory of Civil Engineering, Annaba University, PB: 12, Annaba, Algeria

** Laboratory of Physics and Mechanics of Materials, UMR CNRS 75-54, Metz University, Ile du Saulcy, 57045 Metz cedex 01, France

Summary. This work presents an experimental study on the dynamic behavior of autoclaved aerated concrete. The paper reports a series of tests with a Hopkinson Pressure Bar [1,2] applied to the direct impact technique [5]. Several strain rates were applied varying from quasi-static to impact between $1.4 \times 10^2 \text{ s}^{-1}$ to 10^3 s^{-1} . Two states of the aerated concrete were tested, that is dry and saturated with water. In general, an increase of strain rate causes an increase of the critical failure stress for such materials. In the quasi-static range and up to certain critical impact velocity V_C the autoclaved aerated concrete shows a positive strain rate sensitivity. However, when a critical impact velocity V_C is reached a very specific behavior is observed, that is the cell structure is pulverized near the plane of impact. This effect is completely new.

INTRODUCTION

Cellular concretes are mostly used in the building industry as a material with a low thermal conductivity. However, this material is not so strong and can be easily crushed. It appears that during an impact loading it can be pulverised without difficulty. Such behavior is important, for example, in case of earthquakes or short-time loadings caused by impact. Because the cell structure of such material is very brittle it leads to instantaneous crushing near the loading zone. In order to find the rate sensitivity and an impact resistance to crushing a study was carried out in quasi static compression tests with a servo-hydraulic fast testing machine. In order to cover the widest possible range of strain rates, the range of quasi-static strain rates was applied varying from 10^{-4} s^{-1} to 10 s^{-1} and the high strain range was applied up to 10^3 s^{-1} . Thus in the quasi-static range of strain rates the sensitivity could be found. The next step was to test such materials using specially designed experimental set-up designed and constructed at LPMM.

DIRECT IMPACT TESTS

The first mechanical tests at high strain rate were carried out by B.Hopkinson [1] based on the concept of ballistic pendulum and elastic wave propagation in a bar, called since "Hopkinson bar". It was only since 1948 that the Hopkinson bar has been instrumented by Davies [2]. In both cases the bars served as specific gages to determined short pressures. One year later Kolsky developed technique called the "Split Hopkinson Pressure Bar" or Kolsky apparatus, [3]. There were two instrumented Davies' bars with a small cylindrical specimens inserted in between. The Kolsky apparatus was modified later on by Lindholm [4]. In general, its principle is based on the theory of the elastic wave propagation in bars and makes it possible to obtain a large range of high strain rates varying from $5 \times 10^2 \text{ s}^{-1}$ to 5.10^3 s^{-1} , [3,4,7]. In this study, however, only one Hopkinson bar instrumented with SR gages was applied in combination with non-contact optical displacement gage [5]. The principle of experimental set-up is shown in Fig.1

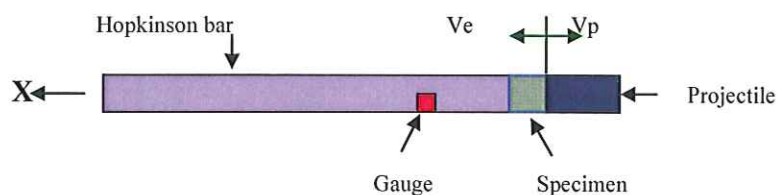


Fig.1 Principle of the Hopkinson bar in direct impact arrangement

DETERMINATION OF THE OUTPUT QUANTITIES

In order to obtain the critical compression stress at failure in the setup shown in Fig.1. A simple theory of wave propagation in bars was applied. During contact between the projectile and the specimen a damage occurs on a part of the thickness of the specimen. The critical force of failure is transmitted into the Hopkinson bar and it can be measured as a function of time by the SR gage. An equilibrium of forces is assumed between the specimen of autoclaved aerated concrete and projectile: $F_{ep} = F_p$, where F_{ep} is the force in the specimen F_p is the force of the projectile, thus $A_{ep} \sigma_{ep} = A_p \sigma_p$, where A_{ep} is the cross section surface of specimen and A_p is the cross section surface of the projectile. The impact velocity V_0 measured

Three sources of light, fiber optics and three photodiodes, Fig.1, is split into two mass velocities in the specimen and projectile, $V_0 = V_{ep} + V_p$. This assumption is valid only at the first instant of the contact specimen/projectile. The well known relation between stress and the mass velocity leads to the following relations $\sigma_{ep} = \rho_{ep} C_{0ep} V_{ep}$ and $\sigma_p = \rho_p C_{0p} V_p$ where C_{0s} and C_{0p} are respectively the elastic wave speeds in the specimen and projectile and ρ_{ep} and ρ_p are the densities of the specimen and projectile. The relation between stresses and the impact velocity is given by

$$V_0 = \frac{\sigma_{ep}}{\rho_{ep} C_{0ep}} + \frac{\sigma_p}{\rho_p C_{0p}} \tag{1}$$

The assumption of the force equilibrium during first instant of crushing leads to the following relation

$$V_0 = \frac{\rho_B C_{0B} \epsilon_T(t)}{\rho_{ep} C_{0ep}} \left[1 + \frac{A_{ep} \rho_{ep} C_{0ep}}{A_p \rho_p C_{0p}} \right] \tag{2}$$

Where $\sigma_B = \rho_B C_{0B} \epsilon_T(t)$ and ρ_B , C_{0B} and $\epsilon_T(t)$ are respectively the density, the elastic wave speed and the transmitted wave recorded by SR gauges as a function of time, all in the Hopkinson bar. This simplified formula allows to estimate the critical failure stress as well as the critical impact velocity V_{0c} for various quasi-brittle materials loaded at various impact velocities when the critical conditions are detected in the $\epsilon_T(t_c)$ signal, where t_c is the instant of failure.

DESCRIPTION OF THE SET-UP FOR DIRECT IMPACT LOADING

The arrangement applied for the direct impact tests is shown in Fig.2. It makes possible to determine not only the critical impact velocity of crushing but also, due to application of the optical displacement gage, to determine the whole stress versus strain relation at high strain rates. This set-up has been developed at the Laboratory of Physics and Mechanics of Materials (LPMM), [5].

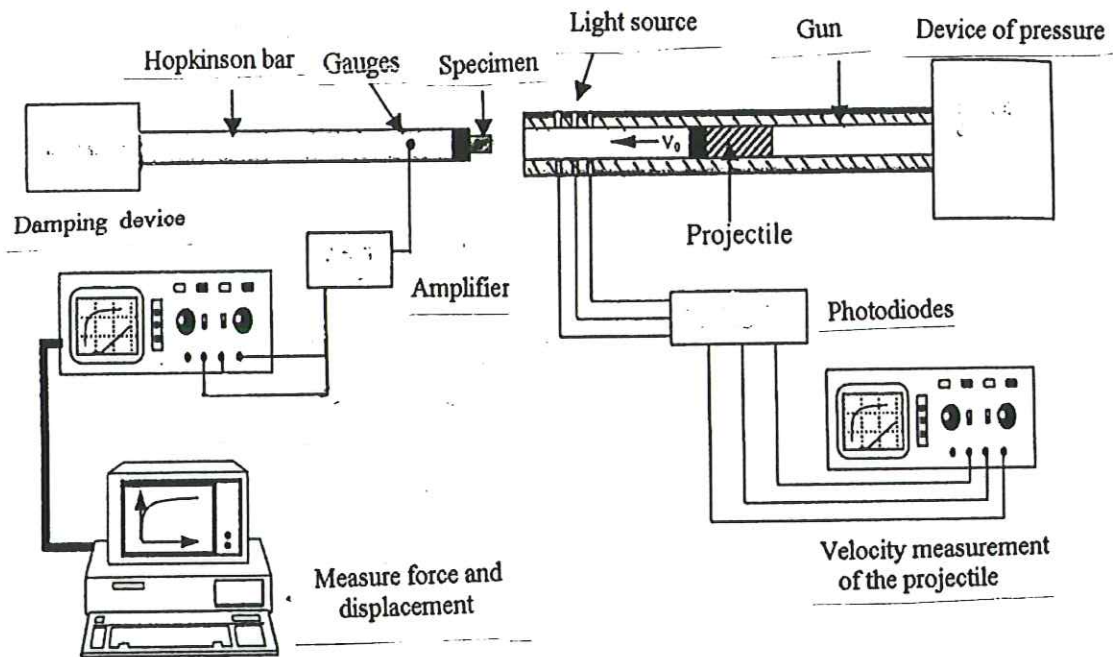


Fig. 2. Arrangement of Hopkinson bar with direct impact, [5].

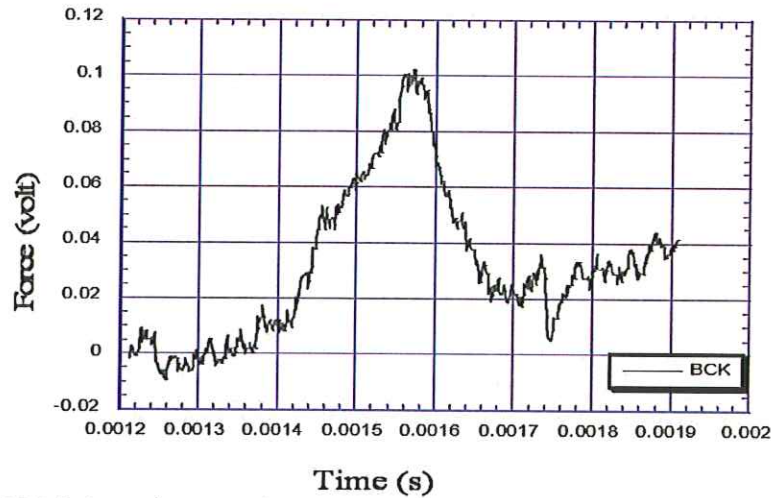


Fig. 3. Digital record representing a typical test of autoclaved aerated concrete of BCK type.

A gas gun launches a projectile at a desired velocity V_0 . The specimen is supported by the Hopkinson tube. The tube is closed in front by a thin steel plate to support a specimen. Application of the Hopkinson tube instead of a bar substantially increased sensitivity of measurement of the transmitted waves. This improvement was caused by a low velocity of crushing found for the aerated concrete being tested. The displacement of the projectile during the contact with specimen is measured by the first canal of the optical displacement gage, the second channel can measure displacement of the tube front. The complete set of measurements consists of the impact velocity V_0 (three photodiodes and two time counters) and the displacement of projectile in contact with specimen $U_A(t)$, the displacement of the tube front $U_B(t)$ and the transmitted elastic wave in the Hopkinson tube $\epsilon_T(t)$. All electric signals after conditioning are stored in a digital oscilloscope with maximum sampling rate 1 GHz. Later the digital records are stored in a PC for further analyses.

ANALYSIS OF STORED SIGNALS

The impact velocity V_0 is directly related to the pressure in the chamber of the gas launcher, and the nominal strain rate is defined as $\dot{\epsilon} = V_0 / l_s$, where l_s is the specimen length. Because both, the displacement of the contact projectile/specimen $U_A(t)$ and the transmitted wave $\epsilon_T(t)$ are recorded it makes possible to determine completely the behavior of a specimen, [5]. The net displacement of the specimen is calculated by the difference between the displacement $U_A(t)$ and displacement of the tube $U_B(t)$, thus the nominal strain can be also found

$$U_{cp}(t) = U_A(t) - U_B(t) \quad \text{and} \quad \epsilon_n = \frac{1}{l_s} [U_A(t) - U_B(t)] \quad (3)$$

The displacement of the tube at the time of loading is related directly to the transmitted wave by the following relation

$$U_B = C_0 \int_0^t \epsilon_T(\xi) d\xi \quad (4)$$

where C_0 is the elastic wave speed.

The stress measurement is possible by the means the SR gauges via the transmitted wave $\epsilon_T(t)$. The stress as well as the force can be given according to the signal of the transmitted wave [JK].

$$\sigma_T(t) = \rho_B C_0^2 \epsilon_T(t) \quad (5)$$

where $E_B = \rho_B C_0^2$ is the modulus of elasticity of the tube. In the case of compression, the force which acts on the surface of contact of the bar and of the specimen is assumed to be the same. Thus the mean force loading the specimen, and consequently the nominal stress σ_n , can be written in the following way:

$$F_{ep}(t) = F_B(t) \quad \text{and} \quad F_{ep}(t) = \rho_B C_0^2 A_B \varepsilon_T(t) \quad (6)$$

$$\sigma_n(t) = \frac{F_{ep}(t)}{A_{ep}} \quad (7)$$

where A_B is the cross section of the Hopkinson tube.

RESULTS OF COMPRESSION TESTS

The tests were carried out on two types of aerated concrete. The specimens were tested in two different states: the dry state and the wet state (saturated with water). For the reason of dispersion of the results, mainly stresses, five tests were performed at each impact velocity V_0 . The assumed impact velocities of the projectiles are : 5 m/s, 10 m/s, 20 m/s, 30 m/s and 35 m/s. The cylindrical projectiles of diameter 49.8 mm were machined out of aluminum alloy 2017A, of density and modulus of elasticity respectively equal to 2.79 g/cm³ and 74 GPa. The specimens were in the form of cubes with the side dimension 40.0 mm. Thus the five programmed velocities for the dynamic tests yield strain rates from $1.43 \cdot 10^2 \text{ s}^{-1}$ to $8.75 \cdot 10^3 \text{ s}^{-1}$.

After analysis of all records the values of the critical stress of crushing were obtained. The results are presented in the form of σ_C versus $\log(\dot{\varepsilon})$ in figures 4a and 4b for dry and wet BCK aerated concrete, Figs 5a and 5b show similar results for BCM aerated concrete. The wet materials show higher critical stresses as compared to dry materials. The sensitivity is observed between speeds 10 s^{-1} and $1.43 \cdot 10^2 \text{ s}^{-1}$. At lower strain rates the rate sensitivity of the critical stress is positive, but at certain strain rate, typically higher than 10^2 s^{-1} , one notices a reduction in the critical stresses when the strain rate is increased beyond of this critical value. In some cases a minimum of the critical stress is obtained. Then an increase in the critical stresses is observed anew. The mean values of the critical stresses are denoted by dark triangles. The results for dry and wet autoclaved aerated concrete BCK are shown in Fig.4. Whereas the results for dry and wet BCM aerated concrete are shown in Fig.5.

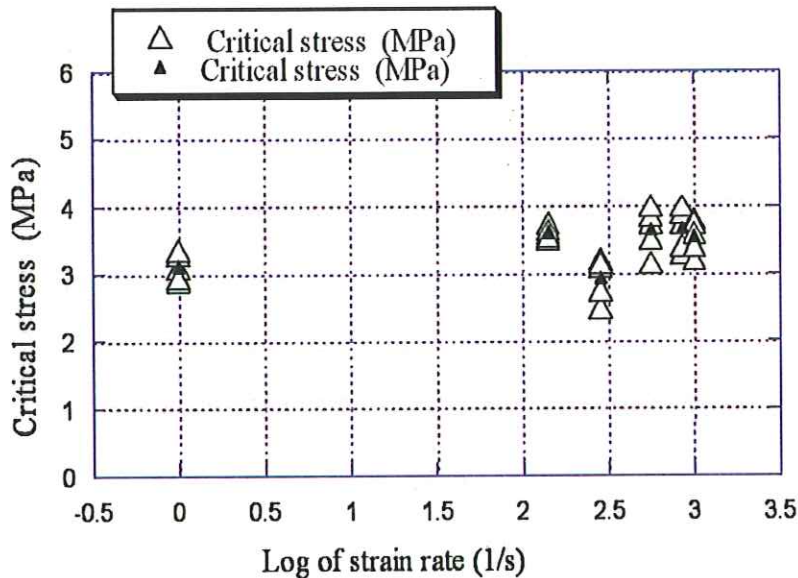


Fig. 4a - Critical stress versus logarithm of strain rate for dry autoclaved aerated concrete BCK.

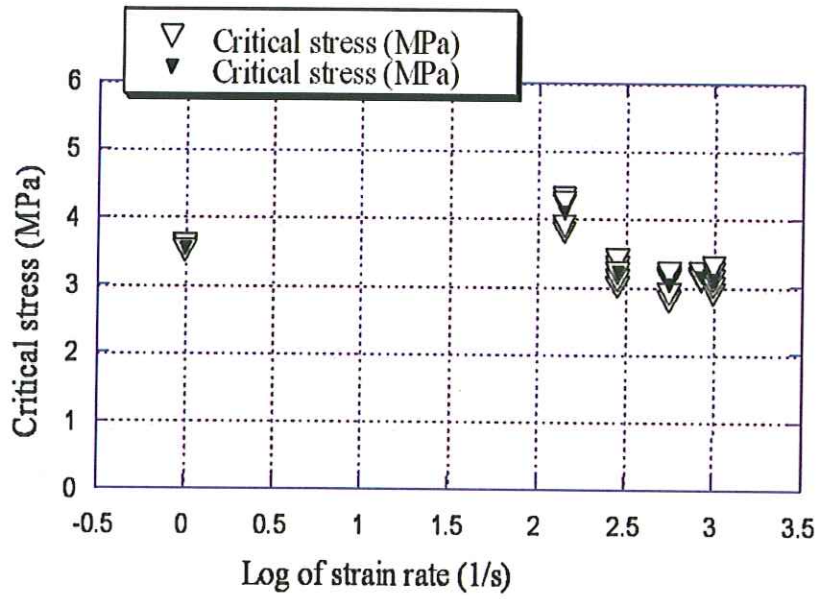


Fig.4b - Critical stress versus logarithm of the strain rate for wet autoclaved aerated concrete BCK.

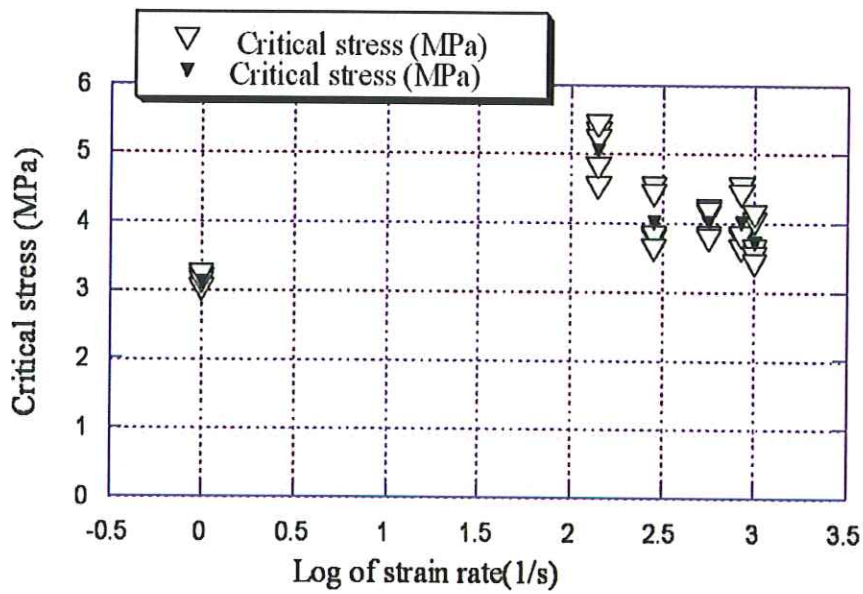


Fig. 5a - Critical stress versus logarithm of strain rate for dry autoclaved aerated concrete BCM.

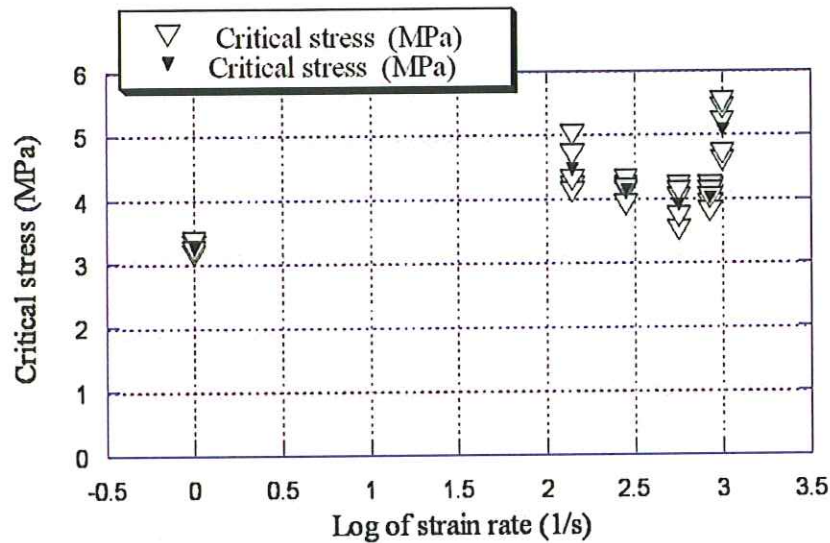


Fig. 5b - Critical stress versus logarithm of strain rate for wet autoclaved aerated concrete BCM

CONCLUSIONS

The scheme of the direct impact experiment seems to be very useful in materials testing at high strain rates [5,6]. Application of the non-contact optical displacement gages enabled to measure the real mean strain in a specimen leading to the complete measurements of stresses and strains. Elimination of time leads to estimation of the stress-strain characteristics at relatively high strain rates.

It is concluded after the results obtained during the dynamic tests of the autoclaved aerated concrete BCK and BCM that the autoclaved aerated concrete has a positive rate sensitivity at low and medium strain rates. But at the high strain rates a critical impact velocity V_{oc} occurs, this velocity is around 5.0 m/s the two materials tested. The BCM reaches a maximum value of the critical stress of 5.3 MPa in dry state and 4.5 MPa in the wet state (strain rate $1.43 \cdot 10^2 \text{ s}^{-1}$). Whereas for the same strain rate the values of the critical stress for the BCK is only 3.75 MPa (in dry state) and 4.00 MPa (in wet state). Both material showed a higher rate sensitivity in the state saturated with water. The effect of saturation of pores with water intervenes in this behavior.

At strain rates higher than $\sim 1.4 \cdot 10^2 \text{ s}^{-1}$ ($\sim 5.0 \text{ m/s}$) the stress of failure decreases. This decrease of the failure stress is due mainly due pulverization of the specimen material close to the impact surface. When the strain rate increases beyond the critical value the material undergoes further damage on a certain thickness and the waves can be transmitted again. Anyway, such behavior proves that the transmission of the waves is disturbed around the critical impact velocities. This effect should be tested with more details in the future.

References

- [1] Hopkinson B., A method of measuring the pressure produced in the detonation of explosives or by impact of bullets, Phil. Trans. Royal Soc. London, A 213. (1913), 437.
- [2] Davies R.M., A critical study of the Hopkinson pressure bar, Phil. Trans. Royal Soc. London, A240 (1948), 375.
- [3] Kolsky H., "An investigation of the mechanical properties of materials at very high rates of loading " Proc. Phys. Soc., London, B62, (1949), 672.
- [4] Lindholm U. S., "Some experiments with the Split Hopkinson Pressure Bar " J, Méch. Phys. Solids, Vol. 12, (1964), p. 317.
- [5] Klepaczko J.R., Advanced experimental techniques in materials testing, Ch.6 in New Experimental Methods in Material Dynamics and Impact, eds. W.K.Nowacki and J.R.Klepaczko, IFTR, Warsaw, (2002), 223.
- [6] Belouettar R., Klepaczko J. R., Abadlia M. T., Étude du comportement mécanique du béton cellulaire autoclavé : influence de la vitesse de déformation , Revue Française de Génie Civil, 5 n° 5 (2001), 667.
- [7] Klepaczko J. R., " Quasi-static and Dynamic Compression Behavior of Coal ", Report n° 1, Department of Mech. Eng. The university of Manitoba, Canada, (1982)